

Monitoring and Control of Metal Additive Manufacturing Processes Using Ultrasound

by

Alejandro Pedro Martinez

A thesis
presented to the University of Waterloo
in fulfillment of the
thesis requirement for the degree of
Doctor of Philosophy
in
Mechanical and Mechatronics Engineering

Waterloo, Ontario, Canada, 2023

© Alejandro Pedro Martinez 2023

Examining Committee Membership

The following served on the Examining Committee for this thesis. The decision of the Examining Committee is by majority vote.

Supervisor: **Ehsan Toyserkani**, Professor
Dept. of Mechanical and Mechatronics Engineering
University of Waterloo

Internal Member: **Behrad Khamesee**, Professor
Dept. of Mechanical and Mechatronics Engineering
University of Waterloo

Internal Member: **Hyock Ju Kwon**, Professor
Dept. of Mechanical and Mechatronics Engineering
University of Waterloo

Internal-External Member: **Alfred Yu**, Professor
Dept. of Electrical and Computer Engineering
University of Waterloo

External Member: **Farbod Khameneifar**, Professor
Dept. of Mechanical Engineering
Polytechnique Montréal

Author's Declaration

This thesis consists of material all of which I authored or co-authored: see Statement of Contributions included in the thesis. This is a true copy of the thesis, including any required final revisions, as accepted by my examiners.

I understand that my thesis may be made electronically available to the public.

Statement of Contributions

Chapter 3 of this dissertation consists of an article that was co-authored by myself, Dr. Reza Esmailizadeh, and my supervisor. Dr. Reza Esmailizadeh and I conducted the experiments. I developed and ran the reconstruction algorithms, and wrote the article. Dr. Reza Esmailizadeh and I measured the surface profile of the samples. All authors guided the research, and helped with reviewing and editing of the article.

Chapter 4 of this dissertation consists of an article that was co-authored by myself, Dr. Maziar Ansari, Mr. Marc Wang, Dr. Asier Marzo, and my supervisor. Dr. Maziar Ansari, Mr. Marc Wang and I conducted the experiments. I developed the analytic model and developed and ran the simulations. Dr. Asier Marzo provided guidance on the experiment design and analysis of the results. All authors guided the research, and helped with reviewing and editing of the article.

Chapter 5 of this dissertation consists of an article that was co-authored by myself, Dr. Maximilian Klumpp, and my supervisor. I developed and ran the simulations. Dr. Maximilian Klumpp and I developed the analytic expressions. All authors guided the research, and helped with reviewing and editing of the article.

Chapter 6 of this dissertation consists of an article that was co-authored by myself, Dr. Maziar Ansari, Dr. Asier Marzo, Mr. Marc Wang, Mr. Sebastian Soo, and my supervisor. Dr. Maziar Ansari, Mr. Marc Wang and I conducted the experiments. I developed and ran the simulations. Mr. Sebastian Soo was in charge of the polishing and etching of the samples. All authors guided the research, and helped with reviewing and editing of the article.

Abstract

Laser powder bed fusion (LPBF) and Directed energy deposition (DED) are two classes of additive manufacturing (AM) that are widely used to fabricate metal components. In these processes, metal powder or wire and a heat source are applied to form a moving melt pool, followed by solidified tracks to form the component in a layer-by-layer fashion. The solidified melt pool track gradually adds material to build a component from scratch or can be used to add material to a damaged component to refurbish it. DED via powder-feeding (DED-PF) uses metal powder as a feedstock and usually uses a laser as an energy source. A DED-PF machine using a laser energy source is referred to as laser DED-PF (LDED-PF). DED-PF has further advantages compared to other DED methods, such as being able to gradually change the volume fraction of different powders to produce functionally graded materials, which can be used to make high-performance aerospace components that are resistant to high temperatures for example.

The first part of this thesis focuses on techniques for in-situ detection of near-surface defects as they are being produced, which may be used for either LPBF or DED. In particular, techniques for LPBF using laser ultrasound (LU); a non-contact method that generates and measures sound waves reflected from defects such as voids inside a metal sample. This is advantageous for in-situ AM metal inspection, since placing and removing a sensor in contact with the high-temperature topmost layer or track could substantially increase the fabrication time. A reconstruction method in the frequency domain was implemented (phase shift migration) that also accounts for the offset between the generation and detection lasers spots for detecting defects that are close to the surface. The method was tested for both AlSi10Mg and Ti6Al4V samples with three different types of artificial defects to determine which artificial defects are most appropriate to test LU setups. The surface roughness induced during these AM processes was mimicked by printing the samples without up-skin. The effect of the sound generation laser on the final surface roughness, which may determine the spreadability of the powder in subsequent layers, was also investigated. Novel computationally efficient methods to filter the expected unwanted signals in the initial ultrasound data in the frequency domain as well as the fast computation of a stationary phase approximation within the reconstruction were also developed. Defects with a size range from about 200 to 300 μm printed in Ti6Al4V can be recognized from the background noise of the reconstruction. The computation time of the stationary phase approximation with a more accurate initial estimate of its stationary point was reduced by 33%.

The second part of the thesis focuses on finer control of the powder stream profile for the DED-PF processes. This is done using sound radiation forces produced by high-intensity ultrasound. These forces can be applied to the powder stream to change the area and/or cross-section of the powder stream to indirectly affect the melt pool and increase powder catchment efficiency. This could be used to change the melt pool size, shape, and/or internal convective flows, to increase printing speeds and/or reduce defects. An initial proof-of-concept study was carried out with Ti6Al4V and SS 316L powders to demonstrate control of the narrowing of the powder stream from a gravity hopper with a DED-PF nozzle analog. The experimental results were compared with an in-house software library, that can quickly calculate the sound force fields from an ultrasound array using automatic differentiation, and can perform particle tracking. Also, a novel Eulerian-Eulerian approach that can model the powder as a dilute phase was developed, which can more accurately model the effect of a force field, by using an initial condition for the particle speeds. An implementation was also carried out in a modified LDED-PF machine to increase the cross-sectional area, and related catchment efficiency, of Ti6Al4V tracks. A novel model of the powder stream subject to a force field was also developed. Using particle track statistics, the powder stream from a DED-PF nozzle can be modeled using a Gaussian beam model, which is conventionally used to model laser beams. Within this model, it is shown that one can model the powder stream particle concentration distribution (PCD) while being subject to a focusing force field with an equivalent optical transfer matrix. For the initial proof of concept study, using Ti6Al4V and SS 316L particles at a particle speed of 0.6 m/s, the downstream powder stream width was reduced by at least 30%. For the experiment implemented in an LDED-PF machine using Ti6Al4V particles at a particle speed of 3.6 m/s, the powder stream width at the substrate was reduced by 38%. This produced an increase in track height of 72%, and cross-sectional area of 111%, for an original average height of 0.4 mm and area of 0.93 mm², when using a laser power of 900 W. The Gaussian beam model was able to produce more accurate cross-section profiles of the powder stream when subject to a force field, while also reducing the simulation time from 34 minutes (using a Lagrangian particle simulation implemented in C++) to 0.2 seconds (using the Gaussian beam model implemented in MATLAB).

With these two techniques, in-situ and ex-situ monitoring and control may be carried out for metal AM processes. Both these research areas could be integrated to produce a novel DED-PF system that has superior sensing capabilities to find defects in situ as well as finer control of the melt pool, allowing for better quality control. One could use such a system, together with the appropriate control algorithms to tune the process in situ to reduce defects or even correct them. This new system has the potential to produce parts at a lower cost due to less material waste.

Acknowledgements

I would like to first thank my PhD supervisor, Prof. Ehsan Toyserkani, for his excellent guidance, mentorship and unwavering support.

I would also like to thank my examining committee, Prof. Alfred Yu, Prof. Behrad Khamee-see, and Prof. Hyock Ju Kwon for their guidance and support in completing this work.

I would like to extend thanks to my teachers, Ulpiana Tarabal, Peter Hanson, Stan Kolenko, and Genadi Geniev.

I would like to thank my Master's supervisor Prof. David Steinman for his guidance and support, and my Master's examiner and instructor Prof. Adrian Nachman, for his contagious passion for applied mathematics, his feedback, guidance and support.

I would like to thank my friends and collaborators Maziar Ansari, Prof. Asier Marzo, Maximilian Klumpp, Marc Wang, Sebastian Soo, Reza Esmaeilizadeh, and Osezua Ibhadode.

I would like to extend a special thanks to the technical and research staff members of MSAM that supported my work throughout the last few years - Jerry Ratthapakdee, Grace Kurosad, Karl Rautenberg, James Farnsworth, Robert Cieniawski, Allan Rogalsky, Mark Kirby, and Farzad Liravi.

I would like to thank Neil Griffett for all his support in helping to assemble the electronics used in this work. I also thank all the machinists at the E3 and E5 Engineering machine shops, in particular, Mark Kuntz, Richard Forgett, Fred Bakker and Jeff McCormick; thank you for all the 3" by 3" Titanium plates!

I have been fortunate to forge numerous friendships at MSAM throughout my time at the University of Waterloo. Thank you to Ken Nsiempba, Sagar Patel, Shahriar Shahabad, Gijs van Houtum, Brian Zhang, Pablo Enrique, Heba Farag, Ruijian He, Gitanjali Shanbhag, Evan Wheat, Ehsan Marzbanrad, Issa Rishmawi, Lisa Brock, Miald Azvar, Ali Zardoshtian, Sera Ertay, Henry Ma, Paola Russo, Ali Keshavarzkermani, Yanli Zhu, Brian Jeong, Pranav Agarwal, Jigar Patel, Elham Davoodi, Yuze Huang, Tatevik Minasyan, Joseph Orakwe, Yahya Mahmoodkhani, Tomisin Oluwajuyigbe, Ramona Fayazfar, Roman Boychuk, Kevin Hugh Zhang, Katayoon Taherkhani, Nivas Ramachandiran, Osazee Ero, Parichit Kumar, Esmaeil Sadeghi, and Paria Karimi.

Finally, I would like to thank my parents, brother, family and dearest friends for their unconditional love and support.

Dedication

I dedicate this work to everyone that is above all curious about what is possible, even more curious about what might be possible, has a beginner's mindset, the courage to risk being wrong, and the satisfaction of having a chance to, maybe, bring something new, all the way from before thought to the material world.

It is not the critic who counts; not the man who points out how the strong man stumbles, or where the doer of deeds could have done them better. The credit belongs to the man who is actually in the arena, whose face is marred by dust and sweat and blood; who strives valiantly; who errs, who comes short again and again, because there is no effort without error and shortcoming; but who does actually strive to do the deeds; who knows great enthusiasms, the great devotions; who spends himself in a worthy cause; who at the best knows in the end the triumph of high achievement, and who at the worst, if he fails, at least fails while daring greatly, so that his place shall never be with those cold and timid souls who neither know victory nor defeat

Theodore Roosevelt

The future cannot be predicted, but futures can be invented

Dennis Gabor

Se nace lo que se es, o se será aquello en lo que se crea

Jorge Drexler

Table of Contents

List of Figures	xvi
List of Tables	xxv
List of Abbreviations	xxvi
List of Symbols	xxix
1 Introduction	1
1.1 Additive Manufacturing: a key game changer in advanced manufacturing	1
1.2 Motivation, challenges and opportunities	1
1.3 Objectives	3
1.4 Thesis Layout	5
2 Background and Literature Review	6
2.1 Metal additive manufacturing and its challenges	6
2.1.1 Additive manufacturing	7
2.1.2 Laser powder bed fusion (LPBF)	8
2.1.3 Directed energy deposition (DED)	10
2.1.4 LPBF and LDED-PF defects	13
2.1.5 LDED-PF analytic modeling	14
2.1.6 LDED-PF numerical modeling	15

2.2	Non-destructive testing (NDT) methods	18
2.3	Acoustics and Ultrasound NDT (UT)	20
2.3.1	Transducers	22
2.3.2	Imaging methods	23
2.4	Laser ultrasonics (LU)	27
2.4.1	Sound generation analytic models	29
2.4.2	Sound generation numerical models	31
2.4.3	Sound generation laser characteristics	32
2.4.4	Laser based sound detection techniques	32
2.4.5	Detection laser characteristics	34
2.4.6	LU commercial setups	35
2.5	NDT use for metal AM in-situ monitoring	36
2.5.1	NDT	36
2.5.2	Ultrasound NDT	37
2.5.3	Laser ultrasonics	38
2.6	Sound radiation force and current applications	40
2.6.1	Applications of sound radiation force in microfluidics	40
2.6.2	Sound radiation force for sorting of aerosol particles	42
2.6.3	Acoustic levitation	42
2.7	Summary	45
3	Laser Ultrasound Tailored for LPBF	46
3.1	Introduction	46
3.2	Materials and methods	50
3.2.1	Sample design and fabrication	50
3.2.2	Laser ultrasound system and setup	52
3.2.3	Expected ultrasound signals	53
3.2.4	B-scan pre-processing	54

3.2.5	Image reconstruction using phase shift migration	57
3.2.6	CT system and setup	61
3.2.7	Surface roughness	62
3.3	Results and discussion	62
3.3.1	Effect of pre-processing B-scan	62
3.3.2	AlSi10Mg samples	65
3.3.3	Ti6Al4V samples	67
3.3.4	Surface signal removal based on the Fourier slice theorem	75
3.3.5	Track surface roughness	75
3.4	Summary	80
4	Demonstration of Ultrasound Particle Lensing with DED-PF powders	81
4.1	Introduction	81
4.2	Proposed ultrasound particle lensing technology	83
4.3	Modeling	87
4.3.1	Individual particle lensing model	87
4.3.2	Sound force field calculation	89
4.3.3	Eulerian particle model	90
4.3.4	Lagrangian particle model	92
4.4	Materials and methods	92
4.4.1	Prototype design and build	92
4.4.2	Experimental setup	94
4.4.3	Experimental procedure	95
4.4.4	Obtaining intensity images	96
4.4.5	Powder widths	97
4.4.6	Catchment efficiency proxy	99
4.4.7	Powder stream divergence angle	100
4.4.8	Particle concentration from thresholded images	100

4.4.9	Initial conditions for simulations	102
4.5	Results and discussion	102
4.5.1	Powder stream 2D concentrations	102
4.5.2	Comparison of downstream particle concentration	103
4.5.3	Powder stream widths	104
4.5.4	Catchment efficiency proxy	104
4.5.5	Powder stream divergence angles	105
4.5.6	Comparison with analytic model	106
4.5.7	Particle concentrations downstream of the sound field	107
4.5.8	Lagrangian and Eulerian simulations	108
4.6	Summary	113
5	Gaussian Beam Representation of DED-PF Powder Stream	115
5.1	Introduction	115
5.2	Theoretical and experimental methods	121
5.2.1	Particle tracking and trajectory extrapolation	121
5.2.2	Ray statistics from divergence angle and nozzle width	125
5.2.3	Lagrangian particle simulation in the presence of a force field	127
5.2.4	The focusing sound field as an optical transfer matrix	129
5.2.5	Optimal powder focusing based on optical analog model	132
5.3	Results and discussion	135
5.3.1	Particle path statistical characteristics	135
5.3.2	Ray statistical characteristics assuming a GBR	137
5.3.3	Lagrangian particle simulation	139
5.3.4	Powder focusing modeled as an optical system	142
5.4	Summary	149

6	Ultrasound Particle Lensing Tailored for LDED-PF	151
6.1	Introduction	151
6.2	UPL technology applied to powder stream control in LDED-PF	153
6.3	Modeling	156
6.3.1	Sound and force field simulation	157
6.3.2	Particle stream GBR	158
6.4	Materials and methods	160
6.4.1	Directed energy deposition machine modifications	160
6.4.2	Experimental setup	164
6.4.3	Particle concentration distribution acquisition procedure	166
6.4.4	Particle concentration distribution measurements	166
6.4.5	Single track runs procedure	168
6.4.6	Track geometry measurements and calculations	168
6.5	Results and discussion	172
6.5.1	Sound field simulation results	172
6.5.2	Powder stream 2D concentrations	172
6.5.3	Downstream particle stream characteristics	176
6.5.4	Track geometry	177
6.5.5	Track dilution zone measurements	180
6.6	Summary	182
7	Conclusions and Future Work	184
7.1	Overall conclusions	184
7.2	Future work	186
	Letters of Copyright Permission	190
	References	199

APPENDICES	228
A Derivations related to the Gor'kov potential	229
B Separable frequency based filter for B-scan	233
C Derivation of the double square root equation	235
D Newton's method design for computing the stationary point for SPA	238
E Particle lensing model	243
F Modeling and algorithms used in software library	247
G Eulerian powder stream model with novel initial condition	250
H Lagrangian powder stream model	257
I Parameters for expected value of coefficient of determination in GBR	263
J Automatic differentiation in the acousticHologram library	268
K Array mesh computation	271
L Fabrication and alignment of UPL array/frame assembly	274
M Sound-particle-laser interactions	281
N UPL feed gas considerations	284
O Repeat of adjacent tracks	289

List of Figures

1.1	Hypothetical multi-beam LDED-PF machine with different sensing (NDT) and control options.	3
2.1	Relationship between build rate, laser power and feature quality. Reprinted with permission from [16].	8
2.2	Diagram of the LPBF process at the machine and powder scales. Reprinted with permission from [19].	9
2.3	SEM images of LPBF fabricated maraging steel (18Ni-300). (a) Top view, (b) side view and (c) magnification of dendritic structure. Reprinted with permission from [17].	10
2.4	DMD IC106 from DM3D, a LDED-PF system, in operation.	11
2.5	Types of LDED-PF setups used in industry. (a) Continuous coaxial (L-C). (b) Discrete coaxial (L-N). (c) Multi-beam (P-N).	12
2.6	Microstructure of LDED-PF manufactured Ti6Al4V part in the y-z plane at different regions. Reprinted with permission from [25].	13
2.7	Predicted (a) vs. experimental (b) powder streams [37]. Experimental conditions can be found in [37]. Reprinted with permission from [37].	16
2.8	(a) Trumpf nozzle in operation, (b) its schematic and (c) gas velocity field. (d) Particle tracks and particle concentration at (e) nozzle cross section and (f) at the substrate. Reprinted with permission from [26].	17
2.9	Diagram relating different UT display methods (courtesy of Sonatest [50]). The L-scan shown in the diagram is a less used display method that is similar to a B-scan but is obtained by sequentially activating the transducers in a linear ultrasound array.	21

2.10	Classification of ultrasound imaging methods (including delay-and-sum methods) based on simplifications and assumptions applied to the elastic wave equation.	26
2.11	Example 8 by 8 flat rectangular array setup levitating a particle (from supplementary material of [147]).	43
2.12	Acoustic traps: twin (left), vortex (center), bottle (right). The pressure isosurfaces shown are for 2 KPa for the twin and vortex traps and 1.3 KPa for the bottle trap [147].	44
3.1	SH 2 sample design. In the embossing on the right HD stands for hole diameter and SD stands for surface depth to the top of the defect.	51
3.2	Schematic (a), and labeled photo (b) of experimental setup used to obtain B-scans. To hold the sample shown, a special sample holder to place the sample against two perpendicular directions for fast-changing was designed and FDM printed.	52
3.3	(a) Scan direction with respect to SH 1 sample (a), and (b) laser and relevant sound wave vectors produced in the LU process.	53
3.4	The way to remove linear features in the B-scan in [166] is to perform a Hough transform and crop the signal peaks in the resulting sinogram. However one needs to rotate the image for many angles and to numerically integrate the B-scan at each angle. As illustrated in this figure, the 1D FT of the angle where the line is expected in the B-scan is simply the 2D FFT sampled at a line through the origin of k-space and at an angle corresponding to the line angle, therefore removing high amplitudes along this line in k-space will have a similar effect to cropping the sinogram. The displayed magnitudes for the FTs are their real components.	56
3.5	(a) B-scan from SH 1 sample, and (b) A-scans # 2 (blue dotted line) and # 162 (orange dotted line) from the same B-scan.	64
3.6	(a) The original B-scan with laser signal zeroed area and cropped RW, (b) B-scan (a) with with AF, (c) B-scan (a) with maximum SLW normalization, and (d) comparison between A-scans from dotted lines in B-scans (a) and (b).	66
3.7	(a) Envelope B-scans of B-scan in Fig. 3.6, and (c) of B-scan in Fig. 3.6.	67
3.8	(a) The reconstructions for SH 1 corresponding to the B-scans in Fig. 3.6, and (b) the signal intensities along x along the red dotted lines.	68

3.9	SH 1 reconstruction.	69
3.10	SH filtered B-scans. The SH 1 filtered B-scans can be seen in Fig. 3.6 (c).	70
3.11	SH reconstructions. The SH 1 reconstruction can be seen in Fig. 3.9.	71
3.12	Filtered B-scans of all Ti6Al4V samples.	72
3.13	Reconstructions of BH samples. For each of the BH and TP reconstructions from top to bottom, the CAD cross-section is shown, followed by the CT scan, the PSM reconstruction and the signal along the red line on the reconstruction, placed 0.2 mm below the top of each defect in the sample.	73
3.14	Reconstructions of TP samples.	74
3.15	(c) B-scan and (a) 2D FT of SH 1 with longitudinal wave normalization. (b) Application of filters (DC, SW notch filters and 2D Butterworth filter) in Algorithm 2 to 2D FT and (d) resulting B-scan.	76
3.16	(a) Comparison reconstructions between the current algorithm and the same algorithm using k-space filters in Algorithm 2. (b) Signal intensity as a function of x along the red dotted lines.	77
3.17	Surface and line roughness measurements for SH 1.	78
3.18	Surface and line roughness measurements for TP 1.	79
4.1	Averaged sound pressure (ASP), potential and force slices along an acoustic vortex. (a) ASP, (b) Gor'kov potential, (c) x component of the force field and (d) z component of the force field. The height and width of the frames is 30 by 20 mm respectively. For this sound field the y component of the force field is equal to the x component due to symmetry about the z axis.	84
4.2	(a) ASP field, with particles tracks, and isosurface with a radial sound radiation force value of -4.0×10^{-9} N per particle, based on the SS 316L at 16 V simulation shown in Section 4.5.8. (b) Sound radiation force in x -axis direction along the red line.	85
4.3	Diagrams showing the variables used in the analytic model for; (a) transducers and sound field and (b) coordinate axes and particle trajectories.	87
4.4	(a) Internal geometry of the hopper and powder feed mechanism. (b) Array frame, hopper and connecting frame assembly. (c) Assembled ultrasonic array attached to the hopper assembly.	94

4.5	Schematic of the experimental setup showing lighting and camera setup (not to scale). The focal axis of the camera and the light were in the same plane, with the array axis normal to this plane, and the sound focus point intersecting it. The distance from the front of the camera lens and the light to the sound focus point was 72 and 51 cm respectively. The angle between the camera and the light center-line axis was 22° and setup to be as small as possible for uniform illumination.	95
4.6	(a) Volumes used in Eq. 4.10 from a Gaussian distribution, and (b) from a new distribution.	98
4.7	Added frames from high-speed camera for first repeat for Ti6Al4V at (a) 0 and (b) 8 V, and first repeat for SS 316L at (c) 0, (d) 10 and (e) 16 V.	103
4.8	Surface plots of added frames from high-speed camera of the first repeat for Ti6Al4V at (a) 0 and (b) 8 V, and first repeat for SS 316L at (c) 0, (d) 10 and (e) 16 V.	104
4.9	Gauss fits downstream of applied sound field for first repeat for Ti6Al4V at (a) 0 and (b) 8 V, and first repeat for SS 316L at (c) 0, (d) 10 and (e) 16 V.	105
4.10	Powder stream widths for all materials and applied voltages.	106
4.11	Mass fraction inside $0 V e^{-1}$ mass fraction powder width for all materials and voltages.	107
4.12	Powder stream divergence angles downstream of sound field for all materials and voltages.	108
4.13	Angles computed using RK4 particle tracking and analytic angles for all materials and voltages.	109
4.14	Actual and estimated mass flow rates for all materials and voltages.	110
4.15	Particle concentration downstream of sound field for 0 and 8 V, for Ti6Al4V.	111
4.16	Particle concentration downstream of sound field for 0, 10 and 16 V, for SS 316L.	111
4.17	Particle concentration downstream of sound field for Ti6Al4V, at 0 and 8 V, overlapped with Lagrangian and Eulerian simulations.	112
4.18	Particle concentration downstream of sound field for SS 316L, at 0 and 10 V, overlapped with Lagrangian and Eulerian simulations.	112
4.19	Particle concentration downstream of sound field for SS 316L, at 0 and 16 V, overlapped with Lagrangian and Eulerian simulations.	113

4.20	Comparison of e^{-1} radii obtained from measured and simulated data. . . .	114
5.1	(a) Period averaged sound pressure (ASP), (b) x component of the resulting force field, (c) z component of the resulting force field. (d) ASP field, with particles tracks, and isosurface with a radial sound radiation force value of -4.0×10^{-9} N per particle, based on the setup for SS 316L particles with sound produced at 16 V in Chapter 4 and (e) sound radiation force in the x-axis direction along the red line.	117
5.2	Particle motion mechanisms; (a) diffusion [198], (b) initial velocities with linearly increasing tangential components (Chapter 4), (c) hypothesis in this chapter.	118
5.3	Powder PCD and some of its properties: symmetry about z, mass conservation (polar integral about z of $c(x, z)$ equal for all z-values), IRW, given by value of powder radius r such that $c(r, z_n)/c(0, z_n) = k$ (where k is a constant such as e^{-1} or e^{-2}) increases linearly with z downstream of the nozzle.	119
5.4	$y-\bar{y}$ diagram corresponding to powder exiting a nozzle and interacting with a focusing sound radiation force field. (a) First case; $w_0 = 2.2$ mm, $z_R = 21.2$ mm, $l_i = 20.0$ mm, $l_{fs} = 10.0$ mm and $\eta = 59.4$ m $^{-1}$. (b) Case shown in a with higher nozzle to sound field distance ($l_{fs} = 19.7$ mm). (c) Case shown in (b) with higher applied transducer array voltage ($\eta = 92.0$ m $^{-1}$).	133
5.5	Powder waist half width downstream of applied sound field as a function of l_{fs} and η	134
5.6	Particle paths from (a) high speed video. (b) Extrapolated paths.	135
5.7	Speed ratio of the particle paths as a function of x -location at different distances from the nozzle.	136
5.8	Measured slope of speed ratio as a function of x and measured r^2 value for different nozzle distances.	137
5.9	Speed ratio of the particle paths downstream of applied force field.	138
5.10	Powder GBR model geometry.	139
5.11	Slope of x vs. speed ratio (slope of line given by Eq. 5.30) and expected r^2 value (given by Eq. 5.38) of fitted line along z	140
5.12	Powder profile along x downstream of the sound force field when using 0 and 10 V.	141

5.13	Powder profile along x downstream of the sound force field when using 0 and 16 V.	142
5.14	Comparison of measured powder stream widths and simulated powder stream widths.	143
5.15	Powder profile along x downstream of the sound field considering speed standard deviation (STD) and air drag, only considering drag or considering only speed STD. (a) Using a y -axis linear scale and (b) a logarithmic scale.	144
5.16	(a) Powder profile, (b) concentration at center-line along z and (c) half width at center-line along z , all at 0 V.	145
5.17	(a) Measured and (b) calculated powder profiles at 0 V.	145
5.18	(a) Powder profile, (b) concentration at center-line along z and (c) half width at center-line along z , all at 10 V.	146
5.19	(a) Measured and (b) calculated powder profiles at 10 V.	146
5.20	(a) Powder profile, (b) concentration at center-line along z and (c) half width at center-line along z , all at 16 V.	147
5.21	(a) Measured and (b) calculated powder profiles at 16 V.	147
6.1	(a) Possible LDED-PF setup. (b) Close-up showing sound field ASP and sound radiation force isosurface at a value of -4.0×10^{-9} N per particle. (c) Sound radiation force in the x -axis direction along the red line in (b). Sound field simulation parameters are the same as in Fig. 4.2.	153
6.2	Types of LDED-PF setups with UPL array. (a) Continuous coaxial (L-C). (b) Discrete coaxial (L-N). (c) Multi-beam (P-N).	155
6.3	(a) Simulated ASP and (b) sound radiation force field as a function of radial distance from vortex sound field with different topological charges. The simulation parameters are the same ones as the ones used in Section 6.5.1.	155
6.4	(a) Averaged sound pressure (ASP) and (b) x -component of the resulting sound radiation force field when applying 10 V to the array setup in this chapter. Both figures have the relevant variables overlaid.	159
6.5	(a) Modified DM3D machine. (b) Top close-up showing ultrasound array, frame and gas cyclone. (c) Bottom close-up showing ultrasound transducers, powder nozzle and water bypass insert.	160

6.6	(a) Meshing result for transducer placement. (b) Edge distance histogram showing mesh quality.	162
6.7	Array design, assembly and control workflow.	163
6.8	(a) Array and frame setup with dimensions used for experiments. The blue cross below the powder nozzle is the SFP and the red cross is the laser focal point. (b) Array features.	165
6.9	Schematic of the experimental setup showing lighting and camera setup (not to scale). The focal axis of the camera and the light were in the same plane, with the array axis normal to this plane, and the sound focus point intersecting it. The distance from the front of the camera lens and the light to the sound focus point was 72 and 51 cm respectively. The angle between the camera and the light center-line axis was 22° and setup to be as small as possible for uniform illumination.	167
6.10	Track geometric features measured from the cut and etched samples. The background optical image is for track 6-2.	172
6.11	(a) ASP for 10 and 14 V. (b) Radial SRF for 10 and 14 V.	173
6.12	Surface plots of added frames from the high-speed camera of the first repeat for Ti6Al4V at (a) 0, (b) 10, and (c) 14 V.	173
6.13	(a) Measured 2D PCD. (b) Simulated 2D PCD using the GBR model. (c) Center-line measured and simulated PCD. (d) Measured and simulated IRW half-widths. Figures (a) to (d) are for no applied SRF.	174
6.14	(a) Measured 2D PCD. (b) Simulated 2D PCD using the GBR model. (c) Center-line measured and simulated PCD. (d) Measured and simulated IRW half-widths. Figures (a) to (d) are for an applied SRF with an array voltage of 10 V.	175
6.15	(a) Measured 2D PCD. (b) Simulated 2D PCD using the GBR model. (c) Center-line measured and simulated PCD. (d) Measured and simulated IRW half-widths. Figures (a) to (d) are for an applied SRF with an array voltage of 14 V.	175
6.16	(a) e^{-1} widths downstream of the applied sound field. (b) e^{-1} widths at build plate location.	176
6.17	(a) PCD profiles downstream of the applied sound field. (b) PCD profiles at build plate location.	177

6.18	Track cross-sectional areas and catchment efficiencies at 15 mm.	178
6.19	Track maximum heights at 15 mm.	179
6.20	Track widths at 15 mm.	179
6.21	Track profiles at 15 mm for the three repeats at 0 and 10 V, at 900 W. . .	180
6.22	(a) 3D track profile for single track with no applied sound. (b) Track cross-sections at 7 and 23 mm from start of track.	181
6.23	(a) 3D track profile for single track with applied sound at 10 V after half way along the track. (b) Track cross-sections at 7 and 23 mm from start of track.	181
6.24	(a) Height map of single track with sound being applied halfway along the track. (b) Average height as a function of distance from start of track. . . .	182
6.25	For etched samples: (a) dilution fraction, (b) penetration depth, (c) HAZ width, (d) HAZ depth.	183
C.1	Three plane waves of different amplitudes moving on the az_a plane in the direction indicated by the arrows. The a axis corresponds to the sample's surface where the sound waves are recorded. The dotted line indicates an isoline of constant phase γ	236
D.1	An example phase function (a), with a frequency ω of 3.5×10^7 Hz, a spatial frequency k_x of -4.8×10^3 m ⁻¹ , and a depth z of 1.6 mm.	239
D.2	The computation time for S with the PSM parameters used for the AlSi10Mg sample B-scans as a function e_{tol}	240
D.3	Two different approximations for β	241
D.4	Histogram for the number of NM iterations for each SP calculated.	242
H.1	Trajectory endpoint distance change for SS 316L at (a) 0 and (b) 10 V Lagrangian simulation runs.	259
H.2	Sample means and variances as a function of number of particle paths for SS 316L at (a) 0 and (b) 10 V Lagrangian simulation runs.	261
H.3	Sample mean RMS values as a function of number of particle paths for SS 316L at (a) 0 and (b) 10 V Lagrangian simulation runs.	261

L.1	(a) Array printed in a single piece. (b) Close-up of the printed array numbering.	274
L.2	(a) Previous prototype printed in one piece with no internal supports. (b) Gas cyclone CAD with section view showing inlet area and vortex finder. (c) Printed and assembled cyclone with fitting and copper tube extension.	276
L.3	(a) DM3D adapter TO result. (b) Final DM3D adapter CAD. (c) UPL array adapter TO result. (d) Final UPL array adapter design.	278
L.4	(a) Side and (b) front view of the UPL assembly, placed on top of the alignment frame.	279
L.5	(a) Aligned nozzle at set angle showing alignment tip on groove of alignment frame. (b) Alignment frame with attached handle to check the final alignment after installing on UPL assembly on LOA.	280
N.1	Percent differences in sound speed and impedance w.r.t air as a function of volume fraction of Ar in Ar-He gas mix.	287
O.1	Track (a) CS areas, (c) maximum heights, and (e) widths using original data. Track (b) CS areas, (d) maximum heights, and (f) widths using original data with tracks 2 and 3 in plate 2 in opposite order.	290

List of Tables

2.1	Advantages and disadvantages of LDED-PF process	11
3.1	Artificial defect types	49
3.2	AlSi10Mg sample geometries	50
3.3	Ti6Al4V sample geometries	51
5.1	Predicted powder stream parameters from optical analog computations and percent error peak particle concentration with respect to Lagrangian model	148
6.1	Fabricated tracks, their DOE parameters, and demonstration tracks. (r) Redone tracks. (h) Demonstration tracks with voltage applied on the second half of the track.	169
G.1	Convergence analysis of Eulerian simulations for SS 316L at 0 and 10 V . .	255
H.1	Required RK4 time steps and number of particle paths for Lagrangian simulations for all particle materials and array voltages to reach convergence .	262
M.1	Table showing parameters used for Eq. M.2 (all in SI units).	283
N.1	Table showing relevant gas acoustic properties in SI units, and fractional changes with respect to air and α_t values in percentages. θ_Δ was calculated at $\theta_i = 10^\circ$	285
N.2	Table showing relevant gas properties in SI units. Density and sound speed where calculated using the ideal gas law.	288

List of Abbreviations

AF	Average filter
AM	Additive manufacturing
ASP	Period averaged sound pressure
BH	Bottom blind hole artificial defect
BLW	Body, or bulk, longitudinal wave
BWF	Butterworth filter
CFD	Computational fluid dynamics
CT	Computed tomography
DAS	Delay-and-sum (method)
DED	Directed energy deposition
DED-PF	DED via powder-feeding
DEM	Discrete element model
DFT	Discrete Fourier transform
DLD	Directed laser deposition (another name for LDED-PF)
DOE	Design of experiments
DSR	Double square root (equation)
EDM	Electrical discharge machining
ET	Eddy current testing
FD	Frequency domain
FDM	Fused deposition modeling
FEA	Finite element analysis

FFT	Fast Fourier transform
FHF	Flattened hyperbolic feature
FMC	Full matrix capture
FST	Fourier slice theorem
FT	Fourier transform
FT-SAFT	FT SAFT
GBR	Gaussian beam representation
GRIN	Gradient index (lens)
HAS	Heat affected zone
HIP	Hot isostatic pressing
HOT	Holographic optical tweezers
IL	Sound intensity level
IR	Infrared
IRW	Intensity ratio width
LDED-PF	Laser DED-PF
LPBF	Laser powder bed fusion
LU	Laser ultrasonics
LZT	Lead zirconate titanate
NDT	Non-destructive testing
NM	Newton's method
OA	Occlusion area (due to artificial defect)
PCD	Particle concentration distribution
POD	Probability of detection
POFFIS	Physical optics far field inverse scattering
PSD	Particle size distribution
PSM	Phase shift migration
PT	Penetrant testing
RW	Rayleigh wave
SAFT	Synthetic aperture focusing technique

SAR	Synthetic aperture radar
SFP	Sound focus point
SH	Side through-hole artificial defect
SLAM	Scanning laser acoustic microscope
SLW	Surface longitudinal wave
SPA	Stationary phase approximation
SPL	Sound pressure level
SRAS	Spatially resolved acoustic spectroscopy
SRF	Sound radiation force
TFM	Total focusing method
TIR	Thermal infrared testing
TO	Topology optimization
TP	Spherical trapped powder artificial defect
TS	Thresholded and summed images
UPL	Ultrasound particle lensing
UT	Ultrasound testing
VED	Volume-based energy density

List of Symbols

A_d	Dilution area
A_t	Track cross-sectional area
B	B-scan matrix or array
C_D	Drag coefficient
c	Powder particle concentration or sound speed
D	Diffusion constant
d_d	Defect surface depth
F	Applied force
f	Temporal frequency
g	Gravitational acceleration or pixel grey level value
H	2D frequency domain filter, Hilbert transform, transducer directivity function or track penetration depth
h_0	LU generation/detection laser spot offset distance
J_n	Bessel function of the first kind and order n
k	Wavenumber (spatial frequency)
l_f	Focal length
l_{fov}	Field of view thickness
l_i	Powder stream interaction length with sound field

l_{offset}	Distance from the SFP along the x -axis where the force is half the peak sound radiation force
l_x	Pixel size
M	Magnification or optical transfer matrix
\dot{m}	Mass flowrate
m_p	Particle mass
n	Index of diffraction
P	2D FT or DFT of B-scan
P_{pp}	Peak-to-peak pressure
p	Complex pressure or pixel location value
q	Gaussian beam complex source position
R	Gaussian beam radius of curvature or e^{-1} ratio powder stream radius
Ra	Arithmetic mean height on a line
Re	Reynolds number
r	Particle normal distance to particle stream center-line or distance to transducer
r_0	Radius offset in powder stream model
r^2	Coefficient of determination
r_p	Particle radius
Sa	Arithmetic mean height on a surface
T	Wave or signal period
t	Time or wave pulse arrival time
U	Gor'kov potential
U_0	Piston speed for sound transducer piston model
\mathbf{u}	Particle velocity, with components u_a (where a is the coordinate axis), and speed (vector magnitude) $ \mathbf{u} $. u_z may also stand for the average u_z of many particles

V_p	Particle volume
V_{pp}	Peak-to-peak voltage
v_t	Track deposition speed
W	2D DFT transform matrix or track penetration width
w	Gaussian beam e^{-2} ratio half-width
w_0	Gaussian beam waist e^{-2} ratio half-width
z	Vertical distance from start of powder stream or specific acoustic impedance
z_0	Gaussian beam offset along its axis
z_R	Gaussian beam Rayleigh range
Δ	Spatial increment
ε	Pixel grey level binarization threshold
η	Catchment efficiency or GRIN optical transfer matrix parameter
θ	Particle deflection angle, powder stream divergence half-angle or angle to transducer center-line
κ	Compressibility
λ	Wavelength
μ	Viscosity
ρ	Density
ϕ	Velocity potential or phase
ω	Angular frequency

Chapter 1

Introduction

1.1 Additive Manufacturing: a key game changer in advanced manufacturing

The use of additive manufacturing (AM) has the potential to produce intricate, lightweight and individually customized parts that are too costly or impossible to produce using subtractive manufacturing techniques. In other words, AM has been shown to address “economies of scope”. The technology can also reduce waste compared to the scraps generated from subtractive manufacturing. Other advantages include: removing the reliance on original equipment manufacturers for critical spares and extending the life of in-service parts through other AM enabled repair methodologies [1].

1.2 Motivation, challenges and opportunities

AM is starting to be deployed for “economies of scale” (mass-production), while retaining its advantages of “economies of scope”. This new trend has opened up many new R&D opportunities as well as challenges, related to quality assurance and inspection while the part is being fabricated as well as for post-process inspection. This is one of the most important factors in industry, which carries out quality management and certification when doing serial production.

The need for reliable and cost effective in-situ monitoring of metal AM processes, such as laser ultrasound (LU), to minimize defect production as well as qualification of AM metal parts, is highlighted in a recent NASA proposal [2]. LU would be very useful for in-situ AM metal inspection, since it can be performed in a non-contact way and at high temperatures [3, 4]. Another very useful feature of LU is that it can be used concurrently for defect detection and residual stress measurements [5]. Commercial companies such as Space Exploration Technologies Corp. (SpaceX) also use AM to produce some critical rocket engine components [1]. Since the publication of [2] in 2017, there have been other commercial companies appearing that also use AM for rocket engine components like Relativity Space Inc. [6], and Launcher Inc. [7]. These companies which aim to produce most of their components with metal AM technologies would benefit even more from LU technology as well. Other aerospace companies specializing in the aviation sector such as General Electric and Lockheed Martin that already produce and use metal AM components [8] would also find LU an attractive technology. As described in Section 2.4.5, Lockheed Martin already uses LU to inspect polymer-matrix composite parts.

The directed energy deposition (DED), in particular the DED via powder-feeding (DED-PF) process, has many advantages such as the ability to produce materials with spatially variable material properties (functionally graded materials or FGMs) as well as extending the life of in-service parts through part repair, but is susceptible to material loss due to the fraction of particle reaching the melt pool (catchment efficiency) being lower than 100%. Any technique that can increase the catchment efficiency in this process is desirable by industry in order to reduce material utilization costs. Another issue is the formation of internal defects, which can be explained in part by the high cooling rate and molten metal convection within the metal melt pool. There has been recent commercial interest in DED-PF for rapid alloy development, for example using the ADF Alloy Development Feeder from FormAlloy Technologies Inc. [9]. With the aim of future private partnerships, NASA is demonstrating the use of DED-PF to fabricate large aerospace components such as rocket nozzle liners, for example through the RAMPT project, where they partnered with DM3D Technology LLC to produce a custom DED-PF machine and fabrication process [10]. In order to show the advantages of DED-PF for manufacturing aerospace components with FGMs, Innstek Inc. manufactured a three ton rocket nozzle [11].

Although most DED-PF machines use a laser energy source (LDED-PF), the machine may use another energy source, therefore, for the rest of the thesis, if a statement does not refer to an LDED-PF machine in particular, the acronym DED-PF will be used.

1.3 Objectives

The main objective of the research is to demonstrate ultrasonic-based techniques that can be used to improve metal AM processes. This proposal focuses on the following two main areas:

- Better in-situ non-destructive testing (NDT) of metal AM processes, using non-contact NDT modalities such as LU
- Finer control of the in-situ placement of feedstock used in metal AM processes, such as the ability to change the powder stream cross-sectional shape and size in DED-PF using sound radiation forces, to increase part quality and material utilization

The above issues fit within the larger trend of producing metal AM machines with closed loop control, in order to increase part quality and material utilization while reducing part cost. A hypothetical LDED-PF machine showing some of the technologies that would allow for closed loop control is shown Fig. 1.1.

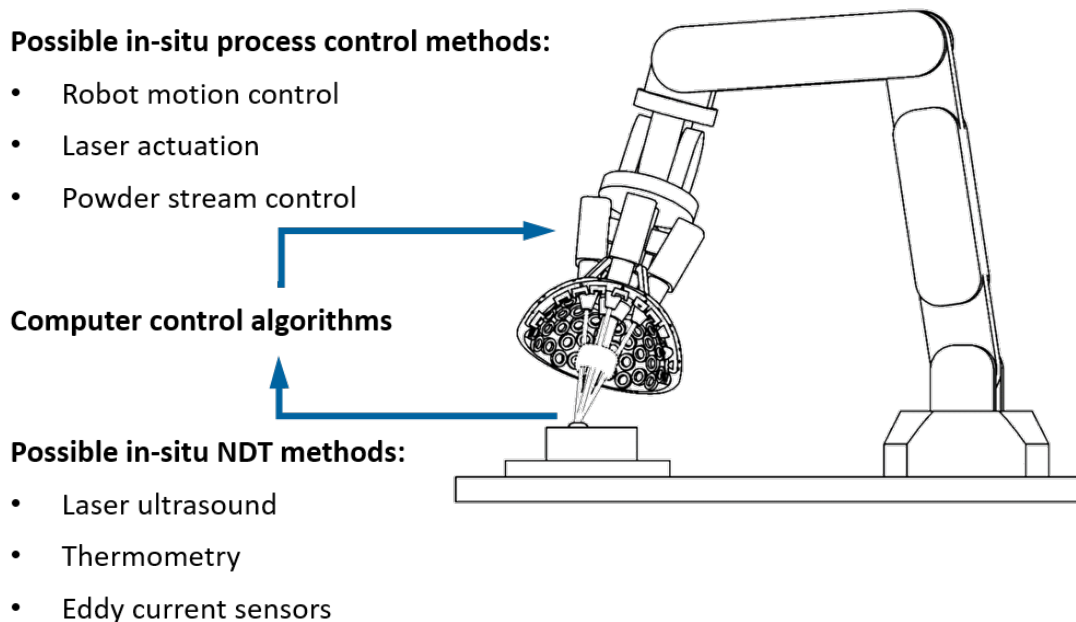


Figure 1.1: Hypothetical multi-beam LDED-PF machine with different sensing (NDT) and control options.

The first part of the research is the development of LU setups and imaging algorithms for non-destructive testing. The scope of this work will be limited to in-situ inspection of parts produced by the laser powder bed fusion (LPBF), using AlSi10Mg and Ti6Al4V powder feedstock. This work was done using LPBF because the artificial defects that can be produced for testing that have a minimum size that is closer to actual defect sizes than the ones achievable with LDED-PF, however the developed techniques from this work may also be used to detect LDED-PF defects.

To carry out this development, the following sub-goals are pursued:

- Calibration of the LU machine used in this research (LUKS-1550-TWM system) with appropriate test samples
- Demonstration of a novel and more accurate imaging algorithm taking into account the LUKS-1550-TWM system and the chosen LU setup
- Testing the imaging algorithm on different types of artificial defects found in the literature, to find which one is most useful for testing the accuracy of an LU setup
- Propose new LU system specifications tailored for the LPBF process

The second part of the research is the development of techniques using sound radiation forces to have a finer control of the powder stream used in the DED-PF process. The scope of this work is limited to Ti6Al4V and SS 316L powders. To carry out this development, the following sub-goals are pursued:

- Development of an analytic model of powder stream focusing due to a force field
- Development of algorithms to calculate and simulate the sound fields needed to achieve a required force field for particle stream focusing
- A proof-of-concept experiment to demonstrate particle focusing
- Demonstration of a particle stream focusing system with an ultrasound array installed on a LDED-PF machine
- Propose further experiments aimed to demonstrate deflection and cross-sectional area control, and to use the above techniques to control the melt pool shape to reduce internal part defects

In addition, further experiments are proposed to demonstrate deflection and cross-sectional area control, and to use the above techniques to control the melt pool shape to reduce internal part defects.

1.4 Thesis Layout

This thesis is organized into six chapters. The current chapter presents the overview, motivations, challenges, and objectives of the research. Chapter 2 gives a literature review and background of LPBF and DED-PF followed by an introduction to non-destructive testing, laser ultrasonics, and current applications of sound radiation forces. Chapter 3 describes a reconstruction algorithm tailored for LPBF, and the testing of various artificial defects found in the literature. Chapter 4 describes a proof-of-concept experiment and simulation approach for the focusing of DED-PF powders using an ultrasound phased array. Chapter 5 describes a more advanced powder focusing model, based on a Gaussian beam ray model, that is both more accurate and faster to compute than the initial model proposed in Chapter 4. Chapter 6 demonstrates the use of an ultrasound phased array in an actual LDED-PF machine and the successful solid-state electronic control, through an ultrasound phased array, of the printed track's cross-sectional area.

Chapters are adapted from the following published or to-be-submitted articles:

Chapter 3: A. Martinez-Marchese, R. Esmailzadeh, and E. Toyserkani, Detection of defects in additively manufactured AlSi10Mg and Ti6Al4V samples using laser ultrasonics and phase shift migration. Submitted to Additive Manufacturing Journal and under review.

Chapter 4: A. Martinez-Marchese, M. Ansari, M. Wang, A. Marzo, and E. Toyserkani. On the application of sound radiation force for focusing of powder stream in directed energy deposition. *Ultrasonics* 127 (2023): 106830. <https://doi.org/10.1016/j.ultras.2022.106830>

Chapter 5: A. Martinez-Marchese, M. Klumpp, and E. Toyserkani. Directed energy deposition powder stream modeling using a Gaussian beam ray representation. *Powder Technology* 412 (2022): 117965. <https://doi.org/10.1016/j.powtec.2022.117965>

Chapter 6: A. Martinez-Marchese, M. Ansari, A. Marzo, M. Wang, S. Soo, and E. Toyserkani, Ultrasound particle lensing: powder stream control in directed energy deposition using acoustic radiation force fields. Being reviewed by co-authors, to be sent to Additive Manufacturing Journal for review.

These articles have been modified to fit the content of this thesis. The corresponding license agreements are provided in Section “[Letters of Copyright Permission](#)”.

Chapter 2

Background and Literature Review

The purpose of this section is to provide some background information on AM and the latest developments in LU for the post-process inspection and in-situ monitoring of the internal material structure of AM metal parts, in particular for LPBF as well as background information for DED, in particular for DED-PF.

Also the common background on acoustics needed for understanding both LU and sound radiation forces will be described. This background will be needed to understand how sound radiation forces can be applied for controlling the DED-PF process.

LU is a non-destructive and non-contact ultrasound imaging system where lasers are used to both generate and measure ultrasound waves within a part in order to image its interior. LU will be described in more detail in the context of NDT techniques, and the imaging methods and algorithms being used both in LU and in ultrasound testing (UT) in general.

Afterwards the applications of sound radiation force fields will be described. Sound radiation forces are produced when a high pressure intensity sound field interacts with an object with a large difference in impedance from the medium where the sound propagates i.e, between metal particles and air. This background will be needed when describing the application of sound radiation force for the control of the DED-PF process.

2.1 Metal additive manufacturing and its challenges

The following subsections will describe AM technologies, then metal AM technologies and then the two technologies considered in this proposal; LPBF and DED-PF.

2.1.1 Additive manufacturing

AM is a type of manufacturing process where a material feedstock is joined to make parts from 3D model data, usually layer by layer [12].

The idea of joining materials to produce objects is actually quite old, with some examples being laying stone blocks or masonry bricks to make a building, making a cake by layering, or making an object with interlocking blocks such as LEGOs. However the difference between these processes and AM is that in AM the joining is done automatically, by following 3D model data. The first AM principle using automatic joining that was patented was stereolithography, where a UV light source is used to cure layers of liquid polymer. The process was patented by Chuck Hull in 1984. Afterwards fused deposition modeling (FDM), where a continuous filament of material is heated to soften it and then formed into layers, was patented in 1989 by Dr. Scott Crump. In the same year, binder jetting, where a bed of powder is consolidated by using a binder, was patented by Dr. Emanuel M. Sachs. Later on, the LPBF process was patented in 1995 by Dr. Dieter Schwarze and Dr. Matthias Fockele. This was the first technology that could produce metal components. The following year, Sandia National Laboratories patented the DED process [13].

There are various ways of classifying the different AM technologies available. One of the new classification standards for AM is the 2015 ISO/ASTM terminology [12] which classifies methods based on; final part material composition, principle of adhesion, material feedstock and distribution, basic AM principle and related category and state of part right after carrying out the AM process (green or ready to use part).

Out of the basic AM principles currently available, only material jetting, binder jetting, FDM, sheet lamination, LPBF and DED can produce metal components [14]. However only LPBF and DED can produce intricate, close to full density metal components [15] which are of interest to the aerospace and automotive industries for example. Close to full density refers to the fraction between the measured density of the produced metal AM component and the theoretical density of the metal being 99.9% or higher.

In general with DED and LPBF, when the build rate is higher, feature quality/resolution decreases. The higher deposition rate also usually requires more laser power. This explains that for high deposition rate AM, post-process surface finishing might be necessary [16]. These relationships are illustrated in Fig. 2.1.

Metallic components made with both technologies experience a varied thermal history, with repeated fast melting and solidification, and high cooling rates that produce finer cellular structures within grains. Compared to machined metal components, the material

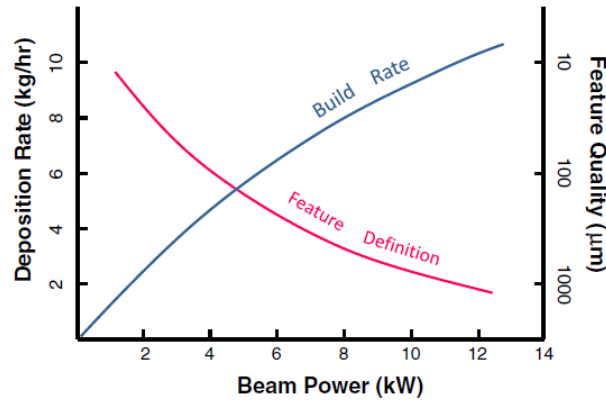


Figure 2.1: Relationship between build rate, laser power and feature quality. Reprinted with permission from [16].

properties are anisotropic, with the direction perpendicular to the layers (usually considered the z direction) being the weakest structurally. Process related defects such as porosity and low surface finish produce parts with less desirable fatigue properties compared to wrought metal components. Parts that have been subjected to annealing and/or hot isostatic pressing (HIP) to minimize residual stresses and pore sizes along with post-machined surfaces have fatigue properties more closely approaching wrought metal components [16]. Both metal AM overviews [16, 17] stress the deleterious effect of defects on the material properties, especially fatigue resistance. This issue together with the need to qualify parts for high value safety critical components, that is also one of the main markets for metal AM [8], highlights the need for a cost effective, accurate and reliable method of post-process inspection and in-situ monitoring of the internal material structure of AM metal parts.

2.1.2 Laser powder bed fusion (LPBF)

In the LPBF process, powder is laid down layer by layer using a powder delivery system and a coater. At each step a powder delivery piston and a fabrication piston move up and down respectively. The fabrication piston moves a distance at each step corresponding to the layer thickness. The energy delivery system is a laser, usually a pulsed or continuous mode Nd:YAG red fiber laser operating at a 1060 nm wavelength [18]. The laser is scanned over the surface using a scanner optics system. The laser selectively melts tracks in the powder to form a close to full density metal layer that is bonded to previous layers [19]. A diagram of the process is shown in Fig. 2.2. In practice there is also a curtain of nitrogen

or argon gas over the build area to protect it from oxygen and clear “spatter” and metal fumes that are generated due to the fast moving laser spot [19]. Also there is usually an overflow container past the fabrication powder bed to get rid of excess powder that was moved by the coater. Good process performance depends on powder properties such as particle sphericity and good “flow” properties (flowability) which are related to the angle of repose of the powder [20].

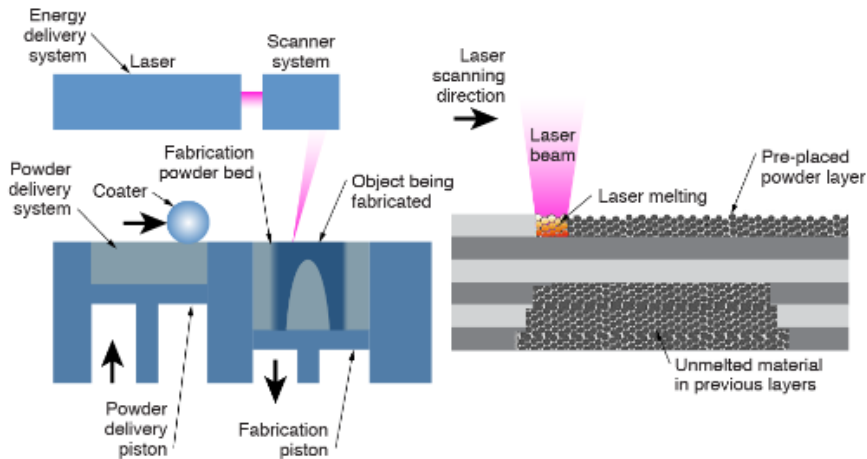


Figure 2.2: Diagram of the LPBF process at the machine and powder scales. Reprinted with permission from [19].

There are many LPBF parameters that can be adjusted, such as laser power and spot diameter, scanning speed and layer thickness, as well as parameters related to the powder alloy composition, particle size distribution (PSD) and particle morphology [18]. There are also various grouped parameters in the literature to describe both grain size and morphology as well as defect formation. One commonly used parameters is the volume-based energy density or VED parameter, which is approximately the average energy transferred per unit volume of material.

The prediction of part material properties from LPBF parameters is difficult to model due to the many physical laws needed to accurately describe the process as well as the large disparities in spatial and temporal scales [19, 21].

The grain morphology of LPBF produced steels for example display a fine solidified microstructure that is produced due to the high cooling rates present in the LPBF process. As seen in Fig. 2.3 (a), one can see the melt track outline, as well as cellular structures with an intercellular spacing down to $1 \mu\text{m}$ (b). The grains are also elongated and oriented

[17]. This is a similar structure to the one seen in DED produced metals. However due to the larger melt pools produced, the grains reported in DED produced materials for steels are larger, in the range of 100 to 140 μm [17].

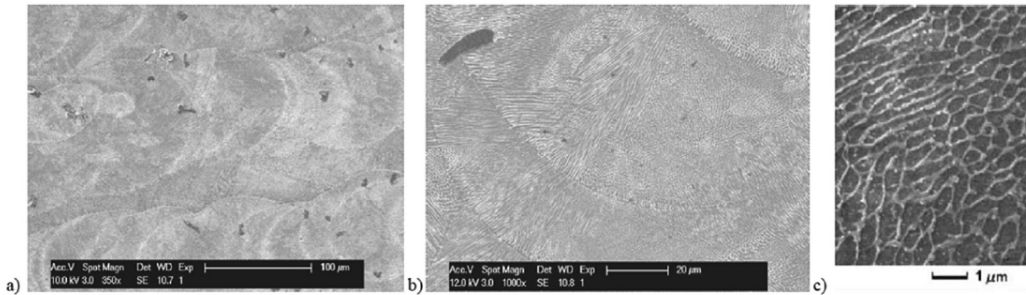


Figure 2.3: SEM images of LPBF fabricated maraging steel (18Ni-300). (a) Top view, (b) side view and (c) magnification of dendritic structure. Reprinted with permission from [17].

In [22] it was found that within the optimum laser parameters (to minimize defects), one can manipulate the microstructure such as grain size and texture. Texture refers to the orientation distribution of the crystals in the microstructure. Some progress has been made recently in predicting material properties such as grain morphology using modeling results and empirical data. This was applied to produce austenitic 316L stainless steels (SS 316L) with superior mechanical properties compared to conventional wrought SS 316L [23]. Both the strength and ductility of this new alloy is higher than the conventional alloy, while in most cases processes to produce stronger steels also reduce the ductility of the resulting material.

2.1.3 Directed energy deposition (DED)

The DED process, otherwise known as laser powder fed process or laser cladding for AM depending on energy source and feedstock, is an AM process where particles or wire needed for the build are dispensed at the same place where the energy to fuse them is being directed. The energy can be transferred to the feedstock through an electric discharge, electromagnetic induction or a laser. The feedstock can be either a wire or powder [15]. This survey will focus on DED systems with a laser power source and powder feed, otherwise known as powder-fed DLD or LDED-PF. Other DED-PF processes may use other energy sources, for example, the powder particle's kinetic energy in cold spray metal AM [24]. An example of an operating LDED-PF system is shown in Fig. 2.4.

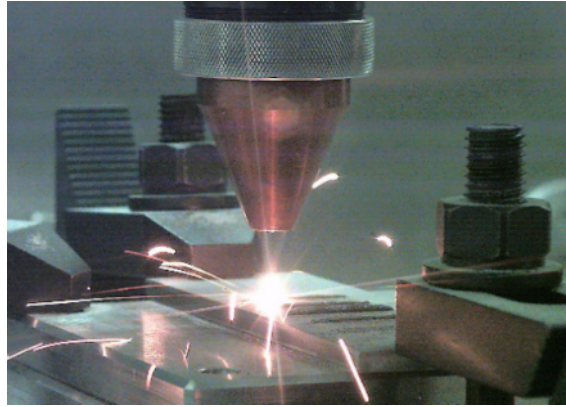


Figure 2.4: DMD IC106 from DM3D, a LDED-PF system, in operation.

The advantages and disadvantages of LDED-PF compared to other AM processes are summarized in Table 2.1. Another advantage of some LDED-PF systems is that they can be integrated with traditional subtractive machining techniques which can be applied right after the part is produced via AM, to increase dimensional accuracy [25].

Table 2.1: Advantages and disadvantages of LDED-PF process

Advantages	Disadvantages
Can produce parts with designed internal closed-off hollow features	Low resolution (but a higher build speed) compared to LPBF processes
Can be used for cladding and part repair as well as for AM	Some loss of powder after it is heated, however it is still a lower percentage compared to LPBF processes
Can use different feedstock materials simultaneously to produce FGMs	Supports might need to be fabricated to prevent part warping due to gravity

From this point forward in this thesis, different laser and powder feed arrangements for LDED-PF machines will be discussed. In order to have a short and unambiguous way to describe the setups in this chapter, the following naming convention will be used: A-B, where A is a letter representing if laser (L) or powder (P) is present at the center axis, and

B is the setup that is used in the annular region. The annular region can have continuous annular (C) or discrete elements of powder nozzles or laser beams where the number of elements is given. If the number of elements can vary, the letter N is used.

There are different LDED-PF powder nozzle and laser arrangements that are common in industry. Three common types are shown in Fig. 2.5.

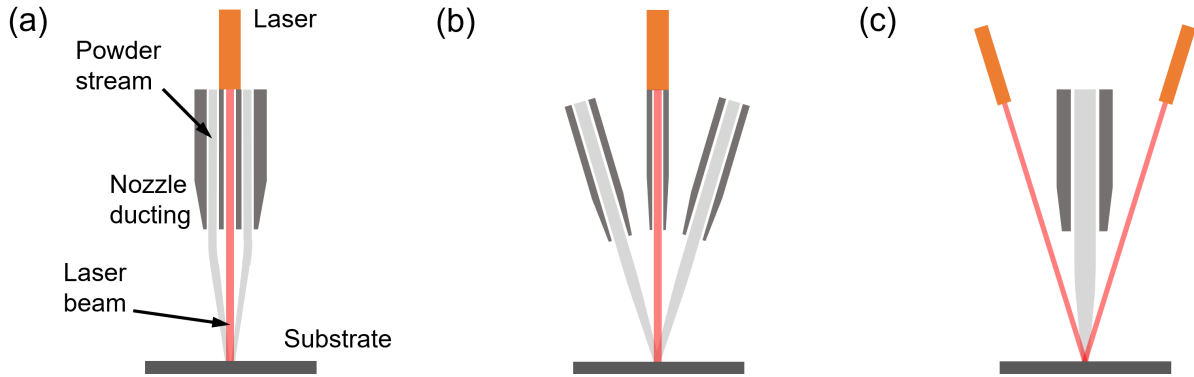


Figure 2.5: Types of LDED-PF setups used in industry. (a) Continuous coaxial (L-C). (b) Discrete coaxial (L-N). (c) Multi-beam (P-N).

A LDED-PF arrangement with a coaxial powder nozzle (L-C) is shown in Fig. 2.5(a). In this case the laser beam is at the center of the inner cone. For the coaxial arrangement, the powder is fed between the inner and outer wall of the nozzle ducting. In some cases a gas flow referred to as “shaping” or “shroud” gas is introduced between the outside of the nozzle ducting shown and another outer cone. Depending on the particle speed and size, this shaping gas can be used to improve the “shape” of the powder stream [26].

The morphology and grain size of LDED-PF manufactured components depends on the location of the tracks, mainly the location with respect to the substrate if the build settings are not being adjusted while building [25].

An example scanning electron microscope (SEM) image of the micro-structure for different layers of deposited Ti6Al4V is shown in Fig. 2.6.

The microstructure in both regions (a) and (b) consist of a Widmanstätten grain arrangement structure (interleaving of lamellae shaped grains), with finer lamellae at the top layers and coarser lamellae otherwise. The shape and aspect ratio of the cellular structure within grains for both DED and LPBF made materials depends on ratio of cooling rate to thermal gradient R and the temperature gradient at the solid-liquid interface G . The value

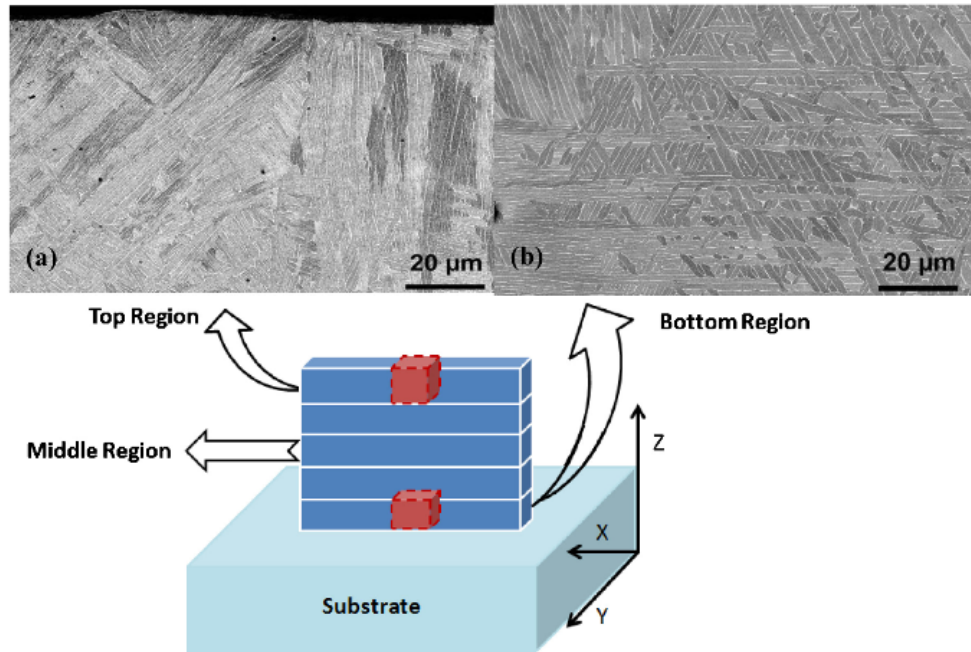


Figure 2.6: Microstructure of LDED-PF manufactured Ti6Al4V part in the y-z plane at different regions. Reprinted with permission from [25].

G/R and GR are referred to as solidification parameters which are able to predict likely cellular morphologies [25].

2.1.4 LPBF and LDED-PF defects

Due to the various physical phenomena taking place in the LPBF and LDED-PF processes, which depend on many factors such as laser settings and powder properties, if care is not taken to properly optimize these parameters, the part will contain internal defects, or visible cracks [19].

The main LPBF and LDED-PF defects can be classified as follows [27, 28]:

- Keyhole: this refers to spherical pores that can be formed due to gas being trapped from the environment due to Marangoni convention [19]. The pores have a size in LPBF smaller than $100 \mu\text{m}$. However these porosities are more common and are caused by the keyhole shaped opening in the melt pool. This is because of the change

of reflectivity of the laser with respect to the powder when it is being molten together with Marangoni convection, which causes an instability that is more likely to trap gas within the built material. This effect as well as gas precipitation due to a decrease of liquid metal gas solubility when the melt pool is cooling has been observed using high-speed synchrotron X-ray imaging [29]. These pores have been observed in LPBF numerical models using an arbitrary Lagrange Eulerian finite element (FEA) type multi-physics model [30]. In LDED-PF this type of defect is also called an intra-layer porosity.

- Lack of fusion: otherwise known as incomplete fusion defects. This type of defect happens when there is not enough laser energy to completely melt the powder and form a metallurgical bond with the previous layer. This can also happen due to having a hatch spacing that is too large even at a nominal laser power. In LDED-PF this type of defect is also called an inter-track porosity. For LPBF these types of porosities have been modeled using a discrete element model (DEM) coupled to a Navier-Stokes solver to simulate melt pool convection [31].
- Cracks due to undissolved powder particles: inclusions could be formed from inclusions present in the feedstock, chemical reactions between metal alloy elements and/or chemicals in the melt pool or reactions between the melt pool and the atmosphere
- Cracking due to internal stresses: cracking due to residual stresses can be classified as hot cracking which happens at high temperatures at the end of solidification and cold cracking that happens when residual stresses exceed the tensile stress of the material at a particular location. Cold cracking happens because the stress field of the whole object is changing when more tracks are being added, which can cause cracking in a location away from where the last track is being deposited. These types of cracks usually form from the surface, which has a high roughness right after fabrication. This type of defect is more likely to happen in low ductility and toughness materials, and in ceramic and cermet claddings

2.1.5 LDED-PF analytic modeling

One of the first models for LDED-PF was given in [32]. The model can predict laser beam velocity as well as powder feed rate in order to produce a required clad height. It can also predict the reduction in effective laser irradiation area due to particle attenuation. The model can only model a single powder nozzle and does not take into account latent heat.

A lumped 1D integral equation for the LDED-PF process was given in [33]. This model can take into account the latent heat of the substrate as well as the reduction in effective laser irradiation area due to particle attenuation, however it cannot take into account an uneven laser power flux distribution or other 2D effects.

An analytic model developed in [34] includes the moving laser beam, the powder stream, the substrate and the melt pool. The model can be used to predict clad geometry and catchment efficiency. The model is able to predict clad dimensions within 8%.

The model can be extended for multiple powder nozzles, and was recently extended for multiple tracks and layers [35]. The powder stream in this model is modeled as a Gaussian distribution fitted a priori to a corresponding luminance distribution from camera measurements and in its current form cannot be coupled to an external force field for a one-way coupling with the particles.

2.1.6 LDED-PF numerical modeling

Some numerical models that take into account particle motion due to the carrier gas simulated by computational fluid dynamics (CFD) are [36, 37, 38, 26]. All models currently found make use of Lagrangian particle tracking. Lagrangian particle tracking means that the powder stream is described using discrete particles and the forces on the particles are integrated to track their location over time. More information on this method as well as an implementation are described in Chapter 4.

In [36] the shape of the powder stream is investigated. The model uses the commonly used $k-\epsilon$ turbulence model implemented with a finite volume discretization in ANSYS FLUENT software. The model is able to also capture changes in the gas flow field due to particle motion (two-way coupling). The type of LDED-PF nozzle that was modeled is a radially symmetric powder nozzle. The main finding in this study is that powder “blob” formation which is sometimes formed in the nozzle tip is caused by particle ricochet from the work piece (substrate).

In [37] the particle and gas flow are modeled with a focus on the accuracy of the model taking into account particle heating, non-spherical particles and the particle size distribution (PSD). This model also uses the $k-\epsilon$ turbulence model implemented with a finite volume discretization in ANSYS FLUENT software and two-way coupling between powder and gas flow field. For the PSD a Rosin–Rammler distribution was used. This PSD is frequently used for representing particle/droplet size distribution of sprays [37]. Non-spherical particles were considered in this model by using a modified drag law taking into account the particle shape factor. The laser attenuation due to particles was neglected

in this study and the same TEM_{00} (transverse electromagnetic mode with $p = 0$ and $l = 0$ written on the first and second subscript) laser beam heat distribution source which was included in [34] was used. The computed powder stream compared to the actual powder stream for a particular setup is shown in Fig. 2.7.

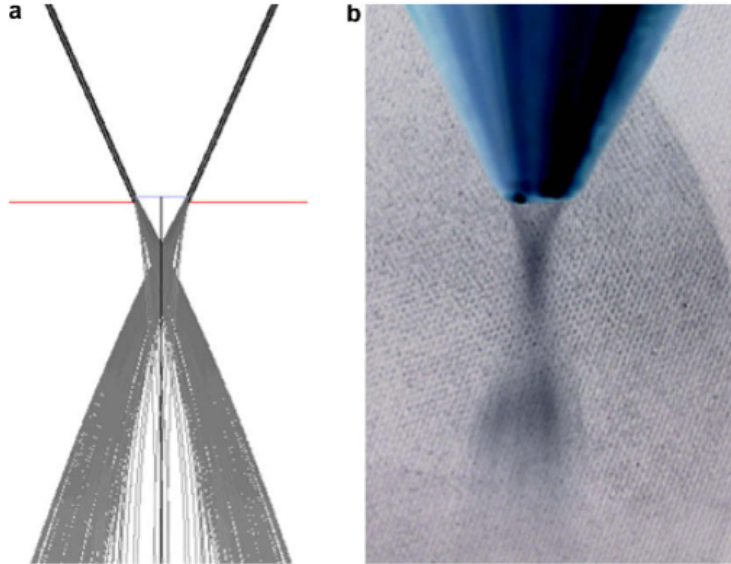


Figure 2.7: Predicted (a) vs. experimental (b) powder streams [37]. Experimental conditions can be found in [37]. Reprinted with permission from [37].

One thing of note in [37] is that the coupling from the gas flow to the particles is done only considering the Reynolds averaged velocity field and not the instantaneous flow field. This was justified by calculating the Stokes number for a LDED-PF setup. The Stokes number is a dimensionless number commonly used for particle tracking and particle separation modeling. It describes how quickly a particle responds to changes in flow velocity. The calculated value was higher than 1, suggesting the particles are not very responsive to changes in the flow field and their paths are similar to ballistic trajectories which is what is observed in Fig. 2.7 for example.

In [38] the powder stream is modeled first and then a ray tracing algorithm is used to calculate the energy absorbed by the particles and the power intensity arriving at the substrate. This can be applied to an arbitrary initial powder stream PSD. The rays are modeled with a triangular cross section, with initial power flux sampled from the original laser power flux distribution. This model uses the $k-\epsilon$ turbulence model implemented in COMSOL multi-physics software with one way-coupling between the gas flow field and the

powder. It was found in this study that the particle size distribution used had a strong effect on the particle absorbed energy before reaching the substrate but a smaller effect on substrate laser attenuation.

In [26] the gas-particle stream is modeled with the intention of studying various nozzle geometries as well as gas flow parameters in order to predict LDED-PF nozzle particle focusing for better resolution builds. The model uses the discretized Navier-Stokes equations directly without turbulence modeling and a fine mesh. It includes one way-coupling between the gas flow field and the powder, which uses a PSD directly from measured values. It also includes particle heating with phase change. One of the unique features of this model is that it models the particles upstream of the nozzle tip, with particle reflections considering a coefficient of restitution between the particles and the nozzle inside surfaces. Results for Nozzle #2 are shown in Fig. 2.8.

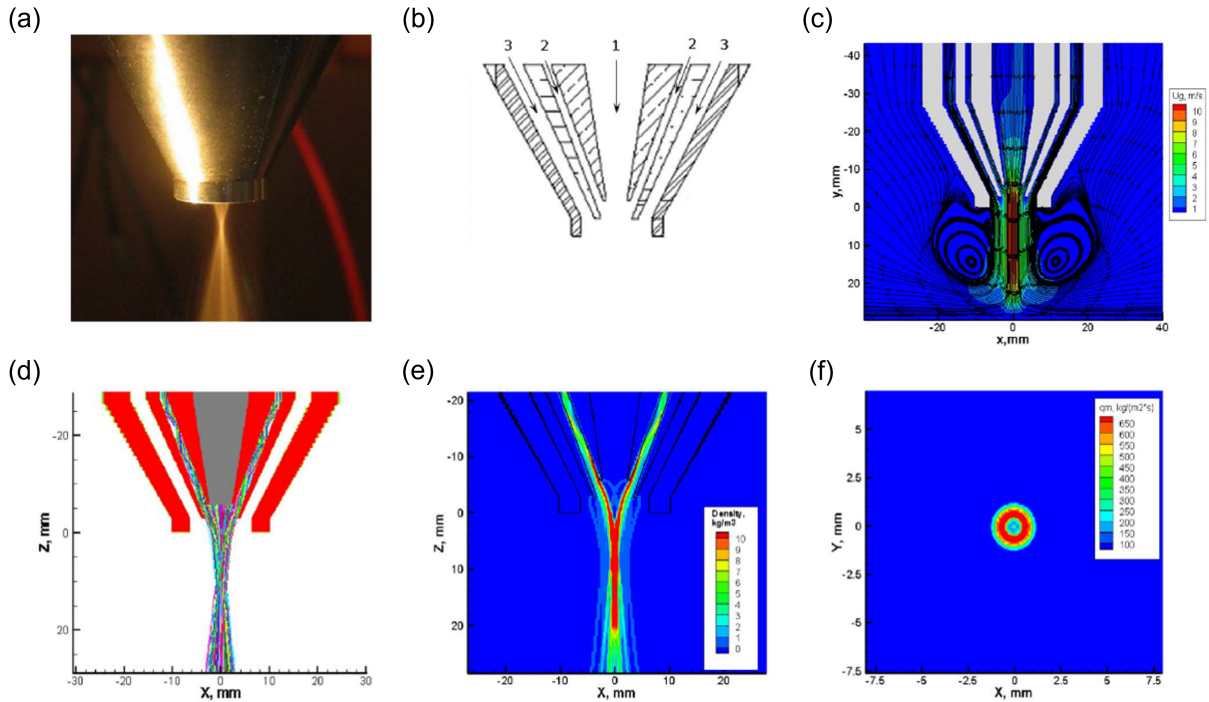


Figure 2.8: (a) Trumpf nozzle in operation, (b) its schematic and (c) gas velocity field. (d) Particle tracks and particle concentration at (e) nozzle cross section and (f) at the substrate. Reprinted with permission from [26].

The main conclusion in this study is that the gas flow field has a modest effect on the final powder concentration distribution close to the substrate and that a lower coefficient of

restitution between the powder and nozzle cones provides a more focused particle stream. This conclusion corresponds with the Stokes number calculations and observations in [37], that for the gas flow rates and particles being used in both studies the particle trajectories do not strongly follow the gas flow field.

The model in [26] is extended in [39] to include the substrate and melt pool geometry. The gas flow and particle stream models are the same as in [26], however the flow field modeling is done with the k - ϵ turbulence model on a coarser mesh. The model uses a linear combination of TEM_{00} and TEM_{01} laser modes in order to more accurately model the laser being used. The model uses a melt pool heat transfer and surface evolution equation described in [40] that can take into account an arbitrary powder concentration distribution. The particles are assumed to only attach to the substrate if they are molten. The model does not include the Marangoni flow within the melt pool.

There is a similar model for wire arc AM that takes into account Marangoni flow, which is important to accurately predict the effective anisotropic heat conductivities found in the melt pool [41]. In this study the clad deposit shape was found to be more accurately modeled by taking into account Marangoni flow.

It could be worth to further investigate how the surface evolution of the melt pools in [39] and [41] are implemented and how closely they match experiments with both models including Marangoni flow.

2.2 Non-destructive testing (NDT) methods

This section will give an overview of different NDT methods and their characteristics in order to compare their merits and disadvantages.

NDT methods have the following advantages compared to destructive testing [42]:

- The component can be used after examination
- Parts can be evaluated for internal features
- Parts can be evaluated while in operation
- Many NDT methods are implemented as portable devices
- Most NDT methods are cost effective

Some of the general disadvantages of NDT are the following:

- The results of an NDT inspection usually require operator interpretation
- Some methods do not provide quantitative data
- Finer features such as shape and orientation of defects may not be resolvable
- Although most methods are cost effective, some methods like computed tomography (CT) can be expensive

A more in depth description of NDT methods together with their physical principles of operations, type of materials that can be tested and their advantages and disadvantages are summarized in [42]. Out of all the methods described in [42], the only ones that can detect sub-surface defects in metals are; X-ray computed tomography (CT), ultrasound testing (UT), eddy current testing (ET) and thermal infrared testing (TIR). Since these methods can detect sub-surface defects they are more relevant to this review and will be described in more detail below. UT will be described in the following section.

CT, sometimes referred to as XCT or iCT (i for industrial) has a good penetration for imaging metal components since it can image objects composed of materials with a high atomic number. The high resolution of the method can be used to image voids and cracks in the μm range. The scanning speeds are from a few minutes to hours depending on the object's size [43]. One of the concerns raised in [43] regarding CT was the testing cost compared to other NDT methods. Another related concern is the use of ionizing radiation and the need to properly shield personnel and other equipment not being tested. The imaging algorithm in CT works by shining the X-ray source though the object at different angles. This gives different projections of the object including internal features. This information is then used to reconstruct an internal image of the object usually for different 2D slices using the inverse Radon transform [44].

ET is the measurement of induced currents in a conductive specimen done in order to determine surface or subsurface defects. It has been used in crack detection, coating thickness measurements, conductivity measurements, heat damage detection and heat treatment monitoring. Its advantages are high sensitivity and no contact between the inductor/sensor and the component. With regard to crack detection, crack sizes down to 1.3 mm can be detected while maintaining false calls below 1% [45]. A recent development in ET is Eddy current thermography or PECT, where the internal feature measurements are done though the measurement of heat generated from the induced currents using an infrared (IR) camera. PECT can detect defects by the difference in ohmic heating due to

the defects causing an obstruction or a shortcut for the induced currents [45]. In [45] it is noted that UT is superior in evaluating the profile of cracks compared to other methods but ET is able to measure cracks without a couplant for ultrasound transducers. This shortcoming of UT can be addressed by the use of LU.

TIR is performed by heating the surface of a part and using an IR camera, and reading its IR emissions over time. Different defects that have different conductivities with respect to the surrounding medium will locally change the IR emissions. There have been many recent advances to increase the image resolution and imaging depth below the surface. Some new techniques focus on “shaping” the spatiotemporal heating profile to increase contrast for imaging of defects 3.5 mm below the surface in mild steel, de-noising using synthetic heat equation simulation data, and inverse solutions to the heat equation using the fast Fourier transform (FFT) and wavelet transforms [46].

2.3 Acoustics and Ultrasound NDT (UT)

UT is a mature and large field, with many overlaps with ultrasound for medical imaging [47], and Fourier optics [48], which deals with the wave approximation for electromagnetic radiation. In UT a sound pulse is sent from a single or an array of sound transducers that can then measure the resulting sound reflected back from the boundaries of the test object or from internal features [49].

The three most common ways to display UT data are [49]:

- A-scan: the signal is acquired at a single point from the surface; the signal (y axis) over time corresponds to possible changes in medium density graphed over distance from surface (x axis). The conversion from time to distance is done by using the mediums speed of sound and a factor of two to account for the back and forth path to a particular location in the sample
- B-scan: A-scans shown on a 2D plot with the x-axis corresponding to the location of the scan on the surface and the intensity on a color scale
- C-scan: A-scans along lines covering a 2D surface, with the x and y axes as locations on the surface and different colors either showing no significant signal, or the signal amplitude or depth corresponding to a defect

A diagram showing the various ways to display UT data is shown in Fig. 2.9.

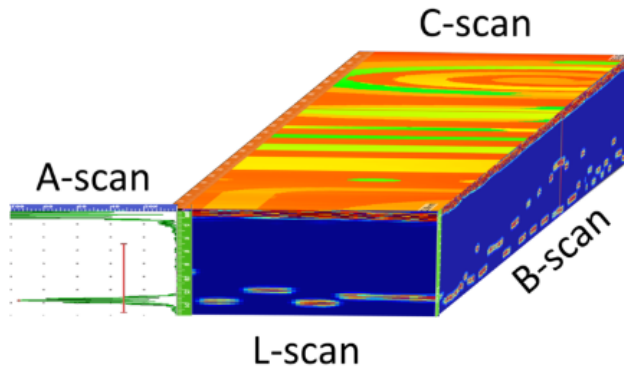


Figure 2.9: Diagram relating different UT display methods (courtesy of Sonatest [50]). The L-scan shown in the diagram is a less used display method that is similar to a B-scan but is obtained by sequentially activating the transducers in a linear ultrasound array.

There are various types of waves that can be produced in a solid, either inside the solid or at a boundary. Inside the solid one can have longitudinal or shear waves. In the former the wave propagation happens parallel to the particle's instantaneous velocity in the medium, in the latter it is perpendicular to it. Waves at a boundary such as a metal surface are called surface waves. The most common example of surface waves are Rayleigh waves, with the particle's instantaneous motion happening in an ellipse with respect to the wave front [49, 51].

When sound propagates through an object, local changes in the medium will produce reflected and transmitted waves. The fraction of energy transmitted or reflected as well as the direction of the new wave fronts will depend on the acoustic impedance. The acoustic impedance is the ratio between the sound pressure and the particle's instantaneous velocity in the medium. It is an analog to resistance in electric circuits. For maximum sound wave transfer the impedances should match. If this is not possible an intermediate (coupling) material with a certain thickness can be used. Also the coupling material should have an impedance equal to the geometric average between the impedance of the two surrounding materials. This matching is essential to send and receive signals from a transducer to the test object. If the feature with different impedance in the medium has a similar size to the wavelength, the wave will scatter; its intensity will be radiated out in many directions. This can also be considered as a form of attenuation since most of the sound intensity will not be detected [49, 52].

One of the main issues in UT is the trade-off between resolution and signal strength. Higher frequencies allow for higher resolution but they also increase sound attenuation. The attenuation also depends on metal grain sizes with respect to wavelength. The energy

loss of ultrasonic waves in polycrystalline metals can be described by losses due to wave spreading, scattering from unresolvable features and absorption.

The attenuation can be modeled using [53]:

$$A_R = A_0 e^{-\alpha t} \quad (2.1)$$

where A_R is the returned signal, α is the attenuation coefficient, and t is the propagation time. Note that if instead of time, the travel distance is used, a factor of 2 should be included to take into account the travel distance to and from a particular location. Also a factor of two might be included since sound intensity is proportional to the ultrasound pressure squared [49]. One should note which form of Eq. 2.1 is being used when calculating attenuation coefficients. The attenuation coefficient can be expressed as a sum of two terms; one from scattering and another one from absorption. For metals the absorption term is very small and can be ignored. The attenuation coefficient due to scattering is dependent on the scattering regime, which depends on the ratio between the ultrasound wavelength and the grain size [53].

It would be useful to investigate ultrasound attenuation using LU as a function of grain size and shape and sound frequency for defect free AM produced metals such as SS 316L, AlSi10Mg or Ti6Al4V for example. This experiment has already been done for machined SS 316L using a focused transducer, with the sample submerged in water [53]. The attenuation results were linked to the grain size and morphology using FEA. Based on measured grain statistics, FEA models of the grains were generated. The results in [53] comply with the different scattering regimes at different ultrasound frequencies, with generally greater attenuation coefficients with increasing frequency. Another FEA simulation of scattering in polycrystalline metals with similar results to the ones reported in [53] was done in [54].

2.3.1 Transducers

Ultrasound transducers are composed of a piezoelectric material sandwiched between two electrodes. Most transducers can be used to both send and receive sound. At the front there is a matching layer to maximize sound transmission and at the back there is a backing layer to dampen vibrations in order to be able to produce short sound pulses. The material usually used is a PZT ceramic, which has a high electro-mechanical conversion efficiency [55, 56]. A transducer attached to a flat surface will produce a sound field with different sound intensities over different distances and angles from its center axis. A plot of this referred to as a directivity (or emission) pattern [56].

Sound measurements from transducers and their directivity patterns are reported as an amplitude or an intensity. Both can be reported in decibels or dBs which is a logarithmic scale. The amplitude, intensity and dB values are related via:

$$L = 10 \log_{10}(I/I_0) = 20 \log_{10}(P_e/P_0) \quad (2.2)$$

where L is either the intensity level (IL) if using the first equation or the sound pressure level (SPL) if using the second equation. These two values can be assumed to be equal if the plane wave or far-field approximation applies ($I = P_e^2/(\rho_0 c)$) and the proper reference values are used. For air the commonly used reference values that make the two levels equal are $P_0 = 20 \mu\text{Pa}$ and $I_0 = 1.0 \times 10^{-12} \text{ W/m}^2$. The effective pressure is defined as $P_e = |P|/\sqrt{2}$ where $|P|$ is the pressure magnitude [52]. If one is only concerned with the relative magnitude between different signals, arbitrary units (a.u.) are sometimes used [53].

2.3.2 Imaging methods

There are various imaging methods for ultrasound that are expected to give higher resolution images with a given transducer arrangement, part shape and expected location of defects. The accuracy and processing speed for each method will depend on what assumptions are expected to hold in a particular test, that then translate to simplifications to the elastic wave equation. One of those simplifications is sound waves moving to and coming back from the “far-field”; i.e. the distance from the surface is much larger than the sound wavelength and the sound source dimensions. Under this and other conditions one can apply the Fraunhofer approximation for example [48, 56] to describe wave motion from the surface to the interior of the object and use more efficient imaging algorithms. For example in [57], this assumption was warranted since it was desired to image defects at large depths. The assumption was used to modify the synthetic aperture focusing technique algorithm (described below) to increase the algorithm’s resolution for the particular test setup. The various imaging methods for UT can be classified into the following techniques [58, 59]:

- Single reflections: this refers to using single reflections to get information about one line inside the sample (A-scan). The correlated information between A-scans from adjacent locations is not taken into account
- Synthetic aperture focusing technique (SAFT): a type of acoustic holography method [60], which uses signals from many different transducers. To find a 2D or 3D image,

the space is divided into pixels (voxels) and all the signals from every transducer at the distance from the transducer to the pixel (voxel) is added up. Through constructive and destructive interference, scatterers produce a total high signal compared to the background [61, 62]. It is also considered a type of time domain delay-and-sum (DAS) method [63]. The first implementations of this method were used to image defects in thick metal sections [64, 65, 66]. In [67, 60] a link is made between SAFT and tomography and a variant of SAFT using the Fourier transform called FT-SAFT is derived. In [68] the same author implements the FT-SAFT algorithm for high resolution 3D imaging. These methods has also been adapted for near-field measurements [69]

- Phased array techniques: these techniques refer to imaging algorithms that use data obtained from a phased array. A phased array is an array of transducers where the timing of their signals can be adjusted. A phased array can produce high intensity sound at certain locations within a sample by adjusting the phase shift of each emitted sound pulse. Arrays can focus, steer or change the directivity pattern of the total sound field. Two well known phased array techniques are the total focusing method (TFM) and full matrix capture (FMC) [70]
- Physical optics far field inverse scattering (POFFIS): the reconstructed image is found by using the inverse Fourier transform of the far field scattering amplitude of possible defects. This method can also be related to SAFT and FTM [71].
- Phase shift migration (PSM): the method is similar to SAFT in the frequency domain (FD) but is derived from the wave equation [63]. The method can shown to be equivalent to Kirchhoff migration [72]. If the same transducer is used as an emitter and receiver (zero offset), this method simplifies to the Stolt method [73]
- Synthetic aperture radar (SAR): this method assumes a point-scatterer model that is transformed to the FD using a stationary phase approximation [72]
- Diffraction tomography [74]: this method is similar to the imaging algorithm for CT tomography, with scatterers within the object producing signals that after applying a Fourier transform are used to fill semi-circles in the Fourier space (k-space), instead of lines crossing the origin. The inversion is done using an inverse fast Fourier transform (FFT) just like in the inverse Radon transform for CT [44]
- Amplitude and time-of-flight locus curve: this is a technique where the signals acquired from an array of transducers are filtered in the time domain, using the fact

that a defect will produce a signal where the time-of-flight locus curves are hyperbolae [58, 75]

- Time-of-flight diffraction technique: this method uses pulsed ultrasound to determine the size of a crack. Instead of measuring the amplitude of the returned signal (which is highly dependent on the crack shape and orientation) the method is tuned to measure the difference in the arrival time between two signals that correspond to the crack tips. Using the medium's speed of sound this time delay can be used to determine the size of the crack [61, 76]
- Methods using multiple wave types: these methods can use both longitudinal and shear wave information for imaging. Two of these methods are the elastodynamic dual mode far-field Fourier inversion method [77] and a method where the waves are separated in k-space using projections of spatially Fourier transformed measured data and the inversion is done using electromagnetic diffraction tomography [78]
- Numerical discretization and inversion methods: these methods use a numerical model (finite differences, FEA, etc.) of the elastic wave equation which is referred to as a forward model. From this model one can calculate an adjoint model to get a gradient of the least squares fit between the acquired and simulated data with respect to the discretized material properties inside the object. Then a non-linear optimizer can use this gradient with the forward model to find the material properties that cause the smallest least squared error between the forward model and the measured data. The gradient obtained from an adjoint is exact up to machine precision, compared to finite differences with associated discretization error, and all the derivatives needed for the gradient can in the case of a least squares fit be computed in $O(N)$ instead of $O(N^2)$ operations, where N are the number of finite difference or FEA nodes with some material property that needs to be determined [79]. This method was implemented for UT in [80]. A close relationship was found between the adjoint model and time reversal based ultrasound imaging methods, where the waves measured by the transducer are back-propagated in time in order to find scattering sources. The advantage of this method is that one could simulate the full elastic wave equation and take into account all the wave types reaching the transducers. However the computation time compared to the methods discussed at present is much higher even using the adjoint calculation

A summary of all the main UT imaging methods described before is given in Fig. 2.10.

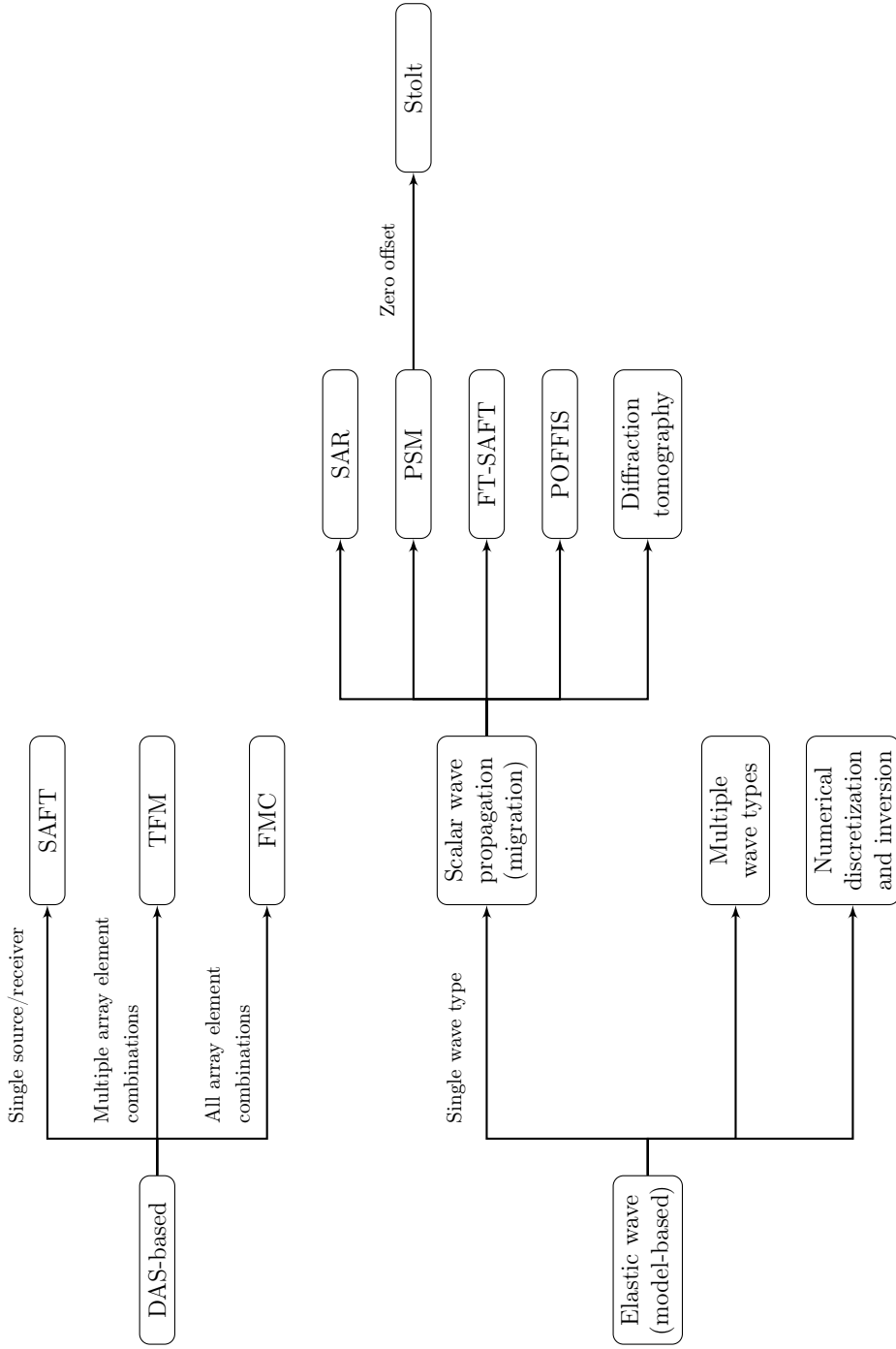


Figure 2.10: Classification of ultrasound imaging methods (including delay-and-sum methods) based on simplifications and assumptions applied to the elastic wave equation.

2.4 Laser ultrasonics (LU)

Prof. Monchalín from the Industrial Materials Institute at the National research council of Canada has published two reviews on LU; one in 2004 [81] and another one as a book chapter in 2007 with a focus on applications [82].

In [82], Monchalín describes the sound generation mechanisms, either thermoelastic or ablation (vaporization), the optical detection of ultrasound using interferometry and the use of various measurements done at different times and locations for image reconstruction, using algorithms typically used in ultrasound phased arrays. A general LU setup consists of a generation laser that generates sound waves by irradiating the sample surface at some offset distance and detection laser coupled to an interferometer, also being applied at an offset distance from the sample surface, that can read the surface vibrations on the sample. The setup used in this thesis can be seen in Fig. 3.2.

The main differences between LU and conventional UT are the following [82]:

- Can do measurements up to a few meters away from object and in vacuum. Electro-magnetic acoustic transducers and air coupled transducers require a small gap due to induction losses and attenuation of acoustic waves in air respectively
- Since the part itself is generating the sound, the shape of the surface as well as its orientation with respect to the laser beam does not substantially affect the resulting signal. However this also means care should be taken to choose the right laser parameters based on the optical absorption properties of the material to produce the required sound wave characteristics without part damage
- For a scattering surface the laser-ultrasonic signal will be weaker but less dependent on the angle of incidence of the measuring laser, the opposite conditions will be true for a polished surface. In both cases the strongest signal is obtained by the laser beam being normal to the surface
- Using optic components it is possible to use various laser profiles (point, disk, circle, line, array of lines, etc.) to get the required wave type, intensity, frequency and directionality
- A laser can provide higher frequencies in the order of Gigahertz and shorter pulse durations compared to piezoelectric transduction, because one needs to quickly damp the oscillation with a backing layer for example

- The sound generation mechanism does not allow selection of a wave type: longitudinal, shear, and surface waves (for thick specimens that can be considered a half space) or plate waves (for thin plates with respect to the sound wavelength) are all emitted at the same time, which can be a benefit or a drawback depending on the imaging method being used
- Waves generated in the thermoelastic regime are of the same magnitude as the ones produced by piezoelectric transducers, but in the ablative regime shock waves might also be produced. This can cause plastic deformation, breakage and other non-linear effects

In the thermoelastic regime, light is absorbed at a short distance from the surface, producing a related strain and stress that produces the sound waves. In metals this penetration thickness is much lower than the associated sound wavelength. Also since the surface is free to move, this means that the three orthogonal force dipoles produced at every point only produce expansion parallel to the surface [82]. Force dipole in this context means two opposite outward forces close to each other.

In the near field in a thin plate a depression on the opposite side of the plate can be observed corresponding to the longitudinal wave arrival, followed by another depression from the shear wave arrival. In the far field the emission (directivity) pattern of the waves is symmetric with respect to the surface normal, with about 30° from the surface normal for shear waves and about 60° for longitudinal waves with no emission for either type of wave along the normal. This emission pattern has been modified by using a phased array setup, using optical fibers of different lengths with a single laser source, different lasers triggered at different times, or using a conical lens that produces a ring shaped laser cross section at the metal surface [82].

In order to produce longitudinal waves parallel to the surface normal, there should be enough light penetration to produce a thermoelastic source that is buried beneath the surface [82]. This produces a source similar to a piston at the object's surface emitting normally propagating longitudinal waves, with are close to independent of the surface curvature and of the orientation of the laser beam. The use of the generation laser at a slight angle to the sample's surface normal can be seen in the setup shown in Fig. 3.2. If it is required for imaging, surface waves can be generated with a certain spot size and pulse duration as well as laser light patterns from a spatial light modulator [82, 83].

For ultrasound detection using lasers there are two main techniques: ones using or not using interferometry. Interferometry refers to the combination of two laser sources with different phases to get an interference pattern beam with varying amplitude. The detection

laser should be high power since the sensitivity is proportional to laser power. Also high power aids in detection on absorbing surfaces and large offset distance applications. The pulse duration should be sufficiently long to allow for adequate sampling [82].

2.4.1 Sound generation analytic models

This section will give a survey of different analytical solution used to describe the type of waves seen in experiments, focusing on the thermoelastic regime. The publications are mostly arranged in chronological order, with an emphasis on reporting their operating assumptions, their solution methods and what physical phenomena they can explain.

In [84], Dewhurst and Hutchins from the Department of Applied Physics at the University of Hull developed a model assuming no heat diffusion or optical penetration in the production of sound waves. However a simple heat diffusion model was used to calculate the deposited energy. This means that this model assumes no thermoelastic stresses in the z direction perpendicular to the surface. One of the conclusions is that the normal displacement right at the surface opposite on the plate where the laser spot center is located (epicenter) is due to longitudinal and shear waves, with the contribution due to shear waves being about 4 times larger. It was found that all the wave amplitudes are proportional to the deposited energy, the waveforms are not strongly dependent on the laser spot shape or size. Using deconvolution on the measured data with the model it was found that the percent of absorbed energy was about 9% which is comparable to measured reflectivity data.

Using an infinite plate approximation with a known Green's function solution, Dewhurst and Hutchins from the Department of Applied Physics at the University of Hull were able to derive a solution for the normal and shear waves generated by a laser [85]. This was one of the first models reported for laser sound generation. The experiments done to corroborate their models were done with a Q-switched Nd:YAG laser on metal cylinders with a high diameter to height ratio to prevent interference from reflected waves from the edges of the cylinder. The shape of the waveforms was found to not change at constant laser energy and different laser powers below the critical power level that causes ablation.

In order to explain the directivity of the resulting sound field with a substantial component that is normal to the surface in the far-field, there has to be some light penetration that can then produce a thermoelastic source that is under the surface [82]. This allows the source to "push against" the layer of material closest to the surface and produce a sound wave normal to the surface. This was measured in [85] as an initial positive displacement at the epicenter. In [86] both 1D and 2D axisymmetric models are given. The laser source

is assumed to have a radial spatial distribution at the metal surface for the 2D model and a time variance modeled by an impulse function for both types of models. The authors focus on explaining the positive displacement right at the surface at the epicenter, which was originally measured in [85]. This initial displacement is referred to as a precursor. This precursor can be explained using the reported 1D models. One of them assumes a plane temperature rise spike parallel to the surface of a half-space and then it is extended to a varying temperature profile assuming thermal diffusion. Another model assumes optical penetration. The conclusion is that either or both phenomena can produce this precursor signal. A 2D model is derived using both thermal diffusion and optical penetration that closely matches experiments.

Another later model was described in [87]. The model provides 3D solutions in cylindrical coordinates for a laser beam that is modeled as a constant power source point that varies with time an impulse function. The model assumes the conductivity equation can be solved independently of the elastic wave equation assuming a small fraction of the laser energy is converted to elastic waves. The model takes into account both the thermoelastic and ablation phenomena. The results are able to predict longitudinal, shear and surface waves. One observation in the thermoelastic regime was that the waveforms remain the same under different laser powers (for the modeled time variance using an impulse function).

A model in [88] is used to predict the amplitude of surface waves in metal. This model is used to predict that the maximum amplitude values normal to the surface for shear waves can be generated using a laser pulse duration equal to d_l/v_R , where d_l is the laser spot width at the surface and v_R is the Rayleigh wave speed of the material.

All the above solutions have many simplifications while their complete solution is either difficult or impossible without numerical approximations. This has been addressed with a newer analytic solution [89] that uses the hyperbolic heat equation which takes into account a finite heat propagation speed. While this equation is more complicated than the heat diffusion equation, if one makes the experimentally based assumption that the heat propagation speed is the same as the longitudinal wave speed in the elastic wave equation, one can substantially simplify the analytic solution. The model can include a laser source with a finite extent, in the form of a Gaussian surface source.

In [90] a solution to a 1D model is obtained that also takes into account the non-Fourier effect in heat conduction (finite heat propagation speed) and the coupling effect between temperature and strain rate to model laser pulses in the nanosecond to femtosecond range. The solution uses Fourier series to represent the laser pulse intensity and the final solution.

A simple analytical model is used in [91] to design a “laser-ultrasonic generated phased array”. Focusing was shown below the sample, with an amplitude 15 times higher than an unfocused array. The resulting beam had a narrower and steerable longitudinal wave directivity pattern.

2.4.2 Sound generation numerical models

An analytic-numerical solution is given in [92] with Monchalin as one of the co-authors. The solution uses the elastic wave equation and the hyperbolic heat equation, which is solved using temporal Laplace and spatial 2D Fourier transformations and their numerical inversion. This method is used to model the sound waves generated in an orthotropic medium. An orthotropic medium has different elastic properties in different directions. The solution can use any 2D spatial laser flux or laser application time distributions. The obtained solutions closely match experiments done with an aluminum and a composite plate.

A model using an analytic-numerical solution with a point-wise discretization of a laser beam profile and using Huygens principle was used in [93] to match experimental results. The solution was implemented in MATLAB. The experiment consisted of a laser with a ring profile producing thermoelastic waves on an aluminum plate. The ring laser spot profile was produced using a bi-convex lens followed by an axicon lens. Another FEA model based on the PZFlex software package was implemented. However this simulation was only able to predict the incoming wave away from the center of the ring and not the Gouy phase shift. The Gouy phase shift is the phase change that happens after the sound (or light) waves are focused to a point. This ring profile used has the advantage that it can more effectively focus the sound normal to the surface along the ring axis [82]. This profile might be more advantageous for imaging defects [94, 95].

One can use finite differences with explicit integration of the elastic wave equation coupled with the hyperbolic heat equation using staggered grids to simulate the thermoelastic laser generation [96]. The heat equation is solved implicitly in order to use the coarser temporal and spatial discretization values as the wave equation and reduce the computation time. The model results match the selected analytic results. The model can simulate transversely isotropic materials.

In [97] an axisymmetric 2D model is implemented in COMSOL as an FEA model. The model is able to compute the longitudinal, transverse and surface wave directivity patterns. The model matches experimental results done on an aluminum cylinder. The paper points out the advantage of LU as a way to identify defects in objects with complex geometries.

Another axisymmetric 2D model FEA implementation is described in [98]. The thesis describes in detail the meshing and time resolutions necessary to match experiments. The model matches experimental results also done on an aluminum cylinder. This implementation was done in Abacus.

2.4.3 Sound generation laser characteristics

The sound generation laser needs to deposit enough energy per pulse in order to produce the required sound time signal and amplitude. The power should be high enough to produce sound either in the thermoelastic or ablative regime as required by the system designer but not high enough to cause damage. Shorter pulse widths are desirable since they can produce higher sound frequencies [99, 3].

2.4.4 Laser based sound detection techniques

Most detection techniques for LU use interferometry. In interferometry distance changes are measured by splitting a laser into two beams, and combining them at the same time of after a time delay, after one or both of them have had a phase change due to a different travel distance. In this case the different travel distance is caused by elastic surface waves. The difference in magnitude of the resulting total signal is then used to calculate the distance change.

The rest of this section will describe non-interferometric techniques and some particular interferometry setups. Non-interferometric techniques can be further classified based on their working principles; knife-edge, surface grating, reflectivity and light filtering [82].

In the knife-edge technique, a laser is pointed at a surface. The reflected laser beam is deflected slightly due to the surface ripples caused by ultrasonic waves from inside the materials or surface waves. This deflection is measured by using a partial obstruction (knife-edge) and the light intensity is measured after the obstruction. This technique has been commercially developed into a scanning laser acoustic microscope (SLAM). To be able to measure this effect the laser spot diameter should be smaller than the surface ripple spacing [100].

In the surface grating technique, a beam that is larger than the surface ripple spacing is used to get a reflected laser with an “intensity corrugation” due to the surface acting as an optical grating. An amplitude signal can be extracted by passing the reflected laser beam

through a Ronchi ruling (parallel alternating transparent and non-transparent stripes) with suitable dimensions [100].

The reflectivity technique uses the change in reflected laser amplitude to measure the ultrasonic stress on the surface, which changes the diffuse reflectivity of the surface due to changes in the refractive index. This method has been used to measure the surface ultrasound signal in some thin film metals such as As₂Te₃ semiconductor using a laser with a picosecond range pulse width [100]. This technique might not be feasible for metals.

The bandwidth (the width of the frequency range) of signals that can be measured for non-interferometry methods depends on the surface medium [100]. In interferometry, this bandwidth can be tuned, but there is a trade off with sensitivity. Interferometers can be subdivided into three general detector setups:

- Optical heterodyning: in this scheme the laser is split into two beams and then recombined after one of the beams is shifted in phase due to a moving surface. If there is a frequency shifter in one of the arms of the setup the setup is called heterodyne, otherwise it is called homodyne. This type of setup with two arms is called a Michelson interferometer. This interferometers have a very high sensitivity to surface roughness and the beam should be very well focused [100]
- Differential interferometry: this scheme uses the interference pattern of two beams. The beams can either be compared after being reflected from the same location at different angles (in-plane) or at different locations (displacement). The method can be used in rough surfaces and to measure in-plane displacements using the interference pattern [100]
- Velocity of time-delay interferometry: this technique combines two beams after they were reflected, however one of them is delayed by a fixed time. In these setups the signal is proportional to the velocity of the moving surface therefore these systems are very insensitive to ambient vibrations [100]. One of these methods is referred to as the Michelson velocity interferometer. The setup is the same as in Figure 18 but instead of a laser the initial beam is the beam reflected off the surface, and instead of the sample another mirror is used which has a different distance to the beam splitter than the original mirror. This difference in length is used to produce the time delay. The mirror sizes and the path length difference could be very large in order to produce a system with the needed sensitivity and étendue [82]. Another type of system that allows for a large effective path difference by using multiple interference events as well as a large étendue is the Fabry-Perot interferometer. In this setup the incident beam produces multiple reflections due to two mirrors, and

the use of concave mirrors means the system is insensitive to the location and angle of the incident beam (producing a high étendue). One thing to note is that the sensitivity for this system is close to zero at low surface motion frequencies which makes the system intrinsically insensitive to vibrations [82].

Taking into account AM applications, due to the rough surface finish a method such as optical heterodyning is applicable. The method also has a high bandwidth, it is insensitive to vibrations and air currents and can be used to measure normal and in-plane vibrations [100]. Another system used in industrial applications that has in addition insensitivity to imprecise alignment and bandwidth selection is a confocal Fabry-Perot [100].

2.4.5 Detection laser characteristics

The laser should be as high power as possible without affecting the material permanently. This is because interferometric methods are more sensitive with a higher power. The high power is also desirable with surfaces with a high absorptivity and for far away distances where there is a small collection solid angle.

The pulse duration should be long enough to capture the required signal. In practical systems this value is between 10 and 100 μ s. A suitable laser is a Nd:YAG red fiber laser operating at a 1060 nm wavelength which can provide high amplification gain [82].

Applications for LU and their imaging methods

This section will go over the use of LU for different applications as well as the corresponding imaging methods being used if they are known. The applications described in this section are focused on using LU for defect and crack detection in metals, which is most closely related to the problem of defect detection in AM metal components. Other applications of LU for measuring tube and coating thicknesses, as well as microelectronic thin films are described in [82].

The SAFT algorithm has been tested and results reported in [101, 102, 103]. Using this imaging method was shown to produce higher quality images compared to plotting C-scans from A-scan data. In this publications the SAFT algorithm was also carried out using F-SAFT which uses the Fourier transform to speed up the computation time. The method was tested in aluminum samples [82]. The SAFT method has also been applied using surface waves, in order to detect near surface defects [104] and using SAFT with “full matrix capture”, meaning data from all sound emission points and different surface sampling point

combinations is recorded [105]. This method should provide higher resolutions, however the data acquisition time is high [82].

Lockheed Martin is using LU for finding internal defects in polymer-matrix composite parts of the F-22 and F-35 fighters manufactured by the company [106, 107]. It is used because it is able to test parts with complex geometries and for a high testing throughput. The system depends on producing longitudinal waves with a high power sound generating laser one meter away from the object [82].

For shiny surfaces the beam interrogating the surface has to be normal to the surface. The solution used in many applications is to mount the inspection system on a robot arm that orients the system normal to the surface based on the testing location using optical profilometry or the CAD file of the component [82, 108].

Due to the broadband nature of the LU generated sound waves, detached composite layers can be made to vibrate, in a similar way to the currently used tap test for composite parts. This induced vibration can also be detected with an LU system [82].

One can detect surface cracks due to stress-corrosion in steel using LU. This was compared with the use of penetrant testing (PT). The imaging method used was F-SAFT [82]. Another application using SAFT was for detecting defects in stir welding. This was compared with immersion ultrasonics and LU was shown to produce much higher resolution images in an aluminum component due to sound generation with a frequency of up to 220 MHz [82, 109, 110]. LU using the SAFT algorithm was implemented to test for defects in multi-pass welds done with arc welding. In order to compute the image using SAFT, the surface profile was measured using laser triangulation [82, 111].

One can also use LU for metal microstructure characterization at elevated temperatures for example austenitic grain growth in steels and even phase transformations such as austenite into ferrite [82, 112, 113].

2.4.6 LU commercial setups

Nearly all commercial LU systems are aimed at part inspection for defects in the aerospace sector. One of these systems uses a robotic arm to move the part in front of a LU system. This product is called tecnaLUS, developed by Tecnatom and Airbus [82, 114].

Another similar system was initially developed within Lockheed Martin. The engineers in charge of developing this technology then started their own company; iPhoton Solutions LLC. The system called the iPLUS can scan up to 6 m²/hr at a distance of up to 1.8 m [82, 115]. A system that uses a gantry instead of a robot arm is the LaserUT[®] system by

PaR systems [116]. The system uses TEA CO₂ lasers for the sound generation laser and it is claimed it can be up to ten times faster than conventional UT systems.

The only currently known LU commercial system aimed for laboratory research is the LUKS-1550-TWM system from Optech Ventures & Intelligent Optical Systems Inc. [117]. This is a table top system that can be used to develop new LU imaging algorithms and experimental methods for defect detection. This system has been used before in the literature to develop composite structure testing [118], testing de-bonding of a lead-alloy structure [119], and detecting defects in LPBF printed ALSi12 samples [120]. This is the system that was used in the experiments described in Chapter 3. Detailed specifications for this system can be found in Section 3.2.2.

For monitoring metallic microstructures there is one system available in the market called the LUMet[®] which stands for “Laser Ultrasonic Sensor for In-Situ Metallurgical Microstructure Studies” from Gleeble [121]. The system can measure grain growth, final grain size, phase transitions and elastic constants.

2.5 NDT use for metal AM in-situ monitoring

This section will give a summary on the NDT methods used for AM metal components, starting with general methods, then UT and then LU. It will focus on the physical principles, the imaging algorithms used and the resolutions achievable if they are available.

2.5.1 NDT

A literature review of NDT techniques applied for both in-situ and part qualification was done for the Department of National Defence of Canada [122]. The review outlines different methods including thermometry using IR cameras. It classifies thermometry methods into two classes; one using the temperature of the object for signal acquisition and another using an external heat source such as a flash lamp. The flash lamp setup might give more repeatable data. Other technologies highlighted are the use of visible light cameras to determine the powder height distribution, which can be the cause of defects after melting. One commercial application of this technology is the Concept Laser’s QMcoating module. The review mentions all the methods described in Section 2.2 as applicable to AM, however it also mentions another method; shearography. Shearography is an interferometry technique that uses the interference pattern reflected from a built sample. With this technique one can test for surface stresses in the part after peening for example.

The review in [123] focuses on both process defects and in-situ NDT techniques for LPBF. The techniques discussed for in-situ NDT are TIR, with either visible or infrared cameras. Some of the “derived signatures” that are most commonly sought after are spatter and the detection of sub-surface defects from thermometry. It is noted in the review that very few studies have been carried out on automatic determination of out-of-bounds measurements and active feedback to correct the detected anomalous features. One new method mentioned in [123] for correcting features is called selective laser erosion, where the laser is used to vaporize a small amount of material. One attractive TIR method [124] achieves thermographic super resolution by taking advantage of the spatially structured laser heating that can be achieved using the galvanometer scanner in a LPBF machine. Other works [125, 126] describe the use of optical cameras, either using the visible range or the near IR spectral range of cameras to inspect the LPBF powder bed surface or melt pools in-situ. However, these types of inspections only give an indication of how likely a sub-surface defect is going to form and are not able to directly image a defect.

A review of CT applied to AM parts for defect detection is given in [127]. It is noted that in the 2005-2010 period, CT was starting to be used as a pore measurement tool. From 2011 to 2014 the applications have moved to not only density measurements but also measuring pore morphology. The authors note that in the available literature, the Archimedes method still gives better overall porosity fraction values compared to most CT systems, due to their resolution limits and the presence of very small pores, particularly in very dense parts. However CT still remains the highest resolution method to determine the distribution of porosities regardless of surface depth in a built component. In [128] microCT is used for testing of a Ti6Al4V component that was manufactured on an EOS M270 LPBF machine. This was an actual production part. Another test was carried out after hot isostatic pressing (HIP). Care was taken to align both data sets so one could be able to see the differences in pore size. Small defects in the order of 50 μm were smaller and fewer in number after HIP. The defects were found along planes normal to the build direction indicating inter-layer lack of fusion defects. Although the part was 99.995% dense, the defects were highly localized, indicating the importance of non-destructive testing for part validation.

2.5.2 Ultrasound NDT

A method to obtain grain boundary statistics using immersion UT is used to obtain filtered images using extreme value statistics. The confidence bounds found from grain noise can be used as time-dependent thresholds for ultrasonic C-scan image segmentation. The method

is able to detect a defect of approximately 100 μm in size in a 316L SS sample manufactured with LPBF with a 15 MHz piezoelectric transducer [129].

UT was used to determine the bonding between different layers deposited in a wire arc DED process in [130]. This was done by doing A-scans in a fixed position below the build plate. The results were confirmed by CT and by cutting the sample in half and using PT. The publication has a good review of different NDT methods applied to metal AM in-situ inspection. The conclusion is that LU, ET, and TIR are promising technologies for in-situ inspection.

An interesting use of piezoelectric transducer UT for in-situ process inspection was done in [131], where a single transducer was attached to the bottom of the build plate in an EOS EOSINT M 280 LPBF machine. A plot of sound speed taking into account build height shows a sudden increase followed by a decrease in slope that has an asymptotic value. It is hypothesized that this might show the speed of sound dependence on the temperature of different layers. It was also observed that the frequency spectrum of the returned waves changes while the top layer is being fused. One can also see that if laser power is reduced, the B-scan shows echoes at that height. This might be due to the formation of lack of fusion defects.

2.5.3 Laser ultrasonics

LU has been applied to the detection of defects in LDED-PF built parts, using 316L SS and Ti6Al4V. In order to capture shallow defects Rayleigh shallow surface waves are used. Wavelet analysis was used to filter the signal [132]. The main author in this publication was Dr. Klein who now works in Optech Ventures & Intelligent Optical Systems Inc.

In [81] and [133], Lévesque and Monchalín describe an LU system that was used to check for defects in metal AM test coupons made using laser DED with powder and wire, and with electron beam wire deposition. Lack of bonding, lack of fusion and individual porosities were detected and confirmed with X-ray micro-computed tomography. The publication highlights further work is needed in; scanning and imaging techniques and the effect on the LU process from higher temperature during deposition and surface roughness.

An LU system with similar specifications to the LUKS-1550-TWM system and an Optech AIR-1550-TWM Adaptive Interferometric Receiver Optech Ventures & Intelligent Optical Systems Inc. was used by Everton in [134]. Samples made using Ti6Al4V were made with LPBF as well as samples with the same dimensions with wrought Ti6Al4V stock material. The dimensions of the block were determined using time of flight calculations to make sure one could do the measurements using surface Rayleigh waves. Holes with a

diameter of 0.563 and 1.265 mm were added by EDM at varying surface depths (0.261-1.226 mm). All the holes with diameters greater than 0.725 mm and all holes up to 0.7 mm in depth identified from B-scans produced using the LaserScanTM software using the developed filtering strategy.

In a later publication [135] by the same authors as in [134], the same LU system is used to inspect different samples. One thing noted in the article is that there are no coupling problems (losses and noise) in LU; this is of particular importance when one is using higher frequencies to resolve smaller defects. Test pieces were designed and manufactured from Ti6Al4V using AM. The test pieces had a 10.0 by 3.0 by 0.2 mm defect zone placed centrally below the top surface of a 20 by 20 by 10 mm block. The defect zone was created by using different laser scan parameters. B-scans were generated and were able to show the intentionally created sub-surface porosity. The results were validated with X-ray computed tomography.

In [136] a LU system with continuous wave laser heterodyne detection is used to inspect a sample that has a spot weld. The sound generation laser used is a Quanta Ray Q-switched Nd:YAG, operating at 355 nm and a repetition rate 100 Hz. This publication had a thorough description of the setup and imaging method but it was not very clear on how the spot weld is related to any defect from particular AM technology.

The experiments reported in [137] focused on testing an AM and a forged block of 80 by 20 by 25 mm made in 316L SS. Notches were made in the block by EDM in order to simulate defects similar to the ones found in the DED process. The generation laser has a wavelength of 532 nm, with a 7 ns pulse duration. The pulse energy is 30 mJ. The probe laser has a 1064 nm wavelength with a pulse duration of 80 μ s. The interferometer is a two-wave mixing interferometer made of a photorefractive crystal. The signal to noise ratio of the returned sound signals was found to be lower for the AM made blocks. This was explained by the difference in grain size and shape between the AM and the forged 316L steel. The size of the smallest notch that could be seen was 50 μ m in width at a 100 μ m depth.

LU inspection for metal AM components was investigated as part of the “Intrapid” project [138]. The project aims to investigate eddy current, laser thermography and laser ultrasonics. The detection system uses a laser interferometer to measure surface waves to detect surface and sub-surface defects, and time of flight measurements of diffracted ultrasound were used to detect defects deeper in the samples. The algorithm used to detect defects fits the data to hyperbolic shaped reflections coming from a point-like scatterer.

In a later paper [139] by the same first author as in [138], LU is tested against laser thermography. Laser thermography is the application of a laser to a surface to apply

localized heating. Depending on the sub-surface thermal properties (in part determined by the existence of voids), the IR image of the surface over time will show local heating/cooling due to sub-surface defects. Inconel 600 coupons were made with LPBF and afterwards blind holes were drilled using laser drilling with different sizes and distances from the surface. The generating laser spot was a 0.1 by 3 mm line, produced by using two cylindrical lenses. Holes with sizes down to 470 μm were detected with both methods. However it was noted that depth and size determination with laser thermography is not as accurate compared to LU.

In [120] the samples being tested were made using built-in holes and the results were validated using CT and immersion UT. The samples used were made by LPBF with AlSi12. The sample was made with five equally spaced 2 mm size holes with varying lengths of 2, 5, 10, 15 and 20 mm. The samples were sandblasted before testing in order to get better signal reception. The LU system used was the LUKS-1550-TWM system from Optech Ventures & Intelligent Optical Systems Inc. [117]. All defects tested were clearly detected with LU.

2.6 Sound radiation force and current applications

This subsection describes how a given sound field can produce a force field on an object with a large difference in acoustic impedance compared to the sound propagation medium.

2.6.1 Applications of sound radiation force in microfluidics

The sound radiation force phenomena has been used extensively within the field of microfluidics (acoustofluidics), in order to sieve and sort particles or particle agglomerations. This is usually done for fast biological particle/agglomeration characterization. A good review of the subject can be found in [140].

For calculating the sound radiation force, one first needs to calculate the sound pressure field and its corresponding Gor'kov potential [141]. This potential is related to the acoustic force on a particle with some particular acoustic material properties via:

$$F = -\nabla U \quad (2.3)$$

The Gor'kov potential is the following [142, 143]:

$$U = V_p \left[f_1 \frac{1}{2} \kappa_m \langle p^2 \rangle - f_2 \frac{3}{4} \rho_m \langle v^2 \rangle \right] \quad (2.4)$$

with:

$$f_1 = 1 - \frac{\kappa_p}{\kappa_m} \quad (2.5)$$

and:

$$f_2 = \frac{2(\rho_p/\rho_m - 1)}{2\rho_p/\rho_m + 1} \quad (2.6)$$

where $V_p = 4\pi r_p^3/3$ is the particle volume, r_p is the particle radius, and ρ is the density. The subscripts m and p correspond to the medium and particle respectively. The variable κ_a is the compressibility either of the particle or the medium, given by $\kappa_a = 1/(\rho_a c_a^2)$, where c_a is the speed of sound in the medium or particle. The angled brackets denote a one wavelength average of the instantaneous pressure and wave particle velocity squared (p^2 and v^2).

A result was given in [142], for particles flowing in a microfluidic channel with two parallel 180° out of phase transducers at opposite walls. The sound pressure in the channel was modeled as:

$$p = p_a \cos(kz) \sin(\omega t) \quad (2.7)$$

with one side channel at $z = 0$ and half a wavelength at the opposite side w meters away ($k = 2\pi/\lambda$ and $\lambda/2 = w$). The derived force field was the following [142]:

$$F = 4\pi\Phi k r_p^3 E_{ac} \sin(2kz) \quad (2.8)$$

where $E_{ac} = p_a^2/(4\rho_m c_m^2)$, and $\Phi = f_1/3 + f_2/2$. Eq. 2.8 is derived in Appendix A.

From this analytic result a few observations can be made:

- The amount of force is proportional to the sound pressure magnitude due to E_{ac} and inversely proportional to its wavelength due to the k dependence
- The maximum force happens at a quarter of the wavelength from the nodes of p and its directed towards the nodes if $\phi > 0$ which happens in most cases where $\rho_p > \rho_m$
- The amount of force crossing its maximum value decreases as one gets closer to the particle trapping point

2.6.2 Sound radiation force for sorting of aerosol particles

Another application of sound radiation forces is to sort particles in a gas; aerosol sorting. The applications are mostly for particle characterization.

In [144], glass bead particles in air are sorted using a resonator channel, similar to the microfluidic channel analyzed in [142]. The movement of the particles within the air flow was visualized by using a laser light sheet formed by passing a laser beam through a cylindrical lens. The laser used was a 4 W argon-ion laser with a 514 nm beam. In [145], particles fall towards an acoustic Fresnel lens that produces an radially symmetric force field that can be used to sort them based on size and/or material properties. In [146] the forces on sub-micron aerosol particles are modeled and measured as a function of the aerosol number density and size distribution, while they move in a flow-through resonator.

2.6.3 Acoustic levitation

In [147], a model of the sound field from an ultrasound transducer array is numerically optimized by varying the phases of each element in order to produce the highest particle trapping forces possible, using the results in [142] that relate the gradients of the averaged instantaneous pressure in a sound field with the generated force field on particles with a given size and material properties.

For particle trapping, all force gradients should be positive close to a required trap point and the trap point location should have a low sound pressure amplitude. Therefore one should maximize the Laplacian of the Gor'kov potential (the negative gradient of the force) and minimize the pressure amplitude there [147]:

$$f = w_p |p| - \nabla^2 U = w_p |p| - (U_{xx} + U_{yy} + U_{zz}) \quad (2.9)$$

One can control the spatial distribution of forces around the levitation point by weighting each of the second partial derivatives of the Gor'kov potential with a bias weight:

$$f = w_p |p| - (w_x U_{xx} + w_y U_{yy} + w_z U_{zz}) \quad (2.10)$$

where $|p|$ is the magnitude of the averaged sound pressure and U_{aa} is a second spatial partial derivative of the Gor'kov potential that is a function of p , the particle size and material properties of the particle and the medium. One example of the arrays used in [147] are shown in Fig. 2.11. Other shapes such as a “v” arrangement with two angled side by side rectangular arrays and a hemispherical array were also used.

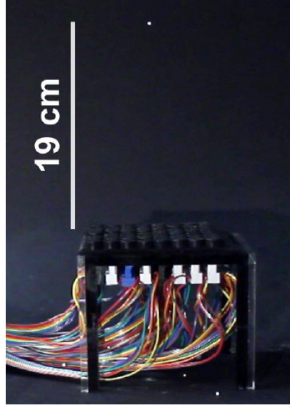


Figure 2.11: Example 8 by 8 flat rectangular array setup levitating a particle (from supplementary material of [147]).

For example, if one has a flat rectangular array with the transducers pointing in the z direction and the levitation point is a certain distance along the z axis like in Fig. 2.11, if one uses a large value for w_x or w_y and low values for all the other weights, one obtains a twin trap, shown in Fig. 2.12. In the three pictures shown, the sound field was generated using a 20 by 20 array of MA40S4S sound transducers from Murata Electronics (more information found in supplementary material of [147]), optimizing for a levitation point 12 cm along the z axis where the z axis intersects the center of the array and is perpendicular to the array.

The twin trap was not reported in the acoustics or optical literature before being reported in [147]. If one uses large w_x and w_y values, one obtains a vortex trap, shown in Fig. 2.12. Vortex traps have been designed before using acoustic and optical setups.

A bottle trap with high forces in the z direction can be obtained by using a large w_z weight. The resulting pressure distribution is shown in Fig. 2.12. Bottle traps have been produced in acoustics but not for particle levitation, however they have been reported in the optical tweezer literature and are usually produced by intersecting two laser beams with different modes [147].

The weightings described apply to a flat transducer array and might need to be changed if the array has a different geometry to obtain the required trap type.

The Gor'kov potential can also be expressed in terms of the instantaneous pressure and its spatial derivatives by [147]:

$$U = K_1|p|^2 - K_2(|p_x|^2 + |p_y|^2 + |p_z|^2) \quad (2.11)$$

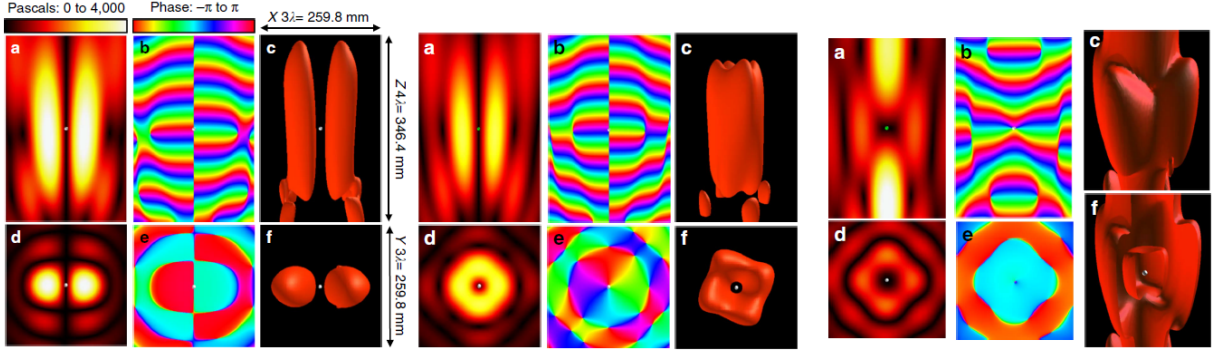


Figure 2.12: Acoustic traps: twin (left), vortex (center), bottle (right). The pressure isosurfaces shown are for 2 KPa for the twin and vortex traps and 1.3 KPa for the bottle trap [147].

with:

$$K_1 = \frac{1}{4} V_p \left(\frac{1}{c_m^2 \rho_m} - \frac{1}{c_p^2 \rho_p} \right) \quad (2.12)$$

and:

$$K_2 = \frac{3}{4} V_p \left[\frac{\rho_p - \rho_m}{\omega^2 \rho_m (\rho_m + 2\rho_p)} \right] \quad (2.13)$$

where p is the sound pressure field that is the sum of the individual transducer pressure fields, $|p|^2 = p \cdot p$ and the dot product operator in this case is defined in [147] as $a \cdot b = \Re(a)\Re(b) + \Im(a)\Im(b)$. The form of the Gor'kov potential given by Eq. 2.11 can be found by finding the required spatial derivatives of the total sound pressure field p , and its derived in Appendix A.

An analytic form of the vortex sound field obtained in [147] for a particular transducer array setup is used in [148] to levitate a large Styrofoam particle that has a size comparable to the sound wavelength (i.e Mie particle). For particles of this size the vortex sound field produces a net torque, that leads to dynamic instability and ejection. This is mitigated by generating sequences of short-pulsed vortices of equal helicity but opposite chirality.

The design of force fields using high intensity sound has been used to design an acoustic levitation system that automatically injects, transports, merges and ejects liquid droplets in mid-air [149], which could be used in applications in biology, chemistry and pharmacy where these operations are done manually using a pipette to transport and mix liquids.

The sound field is calculated taking into account a single reflection from a flat sound reflector. This is done by combining a modified matrix method with the Gor'kov potential equation to simulate the pressure and potential field generated by all the sound sources. This produces similar results to [147] but without using nonlinear optimization. In [149] this calculation was done using an analytical expression for the acoustic pressure generated by the sound sources using the far-field approximation. In [150], an example of the calculation taking into account an infinite number of reflections for ultrasound directed self-assembly to organize particles dispersed in a fluid medium into a desired three-dimensional user-specified pattern. The calculation is carried out by simulating the sound field using the boundary element method for solving the Helmholtz equation and directly solving a constrained optimization problem to obtain the required phases. In [151], multiple acoustic traps can be produced, using an iterative back-propagation algorithm to find the phases of the sound sources, in a similar way to how holographic optical tweezers (HOT) are produced. The algorithm uses a modified version of the iterative angular spectrum approach, which is based on the Gerchberg–Saxton algorithm used to generate HOT.

2.7 Summary

As discussed in this chapter, LU technology has matured to the point of commercial application and it is currently starting to be applied for AM manufacturing. Part of this adoption by industry has been enabled by more capable lasers with more power and shorter pulse times that allow for higher resolutions, as well as integrated robotic systems which are able to be used with LU in order to inspect parts non-destructively, at long distances and with more advanced computer control allowing for inspection of complex geometries.

The recent developments described in this chapter where ultrasound is used to levitate and sort particles, as well as the recent work described in [152] where the grain morphology of an AM part was modified by using an ultrasound transducer attached to a LPBF build plate show the promise of using ultrasound not only for NDT, but also to more finely control metal AM processes.

Chapter 3

Laser Ultrasound Tailored for LPBF

3.1 Introduction

Laser ultrasound (LU) is a non-destructive testing (NDT) method that generates, and measures sound waves reflected from defects such as voids inside a metal part built by advanced and conventional manufacturing methods. In particular, any defects in metallic parts made by additive manufacturing (AM) processes, which are known to negatively decrease the strength and fatigue performance of printed parts [153].

LU can be performed in a non-contact way and at high temperatures [3, 4]. This is very useful for in-situ AM metal inspection, since the use of some sensors in an intermittent fashion could substantially increase the fabrication time considering the fact that the solid topmost layer or track is at a high temperature during the metal AM process. Another attractive feature of LU is that it can be used concurrently for defect detection and residual stress measurements [5].

The current work described herein is done to demonstrate the use of UL to detect and compare the different defects (i.e., cracks and pores) at different location of parts made by AM. In particular, the UL responses for side through-hole, bottom blind hole and trapped powder artificial defects at different depths were studied for different samples composed of different alloys. In addition, the selection and customization of an appropriate reconstruction method that takes into account the UL experimental setup needed for a laser powder-bed fusion (LPBF) machine.

In a previous study with similar aims, LU is applied to the detection of defects in SS 316L and Ti6Al4V samples. To capture shallow defects, Rayleigh surface waves are used. Wavelet analysis is used to filter defect signals [132].

In [111], an LU system was used to check for defects in metal AM test coupons made using laser directed energy deposition (LDED) with powder and wire feedstocks, and with electron beam wire deposition. Lack of bonding, lack of fusion, and individual pores were detected and confirmed with X-ray micro-computed tomography.

An LU system was used by Everton in [134] to detect defects in Ti6Al4V samples, made with LPBF as well as samples with the same dimensions with wrought Ti6Al4V stock material. The dimensions of the block were determined using sound propagation time calculations to make sure one could do the measurements using surface Rayleigh waves. Holes with a diameter of 0.563 and 1.265 mm were added by electrical discharge machining (EDM) at varying surface depths (0.261-1.226 mm). All the holes with diameters greater than 0.725 mm and all holes up to 0.7 mm in depth were identified from B-scans.

LU inspection for metal AM components was investigated as part of the “Intrapid” project [138]. The project aims to investigate eddy current, laser thermography, and laser ultrasonics. These NDT techniques were suggested to be the most promising technologies for in-situ inspection of parts being produced in an LPBF machine due to them being non-contact and having a fast data acquisition rate. The detection system used in the investigation used a laser interferometer to measure surface waves to detect surface and sub-surface defects, and time of flight measurements of diffracted ultrasound were used to detect defects deeper in the samples. The measurements are used in a program that checks the resulting images against some user-defined pass or fail criteria. The algorithm used to detect defects fits the data to hyperbolic shaped reflections coming from a point-like scatterer.

In [120], the samples tested were made using built-in holes and the results were validated using CT and immersion ultrasound testing (UT). The samples were made by LPBF with AlSi12. The sample was made with five equally spaced 2 mm size holes with varying lengths of 2, 5, 10, 15, and 20 mm. The samples were sandblasted before testing to get better signal reception. The LU system used was the LUKS-1550-TWM system from Optech Ventures LLC [117], also used in this work. All defects tested were detected with LU.

Spatially resolved acoustic spectroscopy (SRAS) has been used in [154] in order to detect LPBF surface and subsurface defects up to a depth of about 24 μm . SRAS is a material characterization technique based on measuring the acoustic surface wave velocity.

There are only a few publications describing the use of LU for metal AM, that includes a reconstruction method [111, 155], i.e. in most articles, defect indications were observed directly in the B-scan [120] or extracting the defect location by analysis of the B-scan [138].

Reconstruction methods in UT can be divided into time domain methods, such as delay-and-sum (DAS) or frequency domain (FD) methods such as phase shift migration (PSM)

or wavefield extrapolation [63], due to its accuracy and computation speed, because it is derived from the wave equation and can use the fast Fourier transform (FFT) [73, 156]. One advantage of DAS methods is that the directivity of the sound sources may be readily included [157]. One quantitative study showed a higher signal to noise ratio and higher computation speed when using PSM [158]. Also the FD representation of the signals may also allow for more accurate and faster filtering which will be explored further in this chapter.

Normally PSM is done for a “monostatic” case; the emitter and receiver are the same transducer element, which is then applied at different equidistant positions. There are other methods such as full matrix capture, where a set of positions is chosen, and at every position the source is applied and the receiver records the signal for all other positions. The most common implementation of this is using DAS, and is called total focusing method (TFM). This was applied to detect 1 mm diameter side hole artificial defects in Ti6Al4V samples produced using Wire Arc AM [159]. This method may produce better quality reconstructions due to more A-scans being recorded, however there will be a trade-off between measurement time and accuracy for a given B-scan size.

As described in Section 3.2.2, there has to be an offset between the generation and detection laser, this means that the PSM algorithm has to be modified to account for this offset. In one study where PSM was used with LU for imaging defects in an aluminum plate, an attempt was made to find an equivalent wave velocity in the time domain to account for this offset [160]. However an approximation had to be made for small offsets with respect to the defect depth to get a final expression. One way to consider this offset directly in the frequency domain was described in [161]. Details on how this modified PSM was implemented for the LU measurements of AM samples in this chapter is described in Section 3.2.5.

The types of artificial defects used for evaluating the ultrasound setup and reconstruction can be grouped into 4 types: side through-hole [134], bottom blind hole [132], trapped powder and as printed [111, 162]. Trapped powder defects may be spherical or have other more complex shapes [135]. The types of artificial defects used in the literature are described in Table 3.1.

In this chapter, we use the first three artificial defect types listed in Table 3.1, in order to further quantify their advantages and disadvantages. Also the effect of the generation laser on the surface of the part being built will be investigated by taking surface roughness measurements. The effect of the generation laser on a partially-built part surface while being built was simulated by printing the samples with no up-skin.

Table 3.1: Artificial defect types

Defect type	Advantages	Disadvantages	Reference
Side through-hole	Can produce more accurate dimensions if machined Many parallel tracks can be used to perform measurements in the same sample	Signal difference due to geometry Signal is stronger compared to actual and other artificial defects	[134]
Bottom blind hole	Can remove powder and approach sound impedance defect of actual defect Can produce more accurate dimensions if machined	Signal difference due to geometry Needs post-processing to remove powder if possible	[132]
Trapped powder	Can be made for most sizes Does not need post-processing	Different in shape compared to STL file. Smaller defects below larger built defect and conical feature on top of defect may be observed Trapped powder in artificial defect can give a weaker signal compared to an actual gas-filled defect of approximately the same size, which would give an inaccurate assessment of detection size limit of technique being tested. Might be due to lower acoustic impedance difference between sample material and defect volume	[135]
As printed	Best option for research on NDT system that already has the right resolution (CT)	Features may be too small for research work when using LPBF printed parts	[111, 162]

3.2 Materials and methods

3.2.1 Sample design and fabrication

AlSi10Mg samples were printed by LPBF and machined with side through-holes. AlSi10Mg was used as the sample material for this type of artificial defect because it can be machined faster and more accurately compared to another commonly used LPBF materials such as Ti6Al4V. Ti6Al4V was used for the other two artificial defect types since those artificial defects can be directly printed into the sample. The artificial defects' geometry was designed taking into account the longitudinal and Rayleigh wave arrival times and expected defect signal arrival times.

The side through-hole samples were printed using a Renishaw AM400 system, with a layer thickness of 25 μm , a laser power of 200 W, a point distance of 80 μm , and an exposure time of 140 μs . The samples were printed with no upskin in order to approximate more closely a top surface corresponding to in-situ LU inspection, and cut from the substrate using EDM. The machining of the side through-holes was done using micro-drilling. Samples with side through-holes will be referred to as SH x, where x is the sample number. The AlSi10Mg sample geometries are reported in Table 3.2.

Table 3.2: AlSi10Mg sample geometries

Sample name	Defect sizes (mm)	Defect depths (to top of defect, mm)	Distances from left side of sample (to center of defect, mm)
SH 1	0.5, 1, 1.5, 2	1.25 (x 4)	8, 13, 18, 23
SH 2	0.5 (x 4)	1.5, 1.25, 1, 0.75	8, 13, 18, 23
SH 3	0.5 (x 8)	1.25 (x 8)	8, 8.75, 9.75, 11, 12.5, 14.25, 16.25, 18.5

A drawing of SH 2 is shown in Fig. 3.1. All samples have the same outside dimensions.

Two other sets of samples printed in Ti6Al4V with bottom blind holes and spherical trapped powder defects. The samples were printed using an EOS M290 system, with a layer thickness of 40 μm , a laser speed of 1250 mm/s, a laser power of 195 W, and a stripe width of 5 mm. The samples were also printed with no upskin, and cut from the substrate

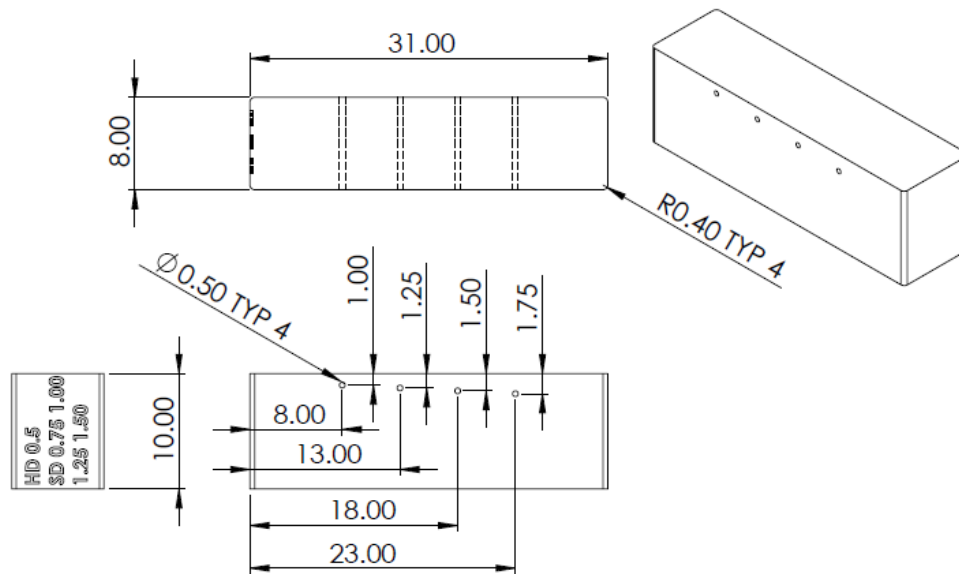


Figure 3.1: SH 2 sample design. In the embossing on the right HD stands for hole diameter and SD stands for surface depth to the top of the defect.

using EDM. The bottom blind hole samples were tapped against a vice to try to remove as much powder as possible from the blind holes. The Ti6Al4V sample geometries are reported in Table 3.3. The samples have the same outside dimensions as the AlSi10Mg samples shown in Fig. 3.1 except for a height of 6 mm instead of 8 mm. The samples are named as BH x for bottom blind hole with a hemispherical end and TP x for spherical trapped powder artificial defects, where x is the sample number in Table 3.3.

Table 3.3: Ti6Al4V sample geometries

Sample number	Defect sizes (mm)	Defect depths (to top of defect, mm)	Distances from left side of sample (to center of defect, mm)
1	0.1, 0.2, 0.3, 0.4, 0.5, 0.6	1.5 (x 6)	8, 11, 14, 17, 20, 23
2	0.3 (x 6)	2.8, 2.3, 1.8, 1.3, 0.8, 0.3	8, 11, 14, 17, 20, 23
3	0.3 (x 8)	1.5 (x 8)	8, 8.75, 9.75, 11, 12.5, 14.25, 16.25, 18.5

3.2.2 Laser ultrasound system and setup

The laser ultrasound system used for the experiments in this chapter is the LUKS-1550-TWM laser ultrasonic system (Optech Ventures LLC). The system has the following specifications:

- 100 mJ free-space Nd:YAG generation laser at 1064 nm with a pulse width of 8 ns and repetition rate of up to 20 Hz
- 400 mW to 2W continuous wave, single frequency fiber detection laser at 1550 nm
- A gantry 2D scanning system with 250 mm travel distance

The generating laser can be focused to a $75 \mu\text{m}$ spot size with a 50 mm focusing lens. The software can record and export A, B or C-scan data. The interferometer is a Homodyne Michelson setup, with a photorefractive polymer as a beam combiner to decrease surface finish susceptibility [163]. The experimental setup is shown in Fig. 3.2.

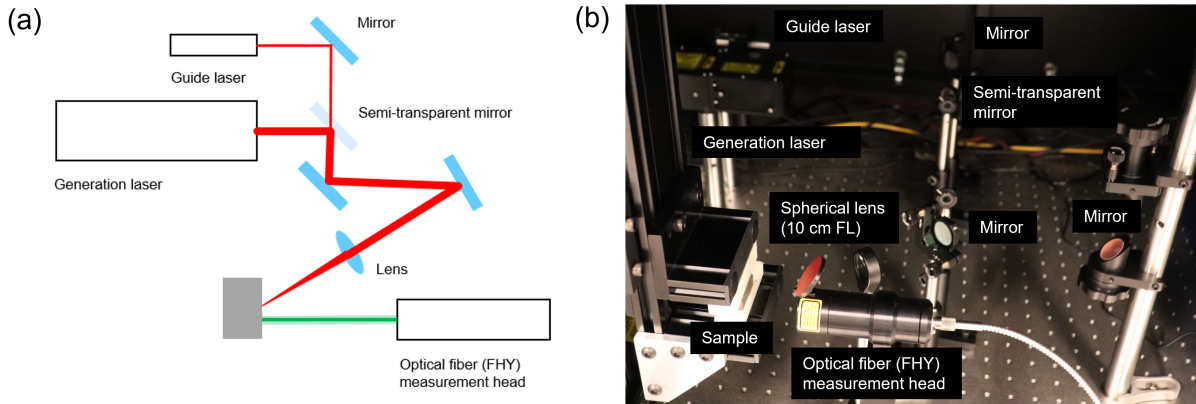


Figure 3.2: Schematic (a), and labeled photo (b) of experimental setup used to obtain B-scans. To hold the sample shown, a special sample holder to place the sample against two perpendicular directions for fast-changing was designed and FDM printed.

The distance between the generation and detector laser beam spots is not zero as expected from other UT NDT applications because the generation laser also produces a shock-wave in the air that travels slower than the longitudinal and Rayleigh waves in the sample to the detection spot. Otherwise, the large signal caused by the shock-wave will occlude the signal given by the sub-surface defect. If higher generation laser powers and/or a sample with a higher absorptivity are used, the induced plasma might affect the interferometer laser if the offset distance is low enough [132].

3.2.3 Expected ultrasound signals

The LU scan direction with respect to the sample and the laser position and vectors to calculate the time of arrival of the expected signals are shown in Fig. 3.3.

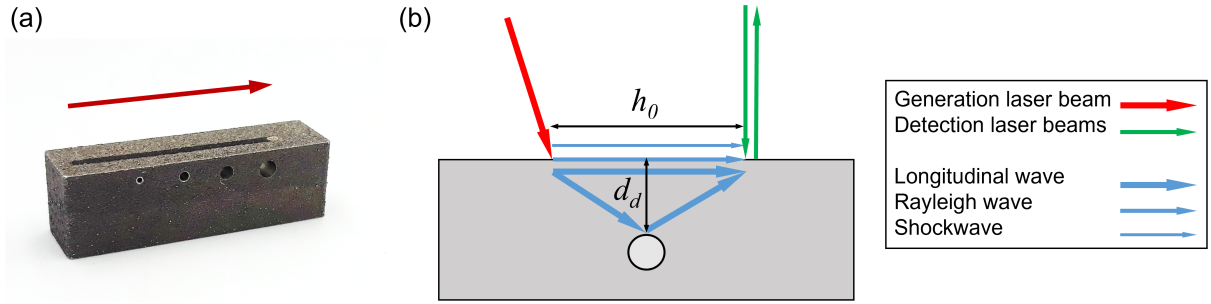


Figure 3.3: (a) Scan direction with respect to SH 1 sample (a), and (b) laser and relevant sound wave vectors produced in the LU process.

The first signal expected is the surface longitudinal wave (SLW), given by:

$$t_{SLW} = h_0/c_{LW} \quad (3.1)$$

where t_{SLW} is the arrival time (with the start time being when the generation laser hits the sample's surface) of the SLW, h_0 is the generation and detection laser spot to spot distance and c_{LW} is the longitudinal wave (LW) speed. The second signal expected is the one acquired when the laser spots are equidistant from the defect i.e the shortest longitudinal wave path to the defect, given by:

$$t_{LW} = \frac{2}{c_{LW}} \sqrt{h_0^2/4 + d_d^2} \quad (3.2)$$

where t_{LW} is the arrival time of the surface longitudinal wave and d_d is the defect surface depth. The wave causing this signal is referred to as the body, or bulk, longitudinal wave (BLW). The third signal expected is from a Rayleigh wave (RW), given by:

$$t_{RW} = h_0/c_{RW} \quad (3.3)$$

where t_{RW} is the arrival time of the RW and c_{RW} is the RW speed. RWs have are composed of longitudinal and shear waves which are out of phase, and have a speed very similar to body shear waves.

For the results reported in this chapter, B-scan measurements were obtained at generation laser powers of 80% (for AlSi10Mg samples) and 60% (for Ti64 samples) of full power, at a detection laser power of 1.2 W, and a laser offset distance of 3.5 mm. The offset distance was determined such that there is enough “space” between the surface wave signals in the B-scan to show the defect indications, with the aid of the equations described in this section. All measurements were done with a 100 mm focal lens (Thorlabs N-BK7 Plano-Convex Lens, 1” diam., $f = 100$ mm, Uncoated, part # LA1509) to focus the generation laser, a track length of 23 mm, a stage moving increment of 0.1 mm, a stage speed of 15 mm/s between increments, and A-scans composed of an average of 16 individual repeat measurements. It was found that using a generation laser power fraction of 80% for the Ti64 samples produced stronger vertical signal variations while not producing a noticeably higher defect indication so a generation laser power fraction of 60% was used. This also accounts for the different absorptivity between the tested alloys for the generation laser wavelength being used. This will be discussed in more detail in Section 3.3.

The time it takes to run the LU system with this setup is about 3 minutes. This can be estimated from the generation laser repetition rate (20 Hz), the readings at each spatial location for averaging (16), and the number of spatial locations (230), giving a time of $16/20(230) = 184$ seconds. This is assuming the travel time between spatial points is negligible. Note that this time would not be representative of an LU system integrated in an LPBF machine since the LU system being used is not optimized for measurement speed.

3.2.4 B-scan pre-processing

In order to obtain accurate time data, one has to take into account a $0.2 \mu\text{s}$ delay between the start of data acquisition and the generation laser hitting the sample, this is done by cropping the data before that time. The remaining spike signal at the beginning of the B-scan due to the interferometer receiving a small fraction of the laser light directly is also zeroed out.

It was found experimentally that a higher quality reconstruction can be obtained by cropping the data at the start of the RW signal instead of filtering it in the same way as the BLW as will be described later in this section.

There are two steps that were found to substantially increase the image reconstruction quality; signal normalization in the spatial direction and filtering of the SLW. The signal is normalized at the peak of the SLW.

A-scans with no defect signals can be averaged and subtracted from the rest of the A-scans in the B-scan to remove the SLW, this will be referred to as an average filter (AF).

The same effect as using an AF can be obtained by zeroing the frequency space (k-space), obtained by computing the 2D Fast Fourier Transform (FFT) of the B-scan, using a notch filter [164], on both sides of the origin and along the temporal frequency direction, a distance corresponding to the frequency component with the highest amplitude of the SLW signal after applying an FFT. This is due to the relationship between the Radon transform (a method that can be used to detect linear features) and the Fourier slice theorem (FST) [165]. This method was shown to have a very similar but slightly lower performance than the AF. This can also be done using a Hough transform (a discrete implementation of the Radon transform) for filtering the B-scan, however this operation is more computationally expensive [166]. The frequency space based method depends on the FST. Its relationship with the Radon transform is illustrated in Fig. 3.4. The advantage of this method is its speed (one only needs to apply the filters by multiplying a subset of k-space), and that it might be used for sample or part surface reflections which might produce linear features in the B-scan [166] that are not perpendicular to the temporal direction.

While in k-space or after applying the FFT to the data after the AF, the data can be filtered in the temporal or spatial directions. This step can be simplified and computed more efficiently, by finding a matrix that is element-wise multiplied with the 2D DFT. Frequency based filtering can also be done to zero the DC component of the B-scan, by applying a notch filter at the origin of the 2D DFT. Both operations can be computed using:

$$H_T = H_{DC} \circ H_{LP} \circ H_L \quad (3.4)$$

where H_T is the k-space representation of the B-scan (in the case of this example the rows holding the spatial frequency data and the columns the temporal frequency data), H_{DC} is a 2D notch filter [164] applied at the origin of k-space, H_{LP} is a filter to reduce undesirable spatial and temporal frequencies, and H_L is the initial k-space representation of the B-scan. In order to filter the B-scan, one would like to use a Fourier based filter (H_{LP}) that has minimal ringing, and can have different cutoff frequencies in the time and space domains. A 2D rectangle filter could be used but the sharp cutoff will produce ringing artefacts.

Another option is to use a separable filter, where the matrix H_{LP} is produced based on some product of two 1D Fourier space filters, computed as follows:

$$H_{LP} = J_f^T J_k \quad (3.5)$$

where J_f^T is the transpose of a 2D matrix and J_k is a 2D matrix. The filters that were used in both directions were Butterworth filters (BWFs) [164]. A proof showing that

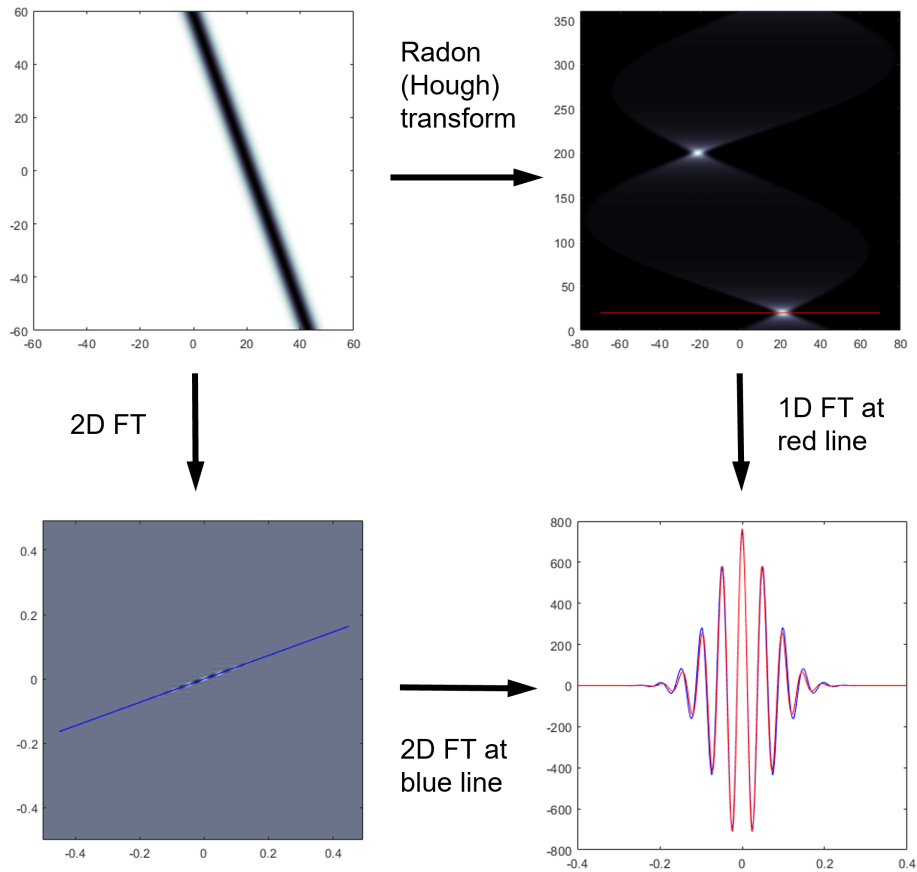


Figure 3.4: The way to remove linear features in the B-scan in [166] is to perform a Hough transform and crop the signal peaks in the resulting sinogram. However one needs to rotate the image for many angles and to numerically integrate the B-scan at each angle. As illustrated in this figure, the 1D FT of the angle where the line is expected in the B-scan is simply the 2D FFT sampled at a line through the origin of k -space and at an angle corresponding to the line angle, therefore removing high amplitudes along this line in k -space will have a similar effect to cropping the sinogram. The displayed magnitudes for the FTs are their real components.

this filter corresponds to applying the 1D filters at each step of the 2D Fourier transform computation, or applying them separately in each in the time and space domains is shown in B. The proof was done using the matrix representation of the discrete Fourier transform [167]. The power n [164] for both BWFs used was 3, the cutoff time frequency was the LW frequency times a factor of 5, and the cutoff for the spatial frequency was the value $k_{x,c}$

times a factor of 5. To calculate $k_{x,c}$, one can note that for a point scatterer (approximating a defect), the resulting features in the B-scan are FHF's. One can see from Fig. 3.6 that the highest slope dt/dx for these curves happens at high values of t (high depths) so one can assume a zero-offset distance. This means that this signal curve at high t values can be modeled as a hyperbola given by:

$$t_{ts} = \frac{2}{c_{LW}} \sqrt{x^2 + d_d^2} \quad (3.6)$$

where t_{ts} is the ‘‘time to signal’’, the x axis is assumed to be centered at the defect location, and the factor of 2 is due to the back and forth time the signal takes to get to and come back from the defect. The value of the slope dt/dx approaches the value $2/c_{LW}$ for large t , or x values; using this ratio, one can relate the width w of a disturbance in the time direction with the corresponding width of the disturbance in the x direction due to the LW signal:

$$\left. \frac{dt}{dx} \right|_{x \rightarrow \infty} \frac{1}{T} = \frac{2}{c_{LW}} f_{LW} = \frac{1}{w} = k_{x,c} \quad (3.7)$$

where T is the period of the LW signal. When filtering along the x direction one should make sure this spatial frequency is included.

The pre-processing used when filtering the SLW with AF is shown in Algorithm 1 and the pre-processing used when filtering the SLW in k-space is shown in Algorithm 2.

The parameters used for pre-processing all samples using Algorithm 1 were the following: emission/interferometer delay (l_{id}) of 200 ns, time range after cropping using l_{id} to zero the rest of the emission signal (t_{la}) of 90 ns, a time window to find the LW frequency (t_{lws} to t_{lwe}) of 0.632 to 0.952 μ s (using a cutoff frequency of 3 MHz), and a RW crop time (t_{sws}) of 0.93 μ s. The emission/interferometer delay is happening in air and is independent of sample material. The RW crop time was chosen from the A-scans; it was found that for both materials it gave the best reconstruction results.

3.2.5 Image reconstruction using phase shift migration

Phase shift migration algorithms [168, 73] rely on the fact that in the wavenumber (based on the measurement step distance along the surface) and frequency domain (doing a 2D FFT of the B-scan measured at the sample’s surface), one can extrapolate into the sample at a certain depth z , by multiplying the FFT by a phase term and then adding the frequency terms and doing an inverse 1D FFT along the wavenumbers.

Algorithm 1 Pre-processing B-scan filtering SLW with AF

- 1: Read B-scan data as $p(t,x)$
 \triangleright p is an $M \times N$ array with time t along rows and location x along columns
 - 2: $p = p(t_{ld}$ to t_m , all x)
 \triangleright Crop p ; using setup dependent laser emission/interferometer delay of 0.2 ns
 - 3: $p(t_1$ to t_{la} , all x) = 0
 \triangleright Zero part of p ; t_{la} being time disturbance to interferometer from laser light

 - 4: **for** $m = 1$ to M **do** \triangleright Find LW dominant frequencies (needs to be done only once)
 - 5: $B_m = FFT_{1D}[b(t_{lws}$ to t_{lwe} , n)] \triangleright 1D FFT along time, for time where LW is present
 - 6: $f_{lw,m} = \text{findFrequencyPeak}(B_m, f_{cut})$ \triangleright Find first peak after cutoff frequency
 - 7: **end for**
 - 8: $f_{lw} = \text{average}(f_{lw,m})$

 - 9: $p = p(t_1$ to t_{sws} , all x) \triangleright Crop p ; up to time SW starts in A-scans

 - 10: $t_{lw,max} = \text{findMaxValue}[p(\text{all } t, m_1$ to $m_{10}))]$
 \triangleright Average time of peak SLW signal from first 10 A-scans
 - 11: **for** $m = 1$ to M **do** \triangleright Normalize A-scans based on location of peak of SLW
 - 12: $p(\text{all } t, m) = p(\text{all } t, m) / p(t_{lw,max}, m)$
 - 13: **end for**

 - 14: $p_{avg} = \text{averageM}[p(\text{all } t, m_1$ to $m_{10}))]$ \triangleright Average along rows of first 10 A-scans
 - 15: **for** $m = 1$ to M **do** \triangleright AF; subtract average of first 10 A-scans from every A-scan
 - 16: $p(\text{all } t, m) = p(\text{all } t, m) - p_{avg}$
 - 17: **end for**

 - 18: $P = FFT_{2D}(p)$ \triangleright 2D FFT along location and time with zero padding
 - 19: $P = P \circ F_{LP}$ \triangleright Apply LP filter; need to compute filter once
-

Algorithm 2 Pre-processing B-scan filtering with k-space frequency filters

- 1: Apply lines 1 to 13 from Algorithm 1

 - 2: $P = FFT_{2D}(p)$ \triangleright 2D FFT along time with zero padding
 - 3: $H_T = F_{DC} \circ F_{N,lw} \circ F_{N,sw} \circ F_{LP}$
 \triangleright Compute filter product once (DC, LW and SW notch, and BTW)

 - 4: $P = P \circ H_T$ \triangleright Apply filter
-

The migration equation in the frequency domain, with $z = 0$ being the sample's surface, and with the generation laser spot (source s) and interferometer laser spot (receiver r) located on the surface along the x axis, is given by:

$$P(k_x, k_h, z, \omega) = P(k_x, k_h, 0, \omega)e^{jk_z z} \quad (3.8)$$

where $j = \sqrt{-1}$, k_x corresponds to the spatial frequency of the midpoint coordinate $x = (r + s)/2$, k_h corresponds to the spatial frequency of the half-offset $h = (r - s)/2$, and k_z is the following:

$$k_z = \text{sign}(\omega) \left[\sqrt{\left(\frac{\omega}{v}\right)^2 - \left(\frac{k_x + k_h}{2}\right)^2} + \sqrt{\left(\frac{\omega}{v}\right)^2 - \left(\frac{k_x - k_h}{2}\right)^2} \right] \quad (3.9)$$

which is known as the double square root (DSR) equation [73, 161]. A derivation of this form of the DSR equation is given in Appendix C.

Eq. 3.9 has a negative sign in [161] and earlier articles, where the FT along frequency ω is done with a complex exponential of opposite sign to the widely used definition of the FT:

$$P(k_a, z_a, \omega) = \iint p(a, z_a, t) e^{-j(k_a a + \omega t)} da dt \quad (3.10)$$

When this definition of the FT is used, corresponding results to the one in this chapter are obtained [169].

The full PSM algorithm for multiple x coordinates and half-offsets is given by [161, 170]:

$$p(x, 0, z, 0) = \iiint P(k_x, k_h, z, \omega) e^{jk_x x} dk_x dk_h d\omega \quad (3.11)$$

The algorithm allows the back-propagation of waves recorded at the surface to time zero where the defects are located. Note Eq. 3.11 can be interpreted as an inverse FT along x .

For the “common-offset” case, the recorded signals can be considered to be recorded at a single h value (h_0); this can be expressed as a recorded signal times the impulse function $\delta(h - h_0)$ [170]. The 2D FT of this signal along x and t is:

$$P_{h_0}(k_x, h, 0, \omega) = P(k_x, h, 0, \omega) \delta(h - h_0) \quad (3.12)$$

The full surface 3D FT signal, along x , h and t is therefore:

$$P(k_x, k_h, 0, \omega) = \int P_{h_0}(k_x, h, 0, \omega) e^{-jk_h h} dh = P(k_x, h_0, 0, \omega) e^{-jk_h h_0} \quad (3.13)$$

and the final form of the PSM algorithm to find the extrapolated wave field for the common-offset case is:

$$p(x, 0, z, 0) = \iiint P(k_x, k_h, z, \omega) e^{jk_x x} dk_x dk_h d\omega \quad (3.14)$$

$$= \int \left[\int P(k_x, h_0, 0, \omega) S(k_x, z, \omega) d\omega \right] e^{jk_x x} dk_x \quad (3.15)$$

where:

$$S(k_x, z, \omega) = \int e^{j(k_z z - k_h h_0)} dk_h \quad (3.16)$$

For the common-offset case, care must be taken in computing the double square root (DSR) equation to prevent imaginary phases. The value of k_z has to be real to satisfy the wave equation in the frequency domain when Eq. 3.10 is applied. In order for this to be the case, both terms inside the square root signs in Eq. 3.9 need to be zero or positive, giving two conditions, which can be reduced to one condition given by [161]:

$$\frac{2}{c}|\omega| \geq |k_x| + |k_h| \quad (3.17)$$

This can be found by considering the 4 quadrants in the k_x, k_h plane and checking how one can write $\max(k_x + k_h, k_x - k_h)$. If the condition given by Eq. 3.17 is not met, the FT of the extrapolated wave field is set to zero.

Eq. 3.16 can be approximated using a stationary phase approximation (SPA) [161]:

$$S(k_x, k_h, \omega) \approx e^{j\phi(k_h, 0)} e^{i\pi \text{sign}[\phi(k_h, 0)]/4} \sqrt{\frac{2\pi}{|\phi''(t_0)|}} \quad (3.18)$$

where $\phi(k_h) = k_z(k_x, k_h, \omega)z - k_h h_0$, and t_0 is referred to as the stationary point (SP), where $\phi'(t) = 0$.

Since finding the SP requires the roots of a 6th degree polynomial, the SP for the SPA was obtained as suggested in [161] using Newton's method (NM) [171]. The method was extended with a "weighted" bisection method [171] that overrides the NM if the next guess for the SP is outside the integration limits, determined from Eq. 3.17. Also, an initial guess for the SP was found, by noting that the DSR is a sum of two ellipses that can be approximated by a single ellipse. The use of an optimized weight and this new initial SP estimate reduces the computation time from 95 to 64 seconds, a 33% reduction. This

particular implementation of the NM is discussed further in Appendix D. The calculation of the S matrix is shown in Algorithm 3.

Another integration method that may be applicable to compute Eq. 3.16 is the Numerical steepest descent method [172], where the amount of calculated integration points can be adjusted to give a result with a given required error.

The resulting reconstructed images have high positive and negative values at the defect locations. One can apply a Hilbert transform along the depth direction to obtain an envelope of the signal representing the defects [173]. Note that it is not possible to reduce the number of operations for the PSM and Hilbert transform steps since the inverse FFT is done in the x direction, while the FFTs used in the Hilbert transform are in the z direction. One can also use a Hilbert transform for visualizing the B-scans, however applying this step as a pre-processing step before applying PSM takes more computation time and was found to not noticeably improve the reconstruction.

The PSM algorithm with the PSA approximation as well as the computation of the envelope function is shown in Algorithm 4. Note the frequency interval is not used in the numerical integration since the reconstructed image is normalized for plotting. In order to reduce ringing artifacts, the B-scan signal is zero padded in x and t to the next power of two before the 2D FT is applied (Algorithm 1, line 18, or Algorithm 2, line 2), and the signal is cropped to its original size after the PSM algorithm and Hilbert transforms are applied (Algorithm 4, line 10). The computation time for performing the PSM algorithm with the Hilbert transform is measured to be 0.64 seconds.

The parameters used in Algorithm 4 were the following: generation/detection laser common-offset (h_0) of 3.5 mm, number of spatial samples 230, number of time samples 1250 (at 8 ns intervals or 125 MHz). The LW speed for AlSi10Mg of 6620 m/s was found in [174], and the LW speed for Ti6Al4V of 6110 m/s was found in [175].

The reported computation times were measured for computations implemented in MATLAB, and running on a Dell OptiPlex desktop, with an Intel Core i7 3.6 GHz CPU processor and 16 GB of RAM. Note that the S matrix calculation needs to be done only once for a particular sound source-receiver distance, measurement step distance, and A-scan sampling rate.

3.2.6 CT system and setup

In order to check deviations between the original STL file and the samples with built artificial defects, CT scans of all the Ti6Al4V samples were conducted. The scans were

carried out using a Xradia 520 Versa 3D X-ray Nano-CT scanner (Zeiss Microscopy, Jena, Germany), with a $10\ \mu\text{m}$ voxel size.

The scans were done in three parts for each sample, with the middle scan at the center of the sample. The total scan volume is a cylinder with its axis parallel to the sample's length. Each of the 3 sampled volumes had a height of 10 mm and diameter of 10 mm. The total stitched image has a length of 25 mm. The planes were planes chosen such that they are the average of the two plane locations closest to the defects where none of the defects are seen in those planes, this is to account for misalignment in the placement of the sample in the scanner normal to the sample length. The planes were adjusted 5% or 10% in brightness and increased 40% in contrast.

3.2.7 Surface roughness

In order to determine the effect of the laser on the sample's surface, surface roughness measurements on the surface of sample 1 along the center-line of the laser track and 2 mm to the side of the track were done using a VK-X250 confocal laser microscope (Keyence Corporation, Osaka, Japan) microscope.

3.3 Results and discussion

3.3.1 Effect of pre-processing B-scan

The original B-scan for SH 1 and two A-scan locations showing the different sound wave related signals are shown in Fig. 3.5. One can observe from Fig. 3.5 (a) that the signals independent of defect position (the surface waves, see Fig. 3.3) generate vertical features in the B-scan. The shape and location of the SLW, the RW along with the BLW in the selected A-scans are shown in Fig. 3.5 (b). Note that at A-scan # 2 with no intersecting flattened hyperbolic features (FHF), indicative of a defect, there is no BLW signal but one is present in A-scan #2 where this A-scan intersects a FHF.

The signal shape on the B-scan from a scattering point feature in the case of zero offset ($h_0 = 0$) is a hyperbola but although the B-scan signals seen look like a hyperbola, one can notice they have a flattened hyperbolic shape or table top shape [168]. This is more apparent when the scatterer is closer to the surface and the offset is fixed.

Algorithm 3 S calculation using SPA

```

1: for  $iz = 2$  to # of depths do
2:   for  $m = 1$  to # of time periods  $N_t$  do
3:     for  $n = 1$  to # of  $x$  intervals  $N_x$  do
4:        $f = (m - N_t/2 - 1)f_s/N_t$ 
5:        $k_x = (n - N_t/2 - 1)/p/N_x$ 
6:        $\alpha = 2|f|/c - |k_x|$ 

7:       if  $\alpha > 0$  then ▷ Checking for this condition to prevent imaginary phases
8:          $z = (iz - 1)\Delta z$ 

9:          $k_{h,0} = 1$  ▷ Newton's method iterations to find SP
10:         $b = z \left[ 2\sqrt{(f/v)^2 - k_x^2/4} - \sqrt{|k_x|\alpha} \right]$ 
11:         $k_{h,0,new} = -\text{sign}(f) \min([1/\alpha^2 + b^2/(\alpha^4 h_0^2)]^{-1/2}, (1 - t_{tol})\alpha)$ 

12:        while  $|(k_{h,0} - k_{h,0,new})/k_{h,0,new}| > k_{tol}$  do
13:           $k_{h,0} = k_{h,0,new}, k_{h,0,new} = k_{h,0} - \phi'(k_{h,0})/\phi''(k_{h,0})$ 

14:          if  $|k_{h,0,new}| > \alpha$  then
15:             $k_{h,0,new} = \text{sign}(k_{h,0,new})[|k_{h,0}| + (1 - e_{tol})(\alpha - |k_{h,0}|)]$ 
▷ Weighted bisection step that keeps SP estimate inside  $(-\alpha, \alpha)$ 
16:          end if
17:        end while

18:         $S(iz - 1, m, n) = e^{j\phi(k_{h,0})} e^{j\pi \text{sign}[\phi(k_{h,0})]/4} \sqrt{\frac{2\pi}{|\phi''(t_0)|}}$  ▷ SPA using SP
19:      else
20:         $S(iz - 1, m, n) = 0$ 
21:      end if
22:    end for
23:  end for
24: end for

25: return  $S$ 

```

Algorithm 4 PSM algorithm

- 1: **for** $iz = 2$ to # of depths **do**
 - 2: $M(1, 1 \text{ to } N_x) = 0$ $\triangleright N_x$ is the # of x intervals

 - 3: **for** $n = 1$ to N_x **do**
 - 4: **for** $m = 1$ to # of time periods N_t **do**
 - 5: $M(1, n) = M(1, n) + P(m, n)S(iz - 1, m, n)$
 - 6: **end for**
 - 7: **end for**

 - 8: $m(iz - 1, \text{all } x) = \text{IFFT}_{1D}(M)$ \triangleright Inverse IFFT along x direction cropping zero padding
 - 9: **end for**

 - 10: $m = |\text{hilbert}(m)|$ \triangleright Find envelope function for each x by computing transform along depths

 - 11: **return** m
-

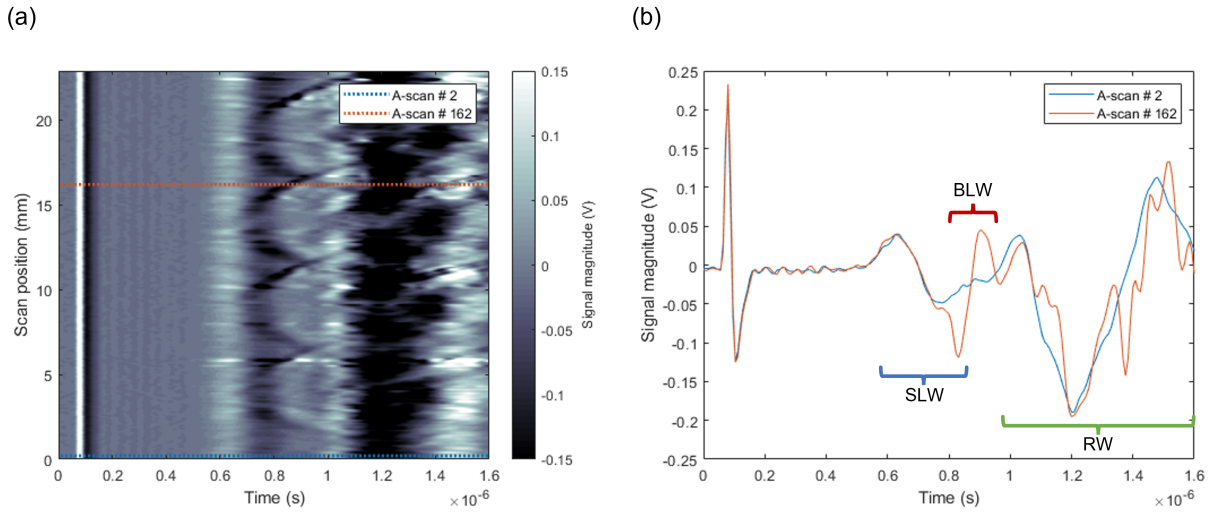


Figure 3.5: (a) B-scan from SH 1 sample, and (b) A-scans # 2 (blue dotted line) and # 162 (orange dotted line) from the same B-scan.

The B-scan from SH 1 shown in Fig. 3.5 (a), with the generation laser light signal zeroed out, and the RW cropped, is shown in Fig. 3.6 (a). The same B-scan with the AF to subtract the SLW signal is shown in Fig. 3.6 (b). A comparison of A-scan # 126 with and without the AF is shown in Fig. 3.6 (c). The B-scan shown in Fig. 3.6 (a),

with the maximum surface longitudinal wave normalization, followed by the AF, is shown in Fig. 3.6 (d). The AF significantly decreases the SLW signal as seen in in Fig. 3.6 (b) and (d); in the A-scans, one can see the SLW is decreased without substantially decreasing the overlapping BLW. The differences in magnitude between A-scans, as seen clearly in the original B-scan on the SLW crest in Fig. 3.6 (a), might be due to the generation laser having different absorptivity depending on the local surface roughness. Performing the maximum SLW normalization is a way of decreasing these effects on the B-scan as seen in Fig. 3.6 (c).

One can compare the initial cropped B-scan with the one using the longitudinal wave normalization and AF by displaying their envelopes, calculated using the absolute value of the Hilbert transform of each of their A-scans. The envelope B-scan corresponding to the B-scan in Fig. 3.6 (a) is shown in Fig. 3.7 (a), and the envelope B-scan corresponding to the B-scan in Fig. 3.6 (c) is shown in Fig. 3.7 (b). One can see from the envelope B-scans that the SLW signal has been substantially decreased, and the FHF's have increased in strength and are more uniform.

The reconstructions from the above B-scans are shown in Fig. 3.8 (a), and the signal magnitude at the depth shown with the dotted line in the first reconstruction is shown in Fig. 3.8 (b). One can see an improvement in the contrast between the resolved defect signals and the background in the last reconstruction, corresponding to the improvement in the corresponding B-scan in Fig. 3.6 (c) without low-pass filtering. The dB values shown in Fig. 3.8 (b) and all other subsequent A-scan comparisons using dB are calculated using $20 \log_{10}[s/\max(s)]$ where s is an array with the A-scan values [173].

3.3.2 AlSi10Mg samples

The final reconstruction for SH 1 is shown in Fig. 3.9. The red dotted lines showing a particular intensity as a function of x are 0.1 mm from the top of the defects for the AlSi10Mg samples and 0.2 mm for the Ti6Al4V samples. One can see the size of the reconstructed defect decreasing with decreasing defect size but the peak intensity stays constant beginning at the SH defect with a diameter of 1mm.

The filtered B-scan data for the SH samples are shown in Fig. 3.10. One can clearly see the FHF's for all defects except the overlapping ones for SH 3. The reason for this type of defect design was to check for this, and to check the quality of the PSM reconstruction when closely overlapping FHF's were present.

The reconstructions for the SH samples are shown in Fig. 3.11. The reconstruction of SH 2 produces satisfactory reconstructions at the right location up to a defect top to

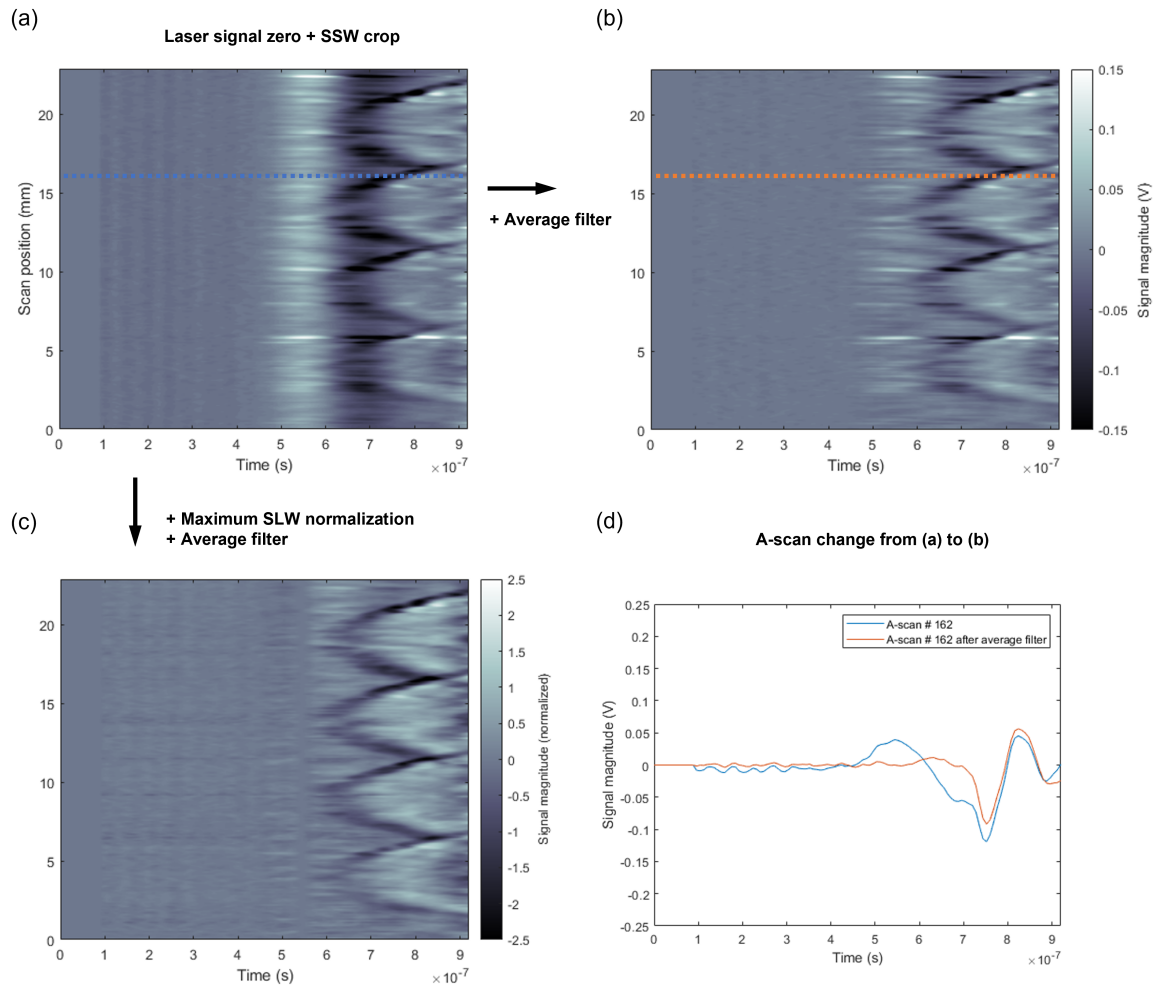


Figure 3.6: (a) The original B-scan with laser signal zeroed area and cropped RW, (b) B-scan (a) with with AF, (c) B-scan (a) with maximum SLW normalization, and (d) comparison between A-scans from dotted lines in B-scans (a) and (b).

surface depth of 1 mm. For the last defect at a depth of 0.75 mm there is a reconstructed feature but its depth is inaccurate. The reconstruction of SH 3 shows all the defects are reconstructed at the right locations.

Overall the SH type of artificial defects have the advantage of dimensional accuracy. Note the reconstructed signals have a tilted elliptical shape; this might be due to not considering the source, defect and receiver directivity functions in the PSM algorithm. One

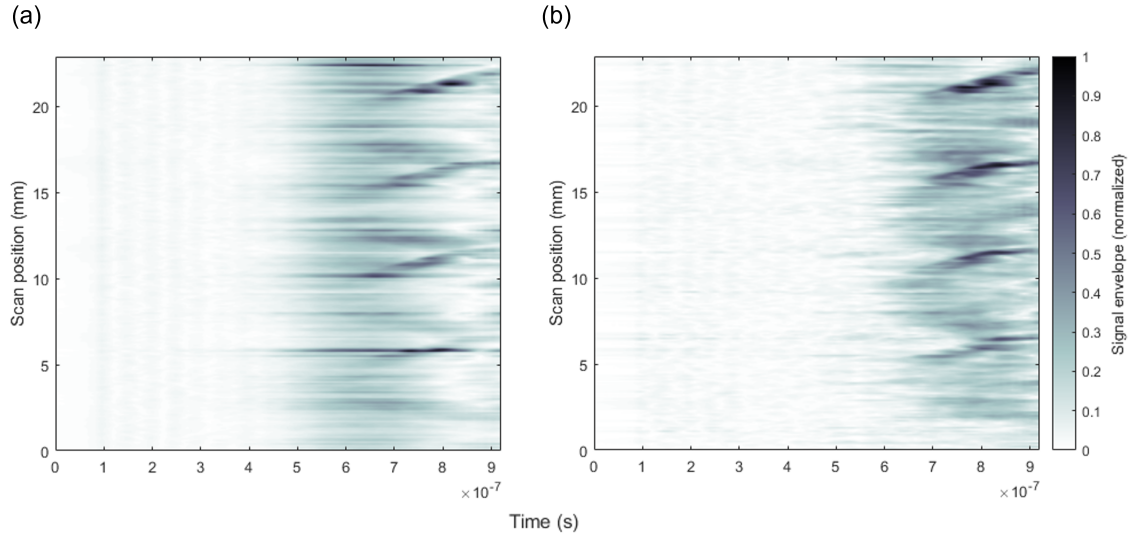


Figure 3.7: (a) Envelope B-scans of B-scan in Fig. 3.6, and (c) of B-scan in Fig. 3.6.

can see from Fig. 3.6 (c) that the FHF is stronger to the right of its center axis at a given x value, this can be explained by part of the sound waves being reflected back away from the interferometer laser spot location when the generation laser is behind the defect. Also, considering the PSM as a way to back-propagate the waves at $z = 0$ towards the defects, if the recorded wave signals are weaker behind the defect, one would expect waves of larger amplitude to converge in front of the defect, causing the observed tilted elliptical shape. As will be seen for the other artificial defect types in the Ti6Al4V samples, this feature is particularly pronounced for SH defects which might be due to the larger “occlusion area” (OA) due to the large side length of the defect.

3.3.3 Ti6Al4V samples

The filtered B-scan data for the Ti6Al4V samples are shown in Fig. 3.12. One can see that the B-scans have a large variation in A-scan signal intensity even after filtering. Factors that might affect this are a higher laser surface absorptivity for Ti6Al4V, a lower surface roughness (Section 3.3.5) and lower laser power (60 instead of 80% of full generation laser power). Although a lower laser power was used to account for the higher absorptivity, a higher amount of absorbed power due to other variables such as surface roughness might also increase the variability between the A-scan signal amplitudes.

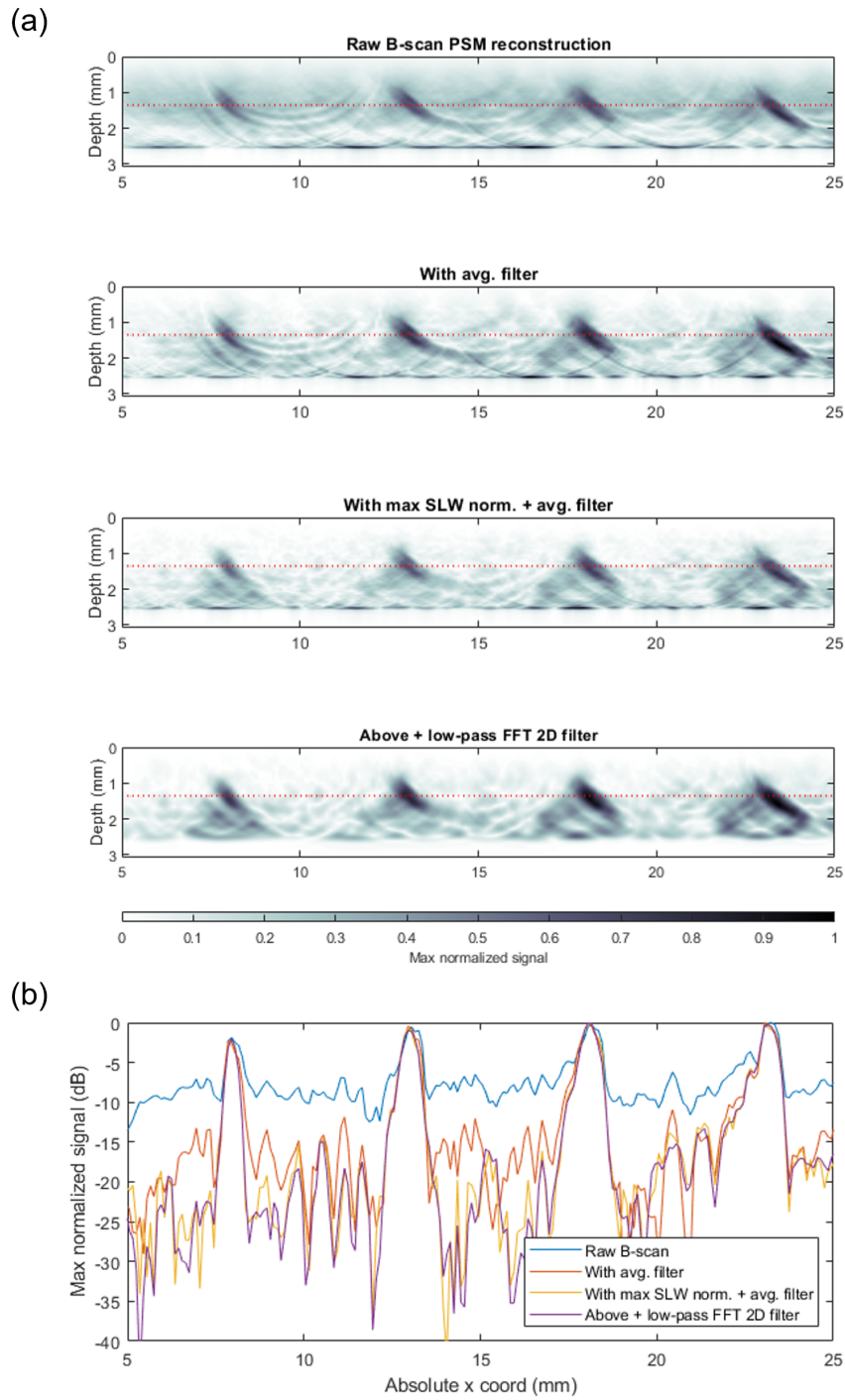


Figure 3.8: (a) The reconstructions for SH 1 corresponding to the B-scans in Fig. 3.6, and (b) the signal intensities along x along the red dotted lines.

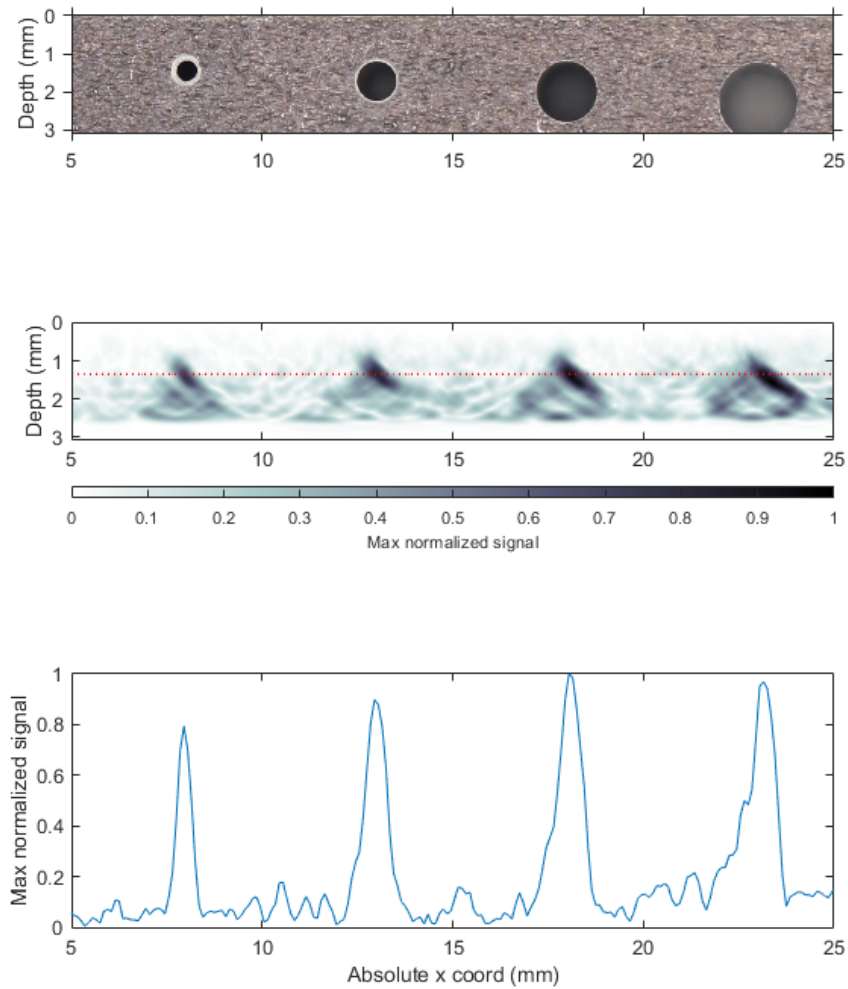


Figure 3.9: SH 1 reconstruction.

The reconstructions for the BH samples are shown in Fig. 3.13. For these samples, all defects were printed successfully, although for the smallest defect in BH 1 one can notice some collapse of the horizontal walls. Also the top of the defects is flatter than the original hemispherical feature shown in the CAD cross-section.

In the BH 1 reconstruction, one can see a peak in the intensity along the red line corresponding to all the defect locations and depths except for the one with a $100\ \mu\text{m}$ diameter. However the signal for $200\ \mu\text{m}$ is very close to the back noise level. For these types of defects, the defect signal values increase with defect size, compared to the reconstructed

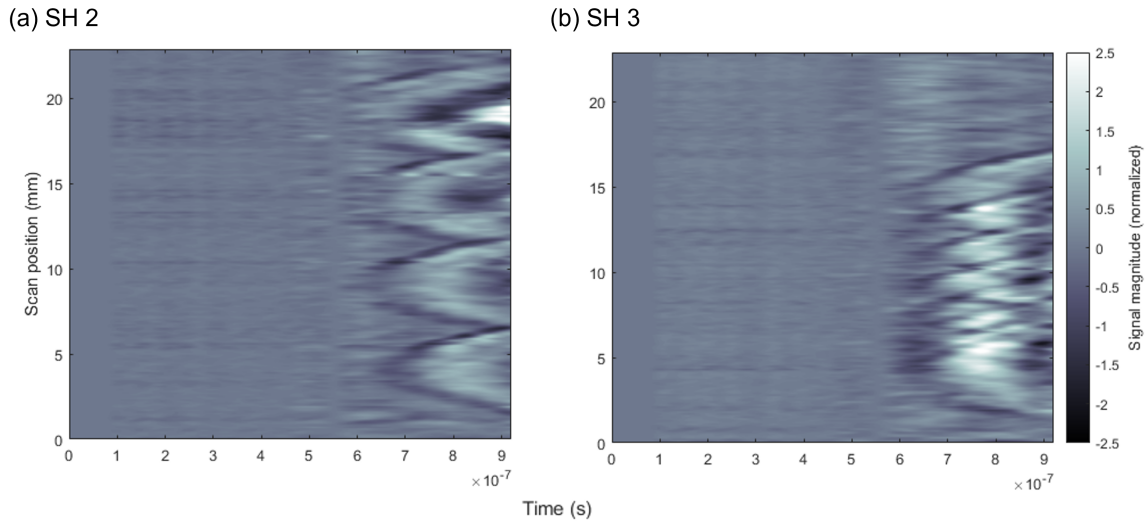


Figure 3.10: SH filtered B-scans. The SH 1 filtered B-scans can be seen in Fig. 3.6 (c).

defects from the SH 1 sample. Note that there is a difference in signal for defects in sample BH 1, for sizes 500 and 600 μm , compared to defects in SH 1, for sizes from 500 and 1000 μm . This might be due to the higher noise seen in the BH 1 B-scan.

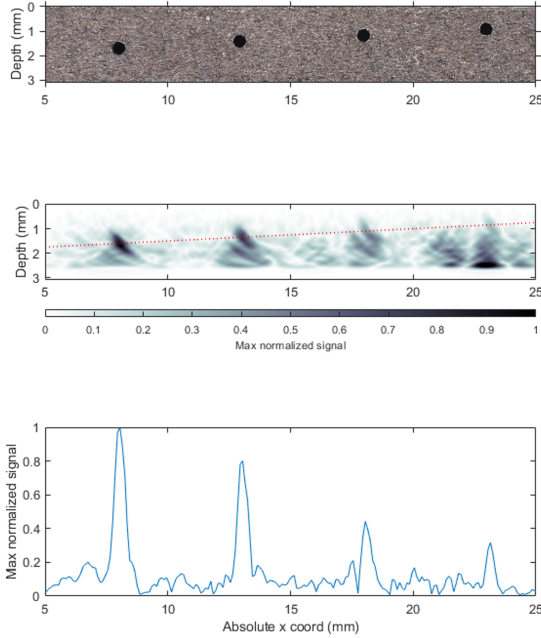
The BH 2 reconstruction produces the right locations for defect depths of 1.3 and 0.8 mm. However for the defect closest to the surface the signal strength and location of the reconstructed defect are lower than expected. This matches the result for SH 2.

For BH 3 the top 8 peaks in the signal at the right depth correspond to the x location of all the defects. The interaction between the signals is higher than in SH 2. This might also be due to higher noise seen in the BH 2 B-scan.

The reconstructions of the TP samples are shown in Fig. 3.14. The TP 1 reconstruction shows defects only for 300 μm and higher, which is corroborated by the CT scan data; this indicates the first two defects were filled-in (after subsequent layers were applied) while the sample was printed. Here one can see the reconstructed defect size decreasing with decreasing diameter, however signal strength remains close to constant for defects of size 400 μm and higher, matching the SH 1 trend. Also the reconstructed defects have a less elliptical and more round shape than the BH and especially the SH reconstructions. This might be due to this artificial defect's lower OA as explained before in this section.

The TP 2 reconstruction follows the same trend as the BH 2 reconstruction; however, the reconstructed defect at 0.8 mm does have a more circular profile. This shows the TP defects might be more useful for representing actual defects particularly for shallow defects.

(a) SH 2



(b) SH 3

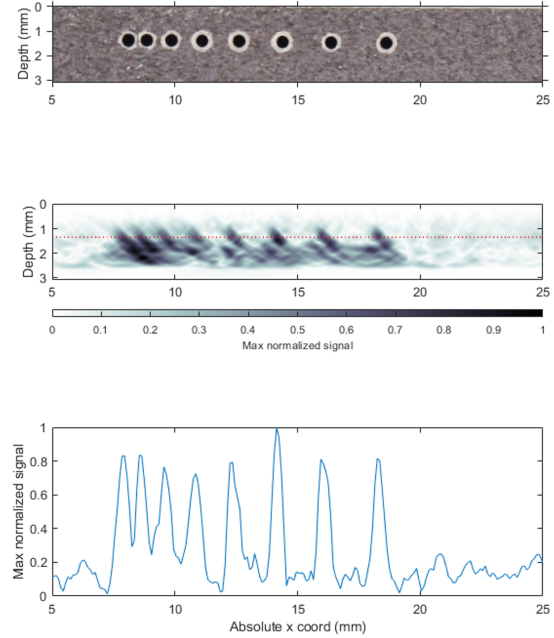


Figure 3.11: SH reconstructions. The SH 1 reconstruction can be seen in Fig. 3.9.

The TP 3 reconstruction has a better contrast when comparing all the defect signals with the background, compared to the BH 3 defect, except for the second and third CAD defects from the left. Note the first defect does not show up in the reconstruction of the CT scan, indicating it was filled-in.

Overall in terms of signal strength and shape of the reconstructed defects, the TP defects produce the best results, while being closer in geometry to actual defects. The higher signal strength might mean that this geometry, approximating a sound point scatterer, and lack of an OA, is more amenable to PSM reconstruction.

This is expected since the PSM algorithm assumes defects of this approximate shape. This seems to be a greater factor than the lower sound impedance mismatch due to powder in the TP defect. This might also depend on how much powder is trapped; for example, less powder by volume might be left inside the defect after the re-coater passes over it if the defect is smaller.

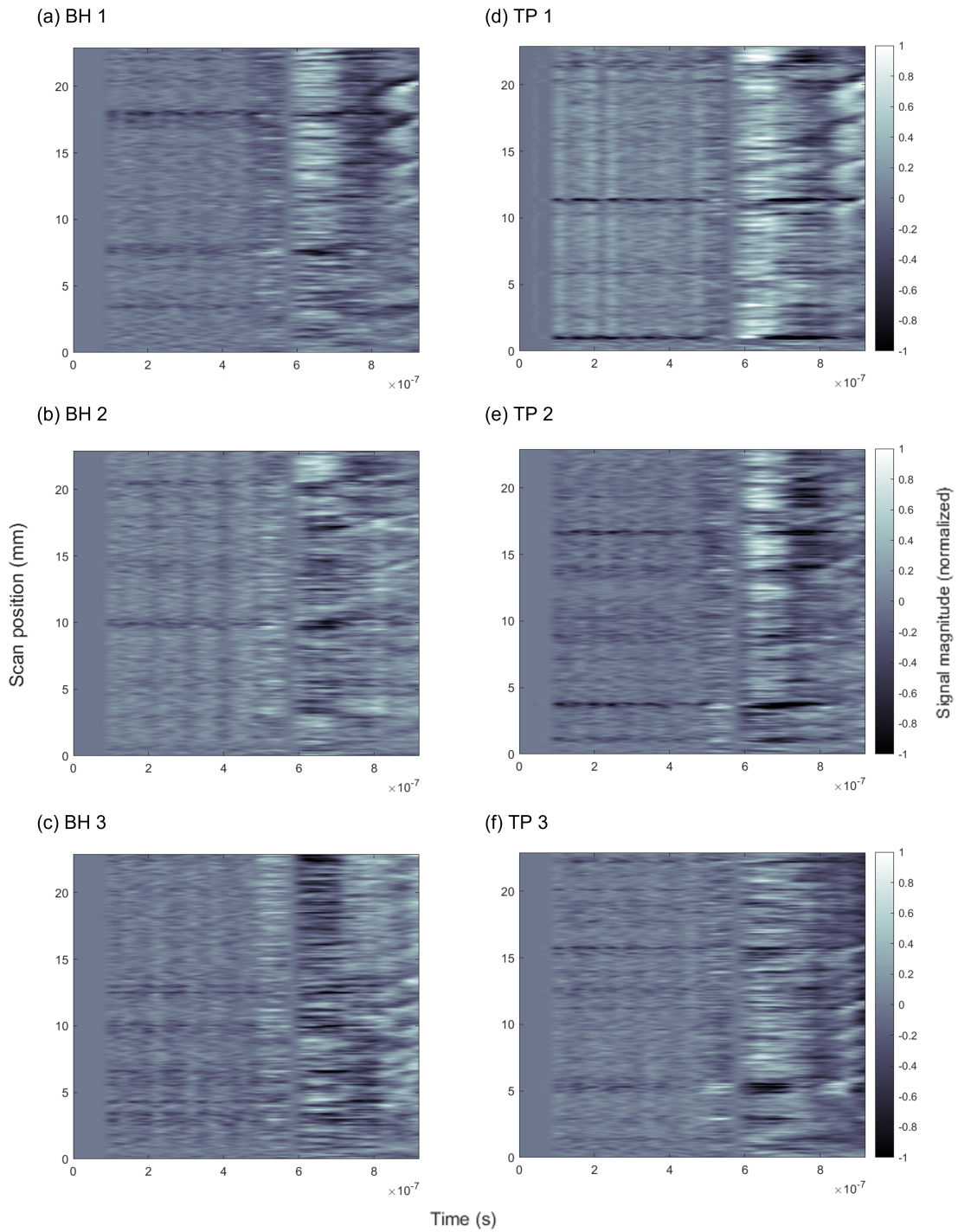


Figure 3.12: Filtered B-scans of all Ti6Al4V samples.

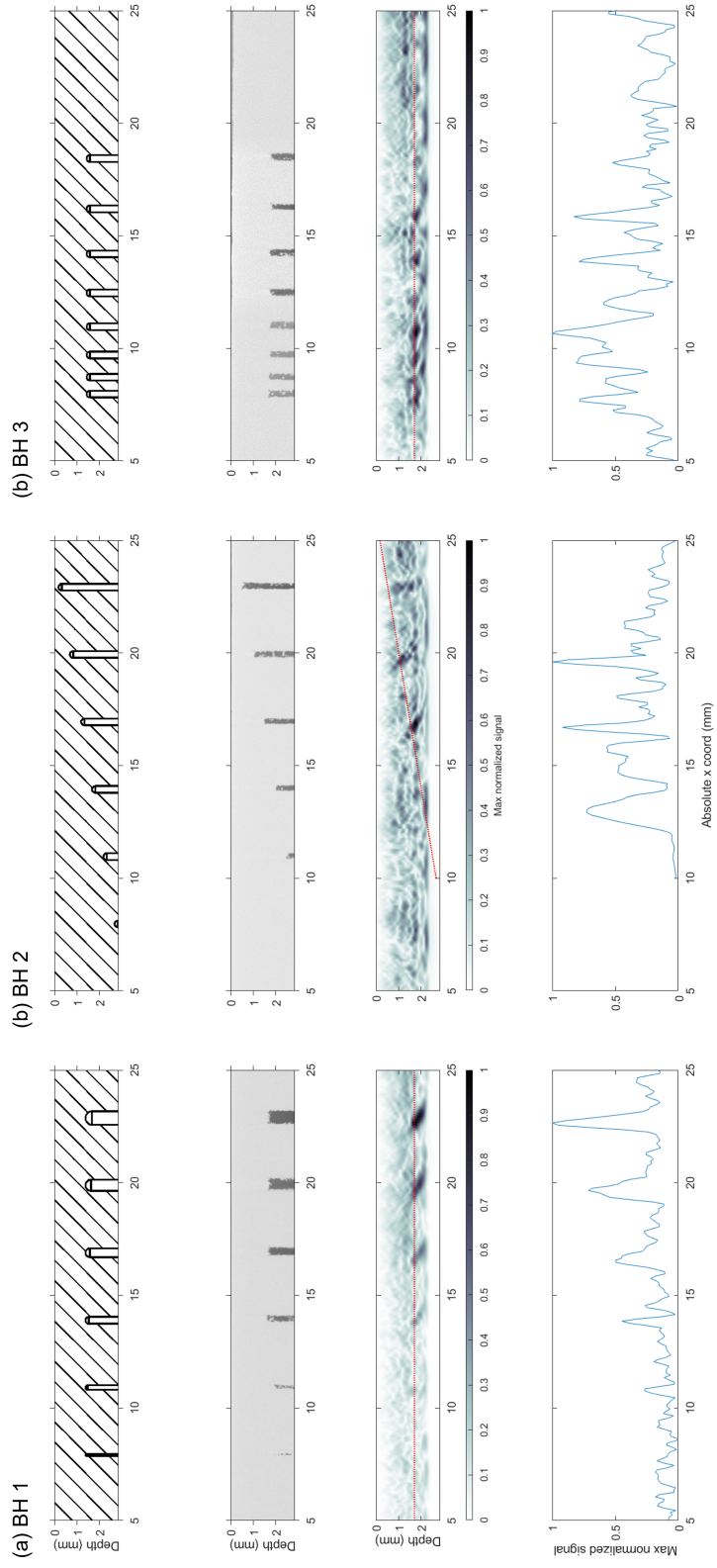


Figure 3.13: Reconstructions of BH samples. For each of the BH and TP reconstructions from top to bottom, the CAD cross-section is shown, followed by the CT scan, the PSM reconstruction and the signal along the red line on the reconstruction, placed 0.2 mm below the top of each defect in the sample.

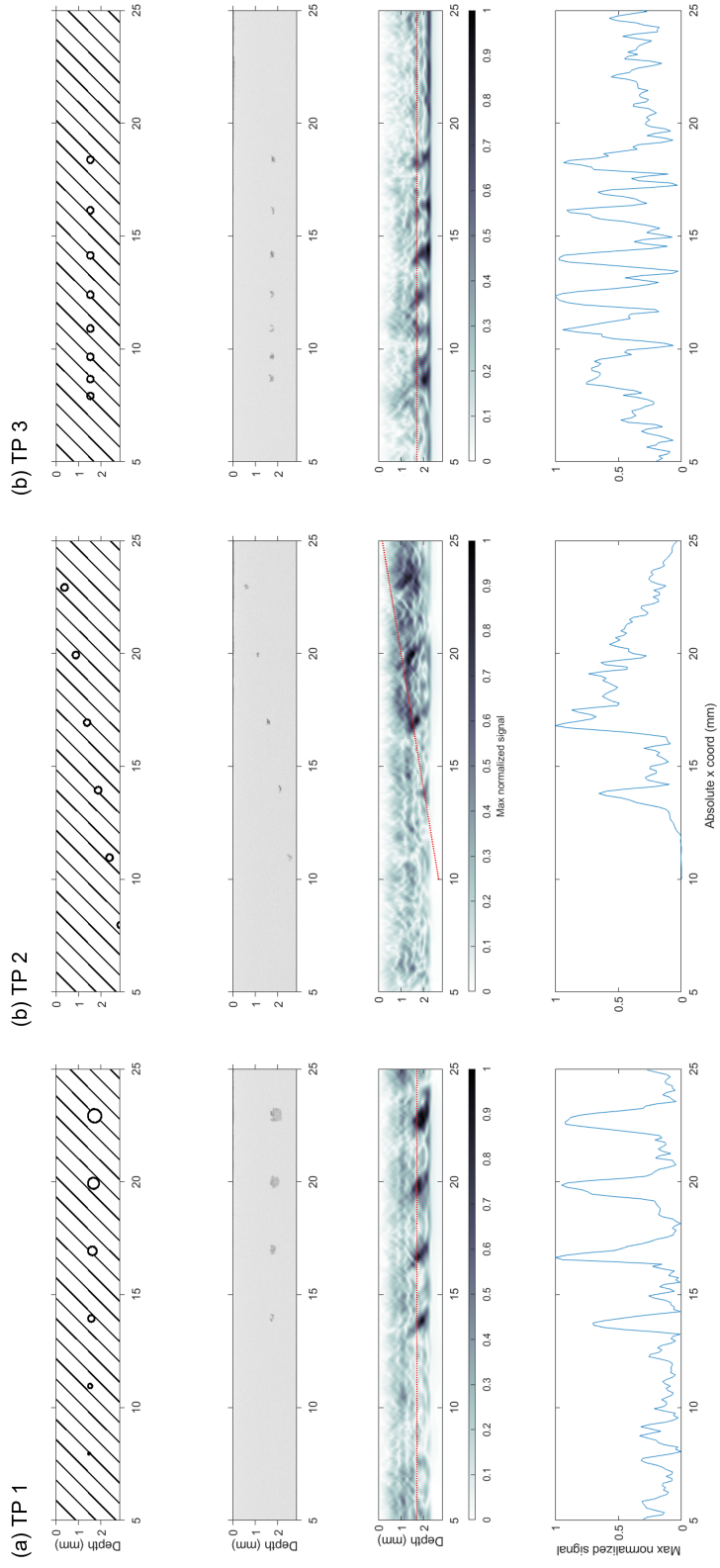


Figure 3.14: Reconstructions of TP samples.

3.3.4 Surface signal removal based on the Fourier slice theorem

The Hugh transform has been used to remove lines in images [166]. This can be done by performing the Hugh transform and removing high-intensity peaks, that correspond to lines in the original image. As discussed in Section 3.2.4, this can also be carried out in k-space by using notch filters, this is faster computationally and can also be applied to linear features that are not normal to the A-scans.

The method of reducing the SLW signal using FFT filters is shown in Fig. 3.15. In order to highlight the k-space values at higher frequencies, the values shown in the figure are calculated using $\log(1 + |s|)$, where \log is the natural logarithm and s is the k-space value [164]. The reconstructed images and signal intensities along x are shown in Fig. 3.16.

One can see that the reconstruction using k-space filters is very similar but slightly worst than the use of the AF, hence its use in this chapter. However this result shows that it can produce comparable results to the AF, and could be used in more advanced algorithms to take out linear features from expected reflections in an AM part while its being printed. This comparison was also done for the BH 1 and TP 1 sample B-scans and the same conclusion were reached.

3.3.5 Track surface roughness

The area surface roughness (Sa) for 600 by 600 μm squares and roughness Ra values along a line were obtained for the top surface for SH 1 (Fig. 3.17) TP 1 (Fig. 3.18).

For the Sa values there is a reduction from 16.3 to 13.9 Sa (-14%) in SH 1, and a reduction from 6.4 to 5.4 Sa (-15%) in the TP 1 sample, when comparing the average of the Sa measurements on the as-built surface with no up-skin with the average of the Sa measurements on the laser track.

For the Ra values taken in the direction parallel to the tracks, the change in values is from 11.5 to 10.5 Ra (-9%) in SH 1, and a reduction from 6.8 to 7.1 Ra (4%) in TP 1, when making the same comparison as above. This preliminary observation for the Sa values matches qualitatively with the observed effect of surface smoothing using ns-pulsed lasers [176].

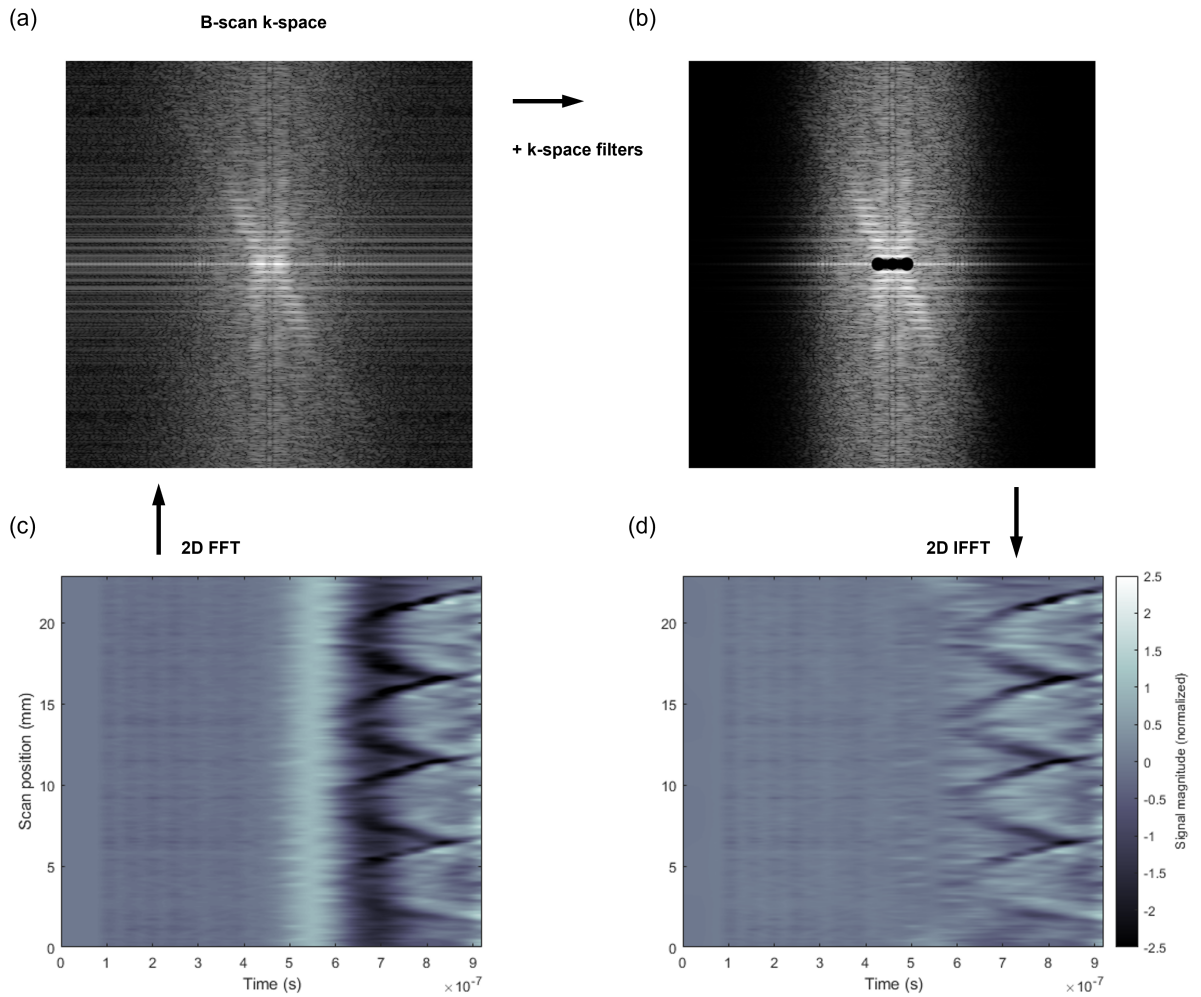


Figure 3.15: (c) B-scan and (a) 2D FT of SH 1 with longitudinal wave normalization. (b) Application of filters (DC, SW notch filters and 2D Butterworth filter) in Algorithm 2 to 2D FT and (d) resulting B-scan.

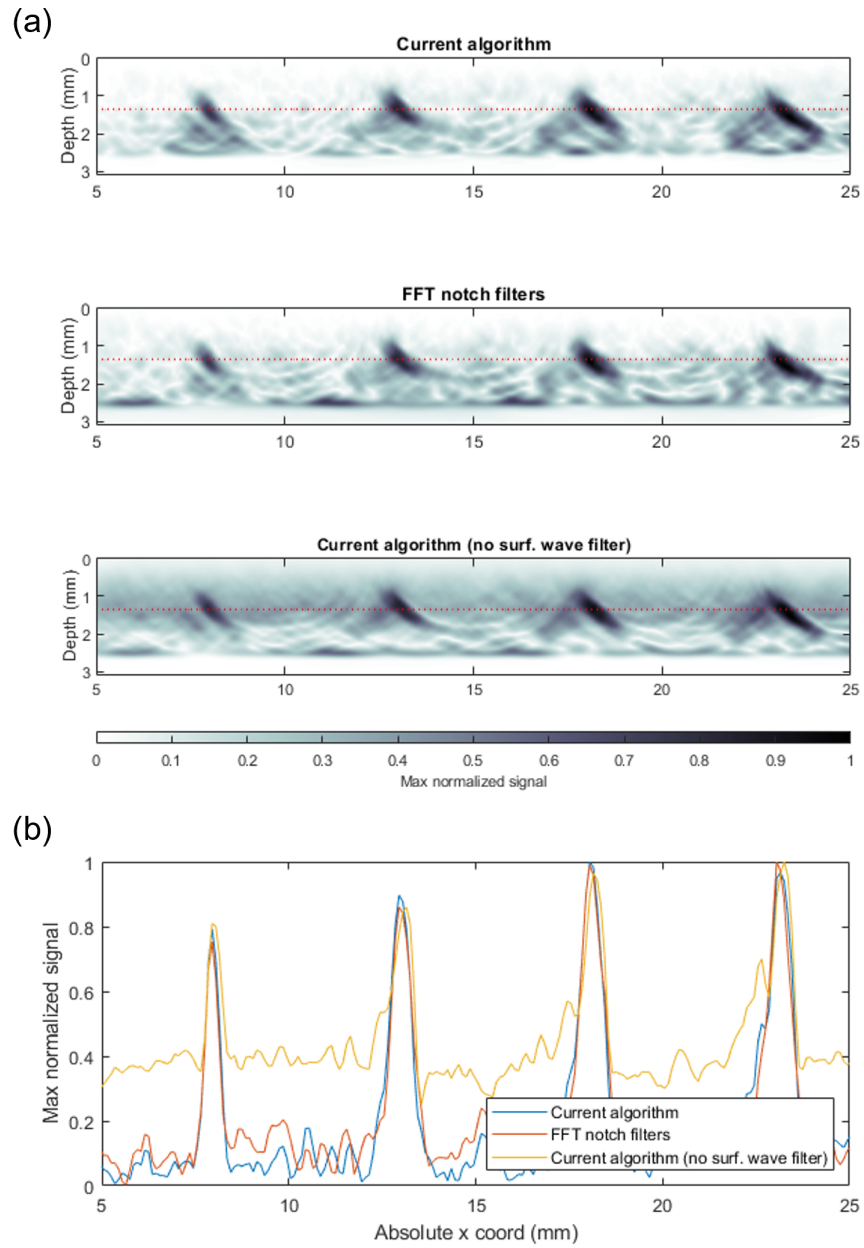
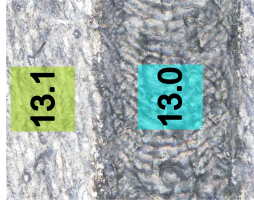
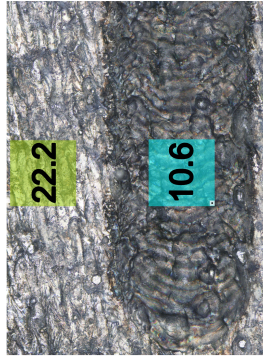
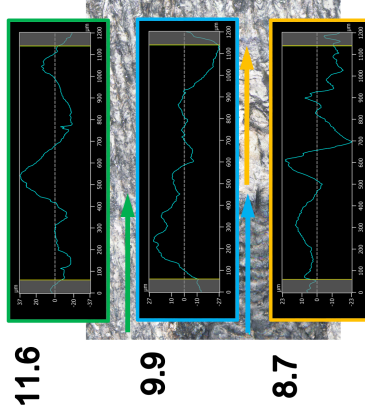
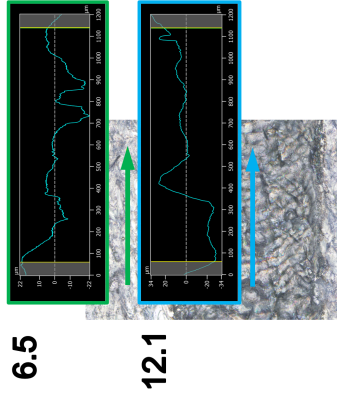
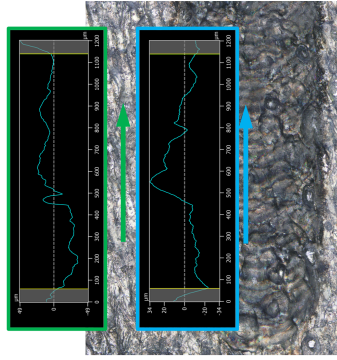


Figure 3.16: (a) Comparison reconstructions between the current algorithm and the same algorithm using k-space filters in Algorithm 2. (b) Signal intensity as a function of x along the red dotted lines.

(a) Sa values:



(b) Ra values:



(c) Surface plots:

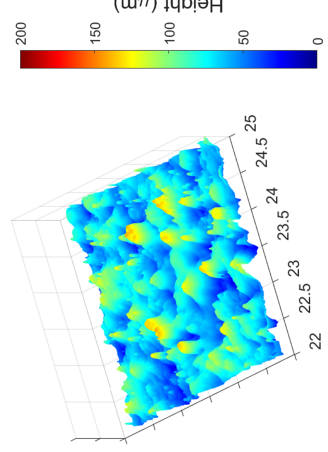
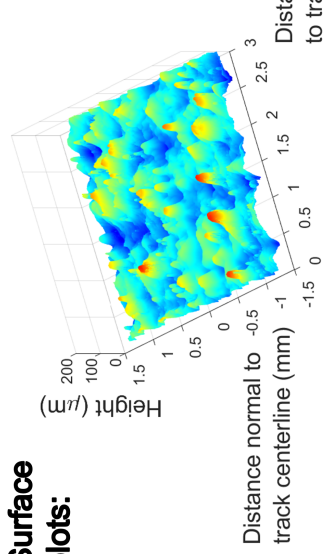
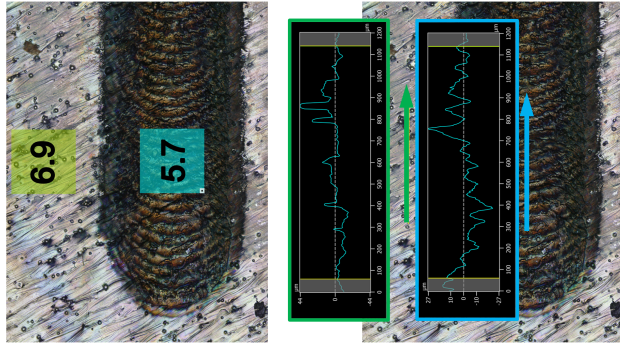
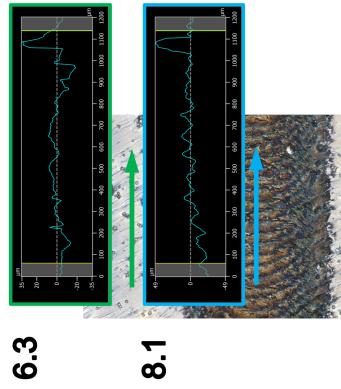


Figure 3.17: Surface and line roughness measurements for SH 1.

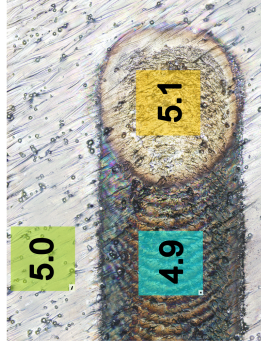
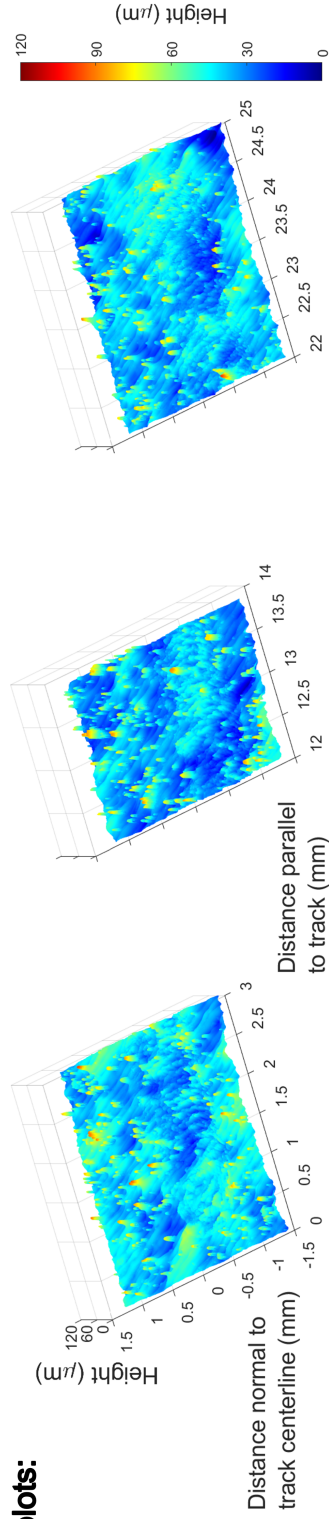
(a) Sa values:



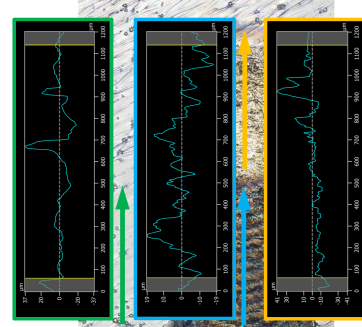
(b) Ra values:



(c) Surface plots:



6.1



6.2

7.8

Figure 3.18: Surface and line roughness measurements for TP 1.

3.4 Summary

Artificial side through-hole defects were reconstructed from laser ultrasound B-scan data, using the PSM algorithm with a SPA for the oscillatory integral that has to be computed for the case of a fixed single transmitter and receiver offset.

The use of a Fourier-based reconstruction algorithm has advantages in terms of speed as the FFT is used, and being able to filter the signal both directly based on undesired frequencies, and filtering linear features in the B-scan, based on the FST.

Defects with a size range from about 200 to 300 μm for bottom blind hole defects can be recognized from the background noise of the reconstructions. The minimum depth for accurately reconstructing defects at the right depth was about 0.8 mm for bottom blind hole and trapped powder defects. The reconstructed signals have a tilted elliptical shape; this might be due to not considering the source, defect and receiver directivity functions in the PSM algorithm. This was especially the case with SH type artificial defects and was not as pronounced with BH and TP artificial defects. BH type defects printed directly in the samples printed more successfully than TP defects, but give slightly more inaccurate reconstructed depths than TP defects.

TP defects produced satisfactory reconstruction even with less sound impedance mismatch between the metal and the trapped powder, however further LPBF parameter optimization is required for a given size defect to be printed successfully.

There is some preliminary work in [177] describing how the source, defect and receiver directivity functions might be taken into account in the PSM algorithm. There is also another Fourier-based reconstruction method similar to PSM called synthetic aperture radar (SAR), where the directivity functions can readily be included [178]. This might also alleviate the reduction in defect signal strength when the defects are close to the surface. Besides the possibility of including directivity functions in SAR, the derivation and performance of both algorithms is known to be similar [72].

There is no significant change in surface roughness at the place where the laser is applied, except for a slight reduction in average Sa values for the laser track area compared to the as-built area. This is similar to what is observed when applying ns-pulsed lasers for surface smoothing; however, more data is required to quantify this relationship. The observed oxidation is expected to reduce or not be present when an LU system is used inside an actual LPBF machine with inert gas flow.

Chapter 4

Demonstration of Ultrasound Particle Lensing with DED-PF powders

4.1 Introduction

Additive manufacturing (AM) has enabled the manufacture of intricate parts that were not possible to produce using conventional manufacturing methods. AM also allows in-situ tailoring of material compositions and properties during the process [179]. However, the high interdependence of AM process parameters with the resulting part geometry and physical characteristics makes the prediction of these parameters difficult. The objective of this research is to demonstrate a technique that can be used to improve the quality of printed parts and productivity of directed energy deposition via powder feeding (DED-PF), a class of metal AM process, by decoupling the in-situ placement of the powder stream from the geometry and gas flow rate of the powder delivery system. In particular, the technique has the ability to adaptively change the powder stream's cross-sectional shape and size, to increase print speed, minimize material utilization and increase the part's dimensional accuracy. Currently the effect of the powder stream features on catchment efficiency, which measures the fraction of material being utilized for printing, is controlled either in the part design [26], process arrangement [180], working distance of the nozzle/s with respect to the substrate [181], or indirectly via optimizing print parameters such laser speed and power [180] or powder properties [182]. In [183], for the same nozzle geometry, it was observed that there is an approximate inverse relation between resolution and catchment efficiency. It was found that a higher laser power and stand-off distance can be used to produce better catchment efficiency, but at the cost of wider tracks.

The sound radiation force phenomenon has been used extensively within the field of microfluidics (acoustofluidics), in order to sieve and sort individual particles or particle agglomerations. This is usually done for fast biological particle characterization [140]. Some works have used sound radiation forces to sort particles in a gas, for particle characterization. In [144], glass bead particles are sorted using a resonator channel in air. In [145], particles fall towards an acoustic Fresnel lens that produces a radially symmetric force field that can be used to sort them based on size and material. In [146], the forces on sub-micron aerosol particles are modeled and measured as a function of the aerosol number density and size distribution, while they move in a flow-through resonator. Some studies have reported on particle levitation using acoustic forces. In [147], a model of the sound field from an ultrasound transducer array is numerically optimized by varying the phases of each element in order to produce the maximum particle trapping forces possible. One of the obtained sound fields is a vortex trap, with an averaged pressure isosurface shaped like an open cylinder. Vortex traps have been designed before using acoustic and optical setups [147]. The design of force fields using high intensity sound has been used to create an acoustic levitation system that automatically injects, transports, merges and ejects liquid droplets in mid-air [184], which could be used in biology, chemistry and pharmacy applications where these operations are done manually using a pipette to transport and mix liquids. Besides aerodynamic and ultrasound particle focusing techniques, electrostatic and optical techniques have been discussed in the literature [185, 186]. However the particles being deflected are in the nanometer size range and have an order of magnitude less density than SS 316L particles used in DED-PF for example. These techniques have been limited to the focusing of small aerosol particles for subsequent physical and chemical analysis. Another method of powder stream focusing using a force field, using electromagnetic fields that could be used for DED-PF is described and simulated in [187]. One configuration employed permanent magnets, that would induce an eddy current in the particles. However, this configuration is likely not suitable for the characteristics of the powder used for DED-PF, mainly because the amount of force due to induction depends on the relative speed of the particles and the magnets, however a higher speed means there is less interaction time between the particle and the electromagnetic force. Another related method using magnetic fields that is able to increase catchment efficiency is described in [183], where a solenoid with a frustum cone was used to focus the magnetic field, is used on the underside of the built plate opposite to the nozzle. This setup demonstrated control of catchment efficiency for ferrous and nickel-based alloys, however for tall walls the effect is reduced.

Models of the DED-PF process that consider particle motion due to the carrier gas simulated by computational fluid dynamics (CFD) were implemented in [36, 37, 26]. All

these models employ Lagrangian particle tracking, meaning that the powder stream is described from the reference frame of discrete particles and the forces on the particles are integrated to compute their motion. Another method in CFD to model particle streams is the Eulerian method [188], where the reference frame is static and the concentration of particles at each location is considered over time. Both methods were used for the modeling of the powder stream from a DED-PF nozzle in [189]. It was reported that the developed Eulerian method was faster to compute but it could not take into account particle crossings. This may be taken into account using a more computationally expensive modified Eulerian model derived using the kinetic theory of gases [190]. It was noted in [37] is that the coupling from the gas flow to the particles is calculated only considering the Reynolds averaged velocity field and not the instantaneous flow field. This was justified by calculating the Stokes number for a DED-PF setup. The Stokes number is a dimensionless number commonly used for particle tracking and particle separation modeling. It describes how quickly a particle responds to changes in flow velocity. The calculated value was higher than one, suggesting that the particles are not highly responsive to changes in the flow field and their paths are similar to ballistic trajectories. The main conclusion in [26] is that the gas flow field has a modest effect on the final powder concentration distribution (PCD) close to the substrate and that a lower coefficient of restitution between the powder and nozzle cones provides a more focused particle stream. This is in line with the Stokes number calculations and observations in [37].

4.2 Proposed ultrasound particle lensing technology

The use of sound radiation forces for levitating and moving particles as described in [147] suggests that it is possible to levitate and move the metal particles directly to the substrate in DED-PF. However, there are issues with this approach; how the metal particles could be moved at a sufficiently high enough mass flow rate, metal particles are too dense to levitate and the effect of sound reflections [184] from the substrate needs to be accounted for.

A more useful setup is one inspired by the control of electron beams in electron microscopes and electron beam melting [191], using magnetic coils acting in a similar way to a lens (electron lenses). One possible way of using a sound field as a lens is using the vortex sound field, but instead of applying it for levitation, it is used in a way similar to particle sorting as described in Section 4.1.

A 2D slice of the period averaged sound pressure (ASP) for a vortex field at the sound and powder center-line, and the components of the sound radiation force field are shown

in Fig. 4.1. As seen in Fig. 4.1 (c), the dominant force component is along the x direction, towards the sound center-line, and decreasing towards the center-line. This is the basis of the patent pending [192] ultrasound particle lensing or UPL technology. The components of the acoustic radiation force were found by computing the gradient of the Gor'kov potential, shown in Fig. 4.1 (b), that can be found using the particle properties and the gradient of the pressure field [147]. This is described in detail in Appendix F.

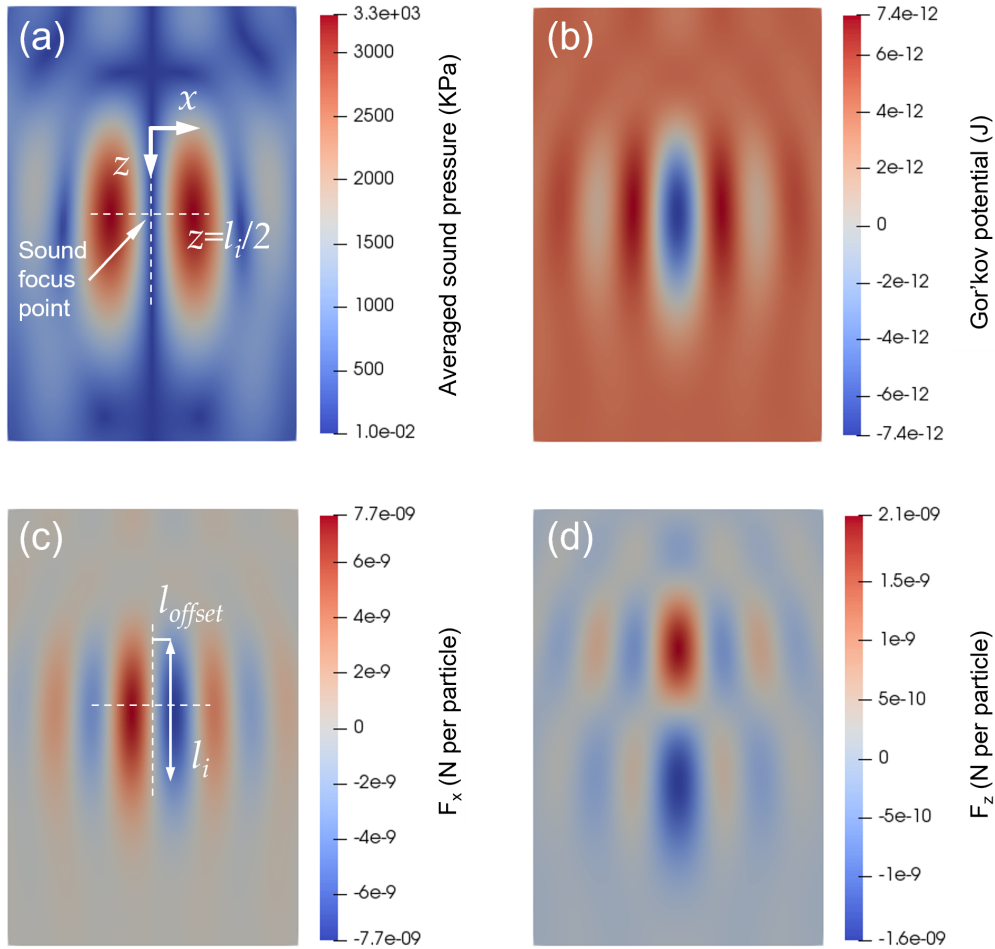


Figure 4.1: Averaged sound pressure (ASP), potential and force slices along an acoustic vortex. (a) ASP, (b) Gor'kov potential, (c) x component of the force field and (d) z component of the force field. The height and width of the frames is 30 by 20 mm respectively. For this sound field the y component of the force field is equal to the x component due to symmetry about the z axis.

Fig. 4.2 shows the ASP on the xz -plane, intersecting the sound focus point, at the center, with an isosurface of the force field. The figure uses the same simulation setting as for Fig. 4.1. As seen from Fig. 4.2, the force field is radially symmetric, and the force along the x -axis is close to linear around the center-line.

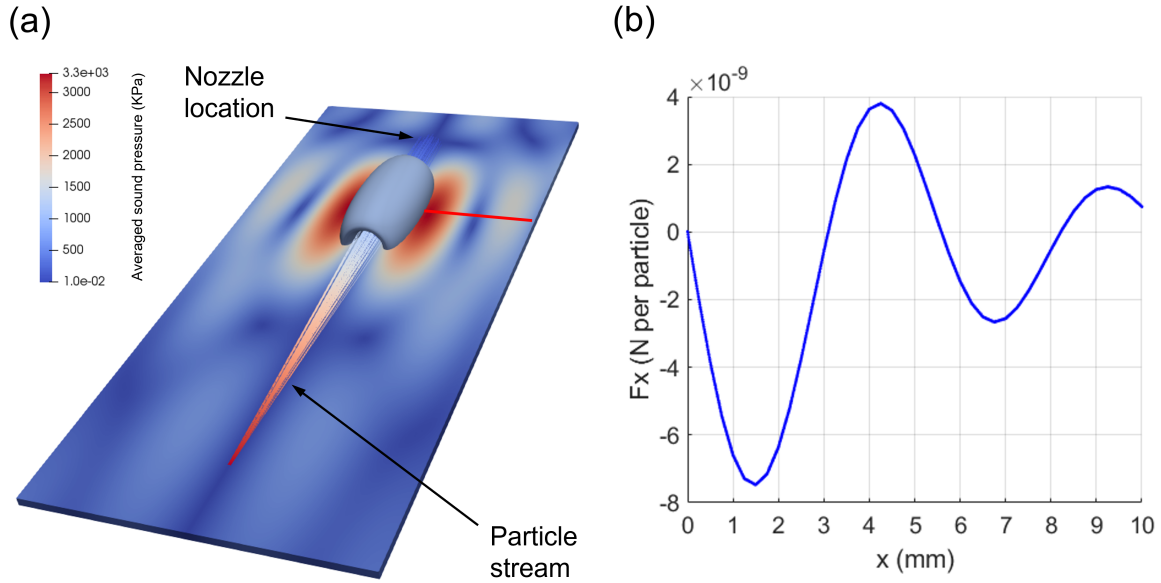


Figure 4.2: (a) ASP field, with particles tracks, and isosurface with a radial sound radiation force value of -4.0×10^{-9} N per particle, based on the SS 316L at 16 V simulation shown in Section 4.5.8. (b) Sound radiation force in x -axis direction along the red line.

Using the setup shown in Fig. 4.2 to focus particles has the following advantages; it decreases the complexity of the powder nozzle (allowing for the focusing to be done electronically with an ultrasound phased array as used in [147] without a fixed nozzle geometry), one can process several particles simultaneously, the particles do not need to be levitated, and the high ASP region of the sound field can be offset from the substrate, to reduce the effect of sound reflections. Using UPL instead of a fixed nozzle geometry that is optimized for a high catchment efficiency and a given track width [26, 193] allows for the control of the powder stream using electronic signals. As will be seen in Section 4.3.1, the particles are deflected with a vortex field in a similar way to an optical or electron lens.

UPL technology could also provide a tool for metal AM machines with closed-loop control, to increase part quality and material utilization while reducing part cost. In the case of using UPL as an in-situ process control method, the powder stream “spot size” and the location of contact with the build plate could be controlled, in order increase

catchment efficiency and dimensional accuracy respectively. Other possible features of a DED-PF machine using UPL technology described in [192] are quick variable focusing, powder stream deflection and melt pool shape control.

UPL technology may also be used in a coaxial arrangement, with the laser beam at the center and an annular nozzle on the same axis as the laser, providing a converging powder stream. In this case, a vortex field may be produced by changing its topological charge to a value larger than one [148]; this will produce a vortex field like the one shown in Fig. 4.1, but with a wider low pressure area at its center, that can accommodate the laser and the annular powder stream. Since the sound field can make the powder stream converge to different degrees, a simpler annular nozzle can be used, instead of the current more complex nozzle geometries that converge the powder to a single focal length. The technology may also be used for three and four-jet nozzles in a coaxial arrangement [194]. These arrangements with radial channels result in a powder stream that is less susceptible to nozzle tilt while producing large complex parts [195]. UPL technology may be applied in this case by adjusting the phases of the ultrasound elements to produce various closely spaced vortex fields, that can be placed downstream of each of the powder jets. This has been demonstrated experimentally, in the context of sample material trapping and transport [151].

The scope of the reported work will be limited to demonstrating UPL technology for powder stream focusing for the DED-PF process, using Ti6Al4V and SS 316L powders. Ti6Al4V was chosen as a material since it is widely used in metal AM and SS 316L was chosen in order to test another widely used material that has a much higher density, so the method proposed in this chapter can be tested for a wide range of powder densities. To achieve this, the following sub-goals were carried out:

- An analytic model of the particle stream and its interaction with a focusing sound radiation force field was derived
- A novel particle speed distribution model was found to more accurately couple the force field to the powder stream
- Algorithms to calculate and simulate the sound fields that produce the force field for particle stream focusing were implemented
- Algorithms for Lagrangian and Eulerian particle tracking were implemented and used to simulate particle concentration due to the sound radiation force field
- A proof-of-concept device was designed and built and experiments to demonstrate particle focusing were carried out

4.3 Modeling

In order to determine the feasibility of UPL, an initial analytic model for the individual particle motion was derived. Another model considering a continuous PCD was derived which has different initial conditions with particles moving away from the nozzle center-line, this was done to more accurately couple the sound radiation force field to the PCD in both the Lagrangian and Eulerian simulations of the process.

4.3.1 Individual particle lensing model

The derivation of this model can be found in Appendix E. Some of the variables that will be referenced are show in Fig. 4.3.

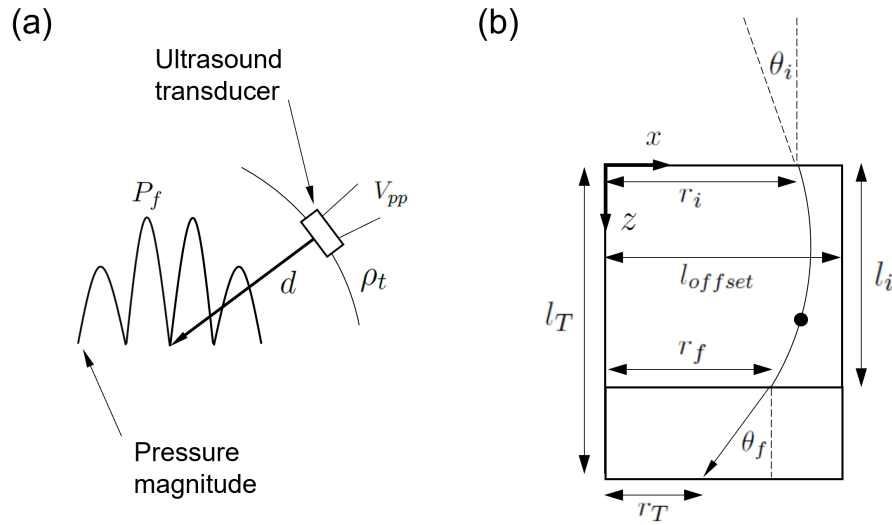


Figure 4.3: Diagrams showing the variables used in the analytic model for; (a) transducers and sound field and (b) coordinate axes and particle trajectories.

In Fig. 4.3, the coordinate axis is located at the particle stream center-line and upstream of the sound field which is affecting the particles. In this figure, r_i is the initial position of a particle, θ_i is its initial angle, l_i is the length along which the sound field affects the particles, l_{offset} is the distance from the powder center-line to the region where the force field is beyond the linear range, r_f is the final position of the particle and θ_f is the final

angle of the particle after the sound interaction region. l_T and r_T correspond to the z and x locations after the sound interaction region.

The force on the particle is given by:

$$F_a = K_a V_{pp}^2 d^2 \rho_t^2 r_p^3 \quad (4.1)$$

where K_a is a constant depending on the array geometry, V_{pp} is the square wave peak-to-peak voltage given to ultrasonic transducers, d is the distance from the transducers to the required sound focus point, ρ_t is the transducer array planar density (the number of transducers in 1 m²), and r_p is the particle radius. The particle deflection angle can be approximated by:

$$\theta_f = \arctan\left(\frac{\dot{r}_f}{u_z}\right) \approx \theta_i \left(1 - \frac{l_i}{2l_{offset}}\beta\right) - \alpha\beta \quad (4.2)$$

where u_z is the downward speed of the particle, and α and β are dimensionless parameters. $\alpha = r_i/l_{offset}$ and β is given by:

$$\beta = \frac{F_a l_i}{m_p u_z^2} = \frac{3}{4\pi} \frac{K_a V_{pp}^2 d^2 \rho_t^2 l_i}{\rho_p u_z^2} \quad (4.3)$$

where m_p is the particle mass and ρ_p is the particle density. The particle final tangential speed after being affected by the sound field is given by:

$$\dot{r}_f = -r_i \sqrt{a} \sin(\sqrt{a}t_i) + u_z \tan(\theta_i) \cos(\sqrt{a}t_i) \approx u_z \left[\theta_i \left(1 - \frac{l_i}{2l_{offset}}\beta\right) - \alpha\beta \right] \quad (4.4)$$

where $a = F_a/(m_p l_{offset})$. The approximate focal length of the stream $l_f = l_T(r_T = 0)$ is given by:

$$l_f = l_i - \frac{r_f}{\dot{r}_f} u_z \approx l_i + \frac{u_z}{\sqrt{a}} \left[\frac{\sqrt{a} \cos(\gamma) + s_{sp} k_d \sin(\gamma)}{\sqrt{a} \sin(\gamma) - u_z k_d \cos(\gamma)} \right] \quad (4.5)$$

where the approximation is derived using the small angle approximation for $\tan()$, k_d is defined as $\theta_i = k_d r_i$, and $\gamma = \sqrt{a} l_i / u_z$. Section 4.3.3 explains why the initial divergence angle can be modeled as being proportional to the particles' initial distance from the powder stream's center-line.

The equations in this section could also be derived by considering the time the particles stay inside the force field, which is equal to l_i/u_z . The greater the time the larger the particles' momentum change will be.

From Eqs. 4.2 and 4.5, one can reach the following conclusions:

- The fact that the deflection angle is proportional to d^2 at low θ_i via β indicates that UPL is feasible; since the size of the phased array can be increased to get the required deflection angle
- The V_{pp} value has a significant effect on the deflection angle and should be as high as possible using the necessary cooling for the transducers
- The particle size is not present in the approximation of θ_f . This is explained by the fact that the sound radiation force and the particle mass are both proportional to particle volume (see equations in Appendix E) when assuming negligible gas drag. This is expected to be the case for the relatively large particles used in DED-PF, where the particles' gas drag is less dominant. This particle size range independence also means a particle stream with a wide particle size distribution may be focused more accurately compared to other methods such as electromagnetic focusing [187], where the degree of focusing was found to be strongly particle size dependent for the particle size ranges used in DED-PF.
- The inverse relationship with particle density via β indicates this technology is more suitable for lighter alloys, which fits with the use cases of DED-PF and the drive for lighter components. However, as reported in Section 4.5, for low particle speeds one is able to focus SS 316L particles if their average speed is low enough
- The particle speed out of the nozzle has a large inverse effect on θ_f which means that UPL is more useful in setups where the operating particle speed is low
- Since the deflection angle is proportional to r_i at low θ_i via \dot{r}_f , particles will be deflected less when they are closer to the focus axis. The approximation of the focal length l_f shown in Eq. 4.5 is independent of initial particle position

4.3.2 Sound force field calculation

In order to simulate the forces exerted on moving particles inside an acoustic field, a C++ library called `acousticHologram` was developed, in order to compute the incident sound field generated by a phased array and its related sound radiation force field as described in Section 4.1 and outlined in [147].

This implementation has the following features:

- The transducers were modeled assuming a piston sound source [196] and take into account the applied voltage
- Forward mode automatic differentiation is used to calculate the needed sound field gradients to compute the sound force field. The advantage of this method compared to finite differences as was used in [147] is that the result is exact up to machine precision, and there is no error due to the grid size or frequency of the emitted sound being modeled
- The software includes a 3D Lagrangian particle tracking model that considers the surrounding gas drag force, the gas considered in this chapter is air

More information on the sound field modeling and the algorithms used in the library are described in Appendix F.

4.3.3 Eulerian particle model

To estimate the focusing obtained with an ultrasound array prototype with 78 elements (as used in the proof-of-concept experiment), a Eulerian continuous particle cloud coupled with body forces was modeled. Since the focusing process can be assumed to be axisymmetric, the Eulerian model can be calculated using a 1D finite element analysis (FEA) simulation. The model includes one way coupling with air through a particle gas drag model [197] and neglects gravitational acceleration.

As described in the literature [34, 198, 199], the observed particle cloud spreads like a flattening Gaussian, with the sides of the Gaussian with a value of e^{-2} or e^{-1} of the function's peak spreading along diverging lines with an angle between them of 2θ and an initial distance between them of $2r_0$, which should be close to the nozzle opening diameter. These equations are derived from a particle diffusion model [198].

In order to couple the particles to a force field in the Eulerian description, a Eulerian continuous concentration distribution particle model should be used [188, 200].

Since the observed particle cloud shape resembles the shape given by solving a particle diffusion model, the Eulerian continuous concentration distribution particle model should have a diffusion term.

Although mathematically this model can be used to couple the evolving particle cloud with applied body forces, it is not following the observed physics for the following reasons:

- The low particle concentrations observed indicate that particles are not colliding, therefore the typical derivation of the particle cloud evolution found in the literature [34, 198, 199] does not seem appropriate, although it produces a model matching measured data
- The assumption of zero initial particle velocity when using the diffusion term may cause a simulation result with a higher degree of focusing, since the particles are assumed to have a zero transverse velocity. Therefore, the same applied force will produce a higher inward displacement compared to the same force being used to change the displacement of initially outward moving particles. From the high speed footage, one can observe an outward transverse velocity that can explain the spreading

One way to address these issues is to use a Eulerian continuous concentration distribution particle model with no diffusion term with the same initial concentration but also an initial particle speed distribution. This initial speed distribution needs to reproduce the observed particle evolution when no body forces are applied. As derived in Appendix G, an initial velocity field that follows the above conditions is:

$$v(r, 0) = u_z \tan(\theta) \frac{r}{r_0} \quad (4.6)$$

where in this case u_z is the average of downward particle speeds, and r is the radial distance coordinate. The resulting 1D partial differential equation (PDE) system can be solved using the FEniCS library for FEA [201].

The simulation results in Section 4.5.8 were run using 80 elements and a time step of $2.0 \mu s$. The average computing time for all simulations was 8 minutes. A convergence study showed that the above parameters produce a converged solution, using a criterion of less than 4% change for the peak concentration.

All simulations in this chapter were carried out using a Dell OptiPlex desktop, with an Intel Core i7 3.6 GHz CPU processor and 16 GB of RAM. More information on the FEA simulation and the convergence study is given in Appendix G.

4.3.4 Lagrangian particle model

The initial particle speed distribution derived for the Eulerian model can also be used as an initial condition in the 3D Lagrangian particle tracking model available in the `acousticHologram` C++ library. The library can calculate the sound pressure and resulting force field on the particles. By calculating the force field at a required particle location, one can perform Lagrangian particle tracking by computing particle paths from an initial to a final position at a required time interval. This can be done using a 4th order Runge-Kutta (RK4) method [171] with a given fixed time step. The algorithms used in the library are described in more detail in Appendix F.

The initial particle concentration at the hopper nozzle position can be approximated by a group of particles, chosen such that their probability function approaches the PCD [34]. A Monte Carlo (MC) simulation [202] can be run with enough particles to have a good estimate of the radial particle concentration. The model uses the same drag model as used in the Eulerian simulation also without considering gravitational acceleration.

The simulation results in Section 4.5.8 were run using 2 time steps for the runs at 0V and 4 time steps for all other voltages for both materials. The number of paths calculated ranged from 2.2×10^4 to 12×10^4 depending on the simulation to achieve the required accuracy. The simulations were done using a Δr (radial sampling interval) value of 0.5 mm to compute the concentration function. The computing times for the simulations ranged from 20 to 63 minutes for all runs.

A convergence study showed that the above simulation parameters produce a converged solution, with an estimated error of less than 2% for the RK4 particle tracking and less than 4% for the MC simulation. The MC simulation and the convergence study are explained in more detail in Appendix H.

4.4 Materials and methods

4.4.1 Prototype design and build

The array control boards were assembled following the instructions in [203]. The signals given to the boards via a USB cable were generated using the Ultrino software [204]. Steps for generating the signal for the vortex sound field used in this chapter and described in [147] can be found in [203].

The array was designed taking into account the following considerations:

- The array surface should be a spherical cap (sphere zone) to obtain a high degree of sound focusing from the array. Based on the directivity function of a sound piston source, the highest sound level is produced along the transducer's axis of symmetry; this means that they should be arranged in such a way that these axes should intersect at a common point. This can be achieved if the transducers are placed on a sphere zone
- For a given number of transducers, the sphere zone area should be made as small as possible to pack as many transducers as possible, to have the highest possible transducer planar density ρ_t
- The center-line normal vectors of the transducers should all point to a location below the hopper nozzle. This is to minimize sound reflections from the nozzle
- The bottom of the array should be above the expected particle focus point to enable proper imaging of the particle stream

The array of ultrasonic transducers was designed to be used with two controller boards, as described in [204]. The final CAD design of the array frame is shown in Fig. 4.4 (b). The array frame was built using a Stratasys F370, oriented with the transducer holder openings pointing upwards, in order to minimize the amount of support material inside them. The print was done with no infill (solid) and a layer height of 0.1778 mm. The build material was F123 ABS.

To obtain a particle stream concentration distribution that resembles the one measured in a DED-PF machine, a hopper with a screw-on conical nozzle, center body and circular insert was designed. The center body and conical nozzle are designed to obtain a Gaussian PCD. A circular insert with a hole diameter of 0.9 mm (STL file dimension) was used to provide a mass flow rate of about 2 g/min for simulating the mass flow rates achievable with a DED-PF machine. The hopper was designed to fit between the 78-element array and the frame used to attach the assembly to an aluminum extrusion. The aluminum extrusion is used to suspend the assembly to prevent unnecessary sound reflections which might affect the sound field. The final hopper feed internal geometry is shown in Fig. 4.4 (a). Since the hopper has small feature sizes, its parts were printed in a Stratasys J750 machine, with a resolution of 27 μm , using the hard Vero material. The final array and hopper assembly, with a frame for attachment to the aluminum extrusion, is shown in Fig. 4.4 (b). In the final assembly, the hopper nozzle tip is 17.5 mm above the array's geometric center which corresponds to the sound focus point.

4.4.2 Experimental setup

A close-up of the hopper and array assembly, wired to the control boards, is shown in Fig. 4.4 (c). A schematic of the experimental setup is shown in Fig. 4.5. The array and hopper were suspended from an aluminum extrusion and the area was covered with an enclosure to minimize the effect of air drafts on the measurements.

The high-speed camera used is the Veo 710S from Phantom, using an EF 180 mm f/3.5L Macro USM lens from Canon. The light used is a MultiLed QT LED array (SN GS01703), powered by a MultiLed G8 Controller (SN GS00484). Both the light and the controller are from GS Vitec GmbH.

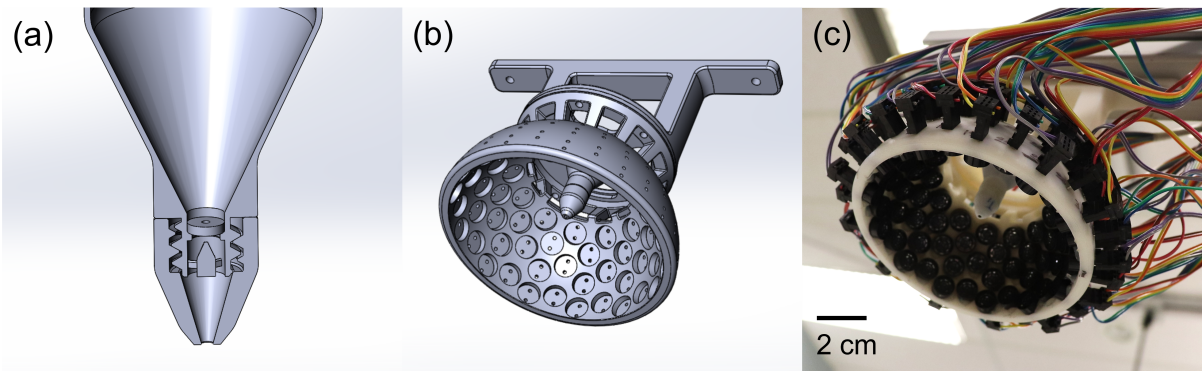


Figure 4.4: (a) Internal geometry of the hopper and powder feed mechanism. (b) Array frame, hopper and connecting frame assembly. (c) Assembled ultrasonic array attached to the hopper assembly.

The boards are set with a jumper to “18 volts” for the “logic supply” (power source for amplifier board and Arduino) [204]. Each one is connected in parallel using a barrel connector to a power supply. The signal from the laptop read by board number 1 comes from the USB connection to the Arduino MEGA board. For only this board the “sync” should be jumped to internal (to receive USB signals) [204]. All the other boards used should be set to external.

The Ti6Al4V powder used is from Raymor (Spherical Ti-6Al-4VGr5 powder), with size ranges from 45-150 μm , IPN 5773-S. The mass average diameter was determined to be 88 μm . The SS 316L powder used is from North American Höganäs (316 L-5320), item

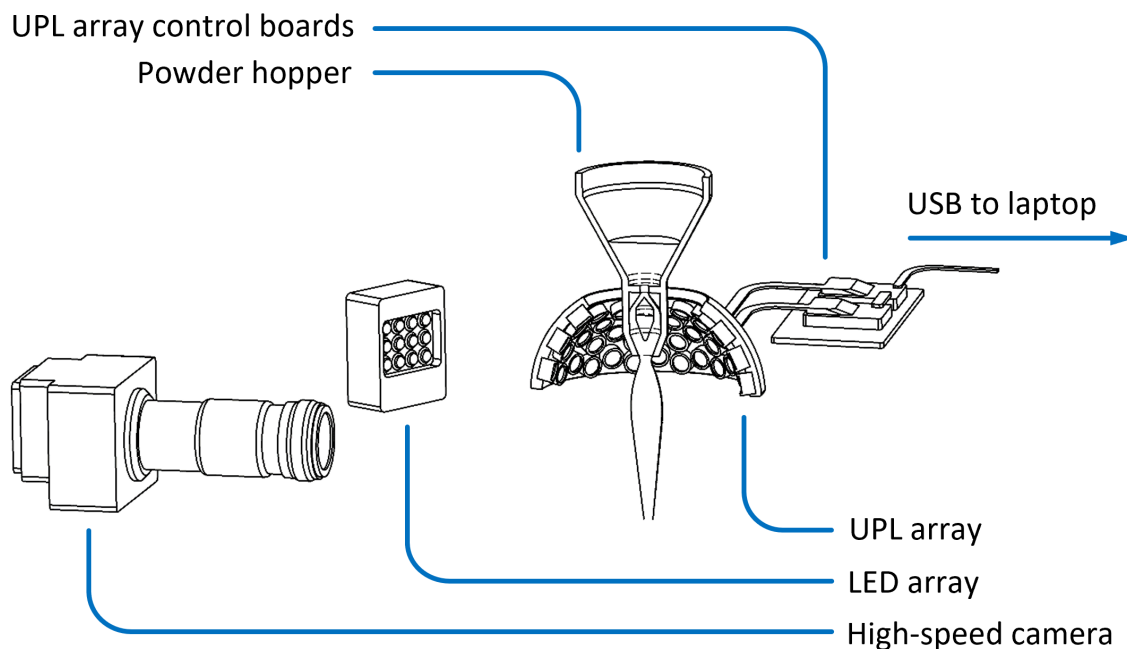


Figure 4.5: Schematic of the experimental setup showing lighting and camera setup (not to scale). The focal axis of the camera and the light were in the same plane, with the array axis normal to this plane, and the sound focus point intersecting it. The distance from the front of the camera lens and the light to the sound focus point was 72 and 51 cm respectively. The angle between the camera and the light center-line axis was 22° and setup to be as small as possible for uniform illumination.

111903. The mass average diameter was determined to be $89 \mu\text{m}$. Both mass average diameters were measured using a Camsizer X2 from Retsch GmbH.

4.4.3 Experimental procedure

The experimental procedure consisted of loading the hopper with powder, turning the ultrasound array on and capturing the high speed video. This was repeated four times for each voltage and material tested. Approximately 2 g for both powders were loaded in the hopper for each run. The exact powder mass was recorded and the amount of time the powder was flowing was measured with a stop watch. This was used to measure the mass flow rates for each run.

The Veo 710S high-speed camera had the following software settings: Bit depth, 12, Aperture 3.5, Resolution, 640 x 800, Sample rate, 13000 FPS, Exposure time, 76.514 μ s, EDR, 0 μ s, and Exposure Index, 1000. The PIV mode for image acquisition was not enabled; this setting adjusts the contrast of the frames and produces large errors in the imaging procedure described in Section 4.4.8. The recorded videos had a length of between 8 and 10 seconds, and they were saved keeping one out of every eight frames to reduce memory requirements. The light was set to 60% intensity.

4.4.4 Obtaining intensity images

Instead of taking a single picture of the powder stream to get an indication of the particle concentration [205], the powder stream was filmed at high speed and the frames were cropped, binarized using a 20% threshold level and summed. This allows the measurement of the average particle size as seen from the camera (described in Section 4.4.8) to estimate the mass flow rate from the frames as well as measuring particle velocity data. The thresholded and frame summed (TS) images for the first run both materials are shown in Fig. 4.7.

Initially, all videos were cropped to 13000 frames. Afterwards each frame was cropped 68 pixels from the top, 132 pixels from the bottom and 70 pixels from the sides (all inclusive). This was done to remove the lower part of the array and side reflections from the array housing. This step is necessary to ensure proper thresholding.

After all the frames for each run were cropped, they were binarized using a 20% ($\varepsilon = 0.2$) threshold level which corresponds to a grey level value given by:

$$g = g_d + \varepsilon(g_l - g_d) \quad (4.7)$$

where g_d is the darkest grey level and g_l is the lightest grey level in each frame. After thresholding, all the frames in each run were added. This part of the analysis was done in python using the NumPy library.

Using the first frames of the high-speed footage, the average downward speed of the Ti6Al4V particles was determined to be 0.585 m/s (0.028 m/s standard deviation) and for SS 316L, 0.591 m/s (0.032 m/s standard deviation). Using a single frame with a reference object placed at the focal plane, the pixel size was determined to be 72.9 μ m.

4.4.5 Powder widths

The effective powder stream width usually used in the DED-PF literature [34] assumes that the concentration of the powder at a line normal to the powder stream axis is Gaussian, and its effective radius is at a distance from the stream axis where the concentration is e^{-1} or e^{-2} times the peak intensity at the axis. In this chapter, the e^{-1} width will be considered.

This radius is found by fitting a Gaussian function to the intensity values at the row being considered and solving for the e^{-1} intensity ratio radius. Note that although the Gauss fit does not fit the tails of the PCD as seen in Fig. 4.9, especially after the powder is subjected to the sound field, it still fits the locations at e^{-1} intensity ratio, i.e., 37% of the peak value from the bottom of intensity plots.

The location in the z axis in pixels where the powder widths, divergence angles and concentration profiles will be measured at, is the point at which the force field magnitude drops to less than 4% of its peak value and the field is assumed to not affect particle motion.

The pixel location downstream of the sound field is the distance from the top of the frame to the sound focus point plus half the distance where the sound field is assumed to not affect the particles (using the half intensity criteria). The corresponding pixel number value (123) is given by:

$$p_{ds} = p_{tba} + \text{round}\left(\frac{l_{af}}{l_{pix}}\right) + \text{round}\left(\frac{l_i}{2l_{pix}}\right) - p_{cropStartZ} \quad (4.8)$$

where ds stands for the downstream of sound interaction region, p_{tba} is the distance from the top of the TS image to the bottom of the sound array (20 pixels), l_{af} is the distance from the bottom of the array to the focus point (2.45 mm) and $p_{cropStartZ}$ is the amount of pixels that were cropped (inclusive) from the top of the TS image (68 pixels). The effective sound application length value ($l_i = 20$ mm) is the effective distance along the particle stream axis where sound is assumed to affect the particles.

One way to extend the typical e^{-1} width metric to the arbitrary axially symmetric non-Gaussian distribution function produced after a force field is applied to the original Gaussian distribution is as follows:

1. For a Gaussian PCD, find the mass fraction of powder out of the total mass that is inside the radius given by the e^{-1} criteria

2. Then find the radius for the new axially symmetric distribution corresponding to a volume of this distribution that yields the same mass fraction

A volume bounded to some radius r by an axially symmetric function is given by:

$$V(r) = 2\pi \int_0^r f(x)xdx \quad (4.9)$$

The effective powder stream width is then twice the radius r that satisfies the following equation:

$$f_V = \frac{V_G(r_G)}{V_G(r_G \rightarrow \infty)} = \frac{V(r)}{V(r \rightarrow \infty)} \quad (4.10)$$

where the subscript G stands for volume bounded by a Gaussian distribution. The different volumes in Eq. 4.10 are shown in Fig. 4.6.

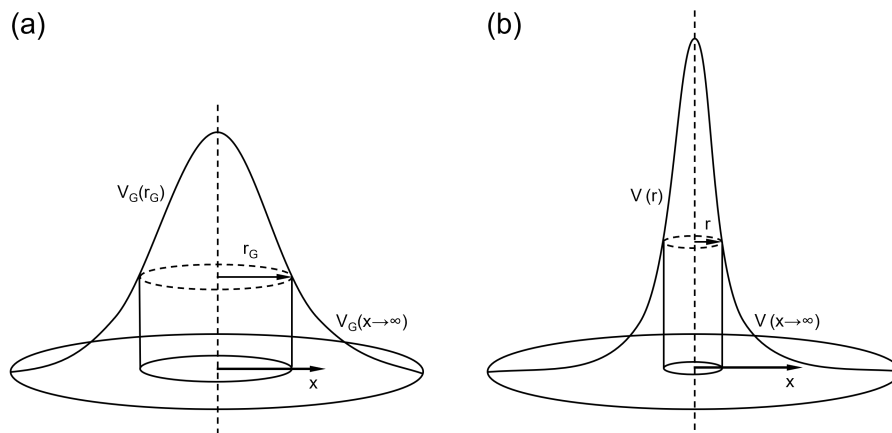


Figure 4.6: (a) Volumes used in Eq. 4.10 from a Gaussian distribution, and (b) from a new distribution.

One can compute f using numerical integration for different values of t . Finally, one can do the same for Eq. 4.9 to get the volume for different values of r . Then one can find the value of r that satisfies the following equation:

$$0 = r_V(r) - r_{VG} \quad (4.11)$$

where r_G is the volume fraction considering distribution f_y , and r_{VG} stands for the volume ratio of a Gaussian distribution, considering the radius given by the e^{-1} or e^{-2} criteria. Half

the width of the Gaussian powder stream profile at a point e^{-1} times the peak intensity is obtained, using a normal distribution with zero average, by solving for x in:

$$\frac{1}{\sigma_m \sqrt{2\pi}} e^{-1} = \frac{1}{\sigma_m \sqrt{2\pi}} e^{-\frac{1}{2} \left(\frac{x}{\sigma_m}\right)^2} \quad (4.12)$$

where σ_m is the powder profile standard deviation. The half width values are $\sqrt{2}\sigma_m$ for the e^{-1} criteria, and following the same method, $2\sigma_m$ for the e^{-2} criteria. Using the Gaussian distribution used in Eq. 4.12 to find $V(r)$ yields:

$$V_G(r) = \sigma_m \sqrt{2\pi} \left[1 - e^{\frac{1}{2} \left(\frac{r}{\sigma_m}\right)^2} \right] \quad (4.13)$$

Using Eq. 4.13, the volume ratio f_{VG} using the half width values are $1 - e^{-1} = 0.63$ for the e^{-1} radius criteria.

The numerical integration is done by first centering the intensity function being considered along the x -axis. This is done by fitting the function with a Gaussian, finding its average pixel value and shifting the row of pixels by that amount. As can be seen in Fig. 4.9, although the Gaussian fit does not accurately follow the powder concentration if it is being affected by the sound field, the peak of the Gaussian function still coincides with the function's axis of symmetry. After centering, the intensity function's radial volume is computed. This is done using:

$$V_I = \pi \left(c_0 [1/2]^2 + \sum c_i [(i + 1/2)^2 - (i - 1/2)^2] \right) \quad (4.14)$$

This corresponds to numerically integrating a radially symmetric function using the mid-point rule [171]. Since V_I is proportional to mass flow rate, it can be used directly for the mass ratio calculations. The V_I value is calculated using the whole row of intensities, to approximate $V(r \rightarrow \infty)$.

To find the mass ratio radius by solving Eq. 4.11, one can start with a pixel width value corresponding to r from the center to the edge of the frame, keep decreasing this value by 1 and cropping both ends of the stored row intensities until Eq. 4.11 changes sign.

4.4.6 Catchment efficiency proxy

One can use the results from the last section to find a catchment efficiency proxy (CEP). Instead of finding the radius in the new PCD that contains the same mass fraction, one

can calculate what mass fraction is contained in the original e^{-1} intensity radius in the new PCD.

This is a way of comparing different powder concentrations without full experimental or simulated results of a DED-PF process, with a given track geometry. In this case it is assumed the melt pool is circular, its radius is the e^{-1} intensity radius of the original powder stream concentration function and all particles reaching the melt pool adhere to it. To calculate this value, the value of V_I at the required radius is calculated and then divided by the value of V_I , considering the whole intensity row in the TS image.

4.4.7 Powder stream divergence angle

The powder stream divergence angle was calculated from the TS images by calculating the e^{-1} intensity radii from a range of 100 pixels above and below the p_{ds} pixel row value in intervals of 20 pixels. Then a polynomial fit is made to the radii as a function of row (z) pixel location, and the divergence angle is found from the derivative of this polynomial at p_{ds} . This intensity criterion to find the spreading angle is commonly used in the literature [198, 199, 34].

It was found that due to the low speeds of the experimental setup, a quadratic fit to the e^{-2} intensity values as a function of pixel row gives more accurate angle data, as there is a small gravitational acceleration. The coefficient of determination (r^2) values were calculated from the norm of the residuals given by the MATLAB function `polyfit()` [206].

4.4.8 Particle concentration from thresholded images

To convert the TS values to a particle concentration number, the following conversion factor was used:

$$f_c = \frac{1}{n_f l_{fov} l_x^2 n_{xp}} \quad (4.15)$$

where n_f is the number of frames being added for each run (13000), l_{fov} is the field of view “thickness” (twice the distance from the focal plane to the distance where the particle is not thresholded due to defocusing), l_x is the image pixel size calculated previously and n_{xp} is the average number of pixels that give a 1 value per particle. The n_{xp} values (16.36 for Ti6Al4V and 29.96 for SS 316L) were calculated directly by calculating the average area in pixels of the 1 value blobs for each frame and averaged for all frames for the 4

benchmark videos. This was done in python by labeling all the blobs in each frame using a 4-connectivity pixel metric and calculating the individual blob areas using the `label()` and `regionprops()` functions from the scikit-image library.

The l_{fov} values (0.70 mm for Ti6Al4V and 0.72 mm for SS 316L) were calculated using the depth of correlation equation given by [207]:

$$l_{fov} = 2 \left(\frac{1 - \sqrt{\varepsilon}}{\sqrt{\varepsilon}} \left[f^{\#2} d_p^2 + \frac{5.95(M+1)^2 \lambda^2 f^{\#4}}{M^2} \right] \right)^{1/2} \quad (4.16)$$

where ε is a threshold value defined in the same way as the value used before (0.3), $f^{\#}$ is the high-speed camera's lens f number (3.5), d_p is the average particle size, M is the magnification and λ is the wavelength of light being used. The magnification (0.33) was calculated using [208]:

$$M = \frac{f_l}{d_{lo} - f_l} \quad (4.17)$$

where f_l is the focal length of the lens (18 cm) and d_{lo} is the distance from the lens to the object, measured to be 72 cm. The value used for λ is an average for visible light (590 nm) [209].

The assumption made for Eq. 4.15 is that the concentration is being measured on a “plane” i.e. $l_{fov} \ll r(z)$ which can be assumed in this case since the minimum effective particle diameter $r(z)$ within all runs assuming the e^{-1} intensity criteria is 3.2 mm. Eq. 4.16 is used in particle image velocimetry applications and has been shown to provide accurate values [209].

Using the conversion factor given by Eq. 4.15, the data for all the TS images can be converted to a particle concentration value. The data used was averaged using the selected row at pixel position `offsetPixels` as well as two rows above and two rows below the selected row.

The data was also normalized using:

$$c_n(r) = c_m(r) \frac{\dot{m}_m}{\dot{m}_c} \quad (4.18)$$

where c stands for particle volumetric concentration, n for a normalized value, m for a measured value, \dot{m} for mass flow rate and c for a calculated value. The data is normalized to consider any differences in the flow rate between runs.

The mass flow rate can be calculated from the concentration data from each TS image. The mass flow rate is given by:

$$\dot{m}_c = m_p u_z f_c \Delta x^2 V_I \quad (4.19)$$

where in this case u_z is the average of downward particle speeds, and Δx is the separation between concentration points i.e. the pixel size l_x .

4.4.9 Initial conditions for simulations

To have an initial condition for the simulations that will reproduce the PCD at 0 V downstream of the sound field interaction length, the measured e^{-1} widths are used together with the divergence angles to calculate the initial particle stream widths, using:

$$r_i = r_f - l_i \tan(\theta_f) \quad (4.20)$$

Eq. 4.20 uses the same variable names as in Fig. 4.3. The angle θ_f is the divergence angle calculated by the method described in Section 4.4.7. In the case of no applied sound (0 V) and assuming negligible gravitational acceleration and air drag on the particles along l_i , the divergence angle does not change along z and it is equal to θ_i .

4.5 Results and discussion

4.5.1 Powder stream 2D concentrations

The TS images for Ti6Al4V and SS 316L are shown in Fig. 4.7. The focusing effect is seen at 8 V for Ti6Al4V and at 10 V for SS 316L. The increase in focusing for SS 316L from 10 to 16 V is not as noticeable. This might be due to the sound radiation field pushing the particles towards the opposite side of the powder stream center-line and non-collimated particles.

Surface plots of the thresholded and added frames for Ti6Al4V and SS 316L are shown in Fig. 4.8. The focusing effect is seen from both the divergence angle decrease as well as an increase in concentration at about 10 mm in the z direction. One can see that at 16 V the downstream concentration is less sharp for SS 316L, following the results shown in Fig. 4.7.

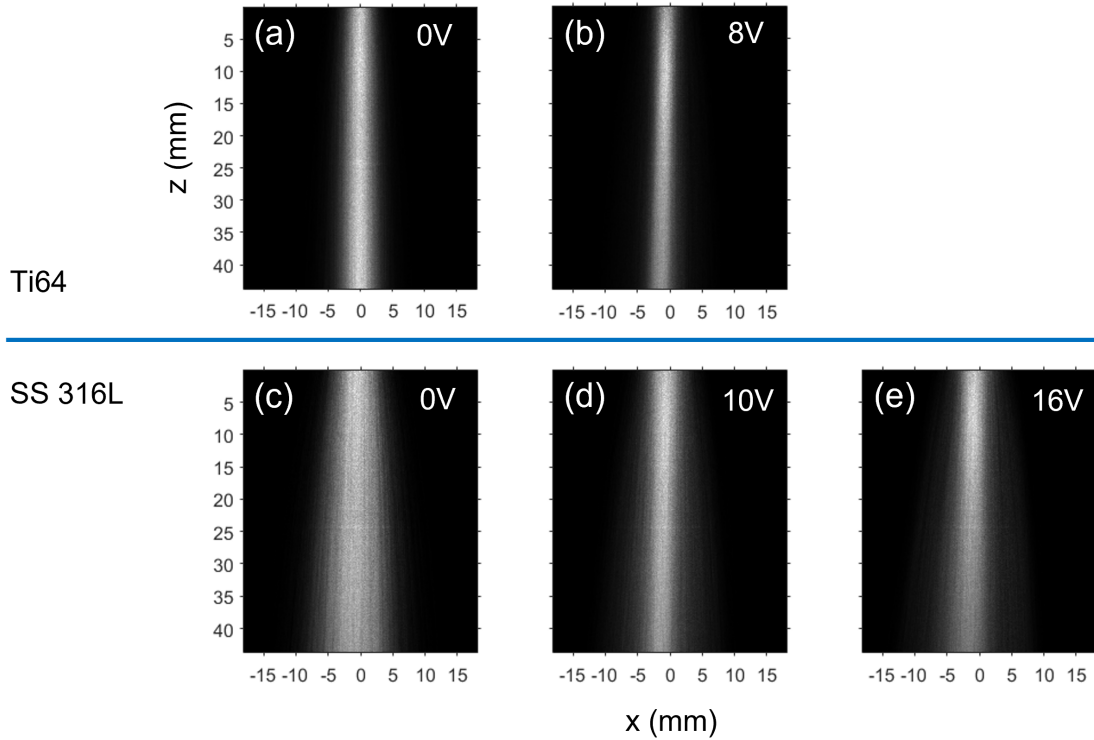


Figure 4.7: Added frames from high-speed camera for first repeat for Ti6Al4V at (a) 0 and (b) 8 V, and first repeat for SS 316L at (c) 0, (d) 10 and (e) 16 V.

4.5.2 Comparison of downstream particle concentration

Gauss fits for the image intensity downstream of the sound field for Ti6Al4V and SS 316L are shown in Fig. 4.9. At 0 V (no sound field) the intensity distribution closely follows a Gaussian, indicating that the designed hopper produces a distribution similar to the concentration profile normally found in a DED-PF machine [34]. However, there is a deviation from a Gaussian profile when the sound field is applied, with larger tails. This is more pronounced in the SS 316L profile.

This might be due to the 0 V divergence angle being larger, meaning more of the powder is being affected by parts of the sound field actually pushing the powder away from the powder center-line i.e., at a distance after half the wavelength of the force field ~ 3 mm.

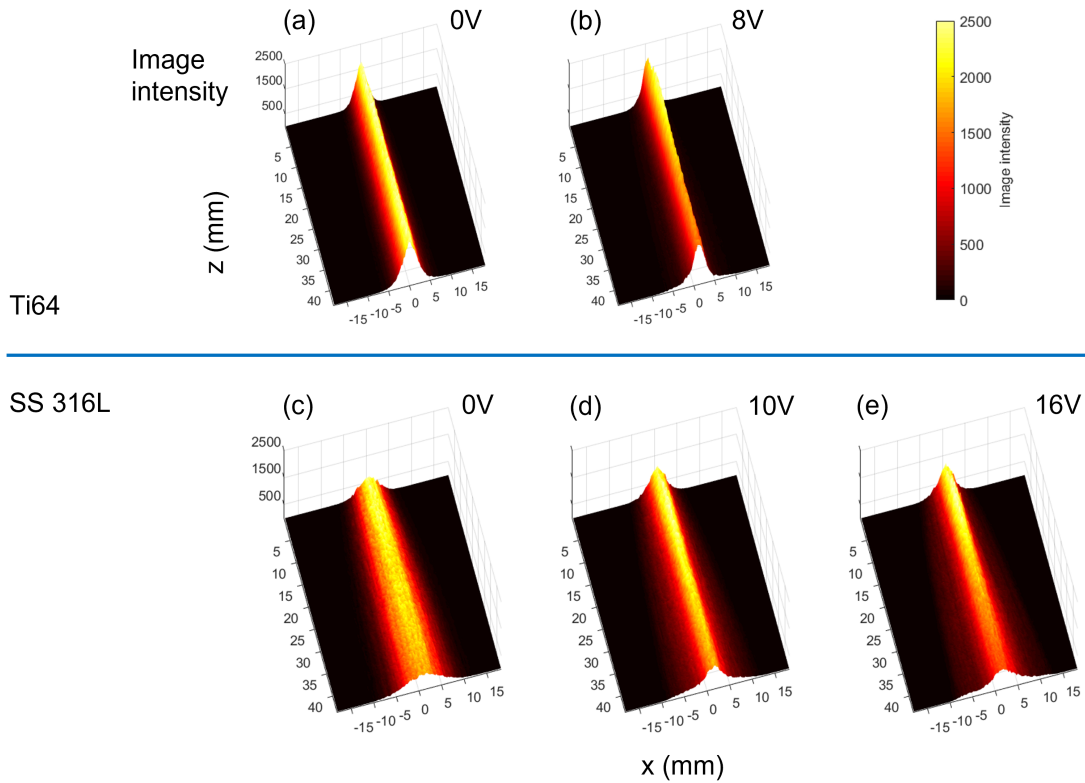


Figure 4.8: Surface plots of added frames from high-speed camera of the first repeat for Ti6Al4V at (a) 0 and (b) 8 V, and first repeat for SS 316L at (c) 0, (d) 10 and (e) 16 V.

4.5.3 Powder stream widths

The e^{-1} and mass fraction widths are shown in Fig. 4.10. There is a clear decrease in the e^{-1} width as the voltage is increased for both materials, however, the mass ratio width decreases less significantly and increases for SS 316L at 16 V. This might be related to the larger tails seen in the Gauss fits in Fig. 4.9, showing powder is being focused but also being pushed away, depending on the powder and sound field geometry.

4.5.4 Catchment efficiency proxy

The mass fraction inside the 0 V e^{-1} mass fraction width for all materials and voltages is shown in Fig. 4.11. The mass fraction increases for all cases at higher voltages, except for

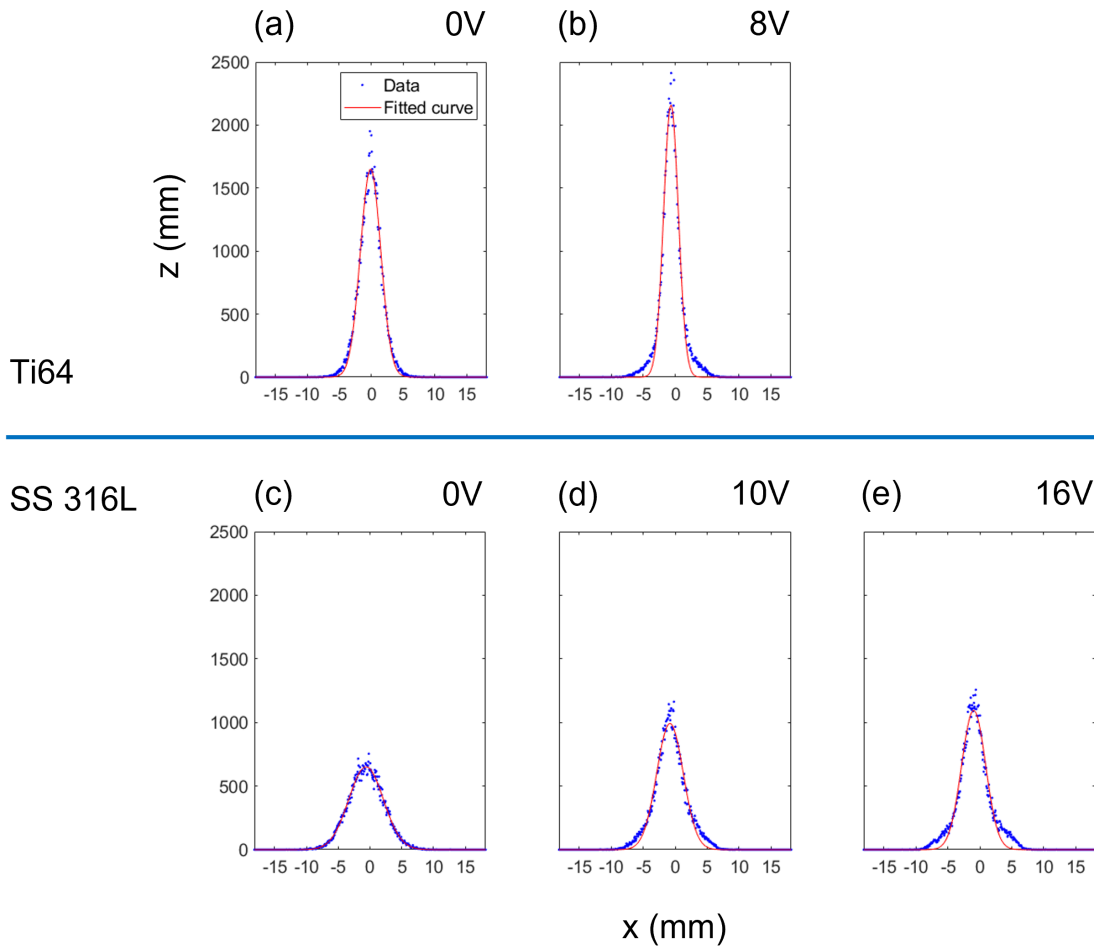


Figure 4.9: Gauss fits downstream of applied sound field for first repeat for Ti6Al4V at (a) 0 and (b) 8 V, and first repeat for SS 316L at (c) 0, (d) 10 and (e) 16 V.

SS 316L at 16 V. This might be due to the same reason the mass fraction widths do not change as significantly as the e^{-1} widths.

4.5.5 Powder stream divergence angles

The powder stream divergence angles downstream of the sound field for all materials and voltages tested are shown in Fig. 4.12. The angles decrease with increasing voltage for

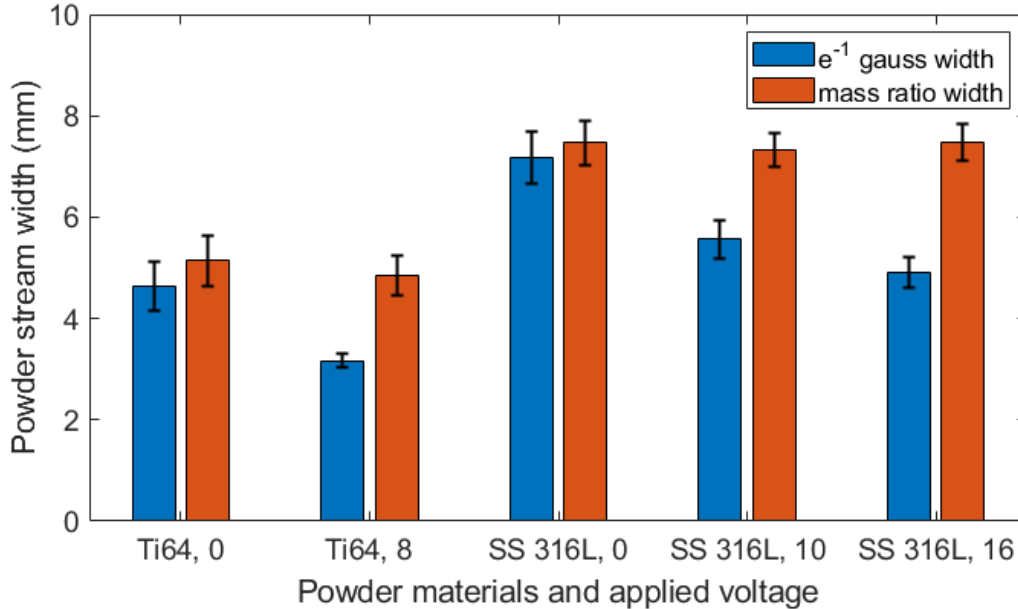


Figure 4.10: Powder stream widths for all materials and applied voltages.

all cases. For SS 316L at 16 V the angle change is less significant. This might be due to particles not being collimated or crossing the powder stream center-line. The minimum r^2 value from all the polynomial fits used to determine the angles from all materials, and repeats at 0 V was 0.95, indicating an accurate fit. The fit is less accurate when a voltage is applied, with a minimum r^2 value of 0.80.

4.5.6 Comparison with analytic model

Since the measured Gaussian powder radii at 0 V are greater than a quarter of the force field wavelength, the analytic model does not give fully accurate divergence angle values. However, one can use the Lagrangian simulation, to check the divergence angle at the linear range of the force field (using $l_{offset} = 0.7$ mm). These simulations are later shown to be able to model the PCD. The F_a value used is the one at l_{offset} , corresponding to half the peak force value along the x -axis. The force was divided by two again since the force in the z -axis can be modeled by a cosine function shifted to a range of 0 to 1, with an average value of 0.5. The calculated values compared to the analytic results obtained from Eq. 4.2 are shown in Fig. 4.13. The analytic model results match closely with the

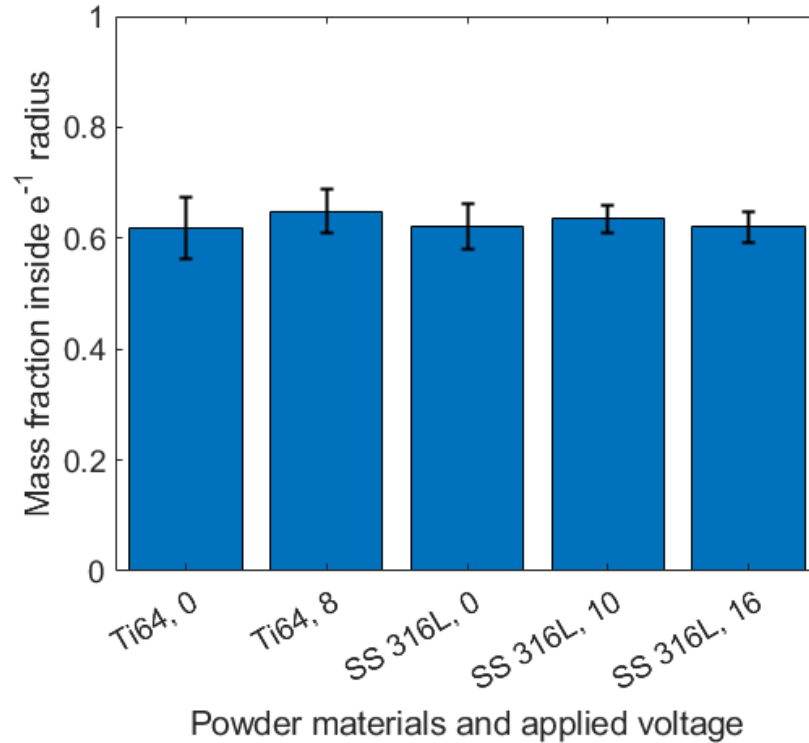


Figure 4.11: Mass fraction inside $0 \text{ V } e^{-1}$ mass fraction powder width for all materials and voltages.

calculated angles. The small-angle approximation error increases with larger calculated angles as expected. The number of time steps used for all Lagrangian path calculations was 32, to keep the change in divergence angle between subsequent time step subdivisions below 1%, following the same convergence study procedure described in Appendix H.

4.5.7 Particle concentrations downstream of the sound field

To test the conversion factor between thresholded image intensity and particle concentration, the mass flow rate was calculated from the images using the conversion factor. The results are shown in Fig. 4.14. The result corroborates the conversion factor calculation. The results for the particle concentrations downstream of the sound field are shown in Figs. 4.15 and 4.16. Each curve is the average of four repeats and includes standard error bars.

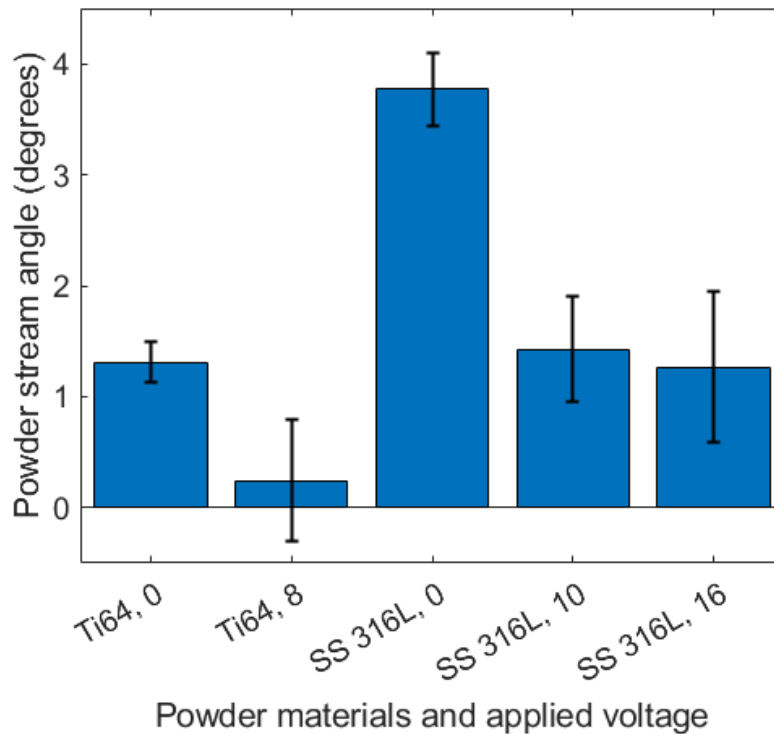


Figure 4.12: Powder stream divergence angles downstream of sound field for all materials and voltages.

4.5.8 Lagrangian and Eulerian simulations

The results of the Lagrangian and Eulerian simulations overlapped over the measured concentration data for all experiments are shown in Figs. 4.17 to 4.19.

The simulations match well with each other as expected. The simulations match the measured concentration profiles when no voltage is applied, validating the new model for particle motion derived in Appendix G, and the assumption of using Eq. 4.20 without considering air drag, to get an initial concentration profile. Note that the initial profile is occluded by the array and its reflected light in the experimental setup used.

The simulations closely match the concentration profiles except when close to the center of the powder stream, especially for SS 316L at 16 V shown in Fig. 4.19, where the peak concentrations reach 3.7 for the Eulerian simulation and 2.9 for the Lagrangian simulation

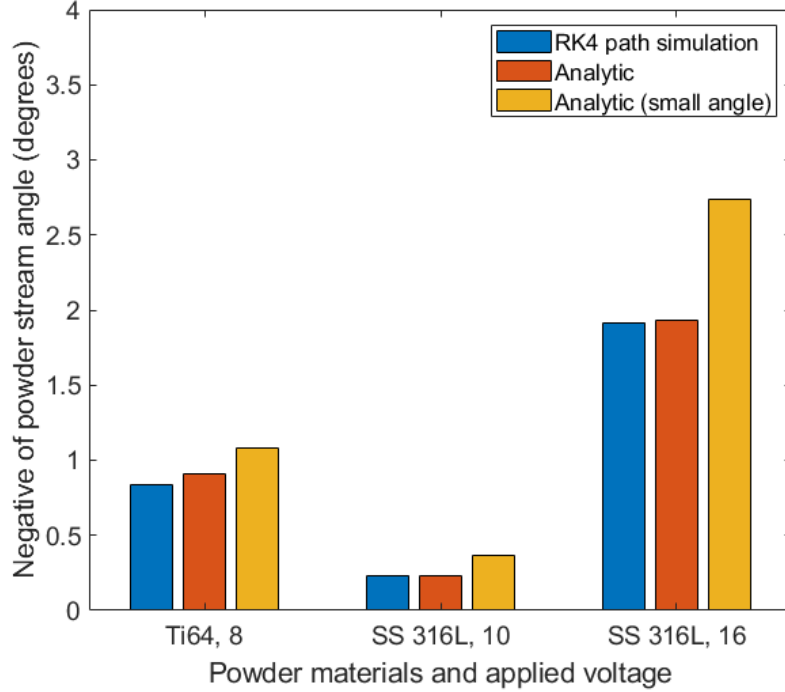


Figure 4.13: Angles computed using RK4 particle tracking and analytic angles for all materials and voltages.

instead of the measured 0.89 particles per mm^3 ; this may be explained by the fact that the models do not take into account individual particle speed and direction deviations as well as particle collisions. The more accurate Lagrangian value might be due to the fact that the model can take into account particle crossings. These effects should be more pronounced close to the powder center when the applied voltage used for focusing increases.

One factor that might affect the measured peak concentration values is similar to the one in the Lagrangian simulations; if there are enough particles being imaged to get an accurate concentration. Using the average measured flow rates for Ti6Al4V and SS 316L (1.66 and 2.15 g/min), the particle masses using the mass-weighted diameters, the fact that one second of frames was used per run, and four repeats were averaged to get the concentrations shown in Figs. 4.17 to 4.19, the approximate number of particles present at any z position is about 6.99×10^4 and 4.84×10^4 particles for Ti6Al4V and SS 316L respectively. Using the Lagrangian simulation convergence plots for mean RMS error as

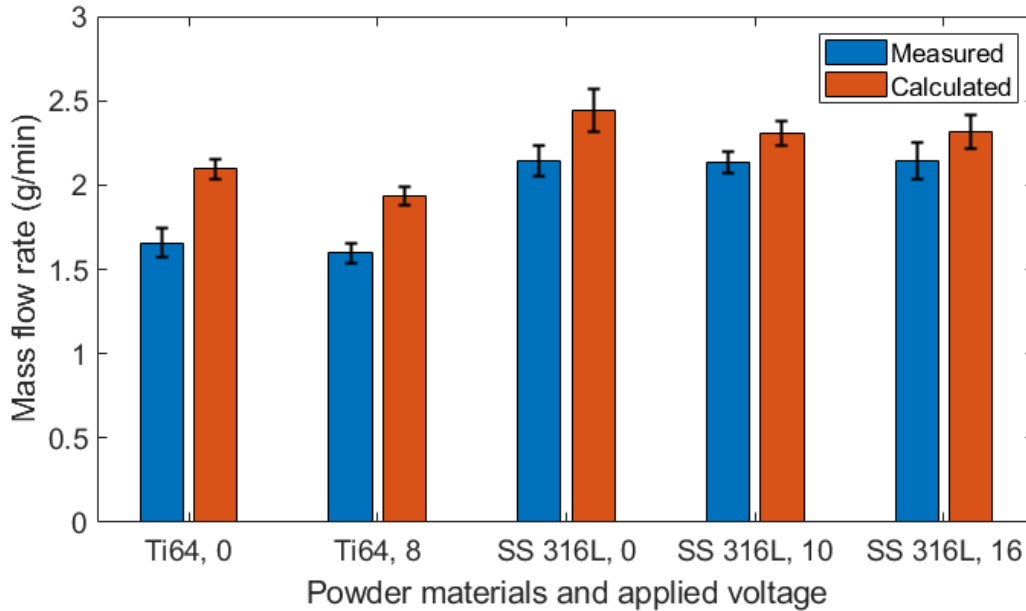


Figure 4.14: Actual and estimated mass flow rates for all materials and voltages.

a function of particle plots for each material and voltage gives expected RMS errors of 3.33 and 2.36% for Ti6Al4V at 0 and 8 V respectively and 6.20, 4.61 and 2.71 for SS 316L at 0, 10 and 16 V respectively. The convergence plots are explained in more detail in Appendix H. In the SS 316L at 16 V case, this value is even lower than the expected 4% RMS error of the simulations and does not explain the large concentration gap between the measured and simulated results.

Note that the errors at the center of the concentration profile go down for a fixed number of particles when the voltage is increased; this is because a higher fraction of the available particles go to the center of the stream when the focusing is increased by the applied voltage. This is seen both in the required number of points for each Lagrangian simulation at the required RMS error of 4%, shown in Appendix H, and in the measured data; although one cannot make a quantitative statement from the error bars given by four repeats, one can see that the measured error bars close to the concentration profile centers are smaller for the non-zero voltage runs compared to the zero voltage runs, which is noticeable in Figs. 4.17 and 4.19.

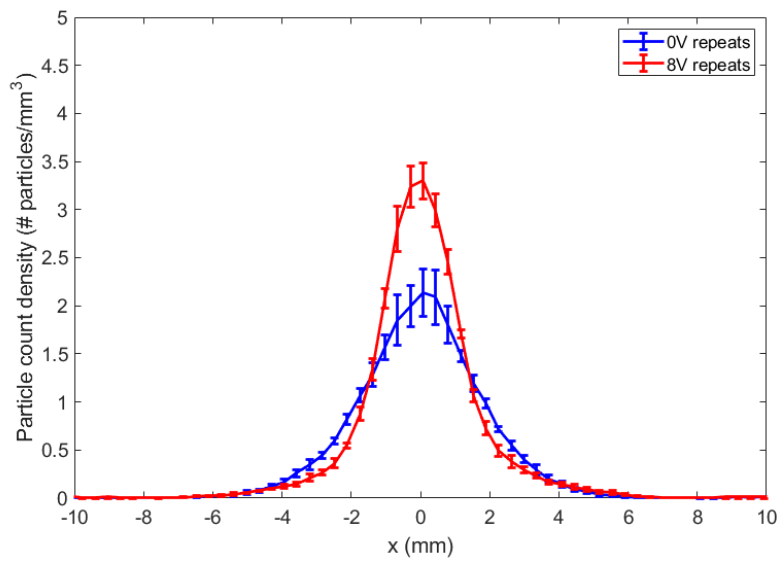


Figure 4.15: Particle concentration downstream of sound field for 0 and 8 V, for Ti6Al4V.

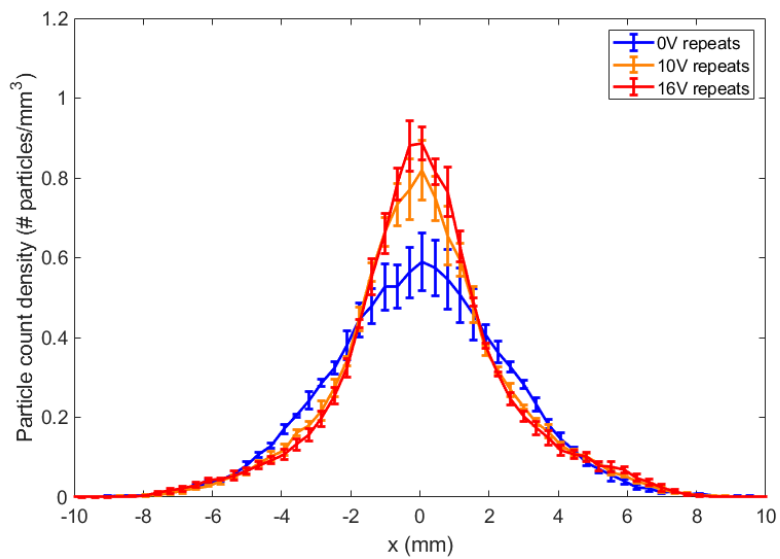


Figure 4.16: Particle concentration downstream of sound field for 0, 10 and 16 V, for SS 316L.

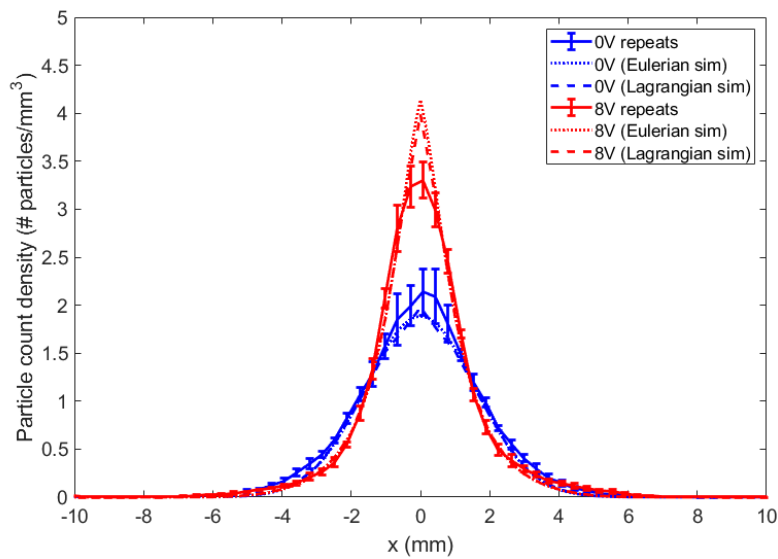


Figure 4.17: Particle concentration downstream of sound field for Ti6Al4V, at 0 and 8 V, overlapped with Lagrangian and Eulerian simulations.

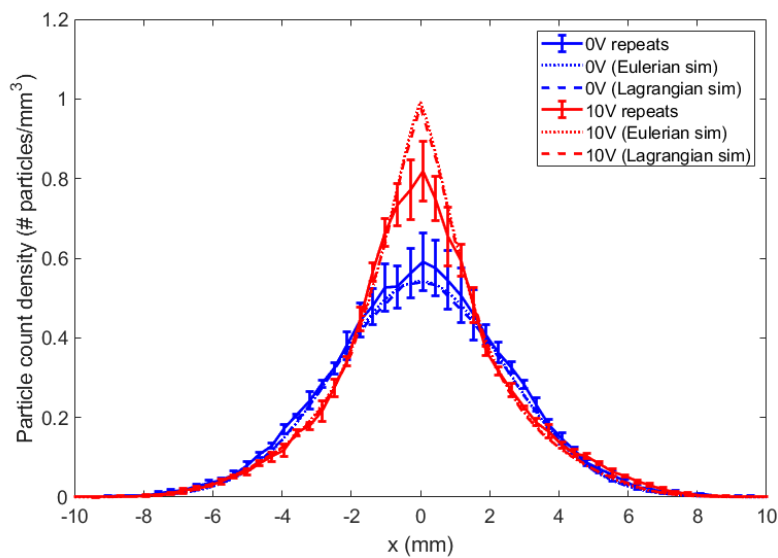


Figure 4.18: Particle concentration downstream of sound field for SS 316L, at 0 and 10 V, overlapped with Lagrangian and Eulerian simulations.

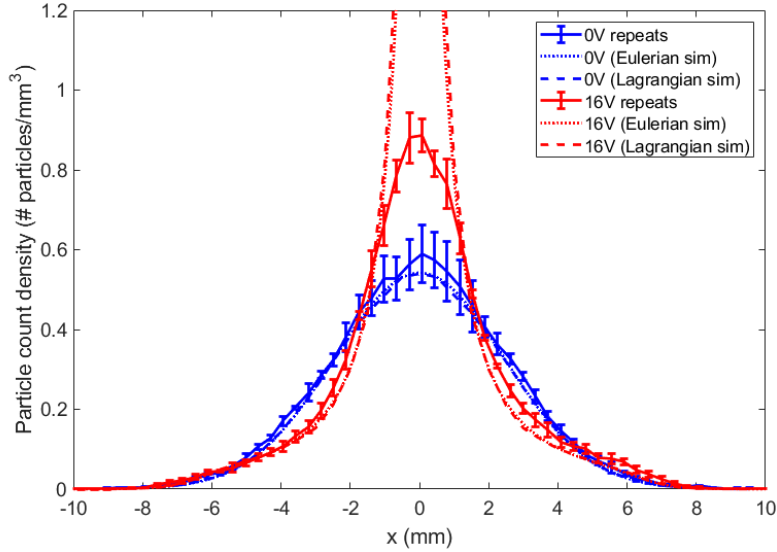


Figure 4.19: Particle concentration downstream of sound field for SS 316L, at 0 and 16 V, overlapped with Lagrangian and Eulerian simulations.

The e^{-1} radii predicted from the simulations compared to the measured values are shown in Fig. 4.20. The radii closely match the data again except for SS 316L at 16 V due to the higher peak concentrations which produce a Gaussian fit with a lower variance, which produces correspondingly smaller e^{-1} radii for both simulations.

4.6 Summary

Based on the results from this chapter, the following conclusions can drawn:

- A Gauss fit for the powder stream without an applied sound field is closely matched with the experimental concentration profile as observed in an actual DED-PF machine, validating the design of the gravity hopper. Applying the sound field produces a function with larger tails compared to a Gauss fit
- The e^{-1} powder stream widths downstream of the applied sound field were decreased for both Ti6Al4V and SS 316L powders. The largest decrease in width, downstream of the applied sound field, for Ti6Al4V was from 4.6 to 3.2 mm at 8 V and for SS 316L from 7.2 to 4.9 mm at 16 V, corresponding to a 30 and 31% reduction respectively.

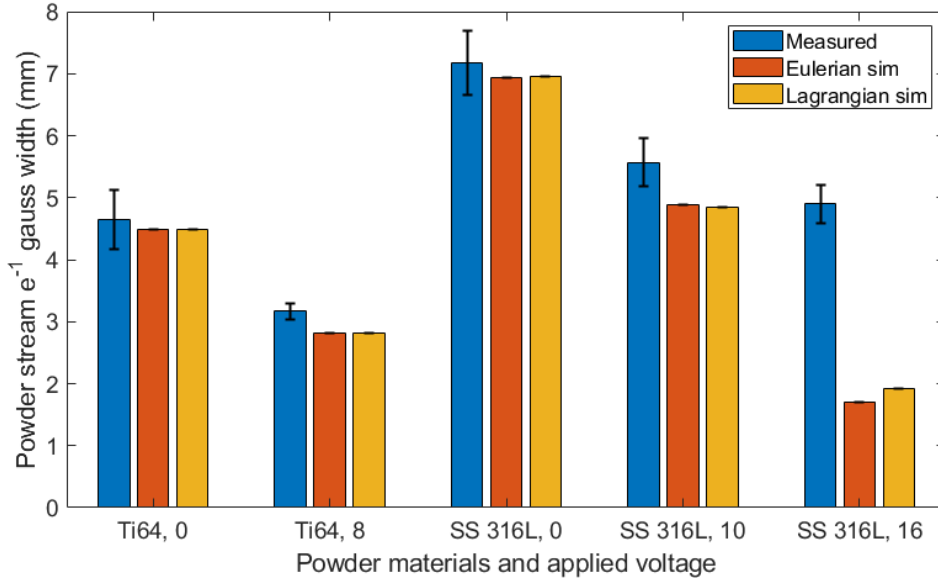


Figure 4.20: Comparison of e^{-1} radii obtained from measured and simulated data.

The powder stream width decreases with increasing voltage for the voltages that were tested, with the width observed to approach a minimum width for SS 316L at 16 V. The divergence angle at this location also decreased for both materials with increasing voltage

- The mass ratio powder stream width reduction for the tested voltages was lower than the decrease seen by considering the e^{-1} powder stream width and increased slightly for SS 316L at 16 V. This is due to the larger concentration function being generated for the sound radiation force field, due to the SS 316L initial powder width and divergence angle are higher than the one for Ti6Al4V. This highlights the need to design a nozzle and force field that have the right geometry, to match the nozzle width with the sound field's l_{offset} value, and to have the right voltage to be able to minimize the powder stream width downstream of the sound field, along l_i
- Both Lagrangian and Eulerian simulations had a close agreement with each other after performing a convergence analysis. For higher applied sound pressure there will be a substantial amount of particle path crossings, which cannot be modeled in the Eulerian simulation i.e.; the particles would “pile up” at $x = 0$. This may be resolved by using a Eulerian model that considers particle crossings.

Chapter 5

Gaussian Beam Representation of DED-PF Powder Stream

5.1 Introduction

The powder motion models found in DED-PF literature are either numerical simulations taking into account nozzle geometry, gas flow and particle motion, or analytic models where the powder stream's powder concentration distribution (PCD) is static.

The gas phase in numerical simulations is usually taken into account and is modeled using computational fluid dynamics [37, 26]. Due to the large mass of the particles and low number concentration, the coupling is done from the gas phase to the particles but vice versa. Most numerical powder motion models consider the powder as a discrete phase, and use Lagrangian particle tracking with reflections, considering the coefficient of restitution, at the simulation boundaries [210]. These models compute the particle motion by integrating the forces acting on the particles, in their reference frame. Recent work also has modeled the particles as a continuous Eulerian phase, where the problem is discretized using finite elements or finite volume, and the reference frame is a fixed mesh with respect to the nozzle and the amount of particles coming in and out of each mesh element is computed over time [189].

Analytic models usually formulate the PCD using a Gaussian function that has a linearly increasing intensity ratio width (IRW) that matches experimental data [34, 211]. These types of models are orders of magnitude faster to compute than numerical models, however the interaction of the powder stream with forces due to shielding gas [33] or reflections with the build plate are not taken into account or are implicitly taken into account

by empirically fitting the model to a measured PCD in a particular DED-PF setup. In this chapter, a third type of model is presented; one that has a computationally efficient analytic solution, but is also able to account for forces being applied to the powder stream. Note that the scope of models in the literature being considered and the one in this chapter are for the powder motion downstream of the nozzle exit.

The mechanism causing linearly increasing IRW in analytic models is usually explained by some diffusion mechanism that reproduces the observed linearly increasing IRW [198, 212]. This mechanism is plausible if one assumes there are a high number of particle collisions in the nozzle exit zone producing some effective diffusion of the particle concentration. In Chapter 4, by observing high-speed camera footage of a powder stream, it was determined that the number of collisions is low for DED-PF relevant process parameters. A more plausible mechanism was then proposed, based on a constant downward component and a linearly increasing outward component, with the outward component being proportional to the distance from the powder stream's center line. This powder motion model was also used to accurately predict the behaviour of the PCD downstream of an externally applied sound radiation focusing force field to a powder stream.

In particular, the focusing force field considered in Chapter 4 is a result of high power sound waves coming for the area surrounding the powder stream, interacting with the particles and producing a force field that permeates the powder stream and accelerates particles depending on their position in the field. Plots of the sound pressure and the resulting components of this particular force field for the case of SS 316L particles with sound produced by applying 16 V to ultrasound transducers in the setup described in Chapter 4 are shown in Fig. 5.1. The variables shown in the figure are explained in Section 5.2.4. The transducers form an array with the shape of the hemisphere with an open top for the powder to move through it, with the center of the sphere aligned with the sound focus point. Note that the methods described in this chapter may also be used to quickly model other types of sound fields being applied, such as force fields due to electromagnetic fields [187], as long as the powder stream can be modeled using a Gaussian beam as described in the rest of this chapter.

For high degrees of focusing, the powder motion model in Chapter 4 shows a higher peak concentration compared to the experimental results, that approach a constant concentration and IRW. A possible explanation for this discrepancy is that besides a linearly increasing outward particle speed, there is also a distribution of possible deviations from this speed. This would introduce an "aberration" in the focused particles that would produce a less focused powder stream for the same applied force field. A summary of the mechanisms used to explain the behaviour of the powder steam for the DED-PF process is shown in Fig. 5.2.

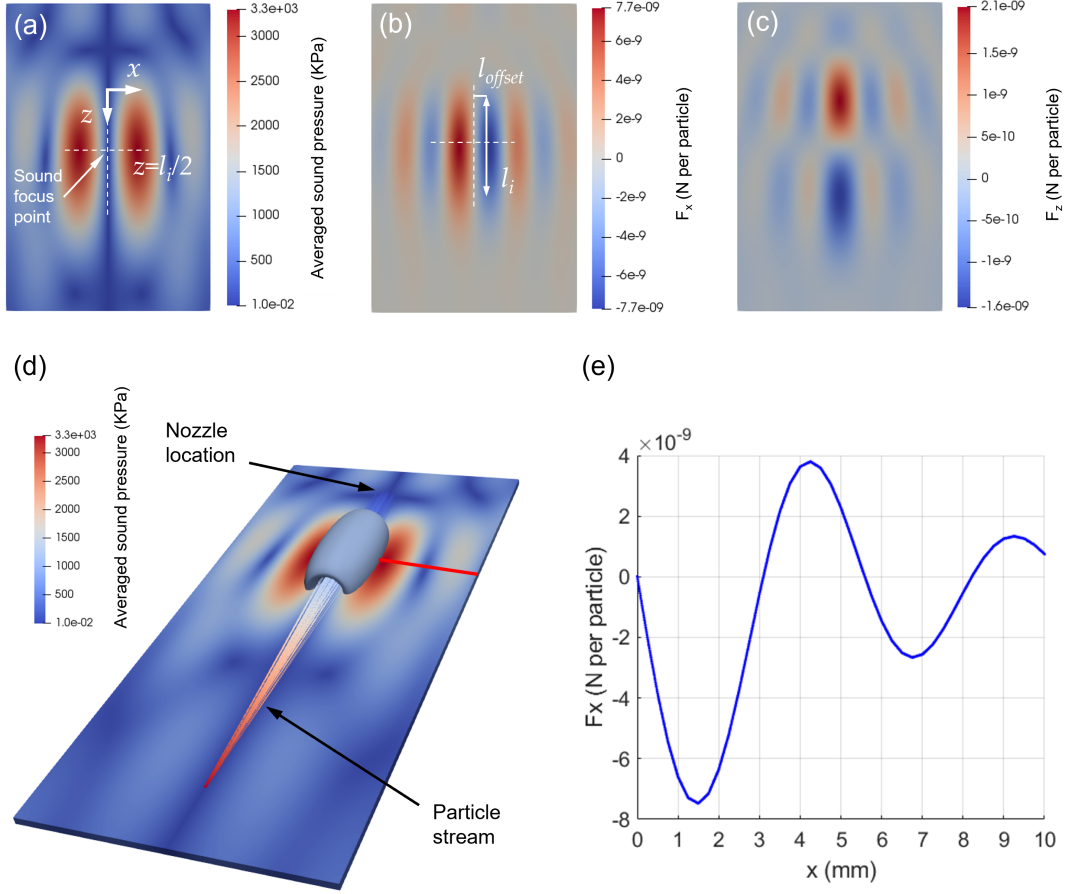


Figure 5.1: (a) Period averaged sound pressure (ASP), (b) x component of the resulting force field, (c) z component of the resulting force field. (d) ASP field, with particles tracks, and isosurface with a radial sound radiation force value of -4.0×10^{-9} N per particle, based on the setup for SS 316L particles with sound produced at 16 V in Chapter 4 and (e) sound radiation force in the x-axis direction along the red line.

The function used to describe the powder flow rate for a DED-PF nozzle in the literature is given by [34]:

$$c = \frac{\dot{m}}{u_z m_p \pi r(z)^2} \exp \left[-\frac{r^2}{r(z)^2} \right] \quad (5.1)$$

where \dot{m} is the mass flowrate, u_z is the average of downward particle speeds, approximately

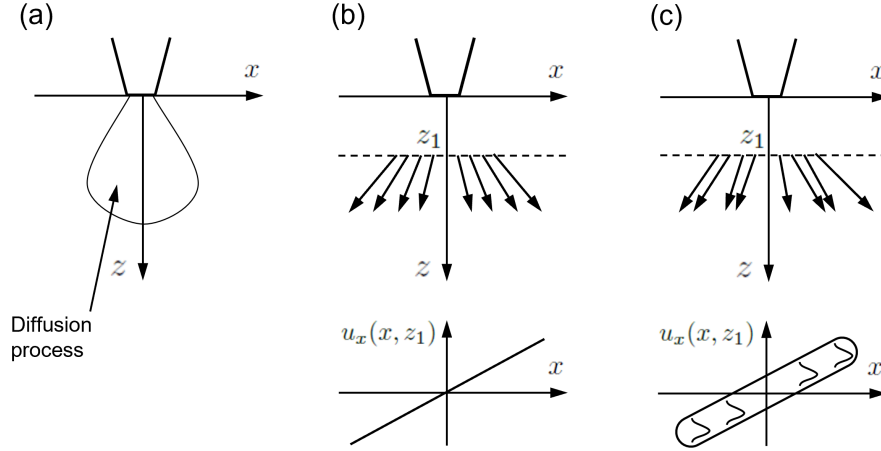


Figure 5.2: Particle motion mechanisms; (a) diffusion [198], (b) initial velocities with linearly increasing tangential components (Chapter 4), (c) hypothesis in this chapter.

equal to the average of the particle speeds $|\mathbf{u}|$ for narrow powder streams, and m_p is the particle mass.

The effective powder radius given by:

$$r(z) = r_0 + \tan(\theta)z \quad (5.2)$$

where r_0 should have a value be close to the nozzle opening radius and θ is the powder stream divergence half angle. Some properties of the PCD based on Eqs. 5.1 and 5.2 are shown in Fig. 5.3

Integrating Eq. 5.1 in polar coordinates results in the number of particles crossing a plane perpendicular to the powder stream axis. As expected, this value is constant due to mass conservation, and proportional to the mass flow rate. The value is given by:

$$n_p = \frac{\dot{m}}{u_z m_p} \quad (5.3)$$

The mechanism that produces the PCD described by Eq. 5.1 can be derived from a diffusion equation [198]. This is a fair approximation for small particles [212], where some particle collisions close to the nozzle might be taking place that can be modeled by a diffusion process. However, as seen in the high-speed video data in Chapter 4, most particles are

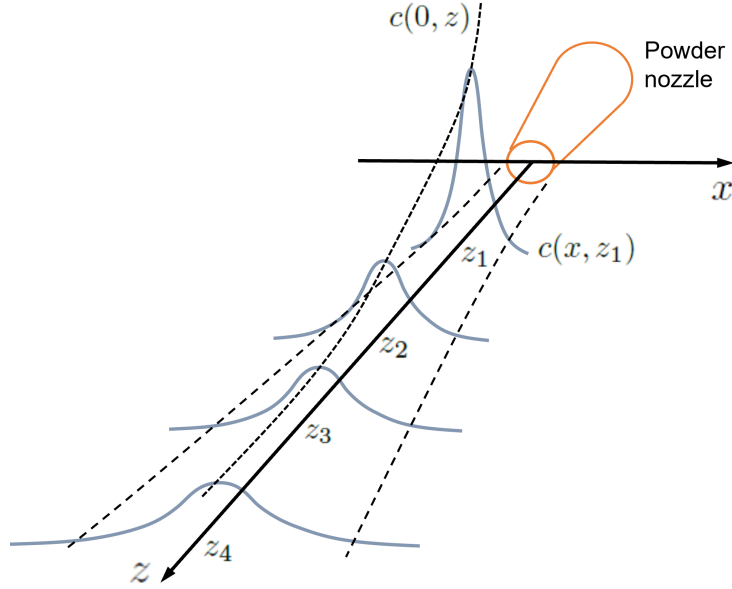


Figure 5.3: Powder PCD and some of its properties: symmetry about z , mass conservation (polar integral about z of $c(x, z)$ equal for all z -values), IRW, given by value of powder radius r such that $c(r, z_n)/c(0, z_n) = k$ (where k is a constant such as e^{-1} or e^{-2}) increases linearly with z downstream of the nozzle.

not colliding, especially away from the nozzle, and are seen to be spreading outwards. In the same study, to accurately couple the powder stream to a force field, a new mechanism was derived, in which an initial velocity field that reproduces Eq. 5.1 without a diffusion mechanism for the particles is given by:

$$u_r(r, 0) = u_z \tan(\theta) \frac{r}{r_0} \quad (5.4)$$

This was done by finding an initial particle speed distribution for the Eulerian continuous concentration distribution equation given in [212] and referenced by Lin in his original derivation of Eq. 5.1 [198], but without a diffusion term, such that the same solution is recovered. In this chapter, it will be shown that a model producing a linear dependence between tangential speed and x -position with some offset due to a probability distribution as shown in Fig. 5.2 (c) corresponds to considering the particle tracks as rays and having the same spatial and angular probability distribution that is used in some models of laser beam propagation [213, 214, 215, 216, 217].

A laser beam can be described via the Helmholtz wave equation or the Fresnel-Kirchhoff integral [218, 219]. One can solve for the electric field of a spherical wave in the paraxial approximation for a beam that has a small angle with respect to one of the coordinate axes. However, the solution using a real number on an axis for the source location produces a nonphysical electric field because its amplitude does not fall off quickly enough in the transverse direction, and therefore carries infinite energy in a transverse plane [219]. One can obtain a more physical solution for the electric field by using a complex source position, producing a real Gaussian factor hence the name Gaussian beam. This also corresponds to the electric field of a freely propagating laser beam. For a beam along the z -axis, this field (normalized to an amplitude of one) is given by [218]:

$$E(x, y, z) = \frac{w_0}{w(z)} \exp \left[-\frac{x^2 + y^2}{w(z)^2} + j\phi \right] \quad (5.5)$$

with $j = \sqrt{-1}$, $\phi = \arctan(z/z_R) - k(x^2 + y^2)/(2R)$ and $k = 2\pi/\lambda$.

The functions for the beam half width w and the beam radius of curvature R can be found from Eqs. 5.6 and 5.7.

$$w(z) = w_0 \sqrt{1 + \frac{z^2}{z_R^2}} \quad (5.6)$$

$$R(z) = z + \frac{z_R^2}{z} \quad (5.7)$$

where w_0 is the beam waist half width. The Rayleigh range, z_R , is given by:

$$z_R = \frac{\pi w_0^2}{\lambda} \quad (5.8)$$

where λ is the wavelength. This free space propagation solution uses the complex source position q given by:

$$\frac{1}{q} = \frac{1}{R} - j \frac{\lambda}{\pi w^2} \quad (5.9)$$

One can describe the propagation of a Gaussian beam by transforming this complex source by using [219]:

$$q_2 = \frac{Aq_1 + B}{Cq_1 + D} \quad (5.10)$$

where the subscripts 1 and 2 denote the initial and final source position and variables A to D are entries in $M = [A \ B; C \ D]$, which is referred to as an optics ray tracing propagation transfer matrix. In the matrix ; denotes the next lower row.

The intensity of the electric field $I = \varepsilon_0 c |E|^2 / 2$, for Eq. 5.5, is given as:

$$I(x, y, z) = I_0 \frac{w_0^2}{w^2(z)} \exp \left[-2 \frac{x^2 + y^2}{w(z)^2} \right] \quad (5.11)$$

where ε_0 is the vacuum permittivity and is included in I_0 . Note that the half width of the beam w is measured from where the laser is at e^{-2} of its peak intensity to its center line at some z -value. Note that the intensity half width at e^{-2} of its peak is equal to the e^{-1} half width for the electric field, due to the intensity being obtained by squaring the electric field.

A 3D model for a laser beam that uses rays projected from the xy -plane to represent the intensity of the beam, is described in [213]. The equivalent spatial distribution is given by Eq. 5.11 with $I_0 = 1$ [213] and the ray origins given by $I(x, y, 0)$. Note that Eq. 5.11 has the same form as Eq. 5.1 which is used to model DED-PF powder streams. The spectrum of the rays given in Eq. 13 of [213] based on the angles (θ_x, θ_y) or equivalently based on $(k_x, k_y) = k[\tan(\theta_x), \tan(\theta_y)]$ can be written as:

$$P_2(k_x, k_y) = \frac{w_0^2}{2\pi} \exp \left(-2 \frac{k_x^2 + k_y^2}{s_0^2} \right) \quad (5.12)$$

$$\Leftrightarrow P_1(\theta_x, \theta_y) = \frac{w_0^2 k^2}{2\pi \cos(\theta_x) \cos(\theta_y)} \exp \left[-2k^2 \frac{\tan^2(\theta_x) + \tan^2(\theta_y)}{k_0^2} \right] \quad (5.13)$$

with $s_0 = w_0/z_R$ which approximates θ_0 in [214] at small angles, $k_x = k \tan(\theta_x)$ and $k_0 = 2/w_0$.

Note that the ray spatial and tangential component distributions can be used directly as an initial condition for the particles in a Lagrangian simulation as done in Chapter 4. The significance of speed variation as well as the drag force on the particle due to the surrounding medium using this new model will be shown later via Lagrangian simulations in Section 5.3.3.

5.2 Theoretical and experimental methods

5.2.1 Particle tracking and trajectory extrapolation

In order to determine the behaviour of the particles in the powder stream, the python particle tracking code Trackpy [220] was used to extract path information from high-speed

video. The video was obtained by filming the powder stream produced by manually feeding SS 316L powder to a gravity hopper connected to a nozzle. The nozzle disperses the powder with a center-body before moving to a converging nozzle with an exit diameter of 0.9 mm, in order to produce the Gaussian distribution with a linearly increasing IRW as observed in the DED-PF literature and Chapter 4. The SS 316L powder used is from North American Höganäs (316 L-5320), item # 111903. The mass average diameter was determined to be 89 μm , measured using a Camsizer X2 from Retsch GmbH.

Trackpy uses the Crocker-Grier centroid-finding algorithm to find particles in a frame [221]. The settings used for finding the particle positions were the following: The frames were cropped to not include the top of the ultrasound array used to produce the force field as done in Chapter 4, an estimated particle size of 7 pixels (found by taking the square root of the avg. pixel area for particles found in Chapter 4, a minimum “mass” (brightness) value of 200 was used. The setting used for extracting paths were the following: A search range of 4 pixels/frame (approximate speed of particles) and a memory of 1 frame (number of frames particle does not have to be present in a frame) were used. The generated paths were filtered by not including short paths (less than 40 frames), and only including paths with particles with a mass variable (Trackpy dimensionless variable) between 500 and 2000, a size between 1 and 1.5 pixels and a circular eccentricity of less than 0.3.

Afterwards the paths are centered in x , rotated, shifted in z such that the nozzle position is at $z = 0$ and scaled by using the pixel size of 72.9 μm measured in Chapter 4. The rotation angle is calculated such that it undoes the offset between the x -averages of the Gaussian fits of the powder stream at the top and bottom of the sum of frames image as done in Chapter 4, which can happen due to camera misalignment. The paths are also filtered by checking that subsequent line segments formed by two subsequent particle positions have an angle of less than 3° (using the absolute value of their dot product) and do not change direction.

The paths are then fitted to a particle trajectory analytic model [222]. It is the analytic solution for a particle’s 2D trajectory taking into account gravitational acceleration and the drag force on the particle from the surrounding medium (still air) assuming a linear relationship with the particle’s relative speed (Stokes’ drag law). Its applicability was checked by computing the maximum Reynolds number (Re) for all feasible trajectories as described later in this section. For this drag law to be applicable, $Re \sim 1$. With these trajectory fits, one can calculate accurate particle statistics such as the angle of the path with respect to the x -direction at any z -value and extrapolate the particle paths up to the nozzle position, which is obstructed by the ultrasound array producing the force field for the data from Chapter 4 used in this chapter.

If the diagonal of the bounding box of the path to be fitted has an angle of 0.29° , corresponding to an aspect ratio of 5.0×10^{-3} , a straight line fit is carried out. This is because the fitting problem is ill posed; when the paths are too close to a vertical line, one can have a large range of solutions for the initial speed. For the fit and evaluation of the line, the axes are switched to prevent numerical errors due to high slope values.

To define a path, the following variables are required: the initial x_0 position, the initial velocity components u_{0x} and u_{0z} , and the drag factor dependent on the particle size k . It is assumed the particles all start at the nozzle z -location ($z = 0$). One can obtain these variables by minimizing the following:

$$f = \sum_{i=1}^N (h_i - z_i)^2 \quad (5.14)$$

where N is the number of points in a path, h_i is the modeled z -position for each point and z_i is the actual z -position for each point. The model z -positions can be found from the actual x -positions x_i by rearranging the equation for x in [222] to get t :

$$t_i = -\frac{1}{k} \log \left[1 - \frac{k}{u_{0x}} (x_i - x_0) \right] \quad (5.15)$$

where k is Stokes' law constant divided by the particle mass [222, 197]:

$$k = \frac{3\pi\mu d_p}{m_p} \quad (5.16)$$

where μ is the air viscosity, d_p is the particle diameter and m_p is the particle mass. Afterwards the t_i values are used to find h_i using the equation for z in [222]:

$$h_i = t_i \frac{g}{k} + \frac{1}{k} \left(u_{0z} - \frac{g}{k} \right) (1 - e^{-kt_i}) \quad (5.17)$$

where g is the gravitational acceleration. Note one can do the same minimization considering the x -locations, however Eq. 5.17 cannot be rearranged analytically for t . One can minimize f by optimizing the path variables for each path using the function `fmincon()` in MATLAB, using the ‘‘Trust region reflexive’’ algorithm [223] with a function tolerance of 1.0×10^{-8} . It was found that providing the gradient of f with respect to the path variables

to `fmincon()` produces a more accurate fit. This gradient can be calculated using the multivariable chain rule as follows:

$$\begin{bmatrix} \mathbf{Q}_{x_0} \\ \mathbf{Q}_{u_{0x}} \\ \mathbf{Q}_{u_{0z}} \\ \mathbf{Q}_k \end{bmatrix} = \begin{bmatrix} (\mathbf{h}_t \circ \mathbf{t}_{x_0}) \mathbf{f}_h^T \\ (\mathbf{h}_t \circ \mathbf{t}_{u_{0x}}) \mathbf{f}_h^T \\ \mathbf{h}_{u_{0z}} \mathbf{f}_h^T \\ \mathbf{h}_k \mathbf{f}_h^T \end{bmatrix} \quad (5.18)$$

where the variables in bold are 1 by N matrices, the subscript stands for partial derivation with respect to the subscript and \circ stands for element-wise multiplication. The matrix \mathbf{f}_h can be found as follows:

$$\mathbf{f}_h = 2(\mathbf{h} - \mathbf{z}) \quad (5.19)$$

Each entry of the other matrix derivatives are the element-wise derivatives of Eqs. 5.15 or 5.17. The optimization function was used with the following bounds:

$$-0.02 < x_0 < 0.02 \quad (5.20)$$

$$-0.5 < u_{0x} < 0.5 \quad (5.21)$$

$$0.0 < u_{0z} < 0.5 \quad (5.22)$$

$$1.0406 < k < 104.0625 \quad (5.23)$$

The bounds enforce for tracks that start close to the nozzle, and that they do not have a high starting velocity or positive z -velocity component. The bounds in Eq. 5.23 were calculated using Eq. 5.16 and particle sizes of 20 and 200 μm . The fits for 2168 paths of various lengths takes about 20 seconds in MATLAB.

The resulting paths were filtered as follows: paths with an initial speed ratio (u_{0x}/u_{0z}) of 5 or more or with an initial position x_0 further away than 2.5 mm from the nozzle were not used. The final number of paths used for powder stream statistics is 2043.

To check the low Re number assumption for the use Stokes' law, for each path fitted with the linear drag model, the travel time of the particle from $z = 0$ to the maximum measured z value (72 mm) from TrackPy was found by numerically solving Eq. 5.17 for t_i and using 72 mm for h_i using the function `fzero()` in MATLAB with a 0 to 1s bound. Afterwards this time is used to obtain the velocity components at the end of the path. The velocity components are given by [222]

$$u_x = u_{0x} e^{-kt_i} \quad (5.24)$$

$$u_z = \frac{g}{k} + \left(u_{0z} - \frac{g}{k} \right) e^{-kt_i}. \quad (5.25)$$

The maximum Re number for all tested paths using the velocity magnitude and air properties was 10. However, only 19 of the 1772 trajectories fitted with the linear drag model (the rest being the paths fitted with a line since they are close to vertical) had a value greater than 6.

5.2.2 Ray statistics from divergence angle and nozzle width

The e^{-1} IRW and divergence angle measured in Chapter 4 (and scaled to values considering e^{-2} IRW) corresponds to the half width w_m and $\tan(\theta_m) = dw/dz(w_m)$. Using these equations and Eq. 5.6, one can solve for w_0 and z_R using Eqs. 5.26 and 5.27.

$$w_0 = \sqrt{w_m^2 - \tan(\theta_m)w_m z_m} \quad (5.26)$$

$$z_R = w_0 \sqrt{\frac{z_m}{w_m \tan(\theta_m)}} \quad (5.27)$$

The divergence angle θ_0 equals $\arctan(w_0/z_R)$ since dw/dz approaches w_0/z_R as $z \rightarrow \infty$. The powder behaviour observed in Chapter 4 suggested that there is a linear function between speed and position normal to the powder stream axis at some distance from the nozzle exit. One would expect the slope of this line to become steeper as one gets close to the nozzle, as well as the coefficient of determination r^2 to approach 1 far away from the nozzle and approach zero when close to the nozzle.

The expected value of r^2 is given by [206]:

$$\mathbb{E}(r^2) = 1 - \mathbb{E}\left(\frac{SS_{res}}{SS_T}\right) = 1 - \frac{\mathbb{E}(SS_{res})}{\mathbb{E}(SS_T)} \quad (5.28)$$

where SS_{res} is the sum of squares of the sampled residuals (difference between predicted and measured data) and SS_T is the sum of squares of the sampled data. The assumption made for the last term is that samples from SS_{res} can be considered independent of samples from SS_T .

From Eq. 1 in [213] and Eq. 5.13 one can do a similar calculation as Eqs. A11-A15 in [213] and derive the probability density for θ_x given x with $k_1(z) = k/\sqrt{z^2 k_0^2 + w_0^2 k^2}$:

$$f_{\theta_x}(\theta_x|x) = \frac{1}{\sqrt{2\pi}k_1(z) \cos^2(\theta_x)} \exp\left(-k^2 \frac{\left[\tan(\theta_x) - \frac{x}{R(z)}\right]^2}{2k_1^2(z)}\right) \quad (5.29)$$

A similar result to Eq. 5.29 was also found in [214]; it is a shifted Gaussian along a vertical line with fixed x which is shown in Fig. 5.2(c). By inspection, one can see from Eq. 5.29 that the peak of the Gaussian happens when the argument of the exponent is zero, or when:

$$\tan(\theta_x) = \frac{x}{R(z)} \quad (5.30)$$

This a line with a zero y -intercept and a slope of $R(z)^{-1}$.

One can see from Eq. 5.11 that the probability density of x is:

$$f_x(x) = \sqrt{\frac{2}{\pi w^2(z)}} \exp \left[-2 \frac{x^2}{w^2(z)} \right] \quad (5.31)$$

With Eqs. 5.29 and 5.31, one can calculate the expected value of a random variable a using Eqs 5.32-5.34.

$$\mathbb{E}_{\theta_x}(a) = \int_{-\frac{\pi}{2}}^{\frac{\pi}{2}} a \cdot f_{\theta_x}(\theta_x|x) d\theta_x \quad (5.32)$$

$$\mathbb{E}_x(a) = \int_{-\infty}^{\infty} a \cdot f_x(x) dx \quad (5.33)$$

$$\mathbb{E}(a) = \mathbb{E}_x[\mathbb{E}_{\theta_x}(a)] \quad (5.34)$$

To calculate Eq. 5.28, one needs:

$$\mathbb{E}(SS_{res}) = \mathbb{E} \left(\sum_{n=1}^N [y_n - \mathbb{E}_{\theta_x}(y_n)]^2 \right) \quad (5.35)$$

and:

$$\mathbb{E}(SS_T) = \mathbb{E} \left(\sum_{n=1}^N [y_n - \mathbb{E}(y_n)]^2 \right) \quad (5.36)$$

with y_n being the measurements of the random variable $Y := \theta_x|x$ and the number of measurements $N \rightarrow \infty$. The exact calculation of these two expected values are given in Appendix I as a power series. To simplify the calculations, we present here the result in paraxial approximation, i.e., $\tan(\theta_x) \approx \theta_x$ corresponds to using the first term of the power series.

Under this approximation:

$$\begin{aligned}\mathbb{E}(SS_{res}) &= N \frac{k_1^2(z)}{k^2} \\ \mathbb{E}(SS_T) &= (N - 1) \left[\frac{w^2(z)}{4R^2(z)} + \frac{k_1^2(z)}{k^2} \right]\end{aligned}$$

Therefore, for $N \rightarrow \infty$:

$$\mathbb{E}(r^2) = 1 - \frac{\frac{k_1^2(z)}{k^2}}{\frac{w^2(z)}{4R^2(z)} + \frac{k_1^2(z)}{k^2}} = 1 - \frac{1}{1 + \frac{k^2 w^2(z)}{4R^2(z)k_1^2(z)}} \quad (5.37)$$

By defining $\theta_1(z) = \theta_0/\sqrt{1 + z^2/z_R^2}$ and using the paraxial approximation a second time for $k_1^2/k^2 \approx \theta_1^2/4$ this can be approximated by:

$$\mathbb{E}(r^2) = 1 - \frac{\theta_1^2(z)}{\theta_1^2(z) + \frac{w^2(z)}{R^2(z)}} = 1 - \frac{1}{1 + \frac{w^2(z)}{R^2(z)\theta_1^2(z)}} \quad (5.38)$$

It follows that $\mathbb{E}(r^2) \rightarrow 1$ for $z \rightarrow \infty$ and $\mathbb{E}(r^2) \rightarrow 0$ for $z \rightarrow 0$ in the paraxial approximation.

Eq. 5.38 explains the close to linear behaviour between sideways particle speed and distance from the nozzle center-line when far away from the nozzle as observed in Chapter 4 and spatial independence of this speed as expected from the ray representation of a Gaussian beam at the nozzle area.

5.2.3 Lagrangian particle simulation in the presence of a force field

The Gaussian beam representation (GBR) and its ray representation can also be used to calculate an initial condition in the 3D Lagrangian particle tracking model described in Chapter 4. This model can be used to calculate the sound pressure and resulting force field on the particles. By calculating the force field at a required particle location, one can perform Lagrangian particle tracking by computing particle paths from an initial to a final position at a required time interval. This can be done using a 4th order Runge-Kutta (RK4) method [171] with a given fixed time step.

The initial particle concentration at the nozzle position can be approximated by a group of particles, chosen such that their probability function approaches the particle

concentration function. A Monte Carlo (MC) simulation [202] can be run with enough particles to have a good estimate of the particle concentration. The model uses a speed standard deviation $|\mathbf{u}|_{STD}$ of 0.032 m/s as measured in Chapter 4, a gas particle drag force model and does not consider gravitational acceleration.

The initial particle spatial and tangent component distributions are generated using Eqs. 5.11 and 5.12 as shown in Algorithm 5. The algorithm uses the Box-Muller algorithm to produce one or two normally distributed values from X_n , sampled from a 0 to 1 uniform distribution [202]. A unit vector is then computed from the randomly sampled tangential components and then multiplied by the sampled speed $|\mathbf{u}|$.

Algorithm 5 Generation of initial positions and speeds for Lagrangian simulation

```

 $N \leftarrow 1$ 
while  $N \leq n_r$  do
   $r \leftarrow w_0/2\sqrt{\log(-2X_1)}$  ▷ Two variable Box-Muller for particle position
   $x(N), y(N) \leftarrow r \cos(2\pi X_2), r \sin(2\pi X_2)$ 

   $t \leftarrow s_0/2\sqrt{\log(-2X_3)}$ 
  ▷ Two variable Box-Muller for trajectory tangential components
   $\tan(\theta_x), \tan(\theta_y) \leftarrow t \cos(2\pi X_4), t \sin(2\pi X_4)$ 

   $x(N), y(N) \leftarrow x(N) + l_p \tan(\theta_x), y(N) + l_p \tan(\theta_y)$ 
  ▷ Calculate positions upstream of force field
   $z(N) \leftarrow 0.0$  ▷ 10 mm upstream of sound focus point

   $|\mathbf{u}| \leftarrow |\mathbf{u}|_{avg} + |\mathbf{u}|_{STD} \sqrt{\log(-2X_5)} \cos(2\pi X_6)$ 
  ▷ One variable Box-Muller to include measured speed variation

   $\tau = \sqrt{1 + \tan^2(\theta_x) + \tan^2(\theta_y)}$ 
   $u_{0x}(N) = |\mathbf{u}| \tan(\theta_x) / \tau$  ▷ Components divided by  $U$  (ray's direction cosines [216])
   $u_{0y}(N) = |\mathbf{u}| \tan(\theta_y) / \tau$ 
   $u_{0z}(N) = |\mathbf{u}| / \tau$ 

   $N = N + 1$ 
end while

```

Note that the w_0 and s_0 values are divided by two to match the variance given by Eqs. 5.11 and 5.12 when using the Box-Muller method which gives values for a standard

normal distribution [202]. The particles are projected forward a distance of $l_p = 44.2$ mm - 20 mm = 22.2 mm in a straight line to before 10 mm of the sound focus point, upstream of the sound interaction region described in Chapter 4, to produce a close match with the measured PCD with no applied force field. Running the Lagrangian simulation for longer distances can produce a mismatch between the measured and calculated PCDs with no applied force field due to air drag.

The Lagrangian simulation was run by simulating the force field due to a vortex sound field [147]. The sound field was produced by an array of ultrasound transducers running at different applied voltages. At 0 V there is no applied force field, and at 10 and 16 V the force fields produced had maximum absolute values of 2.92×10^{-9} and 7.47×10^{-9} N per particle as reported in Chapter 4.

The simulation results in Section 5.3.3 were run using 2 time steps for the runs at 0 V and 4 time steps for all other voltages. The number of paths calculated were 12.7×10^4 , 8.1×10^4 and 3.6×10^4 for the 0, 10 and 16 V simulations to achieve the required accuracy. The simulations were done using a Δr (radial sampling interval) value of 0.5 mm to compute the concentration function. The computing times for the simulations were 60, 72 and 34 minutes for the 0, 10 and 16 V simulations. A convergence study was used to show the above simulation parameters produce a converged solution, with an estimated error of less than 2% for the RK4 particle tracking and less than 4% for the MC simulation. All simulations in this report were carried out using a Dell OptiPlex desktop, with an Intel Core i7 3.6 GHz CPU processor and 16 GB of RAM.

5.2.4 The focusing sound field as an optical transfer matrix

As compared to the Fresnel-Kirchhoff integral [219], the GBR assumes the PCD is composed of rays without a phase component. This representation produces an accurate intensity distribution of the beam if the rays do not change direction to a large degree, such as in situations of high levels of refraction or in diffraction, where closely spaced rays would start to constructively or destructively interfere due to phase differences. Therefore the GBR is an accurate model of a Gaussian beam propagating in free space, or when considering propagation in an optical system where the paraxial approximation is adequate [214]. This means that after adequately modeling the powder stream with the GBR, one could use optical transfer matrix methods for Gaussian beams [219] to model the motion of the powder stream when subjected to a force field as long as the particle deflection is small.

For example, one can derive the particle motion in a radially symmetric force field where the force points towards the z axis and decreases linearly with distance to the z axis (close to l_{offset}) as shown in Fig. 5.1. The resulting equations of motion can be derived from Eqs. 4.4 and 4.2:

$$r_f = r_i \cos(\eta l_i) + \frac{\tan(\theta_i)}{\eta} \sin(\eta l_i) \quad (5.39)$$

$$\theta_f = \arctan[-r_i \eta \sin(\eta l_i) + \tan(\theta_i) \cos(\eta l_i)] \quad (5.40)$$

where r_i and r_f are the initial and final particle normal to the z axis and θ_i and θ_f are the initial and final angles with respect to the z axis. $\eta = \sqrt{F_a/(l_{offset} m_p u_z^2)}$, where F_a is a quarter of the peak force magnitude and u_z is the average downward component of the particle velocities. The parameter l_i is the length along which the sound field is considered to affect the particles and l_{offset} is half the length from the powder stream center-line to the location of peak force magnitude, this is the length where the force field might be considered to be linear as explained in Chapter 4. The last two parameters described are shown in Fig. 5.1.

Using Eqs. 5.39 and 5.40, and considering small particle deflections ($\tan(\theta) \approx \theta$), a symmetric sound radiation force field close to the axis of symmetry, due to a vortex sound field, can be modeled as an optical transfer matrix given by:

$$M_{GRIN}(l_i) = \begin{bmatrix} A & B \\ C & D \end{bmatrix} = \begin{bmatrix} \cos(\eta l_i) & \frac{1}{\eta} \sin(\eta l_i) \\ -\eta \sin(\eta l_i) & \cos(\eta l_i) \end{bmatrix} \quad (5.41)$$

This transfer matrix corresponds to a dielectric rod with a radially varying optical index profile given by Eq. 5.42, called a graded refractive index (GRIN) lens [224].

$$n = n_0 \left(1 - \frac{1}{2} \alpha^2 r^2 \right) \quad (5.42)$$

With a lens center-line index of diffraction $n_0 = 1$ and a parabolic dependence of $\alpha = 1/\eta$. Note the determinant of Eq. 5.41 is one. This means that since we can model the powder stream with representing a Gaussian [214], we can model DED-PF powder stream focusing as a Gaussian beam being calculated using a 2x2 transfer matrix, so called ABCD system. The pitch of the GRIN lens is defined as $\eta l_i/(2\pi)$. A pitch of 1/4 means that a point source on one side of the lens becomes a parallel ray to the z -axis on the other side [225].

The transfer matrix can be used to plot the PCD along z . Using w_0 and z_R by solving Eqs. 5.26 and 5.27, one can compute an effective λ for the powder stream, using Eq. 5.8.

The start of the laser propagation is at its waist, where R is considered zero, with q given by jz_R (solving Eq. 5.9) [226]. Then one can apply Eq. 5.10 repeatedly using ABCD = [1 l ; 0 1], which is the transfer matrix for free space propagation. This is computed at different equally spaced distances l along z , with the start of the beam considered at $z = 0$. When one reaches what is considered the upstream position of the force field, one can keep using Eq. 5.10, but using the following transfer matrix:

$$M_1(z) = M_{GRIN}(z - l_{fs})M_{fs}(l_{fs}) \quad (5.43)$$

where $M_{fs}(l_{fs})$ stands for the free space transfer matrix and l_{fs} is the distance from the start of the beam to the force field. Note that one can combine transfer matrices, by multiplying them, with the matrices closest to the source of the beam on the right [219]. One can apply this again downstream of the force field:

$$M_2(z) = M_{fs}(z - l_{fs} - l_i)M_{GRIN}(l_i)M_{fs}(l_{fs}) \quad (5.44)$$

to find q values at any position downstream of the force field.

At each z -position, one can compute the half width by solving for w using Eq. 5.9:

$$w = \sqrt{-\frac{\lambda}{\Im(1/q)\pi}} \quad (5.45)$$

and then use the normalized (such that its polar integral is equal to 1) version of Eq. 5.11 with $y = 0$, times Eq. 5.3:

$$I = \frac{2n_p}{w^2\pi} \exp\left(-2\frac{x^2}{w^2}\right) \quad (5.46)$$

One can then use Eq. 5.46 to compute the PCD along x . For a z -range of 0 to 140 mm, and an x -range of -15 to 15 mm, both with an interval of 0.1 mm, the above calculations take about 0.2 seconds in MATLAB.

Using the q value right after the force field, using $M_2(l_{fs} + l_i)$, one can compute the distance from the force field to the waist of the focused beam spot using [226]:

$$z_s = -\Re(q) \quad (5.47)$$

This is derived by writing the location of the focus q_f as $q + z$ and using the fact that at a focus point the radius R is infinite, meaning q_f should be imaginary, so $\Re(q) + z = 0$ [227].

The half width at the focus is given by [226]:

$$w_s = \sqrt{\frac{\lambda \Im(q)}{\pi}} \quad (5.48)$$

This is derived by noting that q_f is equal to $-j\Im(q)$ from the result for z_s , and solving for w using Eq. 5.9 [227]. An explicit expression for Eqs. 5.47 and 5.48 is given in [226]. Eqs. 5.47 and 5.48 are valid only for $z_s \geq 0$, i.e.; the beam waist is at the boundary of or after the GRIN lens.

5.2.5 Optimal powder focusing based on optical analog model

Eqs. 5.47 and 5.48 can be written explicitly and are given by [226]:

$$z_s = \frac{[1 + (l_{fs}/z_R)^2 - 1/(z_R\eta)^2] \sin(2\eta l_i) - 2l_{fs}/(z_R\eta) \cos(2\eta l_i)}{2z_R\eta \sqrt{\sin^2(\eta l_i) + [\cos(\eta l_i) - \eta l_{fs} \sin(\eta l_i)]^2/(z_R\eta)^2}} \quad (5.49)$$

$$w_s = \frac{w_0}{z_R\eta \sqrt{\sin^2(\eta l_i) + [\cos(\eta l_i) - \eta l_{fs} \sin(\eta l_i)]^2/(z_R\eta)^2}} \quad (5.50)$$

where w_s corresponds to the minimum powder spot size at a distance z_s from the sound force field. The propagation of the beam along an optical system can also be described graphically, using a y - \bar{y} diagram. A beam can be described by two rays where the rays should satisfy a Lagrange invariant [228]. The coordinates of the points in the lines and curves on the y - \bar{y} diagram are the heights of these two rays, parametrized by the z -distance along the optical system. An example of the diagram for the analog optical setup in this chapter is shown in Fig. 5.4 (a). In this case the two rays used are the divergence ray (height $\bar{y} = 0$ and angle $\bar{u} = \theta_0$) and the waist ray (height $y = w_0$ and angle $u = 0$) [228]. The diagram can be calculated by applying the same transfer matrices in Section 5.2.4 for the two rays being considered. The y - \bar{y} curve for a GRIN lens can be shown to correspond to a rotated ellipse [229, 230]. Its dimensions are also derived in [228].

Assuming that reducing the width of the powder nozzle ($\approx w_0$) will proportionally decrease the divergence angle [231] (z_R is approximately constant with respect to w_0), one can find the optimal w_0 and θ_0 values that minimize w_s . Note that Eq. 5.8 cannot be used directly since there is no physical analog to the light wavelength λ in this model. From inspection of Eq. 5.50 one can see that smaller w_0 values produces a smaller w_s value. Expanding the denominator of Eq. 5.50 one can also note that a larger z_R value gives a lower w_s value which corresponds to minimizing θ_0 for a fixed w_0 .

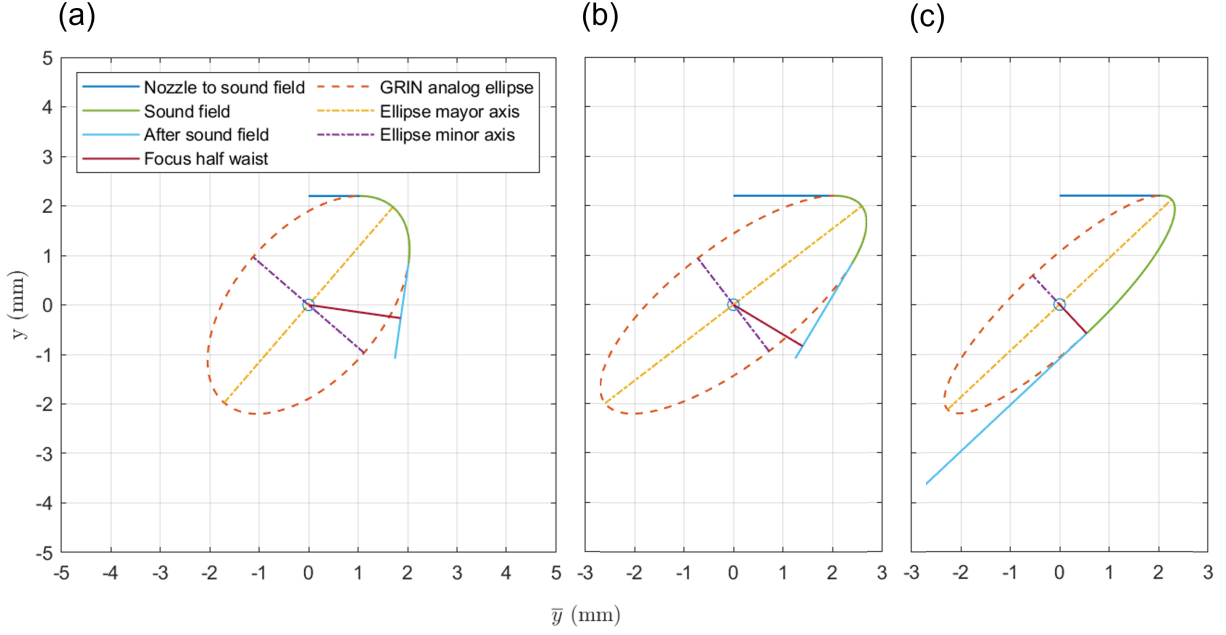


Figure 5.4: y - \bar{y} diagram corresponding to powder exiting a nozzle and interacting with a focusing sound radiation force field. (a) First case; $w_0 = 2.2$ mm, $z_R = 21.2$ mm, $l_i = 20.0$ mm, $l_{fs} = 10.0$ mm and $\eta = 59.4$ m⁻¹. (b) Case shown in a with higher nozzle to sound field distance ($l_{fs} = 19.7$ mm). (c) Case shown in (b) with higher applied transducer array voltage ($\eta = 92.0$ m⁻¹).

A plot of Eq. 5.50 for different l_{fs} and η values for cases where $z_s \geq 0$ is shown in Fig. 5.5. One can see a weak inverse relationship between l_{fs} and w_s at high η values.

This can also be observed in Fig. 5.4 (b), where the y - \bar{y} diagram is plotted for a larger l_{fs} value, which reduces the minor axis length of the ellipse. Note that for larger η values w_s is reduced, however the powder spot size should remain outside or at the edge of the sound field. As observed in Fig. 5.4 (c), increasing η moves the start of the y - \bar{y} diagram line after the GRIN lens ellipse toward the minor axis. One can find the beam waist of this beam from its closest (normal) distance from the line in the diagram to the diagram's origin, which corresponds to when this line exits the GRIN lens ellipse at its minor axis. This also corresponds to the beam's waist location where the beam focuses. Therefore, one should use the highest η (proportional to the applied ultrasound transducer voltage) possible as long as the focus point is outside or at the boundary of the sound field (η in Eq. 5.49 such that $z_s = 0$, shown in Fig. 5.4 (c)).

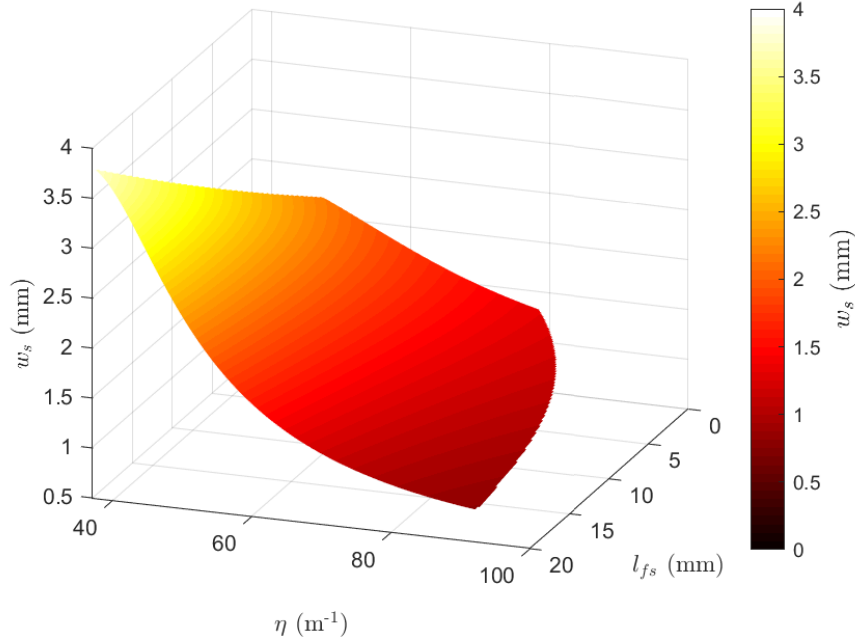


Figure 5.5: Powder waist half width downstream of applied sound field as a function of l_{fs} and η .

Taking into account material utilization, there is also a constraint on how long l_{fs} can be; the width of the beam at the start of the force field should be smaller than what is considered twice the force field’s “radius”. This is the point where the force field is not considered to be linear in the radial direction as described in Chapter 4. The required distance is given by using Eq. 5.6 and solving for z using $z = l_{fs}$:

$$l_{fs} = z_R \sqrt{\left(\frac{kr}{w_0}\right)^2 - 1} \quad (5.51)$$

where r is the effective force field radius and k is a factor smaller than one to take into account “limiting rays” [232], corresponding to the fact that the beam for some distance into the force field is still expanding. Therefore, to find the optimal l_{fs} and η values one should use Eq. 5.51 to find l_{fs} and then use this value to find η such that the numerator of Eq. 5.49 is equal to zero.

A more detailed analysis taking this into limiting rays requires η to be known [232]. This could be done finding the optimal l_{fs} and η values iteratively.

5.3 Results and discussion

5.3.1 Particle path statistical characteristics

The filtered and extrapolated paths are shown in Fig. 5.6. Every 100 paths were plotted in Fig. 5.6 (a) and every 20 paths were plotted in Fig. 5.6 (b).

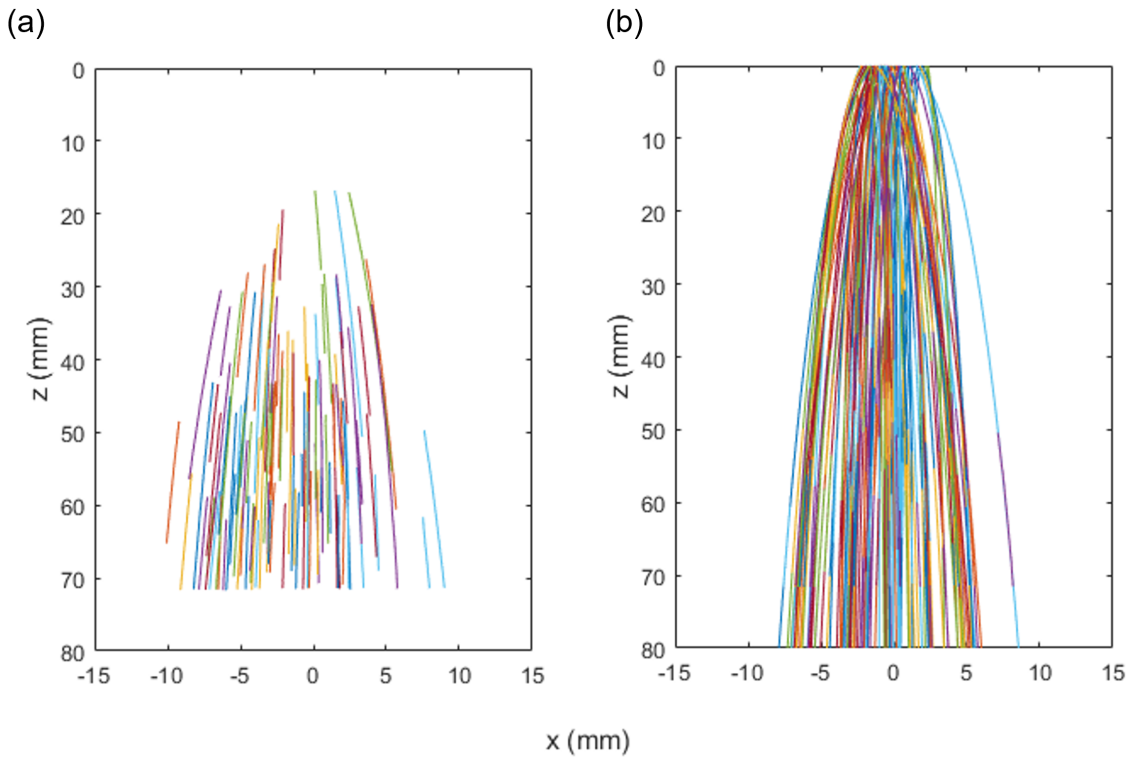


Figure 5.6: Particle paths from (a) high speed video. (b) Extrapolated paths.

The speed ratio (u_{0x}/u_{0z}) of the particle paths as a function of x -location at different distances from the nozzle are given in Fig. 5.7. Note the decrease in spatial dependence as the paths approach the nozzle location.

The increase of concentration data points at a speed ratio close to zero is due to fitting close to vertical paths with a straight line to prevent ill posed fitting are described in Section 5.2.1.

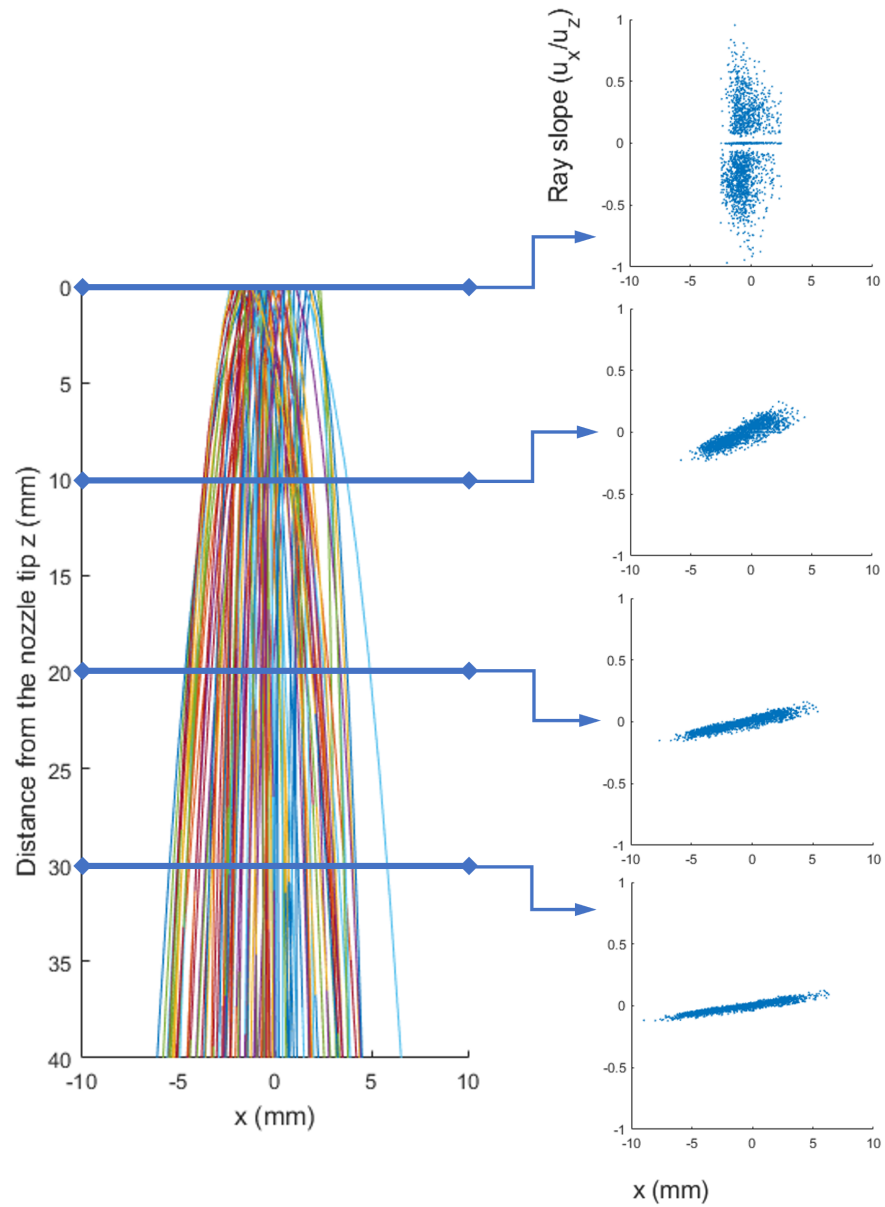


Figure 5.7: Speed ratio of the particle paths as a function of x -location at different distances from the nozzle.

The slope of the fitted lines and their r^2 values along z are shown in Fig. 5.8. One can see a decrease in the r^2 value of the fit as the paths approach the nozzle location, showing a decrease in spatial dependence.

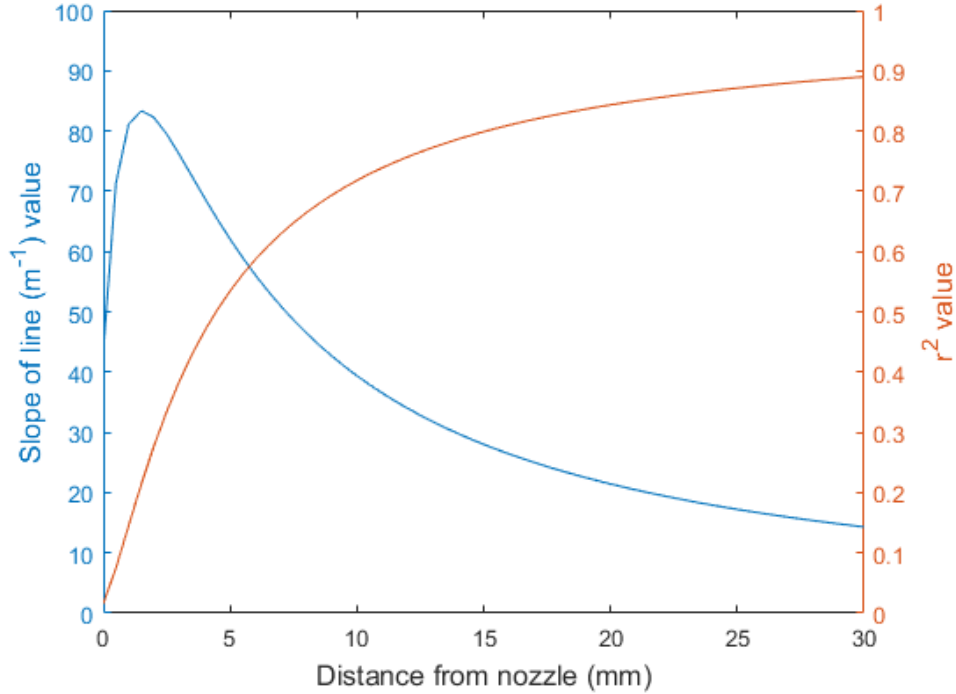


Figure 5.8: Measured slope of speed ratio as a function of x and measured r^2 value for different nozzle distances.

The distribution of speed ratios at the z -value of interest downstream of the applied sound field is shown in Fig. 5.9. One can see that disregarding spatial dependence, the distribution is observed to be close to normal, with a corresponding s_0 (twice the standard deviation, see Eq. 5.12) of 0.0864. This value is not sensitive to reducing the number of trajectories: using trajectories within x from -1.5 to 1.5 mm gives a value of 0.0860, and from -0.45 to 0.45 mm (corresponding to the nozzle diameter) gives a value of 0.0878. However, using these shorter ranges decreases the number of available trajectories for calculating the r^2 statistics.

5.3.2 Ray statistical characteristics assuming a GBR

To account for gravitational acceleration, using the extrapolated path variables, one can calculate the average downward speed of the particles downstream of the applied force field and how long they take to reach that location from the nozzle location. This gives

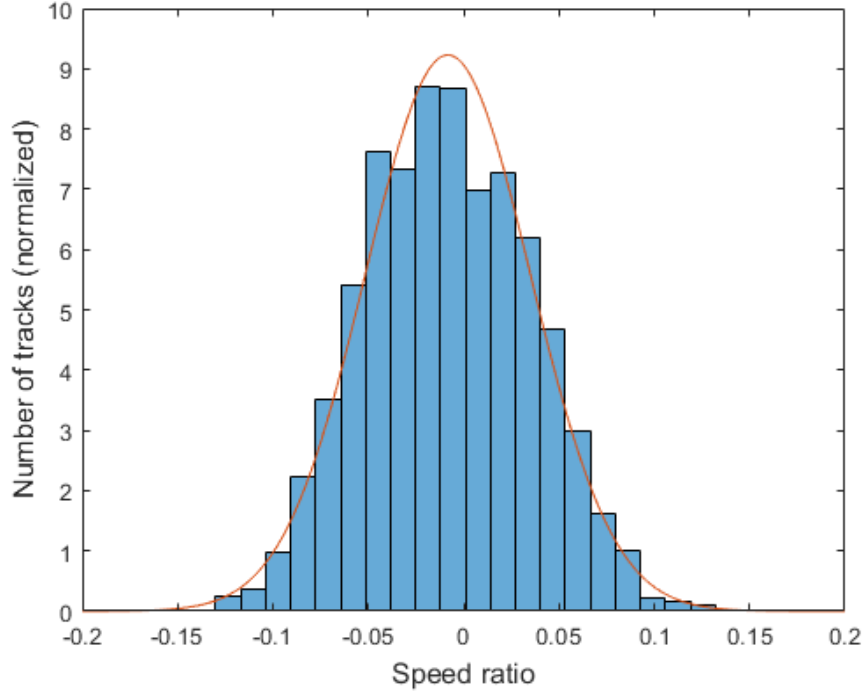


Figure 5.9: Speed ratio of the particle paths downstream of applied force field.

a distance of 44.2 mm. Then using the width and powder stream angle measured in Chapter 4, Eqs. 5.26 and 5.27 can be used to find w_0 and z_R . The e^{-1} intensity values used are 3.59 mm for w_1 and 3.77° for θ_1 , note that these values should be multiplied by $\sqrt{2}$ to obtain the e^{-2} intensity values. The values found for w_0 and z_R were 2.2 mm and 21.2 mm respectively, with a ratio s_0 of 0.1035. This corresponds to the measured s_0 value from the path angles downstream of the sound field (0.0864), with an error of 19.8%. The corresponding powder Gaussian beam geometry is shown in Fig. 5.10.

The expected slope and r^2 value of the x -location vs. speed ratio along z are shown in Fig. 5.11. This plot has values quantitatively close to the ones in Fig. 5.8 at a z -value of 44.2 mm, while comparing it to the measured values at 27.5 mm. These values correspond to the same powder stream conditions downstream of the applied force field. The plot also has similar values at their corresponding nozzle position (0 mm), however the intermediate values are different especially for the speed ratio slopes; this is expected since the measured paths in Fig. 5.8 are subject to gravitational acceleration which “warps” the slope and r^2

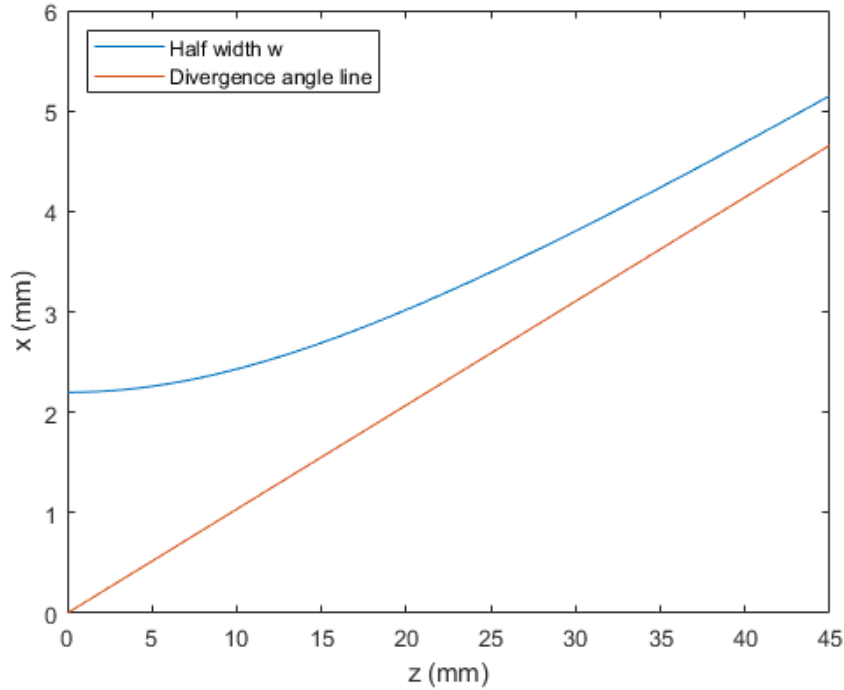


Figure 5.10: Powder GBR model geometry.

values towards $x = 0$ mm. One expects the speed ratio (u_{0x}/u_{0z}) to increase when x approaches zero since the u_{0z} values are expected to be lower at that location.

5.3.3 Lagrangian particle simulation

The calculated powder profile along the x axis downstream of the sound force field when using 10 V with the one at 0 V is shown in Fig. 5.12. For the force field corresponding to 0 V, since the paths extend to the z -location with no force being applied, there is a close match between the measured and simulated data as expected. There is also a good agreement with the simulated results at 10 V. The profile at 16 V with the one at 0 V is shown in Fig. 5.13. The peak PCD for 16 V of 1.8 particles/mm³ is still higher than the measured value of 0.9 particles/mm³, (a 100% difference) but it is still much lower than the result of 2.9 particles/mm³ (a 222% difference) when assuming a deterministic linearly increasing outward velocity component as assumed in Chapter 4.

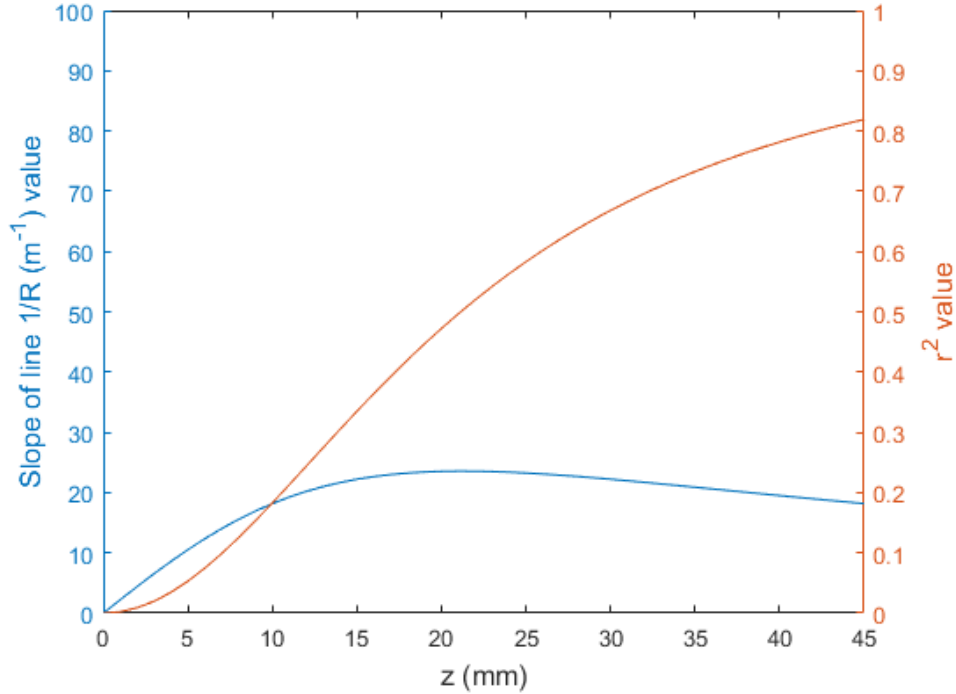


Figure 5.11: Slope of x vs. speed ratio (slope of line given by Eq. 5.30) and expected r^2 value (given by Eq. 5.38) of fitted line along z .

Other factors causing this discrepancy could be due to particle collisions and/or air drafts present when recording the high-speed data, which had to be minimized with an enclosure as described in Chapter 4.

A comparison of the e^{-1} powder widths are shown in Fig. 5.14. As expected, the closer PCD profiles seen in Figs. 5.12 and 5.13, produce a closer match between the measured and calculated powder widths for all voltages when using the GBR model, compared to the linearly increasing outward velocity component model in Chapter 4.

Using the Lagrangian simulation, one can check the effect of each phenomenon modeled on the final particle concentration, as shown in Fig. 5.15. There is no clear difference seen in Fig. 5.15 (a) between the full Lagrangian simulation and the simulation without a standard deviation of the particle speed or without drag, except for the expected 4% variation at the concentration peak due to the number of particle paths used in the MC model. However, there is a slight decrease in the peak concentration above 4% for the case of no drag. This

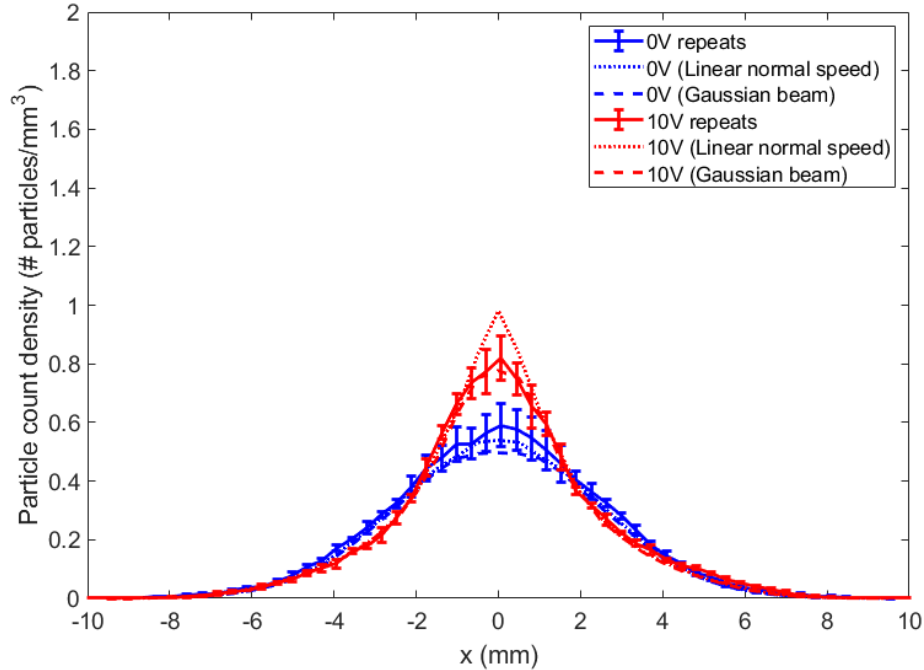


Figure 5.12: Powder profile along x downstream of the sound force field when using 0 and 10 V.

is shown more clearly using a log scale for the y -axis, as shown in Fig. 5.15 (b), where there is an increase in the concentration in the tails of the PCD. This is explained by the fact that with no drag force, the particles are expected to focus less due to less drag force applied to the particles in the same direction as the focusing force field. For the speed standard deviation measured, the particle size density, particle speeds, and the 20 mm sound interaction length being considered in this setup, the effect of the standard deviation and drag is not significant.

The speed variation might not be a significant factor in the shape of the PCD for the following reason; although the particle's deviation in a focusing force field approximately depend on their downward speed squared (see Chapter 4), the change in deviation will decrease towards the center of the powder stream, where the particles are not affected by the field. If a particle that is moving on the powder stream center-line, has a deviation in its speed, and it is not affected by the force field, it will reach the same location regardless of the speed variations.

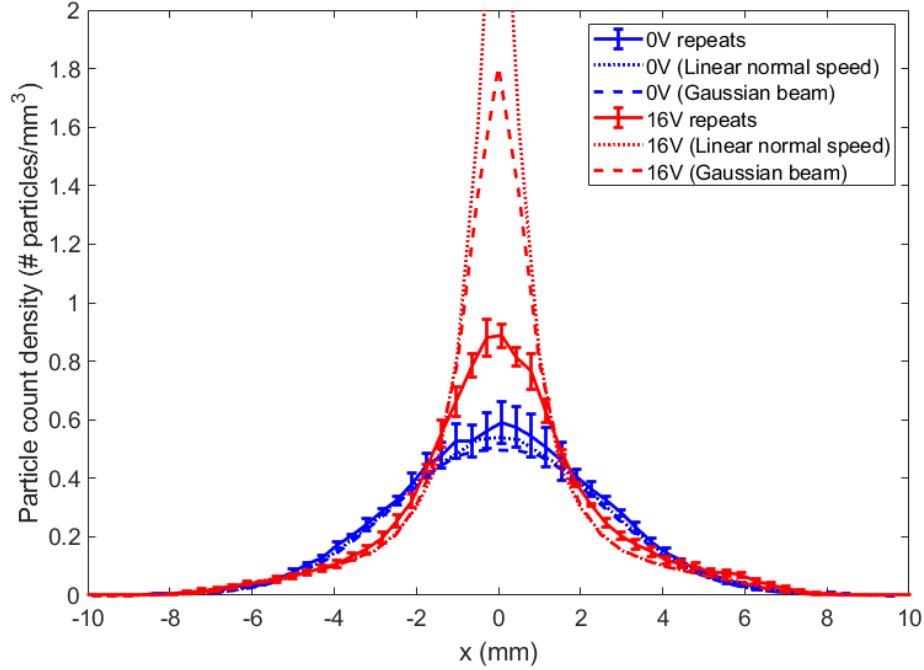


Figure 5.13: Powder profile along x downstream of the sound force field when using 0 and 16 V.

5.3.4 Powder focusing modeled as an optical system

The calculated powder profile and width along z when an external sound force field using 0 V is applied is shown in Fig. 5.16. As seen in Fig. 5.16 (c), the width increases linearly along the z -axis at large values of z , as suggested in the DED-PF literature [34]. The calculated powder profile with the measured powder profile is shown in Fig. 5.17. The recorded powder profile is in close agreement with the simulated profile up to about $z = 35$ mm but there is less agreement for higher values of z . This might be due to gravitational acceleration of the particles.

The calculated powder profile and width along z at 10 V is shown in Fig. 5.18. As seen in this model with this force field, one can predict a “shallow” focus, where the width and particle concentration change slowly along z , corresponding to the particle’s angles with respect to the powder center-line on average being close to zero. This is seen in Figs. 5.18 (b) and (c). The calculated powder profile is compared with the measured powder profile

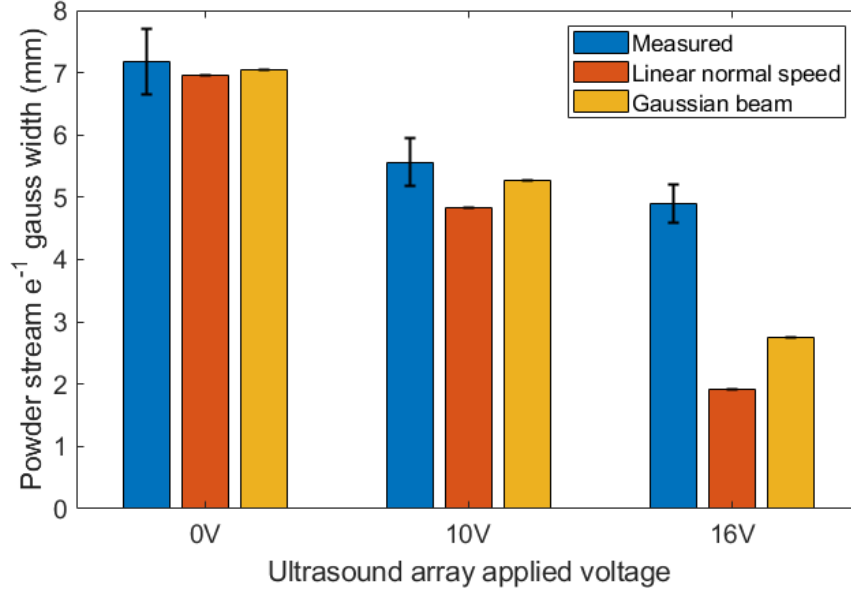


Figure 5.14: Comparison of measured powder stream widths and simulated powder stream widths.

as shown in Fig. 5.19. For this force field strength corresponding to 10 V there is close agreement between the simulated and measured data. Note that since particles are moving on average close to parallel to the powder stream center-line, the effect of gravitational acceleration should be less noticeable.

The calculated powder profile along z at 16 V is shown in Fig. 5.20. The calculated powder profile is compared with the measured powder profile in Fig. 5.21. The model predicts a sharp increase in concentration to $5.6 \text{ particles/mm}^3$ at $z = 59 \text{ mm}$. Comparing this result with the experimental data in Fig. 5.21 (b), the concentration peaks at about 1 particle/mm^3 and decrease downstream. The main cause of this discrepancy is the fact that the experiment carried out in Chapter 4 had an initial e^{-1} powder stream width of $7.2 \text{ mm} - 2(20.0)\tan(3.77^\circ) \text{ mm} = 2.6 \text{ mm}$, compared to a force offset width of about 2 mm (see Chapter 4), corresponding to the distance from the powder stream center-line where the force field can be assumed to be linear.

This means that the GRIN lens model is overestimating the amount of focusing for particles farther away than 1 mm from the center-line, producing a higher concentration at the focus point.

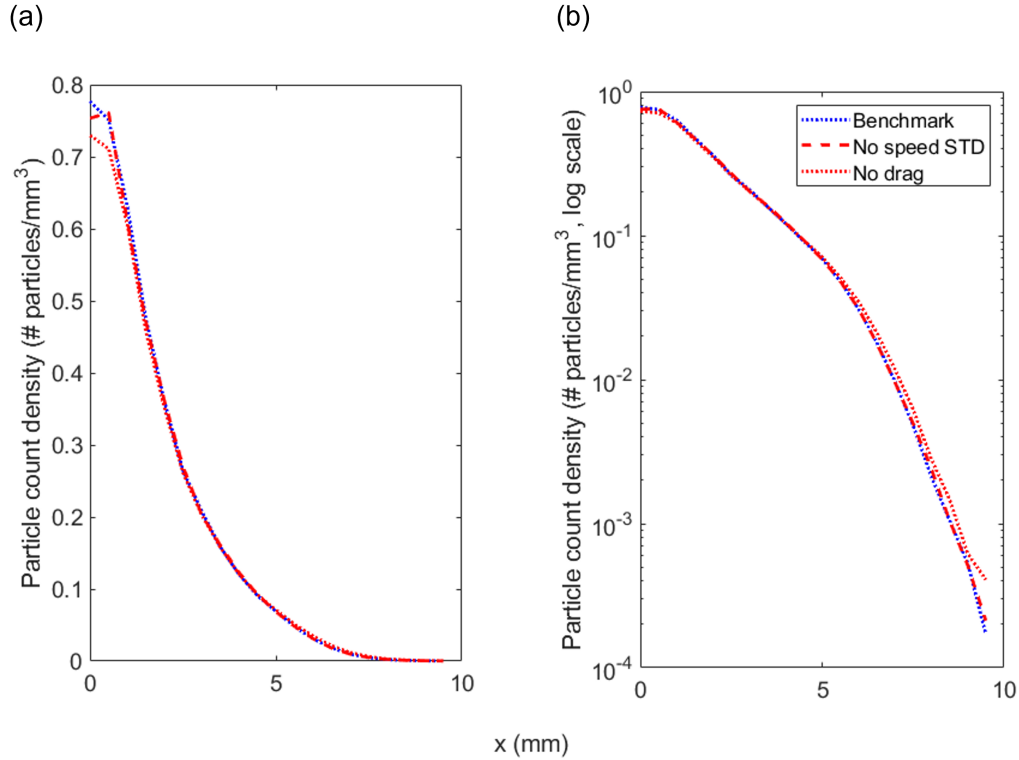


Figure 5.15: Powder profile along x downstream of the sound field considering speed standard deviation (STD) and air drag, only considering drag or considering only speed STD. (a) Using a y -axis linear scale and (b) a logarithmic scale.

Other factors causing this discrepancy could be due to the small-angle tangent approximation used for the GRIN lens analog model (Eq. 5.41), particle collisions and/or air drafts present when recording the high-speed data reported in Chapter 4.

A summary of the obtained parameters for the three simulations is shown in Table 5.1. The peak concentration was the maximum concentration after $z = 50$ mm and the powder width location is defined as the distance from downstream of the force field to the powder “beam” waist. Note that the model indicates that using 16 V one may achieve a waist width smaller than the initial width $2w_0$ of 4.4 mm. The peak concentrations downstream of the force field ($z = 44.2$ mm) shown on Table 5.1 closely agree with the Lagrangian model, with a percent error with respect to the Lagrangian model that may be due to the expected error due to the random sampling of the particle paths or because a speed standard deviation and air drag is considered in the Lagrangian model.

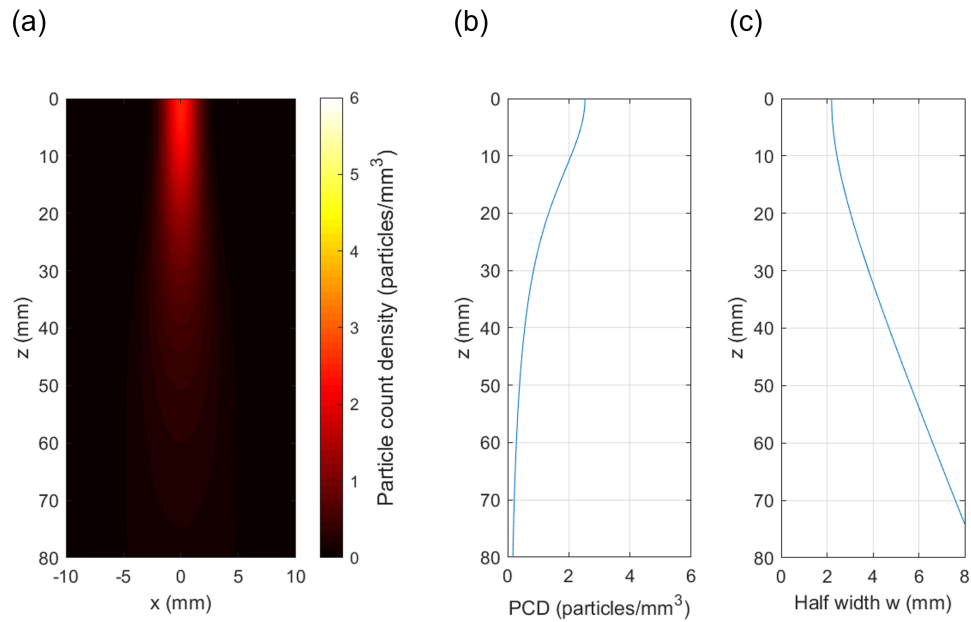


Figure 5.16: (a) Powder profile, (b) concentration at center-line along z and (c) half width at center-line along z , all at 0 V.

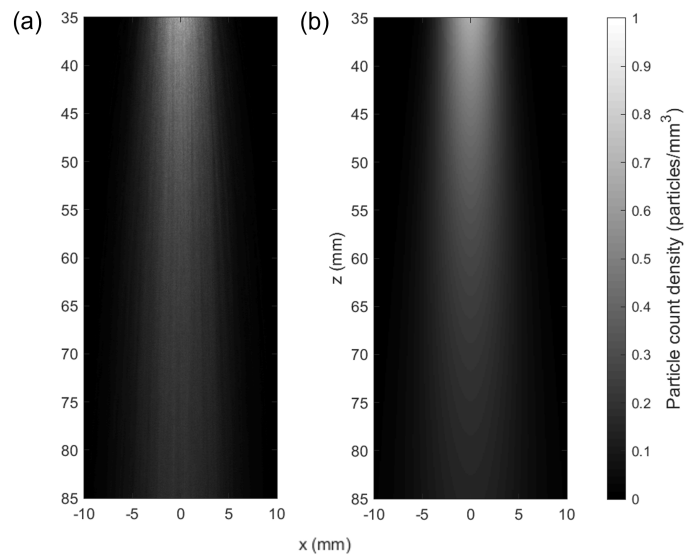


Figure 5.17: (a) Measured and (b) calculated powder profiles at 0 V.

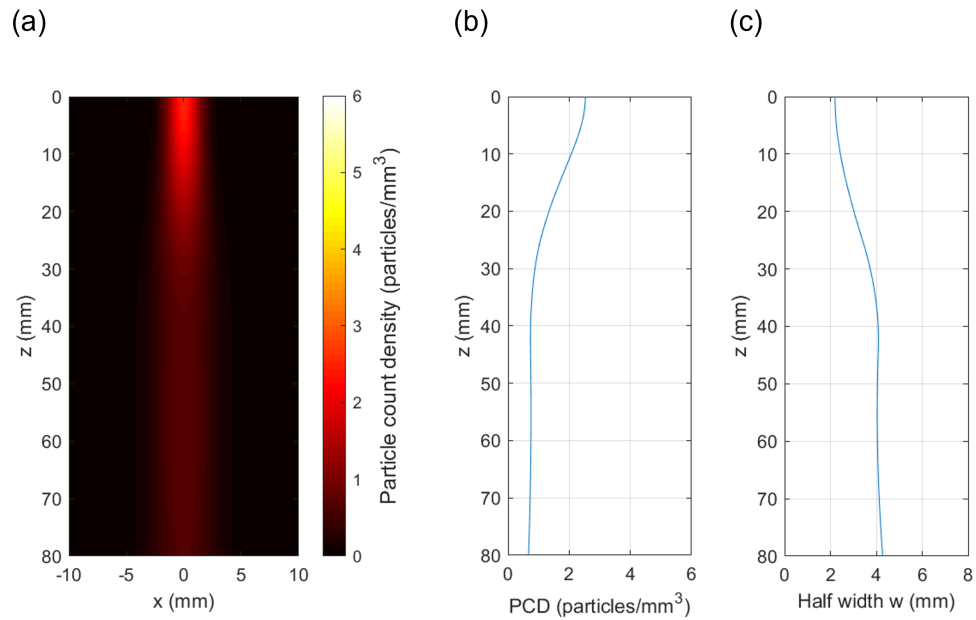


Figure 5.18: (a) Powder profile, (b) concentration at center-line along z and (c) half width at center-line along z , all at 10 V.

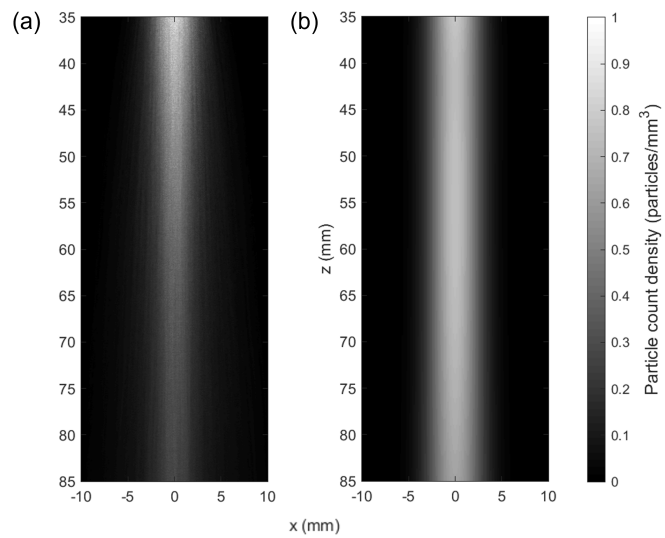


Figure 5.19: (a) Measured and (b) calculated powder profiles at 10 V.

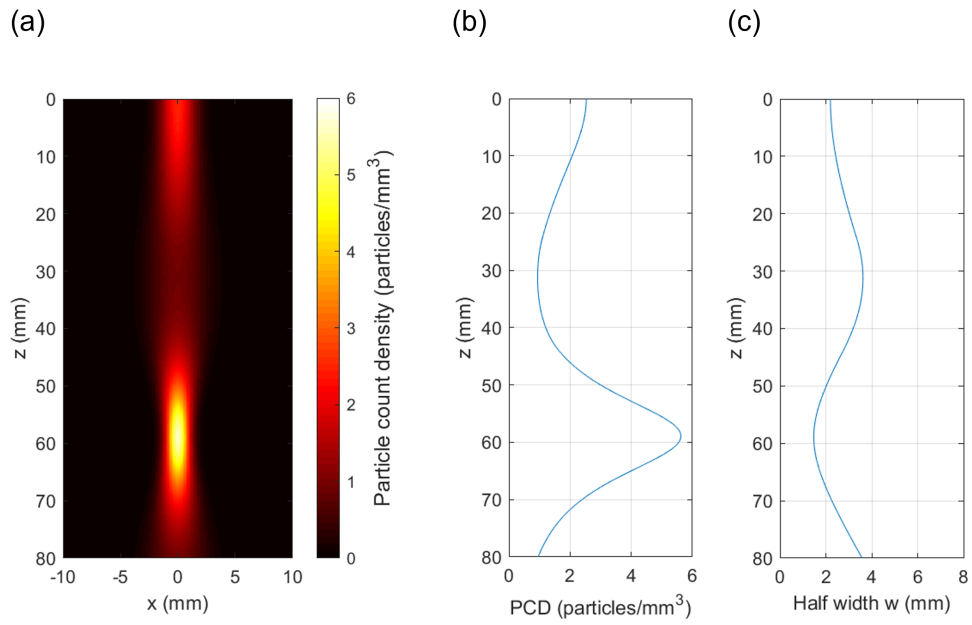


Figure 5.20: (a) Powder profile, (b) concentration at center-line along z and (c) half width at center-line along z , all at 16 V.

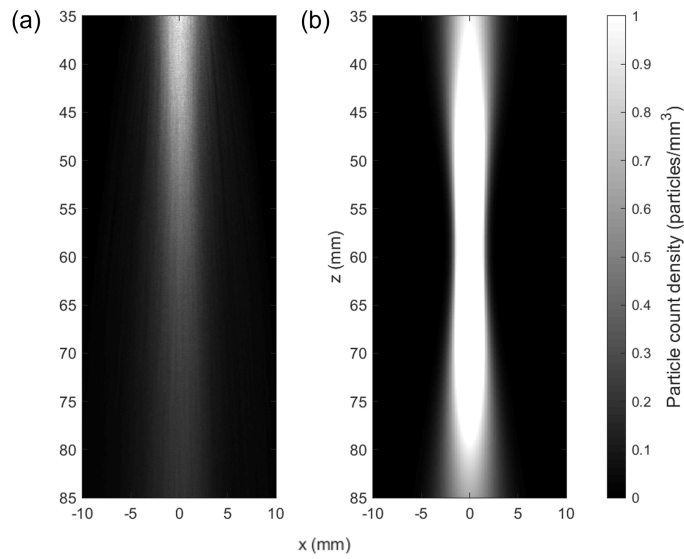


Figure 5.21: (a) Measured and (b) calculated powder profiles at 16 V.

Table 5.1: Predicted powder stream parameters from optical analog computations and percent error peak particle concentration with respect to Lagrangian model

Applied voltage (V)	Force GRIN lens pitch	Powder waist location (mm)	Powder waist width (mm)	Peak concentration (particles/mm ³)	Concentration downstream of force field (particles/mm ³)	% error w.r.t Lagrangian simulation
0	0.0	NA	NA	NA	0.47	-4.4
10	0.12	11.0	8.1	0.75	0.73	-5.9
16	0.19	14.7	3.0	5.6	1.65	-8.9

As an example of the powder waist width that may be achieved using a particular force field, using the same w_0 and z_R values used in the results, Eq. 5.51 to find l_{fs} and then using this value to find η such that the numerator of Eq. 5.49 equals to zero, one obtains the values shown in Fig. 5.4 (c). The η was found using the function `fzero()` in MATLAB, with an initial guess of 70. The assumed k value was 1 and the force field radius was assumed to be 3 mm.

This produces a waist width of 1.6 mm at the force field boundary, which is 2.75 times smaller than w_0 , equal to 4.4 mm. This corresponds to a GRIN lens pitch analog of 0.29, a peak particle concentration of 19.1 particles/mm³. The η value corresponds to an ultrasound array applied voltage of 25 V, assuming that the particle applied force F_a for the definition of η is proportional to the applied voltage squared (see Chapter 4), and the η value is 59.4 m⁻¹ at 16 V.

5.4 Summary

A model that more accurately predicts the behavior of a powder stream, with similar characteristics to the ones in DED-PF, when subject to a focusing force field was described. The model uses a Gaussian distribution for the initial particle positions, and a Gaussian distribution for the normal component of the initial particle velocities. The following conclusions can be drawn from this work and the Gaussian ray representation applied to powder stream modeling:

- The model closely matches the initial conditions seen in the extrapolated particle tracks that are close to the nozzle, with normally distributed normal velocity components, and close to zero spatial dependence. The sideways speed standard deviation calculated using particle trajectories and assuming the novel GBR model, only considering the final PCD from all the particles, match within 20%
- Both the slope of the angle of the trajectories with respect to the z axis as a function x and the r^2 values measured from the trajectories and derived from the model are similar towards larger z values (Figs. 5.8 and 5.11) when the effect of gravitational acceleration is less pronounced
- The model follows mass conservation
- At values far from the nozzle the IRW in this model approaches a linear function with respect to z , as seen in the experimental data
- The model also predicts a parabolic function of the form $w = w_0 + az^2$, where a is a fitted constant, for the region close to the powder nozzle as observed in [33]. This can be seen by computing the first two terms of the series expansion of Eq. 5.6 at $z = 0$, yielding $w \approx w_0[1 + z^2/(2z_R^2)]$
- The model can also be used to predict a minimum achievable powder spot width when an external symmetric force field is applied to the powder stream. It can be used to more quickly compute the PCD, using an optical system analog and can be used to predict what factors in the DED-PF powder feed affect the minimum powder spot width
- When the assumption of a normally distributed sideways particle speed is implemented as a Lagrangian model, it predicts with more accuracy the PCD downstream of the field and the observed e^{-1} intensity widths (Figs. 5.12 to 5.14)

- The above Lagrangian model with different force field magnitudes was then compared with the novel GBR model; the percent error of the peak particle concentration downstream of the force field between the Lagrangian model and the GBR model was below 6% at 0 and 10 V and below 9% at 16 V (Table 5.1)
- The calculation of the PCD using the new GBR model takes 0.2 seconds in MATLAB, compared to a minimum of 34 minutes (16 V case) for the converged Lagrangian simulation written in C++
- Both Lagrangian and GBR simulations still deviate from the measured concentrations at higher forces (corresponding to 16 V); this might be due to inaccuracies in the measured values used to fit the model, particle collisions and/or air drafts present when recording the high speed data, which had to be minimized with an enclosure as reported in Chapter 4. In the case of the laser propagation model, the inaccuracy of the model for large applied force fields (when using 16 V) might be related to the large width of the powder stream upstream of the sound with respect to the linear range of the sound assumed in the analytic derivation of the particle paths done in Chapter 4. This discrepancy could be reduced when simulating an initially narrower powder stream or force field with a different radial profile. More experimental data and a Lagrangian model with particle collisions could be used to investigate this hypothesis
- The Lagrangian simulation was used to determine that Gaussian speed variations and air drag (only due to the force field moving the particles) do not significantly affect the PCD for the speed standard deviation and divergence angle measured
- Better simulation results are expected when the initial powder stream width is smaller than the force field offset width (see Chapter 4). Better predictions should also be possible when modeling powder streams with higher speed particles, normally used in DED-PF equipment, where the effect of particle gravitational acceleration is less significant. In this case one could also obtain the w_0 and z_0 parameters using two stream widths at two different z -values instead of using Eqs. 5.26 and 5.27

Chapter 6

Ultrasound Particle Lensing Tailored for LDED-PF

6.1 Introduction

Additive manufacturing (AM) has enabled the manufacture of high-complexity parts that have not been possible to produce with conventional manufacturing methods. However, the high interdependence of AM process parameters makes the prediction of part geometry and material properties difficult. In order to increase the industrial adoption of AM the reliability of the resulting part geometry and material properties needs to be increased. This has been addressed in the LDED-PF process, in particular by the use of close-loop or feed-forward control [233, 234].

Another possibility for increasing the reliability of AM processes is to increase the number of AM process parameters, as long as their interdependence to current parameters is low, in order to increase process control. For example, by controlling the powder stream in LDED-PF as reported in this chapter. Further challenges will arise from the commercial need for printing large-scale and high-performance components. This will require LDED-PF machines that have high-deposition rates and the flexibility of retaining or even reducing the feature resolution found in smaller LDED-PF machines [235].

Power stream control has been applied in other fields such as microfluidics to levitate or sort particles using electrostatic [185], optical [186], or sound radiation forces (acoustofluidics) [147, 144]. For focusing a powder stream in DED-PF, besides the current nozzle's geometric and aerodynamic focusing with fixed powder stream spatial properties, there are

published methods that make use of electromagnetic fields. One configuration employed permanent magnets [187], that would induce an eddy current in the particles to focus them before reaching the build plate. However, this configuration is likely not suitable for the powder used for DED-PF, mainly because the amount of force due to induction depends on the relative speed of the particles and the magnets. A higher speed means there is less interaction time between the particle and the electromagnetic force. Also, the degree of focusing is highly dependent on particle size for the same applied magnetic field. Another related method using magnetic fields that can increase catchment efficiency is described in [183], where a solenoid was used on the underside of the built plate opposite to the nozzle. This setup demonstrated control of catchment efficiency for ferrous and nickel-based alloys. This method is limited by the types of alloys that can be used and the low magnetic field available at the melt pool when the part is tall.

In Chapter 4, a novel method to control the powder stream in DED-PF using sound radiation forces (SRF) was proposed. This technology is referred to as ultrasound particle lensing (UPL). Some of the features of UPL technology are as follows:

- Uniform focusing independent of particle size for DED-PF relevant range of sizes
- Higher particle focusing at the same sound intensity for lower density alloys
- Although the applied force is independent of downward speed compared to eddy current focusing, the degree of focusing is inversely proportional to the particle's downward speed squared; this is because the higher speed means the particle is affected by the force field for a shorter amount of time
- Simplified powder nozzle (a copper tube) and expected lower internal channel erosion [236]
- Solid-state equipment; the powder stream focal length and cross-sectional profile are no longer fixed by the nozzle geometry and can be controlled digitally and changed in-situ. This is particularly useful for multi-resolution printing; large parts can be printed quickly using a large powder spot size and the spot size can be reduced in sections of the part where higher resolution is needed. This may be useful for high-deposition rate DED-PF systems
- Response time in the order of the time it takes for the new sound waves to move from the transducer to the powder stream, in the order of the UPL ultrasound transducer array radius over the medium sound speed, $\approx 0.125/341 = 0.4$ ms for the setup described in this chapter. This may be particularly useful for DED-PF close-loop or feed-forward control

6.2 UPL technology applied to powder stream control in LDED-PF

A possible implementation of UPL in a LDED-PF machine using lasers around a coaxial powder nozzle is shown in Fig. 6.1. One can see in Fig. 6.1(b) the axisymmetric averaged sound pressure (ASP) field and force isosurface. The force field along the x -axis corresponding to the red line in Fig. 6.1(b) is shown in Fig. 6.1(c).

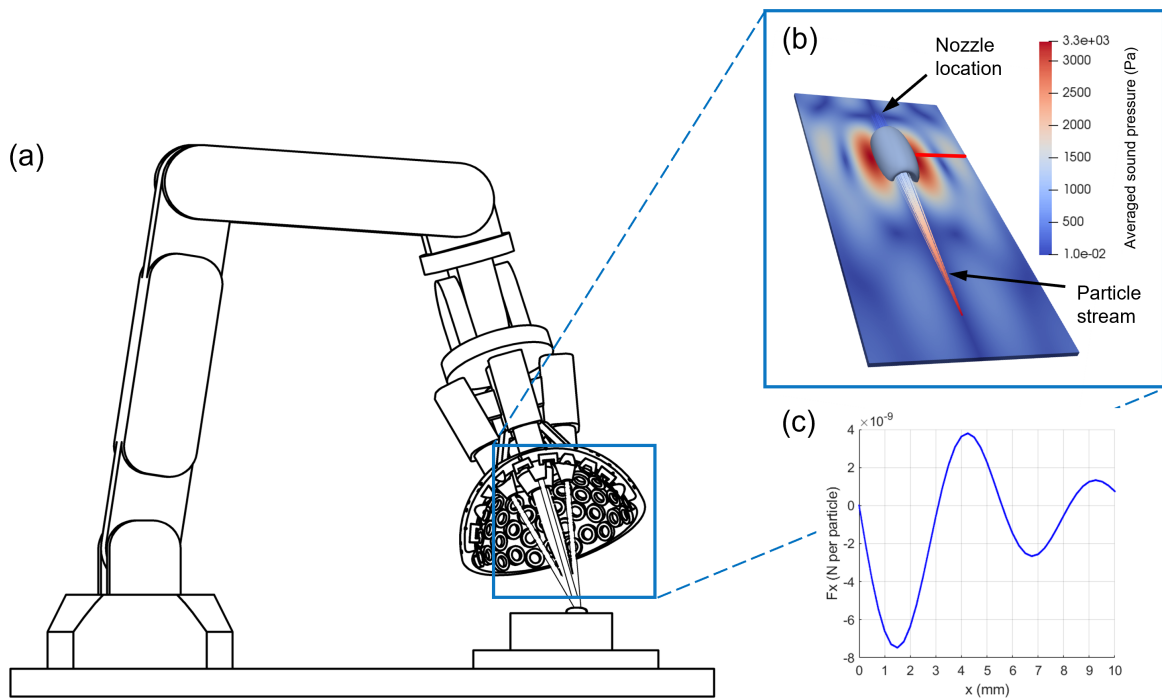


Figure 6.1: (a) Possible LDED-PF setup. (b) Close-up showing sound field ASP and sound radiation force isosurface at a value of -4.0×10^{-9} N per particle. (c) Sound radiation force in the x -axis direction along the red line in (b). Sound field simulation parameters are the same as in Fig. 4.2.

The main factor that determines the allowable distance between the build plate and the powder nozzle, which does not affect the track geometry, is the size of the sound field wavelength which is directly related to the transducer operating frequency [196]. The current phase control setup described in Chapter 4 and used in this chapter does not

allow for finer control of the force profile; the effective lens height and width ratio is approximately constant with transducer frequency. Independent control of the effective lens height and width may be done by adjusting both transducer phase and amplitude, using a Field Programmable Gate Array (FPGA) as described in [237] for example. The required transducer amplitudes and phases may be generated from a required force field profile using the angular spectrum method [238, 48], that can simulate curved transducer arrays [239, 240, 241], and can also account for sound non-linearity [47] when a high-intensity sound field is required [242, 243].

As mentioned in Chapter 4, UPL technology can also be used to change the cross-sectional area of the powder stream and deflect the powder stream by a small angle. This could be modeled using the Gaussian beam representation (GBR) of the powder stream described in Chapter 5 and the tensor ABCD law for predicting the deflection of Gaussian laser beams in 3D [244]. UPL technology may also be used to apply sound in the vicinity of the cooling track; this could be used for controlling metal microstructure [245, 152, 246] or residual stress [247]. This would overcome the issues in some of the techniques in the literature due to fixturing, or from trying to apply the sound field from the build plate, where the properties of the propagated sound that reaches the track depend on the shape and wall thicknesses of the part being built. These may be significant issues when the part being built is large.

From this point forward in this chapter, the naming convention for different LDED-PF setups described in Section 2.1.3 will be followed. In this naming convention, the setup is named “A-B”, where A is the component present at the center axis (laser (L) or powder nozzle (P)), and B is the setup that is used in the annular region (continuous (C), number of components, or undefined number (N)).

As explained before in Chapter 4, UPL technology may be used in a coaxial arrangement (L-C) by changing the topological charge (m) of the vortex field to a value greater than one [148], or for three and four-jet nozzle setups in a coaxial arrangement (L-3, L-4) [194], by generating more than one vortex sound field in the same working area [151]. This can also be done using automatic differentiation [248], which is also used within the sound field simulation program described in Section 6.3.1, in order to quickly and accurately compute the related SRF field. Multi-jet L-N arrangements are less susceptible to nozzle tilt compared to L-C arrangements [195]. Note that an L-C arrangement would require the nozzle to convey the powder stream in a direction parallel to the nozzle center-line, for the sound to focus it afterward and allow for variable focal length. Three possible LDED-PF arrangements can be seen in Fig. 6.2 [249, 250].

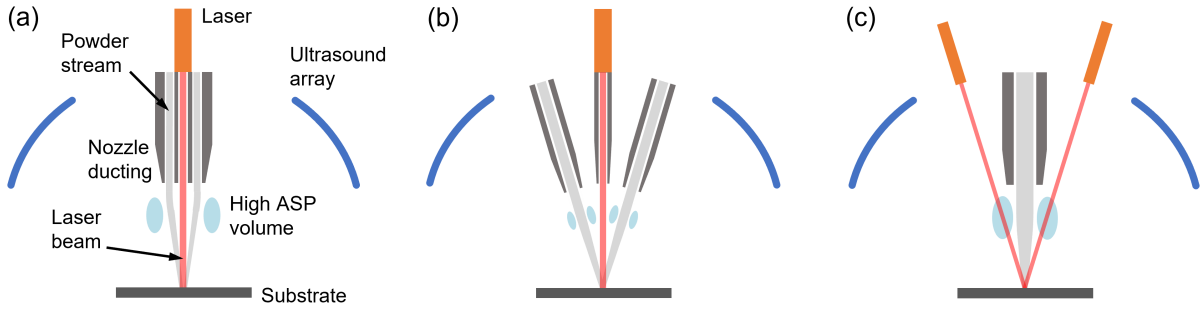


Figure 6.2: Types of LDED-PF setups with UPL array. (a) Continuous coaxial (L-C). (b) Discrete coaxial (L-N). (c) Multi-beam (P-N).

In order to decide between these setups, taking into consideration the amount of focusing achievable for a fixed maximum sound intensity available from the ultrasound array described in this chapter, one can plot the ASP and its related SRF field as a function of topological charge at a fixed voltage. This is done in Fig. 6.3 using the parameters used in Section 6.5.1, at an ultrasound applied voltage of 10 V.

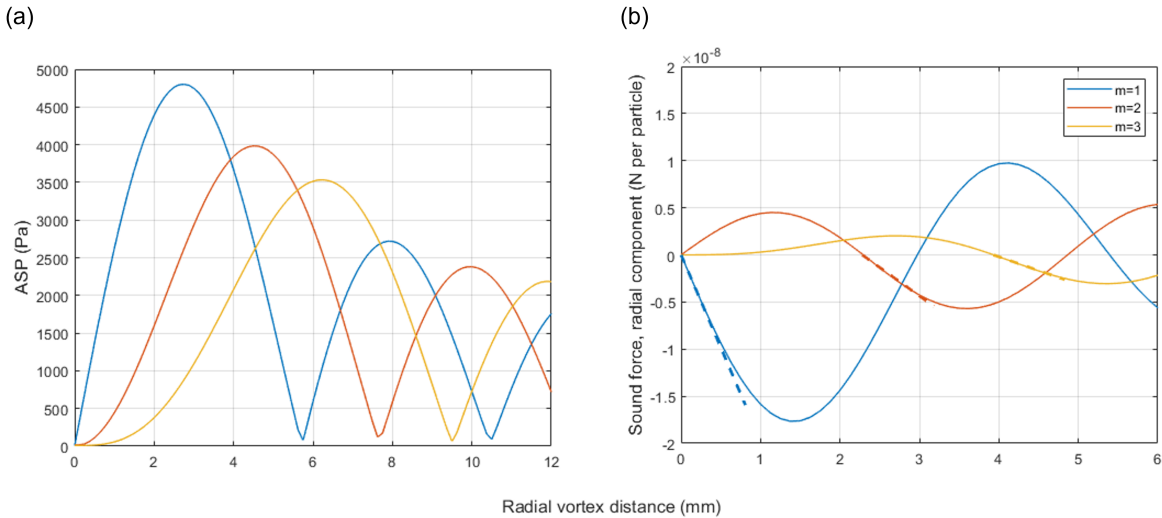


Figure 6.3: (a) Simulated ASP and (b) sound radiation force field as a function of radial distance from vortex sound field with different topological charges. The simulation parameters are the same ones as the ones used in Section 6.5.1.

In order to deflect the powder in an annular region when using L-C setups, for a powder annular opening of 4.2 mm inner radius and 0.4 mm thickness, one should use a

topological charge of about 3. Note that as shown in Fig. 6.3(b), the peak SRF decreases as the topological charge and effective sound ring “radius” increases; for example the peak force for $m = 1$ is -1.8×10^{-8} N and for $m = 3$ it is -3.0×10^{-9} N (17% of the peak force at $m = 1$). The same peak force decrease phenomenon is expected when multiple vortex sound fields are generated in the same working area (when using L-N systems). Because of this decrease in peak SRF seen when the topological charge is increased for the same applied array sound intensity, the higher complexity of designing and fabricating a modified coaxial nozzle, and the limited power of the prototype array described in this chapter, it was decided to use the side-feed like arrangement described in Section 6.4.1, using a vortex field with a topological charge of one. This also allows the related force field to be modeled along with the powder stream with the GBR described in Section 6.3.2. This corresponds to either setup L-N or setup P-N with $N=1$. Setup P-1 was chosen since the powder stream is moving vertically and is not affected by gravity, making the alignment of the powder stream, laser spot, and sound field focal point for the setup geometry and particle speed used in this chapter easier to achieve.

The scope of the reported work will be limited to demonstrating UPL technology for powder stream focusing and its effects on track fabrication in an LDED-PF machine, using Ti6Al4V powder. To achieve this, the following sub-goals were carried out:

- A high-power ultrasound array with 150 elements was designed, optimized and fabricated
- A DMD-IC106 LDED-PF machine from DM3D was modified to work with a P-1 arrangement
- Powder stream properties were measured for different voltages using a focusing sound field and compared to a GBR described in Chapter 5
- A DOE was carried out at different laser powers and array applied voltages using a focusing sound field, and resulting single track geometric features were measured

6.3 Modeling

The procedure for modeling the UPL sound field and the resulting effect on a particle stream consists of simulating the sound field and resulting SRF field, and then simulating the effect of the force field on the powder stream.

6.3.1 Sound and force field simulation

To simulate the sound field from the phased ultrasound transducer array used in UPL technology, a C++ library called `acousticHologram` was developed. The library uses the sound propagation medium and particle physical properties, as well as a list of all the transducer locations and orientations, and computes the ASP field, Gor'kov potential, and SRF field. The software also includes a 3D Lagrangian particle tracking model for simulating particle trajectories and considers the surrounding gas drag force.

The transducers are modeled as a piston source [196], and their sound field is calculated using forward mode automatic differentiation [251, 79], which is exact up to machine precision, and has no error due to grid size or frequency of the emitted sound being modeled compared to finite differences as used in [147]. This is done by using the FADBAD++ C++ library [252, 253] with custom code to compute Bessel functions and related expressions. More details on these modifications can be found in Appendix J.

In order to calibrate the simulation, the peak-to-peak pressure (P_{pp}) was measured directly from a batch of 10 MSO-A1640H10T Manorshi ultrasonic transducers, each running at the voltages used in this chapter (10 and 14 V, push-pull mode in the software), at a distance of 10 cm from a calibrated microphone (4138-A-015 1/8-inch Pressure-field Microphone from Bruel & Kjaer Sound & Vibration Measurement A/S). The obtained values were 138 and 179 Pa for 10 and 14 V respectively. The sound field from an ultrasound transducer can be modeled as a sound piston source [196]:

$$p = j \left\{ \frac{\rho_m c k a^2 U_0}{2r} \right\} \frac{2J_1[ka \sin(\theta)]}{ka \sin(\theta)} e^{j(\phi - kr)} = j \{P_{axial}(r)\} H_p(\theta) e^{j(\phi - kr)} \quad (6.1)$$

where $j = \sqrt{-1}$, ρ_m is the medium density, c is the medium sound speed, a is the piston source radius (measured to be 5 mm), r is the distance to the transducer, θ is the angle to the transducer center-line, ϕ is a phase delay, and $k = 2\pi f/c$ (where f is the transducer frequency, 40 kHz). The functions $P_{axial}(r)$ and $H_p(\theta)$ are the pressure along the transducer's center-line normal direction and the transducer's directivity function respectively. Using Eq. 6.1 and the measured pressures from the calibrated microphone, one can obtain the piston speed value U_0 that is used in the simulation. Noting that the measurements were taken at the transducer's center-line ($H_p(0) = 1$) and that in that case $|p| = P_{axial}$ equals $P_{pp}/2$ at $r = 0.1$ m, the calculated U_0 values used in the simulation were 1.79 and 2.32 m/s for 10 and 14 V respectively, using air at standard conditions.

6.3.2 Particle stream GBR

In order to estimate the degree of powder stream focusing due to an applied SRF field, a novel powder stream model was developed. In this model, the particle trajectories in the powder stream are modeled as “random” rays, with a Gaussian concentration distribution as well as a Gaussian sideways speed component (see Chapter 5). The GBR is usually applied when modeling laser beams, where the amount of expected refraction and diffraction is low, i.e. no ray phase information is taken into account [213]. It was also found that the analytic solution to the particle trajectories when subject to a SRF found in Chapter 4 correspond to rays bending due to a gradient index lens (GRIN); this allows for the simulation of powder stream focusing that is orders-of-magnitude faster than a corresponding Monte-Carlo simulation where every ray is taken into account as shown in Chapter 5.

The GBR describing the particle concentration distribution (PCD) of the powder stream is given by Eq. 5.46, where $w(z) = w_0\sqrt{1 + z^2/z_R^2}$. The values w_0 and z_R are constants. Before applying the GBR, one has to fit the measured PCD when no SRF is applied. The first step is to measure the divergence angle and e^{-1} width from the PCD, at some location z_m along the powder stream from the nozzle exit. A good location to make this measurement is the location where the SRF will be applied (at the sound focal point). The corresponding pixel number value in the array with the added frame data is given by:

$$p_{sfp} = \text{round}\left(\frac{l_{ne-sfp}}{l_{pix}}\right) + p_{ti-ne} - p_{crop,af} - p_{crop,rot} \quad (6.2)$$

where p stands for a pixel row value, sfp stands for sound focal point, l_{ne-sfp} is the distance from the nozzle exit to the SFP, l_{pix} is the pixel size, p_{ti-ne} is the number of pixels from the top of the array to the nozzle exit, $p_{crop,af}$ is the number of pixels cropped from the top of the original added frames with light reflected from the array and $p_{crop,rot}$ is the number of pixels cropped from the top after rotating the data in the array (done to correct for any offset of the powder stream with respect to the camera).

The same methods and MATLAB functions used in Chapter 4 were used to measure the widths and divergence angles. The second step is to use the above values to obtain the w_0 and z_R for the analog GBR. This can be done using Eqs. 5.26 and 5.27. If the particle speed is low, one can obtain better results by finding an equivalent distance to the nozzle, taking into account the acceleration time of the particles as done in Chapter 5. In this chapter the particle speed is higher, and one can use the actual z value where the width and divergence were measured. Note that the measured e^{-1} width and divergence angle values should be multiplied by $\sqrt{2}$ to get the corresponding e^{-2} width and spread angle, which is used in the GBR.

The transfer matrix for the corresponding GRIN lens is given by Eq. 5.41 where $\eta = \sqrt{F_a/(l_{offset}m_p u_z^2)}$, F_a is a quarter of the peak force, l_{offset} is the distance from the z -axis at the SFP where the force is half the peak force, m_p is the particle mass using the mass average particle size and u_z is the particle speed along the z -axis. The peak force is divided by 4 because the slope of $2F_a/l_{offset}$ is used to model the linear range of the force variation along the x -axis, and along the z -axis the force has a shape approximating a single wavelength of a sinusoid from 0 to $2F_a$, with an average value of F_a . The value l_i is this wavelength value, which is the effective distance along the particle stream axis where the sound is assumed to affect the particles. This can be defined as the z -distance between two minimums before and after the SFP of the SRF field x -component profile at $x = l_{offset}$. All the variables discussed are shown superimposed on the ASP and SRF field x -component in Fig. 6.4.

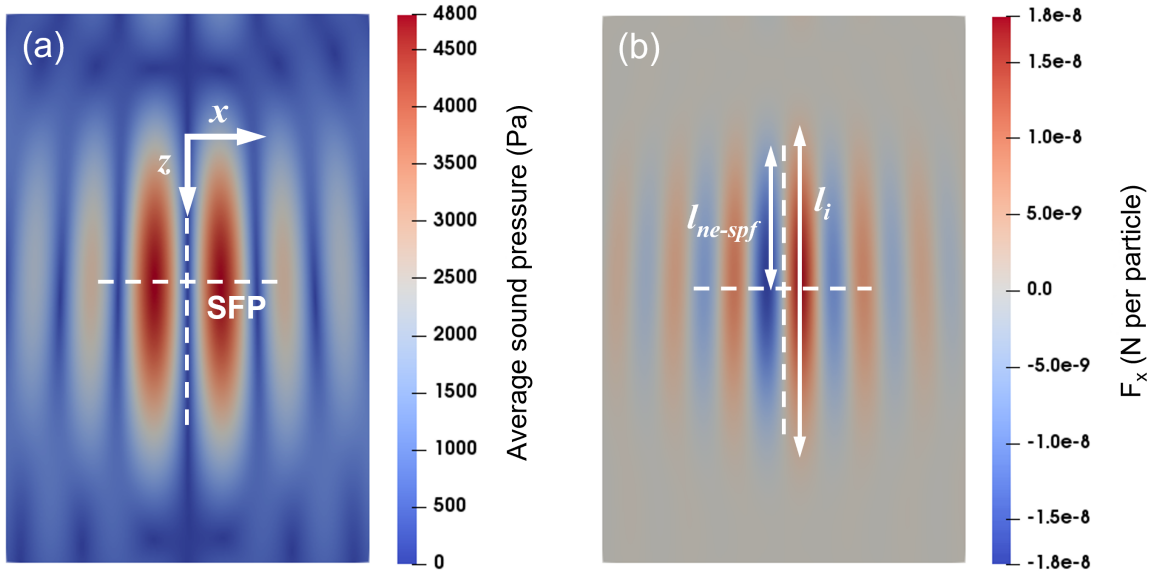


Figure 6.4: (a) Averaged sound pressure (ASP) and (b) x -component of the resulting sound radiation force field when applying 10 V to the array setup in this chapter. Both figures have the relevant variables overlaid.

With all the above information, the powder stream can be simulated for all positions along z as described in Chapter 5. If $l_i/2$ is longer than l_{ne-sfp} , the simulation may be run with a length equal to $2l_{ne-sfp}$ (l_{i2}) and the value of F_a can be multiplied by l_i/l_{i2} to account for the shorter length. In order to compare the results to the measured e^{-1} widths, the simulated widths should be divided by $\sqrt{2}$.

6.4 Materials and methods

6.4.1 Directed energy deposition machine modifications

The DMD-IC106 LDED-PF machine with all the modifications and attached ultrasound array is shown in Fig. 6.5.

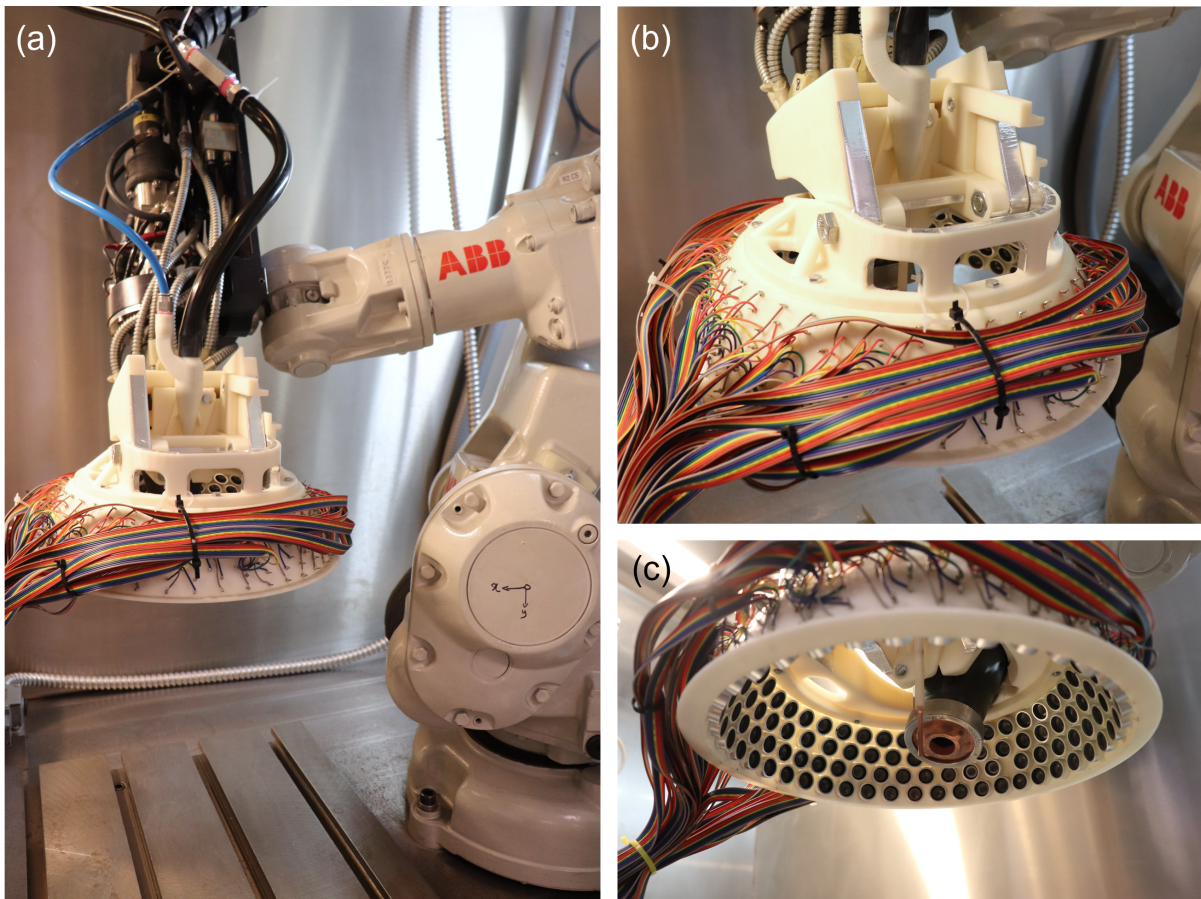


Figure 6.5: (a) Modified DM3D machine. (b) Top close-up showing ultrasound array, frame and gas cyclone. (c) Bottom close-up showing ultrasound transducers, powder nozzle and water bypass insert.

The 150-element UPL array was designed with the shape of a sphere zone, as described in Chapter 4. This allows for a high degree of sound focusing, by having the transducers' axes of symmetry intersecting at a single point. This point is defined as the sound focal

point. The array should also be as small as possible, with the transducers as close to each other as possible, in order for the transducers to be as close as possible to the sound focal point.

The transducer placement in the final design was determined by the vertex locations from a mesh generated using a modified DistMesh algorithm [254], which extends the original algorithm from closed surface to open convex surface mesh generation. The original DistMesh algorithm produces high-quality meshes by considering the edges of an initial mesh produced by a Delaunay triangulation [255] as springs that are then relaxed to an equilibrium position. The distance function of the surface is used to project the nodes back to the surface after each re-triangulation and relaxation iteration. The modification involves having a distance function to the boundaries of the openings in the surface and also computing a projection there, and using a convex hull operation [255] for the re-triangulation instead of a Delaunay triangulation. The resulting high-quality mesh with close to uniform edge lengths allows for the placement of the maximum number of elements on a given surface [256]. This meshing process can be used for other array designs with different surfaces depending on DED-PF machine requirements as long as the surface distance function can be computed. The parameters used for meshing are the following: lower sphere zone angle 23° , upper sphere zone angle 34° , sphere radius 125 mm, and edge equilibrium length used in DistMesh 17.5 mm. The mesh used to design the UPL array, and its edge distance histogram are shown in Fig. 6.6. The histogram of edge lengths corresponding to the transducer center-to-center distance shows that they have high uniformity, since the values have a spread that is much lower than the required edge length of 17.5 mm (Fig. 6.6(b)). The minimum edge length of 16.4 mm was checked to see if it is higher than the transducer diameter (16.1 mm) to see if no transducers will overlap. The modified DistMesh algorithm is described in more detail in Appendix K.

The MATLAB program running DistMesh can output the ordering, location and normal vectors (geometry information) of the transducers for simulating the sound field and related radiation force field using the `acousticHologram` C++ library described in Section 6.3.1. The geometry information is also used as an input to the Ultraino program, which is used to send signals via a USB cable to signal amplifiers with a power supply, which then sends signals to the individual transducers on the array.

This array geometric information was then used in custom Python code that was ran using the FreeCAD API to produce an initial CAD model; the model has a thickness of 6 mm, 2.7 mm deep circular recesses for attaching the transducers, a rectangular recess to prevent filling in of the circular recesses due to the layer-by-layer FDM printing process, and engraved numbers corresponding to the transducer order given by the geometry information. The number was engraved with a letter height of 5 mm and a depth of 0.8 mm.

These features can be seen in Fig. 6.9(b). This model was then exported to SolidWorks as a STEP file and further features were added such as a lip at the edge of the array (Fig. 6.9(b)) and a top ring (with nut inserts for attachment to the frame) to make it stiffer normal to the array’s center-line.

After printing the array, 150 MSO-A1640H10T Manorshi ultrasonic transducers were attached to it using hot-melt adhesive, and each transducer was individually soldered to a ribbon cable following their MOLEX connector connection number, that is then connected to 5 inter-connected Ultraino boards, following the printed array numbering. More information on how the electronics are set up is described in Chapter 4. The only difference to the setup in the referenced chapter is that the boards are wired with the transducers using two subsequent signal leads (the grounds are not used), and set through the Ultraino software to “push-pull” mode, where the transducers are excited from the negative to the positive of the programmed voltage. For example, if 10 V is specified, instead of providing a 0 to 10 V output peak-to-peak, the boards provide an output of -10 to 10 V peak-to-peak. In this case, the transducer pressure signal amplitude is generated by going from the negative of the set voltage to the positive set voltage.

A close-up of the UPL array can be seen in Fig. 6.5(b) and (c). A diagram showing all the design and assembly steps, as well as the use of the array’s geometric data for producing control signals, is shown in Fig. 6.7. The fabrication of the array is described further in Appendix L.

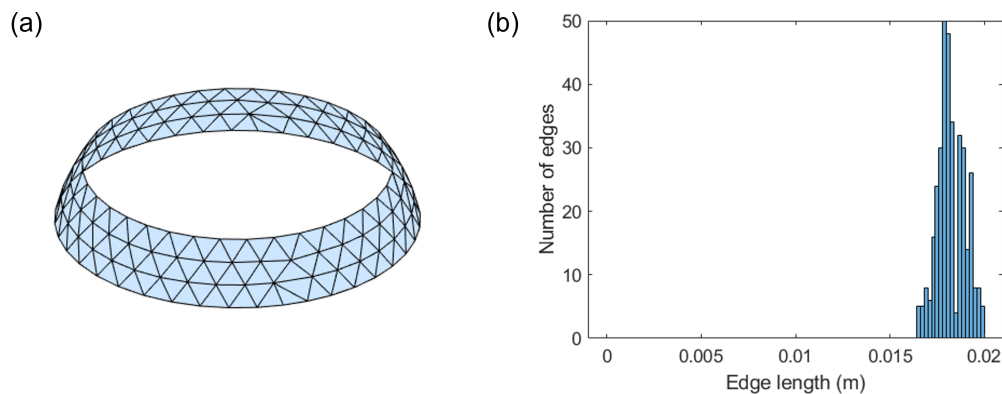


Figure 6.6: (a) Meshing result for transducer placement. (b) Edge distance histogram showing mesh quality.

In order to have finer control of the powder particle speed, a gas cyclone was designed and built. The cyclone is integrated with a powder nozzle consisting of a 100 mm long

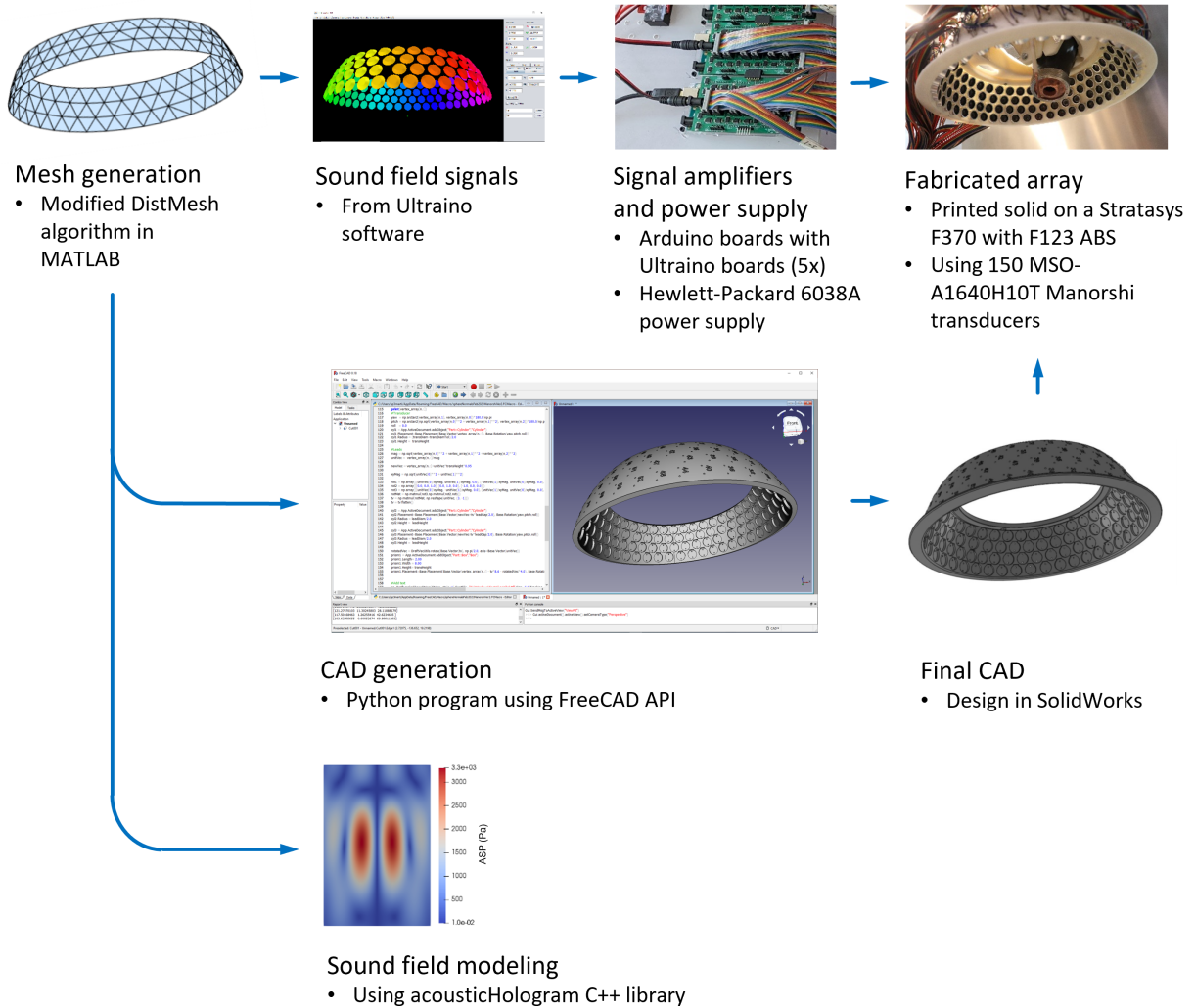


Figure 6.7: Array design, assembly and control workflow.

copper tube, with a 1/8" outside diam. and 0.032" thickness. The cyclone inlet is attached to the powder feeding tube (blue tube in Fig. 6.5(a)) coming from the DMD-IC106 hopper assembly. The cyclone assembly can be seen in Fig. 6.5(a) and (b). The design and fabrication of this cyclone and nozzle assembly is described further in Appendix L.

The above components were attached to the machine by an adjustable frame. A close-up of the frame can be seen in Fig. 6.5(b). The design of the frame was assisted by the use

of Altair Inspire software, using the topology optimization (TO) facility. Care was taken to obtain proper results by extending the design space as far as possible, the “domain extension approach” [257], in order to have inaccurate results due to the TO result having the tendency to attach to the boundaries of the design space. The design and fabrication of the frame is described further in Appendix L. The frame was designed in order to be able to adjust the angle between the laser and the powder stream, while keeping the powder stream and the sound focal point aligned. This is done by tightening a group of bolts in a certain order. This is described further in Appendix L.

The array, frame components, and gas cyclone were printed on a Stratasys F370 with no infill (solid) and a layer height of 0.1778 mm. The build material was F123 ABS. The machine was modified by removing its default copper coaxial powder nozzle and replacing it with a copper insert with internal channels. This insert was designed to close the cooling water loop that is needed for the laser optics, while allowing the laser beam to pass through. The insert can be seen where the placement of the coaxial nozzle was in Fig. 6.5(c).

6.4.2 Experimental setup

In order to produce a focused powder stream while the LDED-PF process is taking place, the following interactions should be quantified:

1. Sound field and nozzle interaction. If the sound focal point is too close to the nozzle, it was found that when troubleshooting the sound field the ASP was compromised
2. Sound field and melt pool interaction. It was observed that the melt pool would be affected by the sound field at a minimum sound focal point to build plate distance
3. Particle-sound interaction if the particle is being heated by the laser. There were not many current models or experiments found in the literature regarding this issue, however, in setup P-1 and all other setups shown in Fig. 6.2, this interaction should be minimal. This is because the area of high ASP is away from the laser beam
4. Sound field and laser interaction. In this case, the sound waves produce a time-dependent spatial gradient in the process gas index of refraction, which has the effect of deflecting it back and forth. An estimate of the maximum deflection at the build plate position was found to be $\sim 10 \mu\text{m}$ for Nitrogen

More information regarding interactions 2 to 4 can be found in Appendix M.

The final UPL system setup used for the DOE, with the shown dimensions determined by taking into account all the above interactions, is shown in Fig. 6.8.

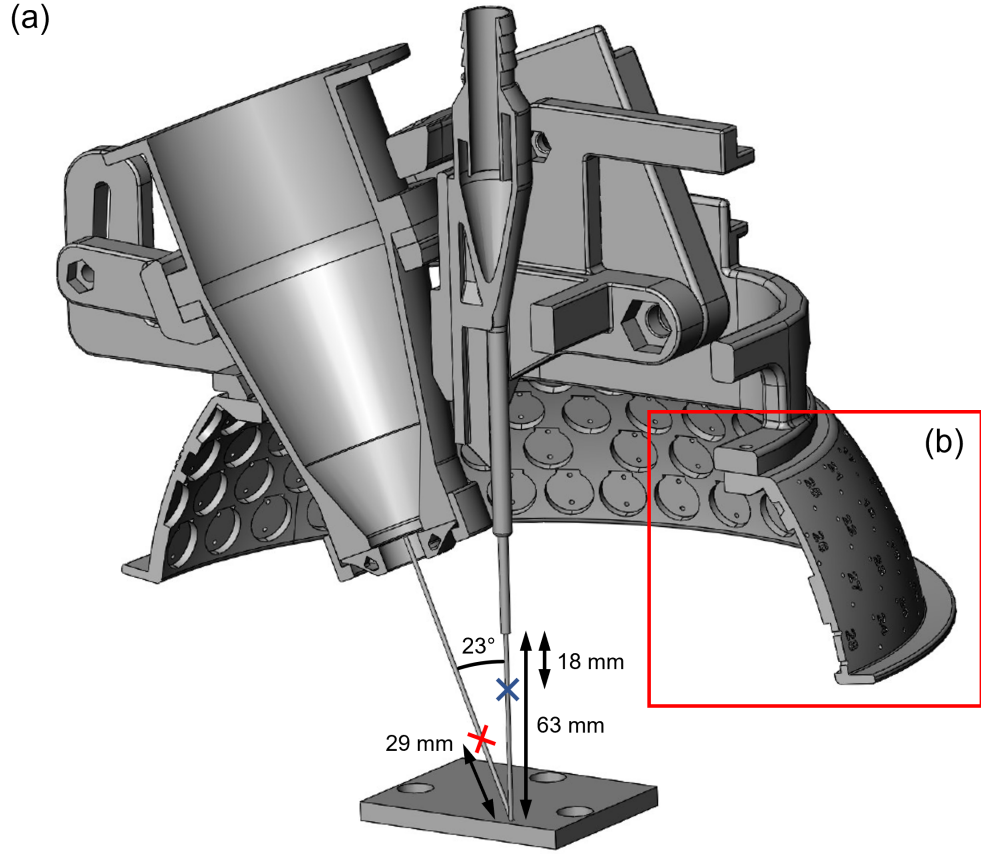


Figure 6.8: (a) Array and frame setup with dimensions used for experiments. The blue cross below the powder nozzle is the SFP and the red cross is the laser focal point. (b) Array features.

Due to the distance to the substrate, current setup has a defocused laser. One can calculate the spot size at the substrate from the data in [258], where approximate laser spot width measurements were done from burnt spots formed on Kapton film with a thickness of $100 \mu\text{m}$, at 21 distances from the coaxial nozzle tip. The measurements were done in the same DMD-IC106 machine used in this chapter. This data can be fitted to the laser Gaussian beam spreading model given by Eq. 5.6, but with $z \Rightarrow z - z_0$, where z_0 is the location of the laser focal spot. One can fit a quadratic polynomial using least squares to

the square of the measured widths at different distances from the coaxial nozzle exit, and find the constants for the modified form of Eq. 5.6 using:

$$z_0 = -b/(2a) \quad (6.3)$$

$$w_0 = \sqrt{c - az_0^2} \quad (6.4)$$

$$z_R = w_0 a^{-1/2} \quad (6.5)$$

where a , b and c are the quadratic polynomial coefficients. The results of the fit are an offset of 16.2 mm, a focal spot width of 1.3 mm and $z_R = 13.8$ mm, with $r^2 = 0.97$. Using these values, the spot size at a distance of 29 mm from the laser focal point as used in the experimental setup in this chapter is 3.0 mm.

The Ti6Al4V powder used is from Raymor (Spherical Ti-6Al-4VGr5 powder), with size ranges from 45-150 μm , IPN 5773-S, and a mass average diameter of 88 μm . The mass average diameter was measured using a Camsizer X2 from Retsch GmbH.

As described in Appendix N, Nitrogen was selected to be used as a shielding and carrier gas, in order to minimize effects due to changes in sound speed and impedance between air and the process gas, which can distort the sound field from the array [196].

6.4.3 Particle concentration distribution acquisition procedure

The setup used to measure the powder concentration distribution, using the same applicable dimensions shown in Fig. 6.8, is shown in Fig. 6.9.

The Veo 710S high-speed camera had the following software settings: Bit depth, 12, Aperture 3.5, Resolution, 640 x 800, Sample rate, 13000 FPS, Exposure time, 76.514 μs , EDR, 0 μs , and Exposure Index, 1000. The PIV mode for image acquisition was not enabled as this might introduce an error when summing the frames to estimate the PCD as described in Chapter 4. The recorded videos had a length of between 6 to 7 seconds, and they were saved keeping all frames. Both lights were set to 80% intensity and their cooling fans were ducted to reduce drafts.

6.4.4 Particle concentration distribution measurements

In order to estimate the PCD of the powder stream for the applied array voltages in this chapter, the powder stream was filmed at high speed and the frames were cropped, binarized using a 50% threshold level and summed.

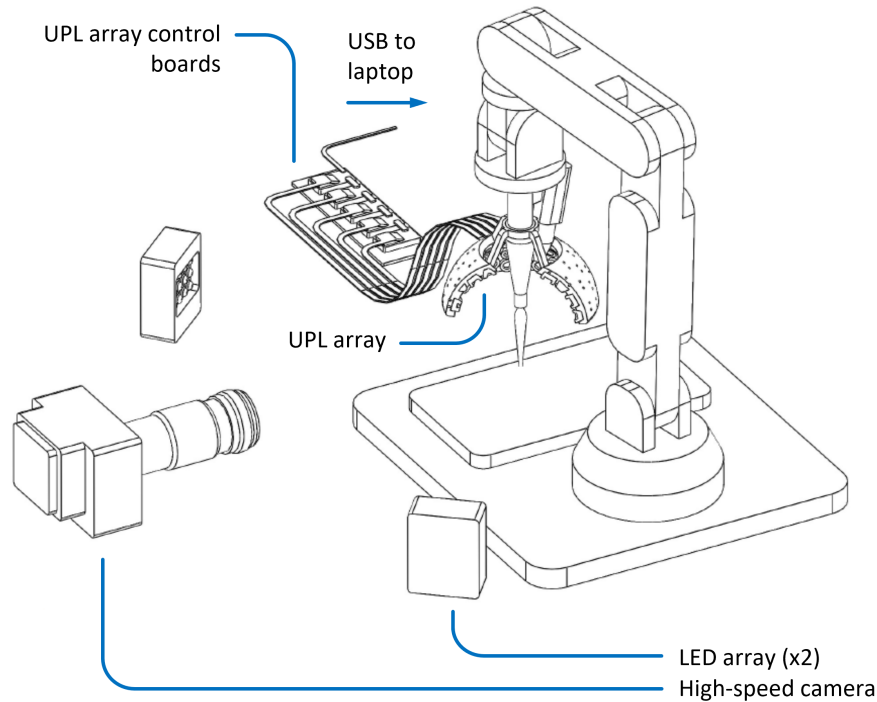


Figure 6.9: Schematic of the experimental setup showing lighting and camera setup (not to scale). The focal axis of the camera and the light were in the same plane, with the array axis normal to this plane, and the sound focus point intersecting it. The distance from the front of the camera lens and the light to the sound focus point was 72 and 51 cm respectively. The angle between the camera and the light center-line axis was 22° and setup to be as small as possible for uniform illumination.

These thresholded and frame summed (TS) images were obtained from the high-speed videos that were cropped to 78000 frames (6 seconds). Afterwards, each frame was cropped 100 pixels from the top, 0 pixels from the bottom, 20 pixels from the left, and 40 pixels from the right (all inclusive). This was done to remove the lower part of the array and side reflections from the array. This step is necessary to ensure proper thresholding. After all the frames for each run were cropped, they were binarized using a 50% ($\varepsilon = 0.5$) threshold level using Eq. 4.7. After thresholding, all the frames in each run were added. In order to prevent the computer RAM from filling up, the above operations were done for 6500 frames at a time in 12 batches. This part of the analysis was done in python using the NumPy library.

6.4.5 Single track runs procedure

The tracks specified in Table 6.1 were printed on Ti plates with a length of 40 mm and a spacing of 10 mm. As shown in the Table, two of the tracks were redone after the DOE was performed. Why this was done is explained in Section 6.5.4. In order to prevent possible effects on the sound field from sound reflections, a rig was made to hold Ti build plates at an elevated location. They were cut using water jet from a 1/4" thick, 6 by 12" Grade 2 Ti sheet from McMaster-Carr (SKU # 9051K127), resulting in 8 equal-sized square plates. The DMD-IC106 machine parameters used were the following: hopper speed 600, laser speed 3 mm/s, hopper cover gas 10 l/min, carrier gas 10 l/min, and shielding gas 6 l/min.

In order to prevent powder accumulation in the modified powder feed system, while also reducing the pressure build-up due to the high-flow of the DMD-IC106 machine default purge procedure, an alternative purge-type procedure was carried out, where all the gas feeds were run for 30 seconds, but running the hopper cover gas at 20 l/min, and the carrier gas at 20 l/min.

Before starting to print in each plate, less than a second of high-speed camera footage was recorded, and the speed of the particles was measured in 10 frames. Also the electronics were checked by running the array at 10 V to check that the powder was being focused and the powder mass flowrate was measured.

6.4.6 Track geometry measurements and calculations

Surface height maps of each track were measured using a VHX-7000 digital microscope (Keyence Corporation, Osaka, Japan). The measurements for many positions on the track were stitched into a final height map at 50x magnification and using the "full coaxial" light source option for more accurate height measurement.

Afterwards, cross-section profiles of the height maps were extracted. For all the DOE tracks this was done by averaging 20 parallel profiles on either side and including the profile at 15 mm from the start of the track and perpendicular to the track axis. The profile separation increment was 250 μm . The start of the track is assumed to be the location where the center of the laser spot is when the track is started. For the last 3 tracks of P6 where the sound is applied on the second half of the track, the average profile on the first half of the track was done at a distance of 7 mm from the start of the track and using 20 profiles on either side, with a separation increment of 50 μm . For the second half, the same parameters were used except that the distance from the start of the track was 23 mm.

Table 6.1: Fabricated tracks, their DOE parameters, and demonstration tracks. (r) Redone tracks. (h) Demonstration tracks with voltage applied on the second half of the track.

Plate	Track	Laser power (W)	Array voltage (V)
1	1	700	0
	2	800	14
	3	700	10
	4	900	14
	5	700	14
2	1	900	10
	2	800	0(r)
	3	800	10(r)
	4	900	0
	5	700	0
3	1	700	14
	2	900	14
	3	800	0
	4	900	10
	5	900	0
4	1	800	10
	2	700	10
	3	800	14
	4	800	14
	5	900	10
5	1	900	0
	2	700	0
	3	700	14
	4	800	0
	5	700	10
6	1	900	14
	2	800	10
	3	700	14(h)
	4	700	0(h)
	5	700	10(h)

The tracks were further processed and the track properties were measured with the following steps:

1. The length of the profile and height (Δh) increments were extracted from the exported data for computing track properties and displaying the profiles. The length of the profile and number of height values was used to find the horizontal increment distance (Δx)
2. The ends of the profile that had any other height data such as the profile of the counterbore used to secure the build plate were manually removed
3. The first and last 101 height measurements were averaged to find the averaged heights of the ends of the profile
4. The average of these two measurements was subtracted from the heights
5. The profiles were tilt-compensated by subtracting the values at each horizontal position with the values given by the line intersecting the averaged height values at the 51st height measurement location of the 101 height measurements at each end of the track profile (assuming a shallow tilt angle)
6. The maximum height was calculated from the processed heights
7. The origin of the horizontal x position is set at the location of the maximum height
8. The width was calculated by checking the locations where the absolute value of the slope of the track is closest to 0.2 (not taking into account Δx and Δh). The slope was calculated using the forward difference method [171]
9. The track cross-sectional area A_t was calculated using the trapezoidal method [171] for the heights inside the calculated width

The increment values from the microscope data were $\Delta x = 2.0793 \mu\text{m}$ and $\Delta h = 1 \mu\text{m}$. The tracks and their measurements were plotted and checked manually for all tracks.

The catchment efficiency can be estimated as the fraction of material being deposited in a track per second over the total mass going into the process area, which is the mass flowrate from the nozzle:

$$\eta = \frac{\rho A_t v_t}{\dot{m}} \quad (6.6)$$

where ρ is the material's density, v_t is the track deposition speed and \dot{m} is the mass flowrate from the nozzle. One can see from Eq. 6.6 that the catchment efficiency is proportional to A_t , therefore one can plot both variables in a plot with two y axes.

In order to scale the axes, the A_t y -axis upper limit should be used in Eq. 6.6 to get the upper limit of the η y -axis. This was done for plotting the data shown in Fig. 6.18.

To measure the dilution zone geometry of the selected tracks, each sample was cross-sectioned, ground, polished, etched, and imaged using an optical microscope.

Out of all the 27 tracks for the DOE, 9 tracks were chosen, with different DOE parameters and the repeats that had the median cross-sectional area. The tracks that fit this criterion were: 1-1, 1-5, 2-1, 3-2, 3-3, 4-2, 4-4, 5-1, and 6-2, where the first number is the plate, and the second number is the track, with the DOE parameters shown in Table 6.1.

Samples from the tracks with dimensions of 10 by 8 mm were cut with EDM. The 10 mm dimension is normal to and centered with the track, and the 8 mm dimension is from the center along the track towards the start of the track. Since the build plate had a thickness of 6.35 mm, this gives a cut profile dimension of approximately 6.35 by 10 mm.

The first 5 samples and the last 4 were hot mounted to 2 mounts made using a CitoPress-5 (Struers LLC) machine. The cut profiles were ground using a LaboPol-20 (Struers LLC) auto-polisher with 80, 320, 500 and 800 grit, followed by manual sanding with 1200, 2400 and 4000 grits. The cut profiles were polished using a Vibromet 2 (Buehler) vibratory polisher, for 4 hours using an amplitude setting of 80, with a MasterPrep 0.05 μm alumina polishing suspension (Buehler). The samples were etched with Kroll's reagent swabbed over the sample for 10 s. Both polished and etched surfaces were cleaned with distilled water and compressed air.

The dilution area width W and penetration depth H , as well as the heat affected zone (HAZ) width and depth [259] for each sample were measured using the same VHX-7000 microscope and software, at 50x magnification. The dilution area is estimated assuming a parabolic profile ($A_d = 2/3WH$) [258] and the dilution fraction is defined in this chapter as the fraction of the dilution area over the total track cross-sectional area ($A_d/(A_t + A_d)$). Some of the measured variables and derived quantities are shown in Fig. 6.10.

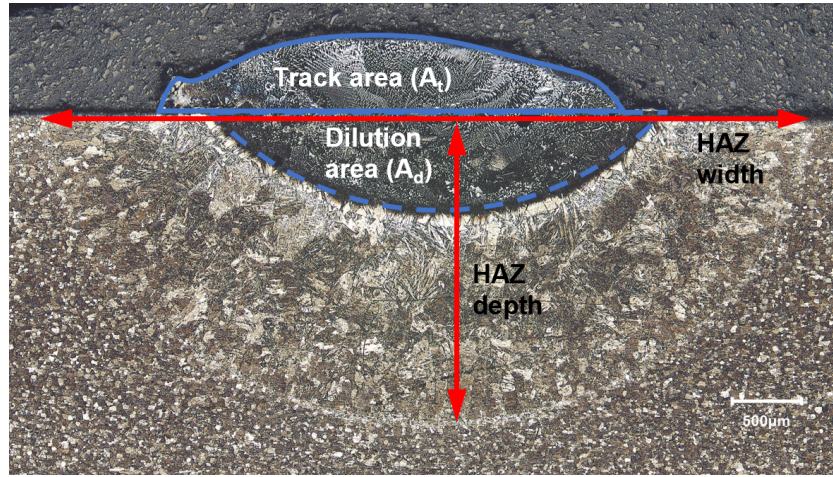


Figure 6.10: Track geometric features measured from the cut and etched samples. The background optical image is for track 6-2.

6.5 Results and discussion

6.5.1 Sound field simulation results

The ASP and the SRF in the radial direction are shown in Fig. 6.11. From the plots one can observe that increasing the voltage scales the ASP plots, as well as the force field. From Fig. 6.11(b) one can observe the l_{os} parameter used in the GBR described in Section 6.3.2, where the force decreases by half, is 0.47 mm. As seen in Fig. 6.11(b), the peak force F_a is 1.8×10^{-8} N at 10 V and 3.0×10^{-8} N at 14 V. The l_i value was found to be 40 mm, where half of this length is higher than the nozzle exit to SFP distance of 18 mm. Therefore, the F_a values were multiplied by $40/36=1.11$ and l_i was set to 36 mm for the GBR simulation.

6.5.2 Powder stream 2D concentrations

The TS images for Ti6Al4V are shown in Fig. 6.12. From Fig. 6.12(a) to (b), corresponding to 0 and 10 V, one can clearly see a more concentrated stream, especially close to 63 mm which is the build plate location. Fig. 6.12(c) one can see a higher upstream concentration compared to Fig. 6.12(b), however, the powder diverges faster downstream. This might be due to air drafts that produce a more obvious disturbance for a high degree of focusing as observed in Chapter 4.

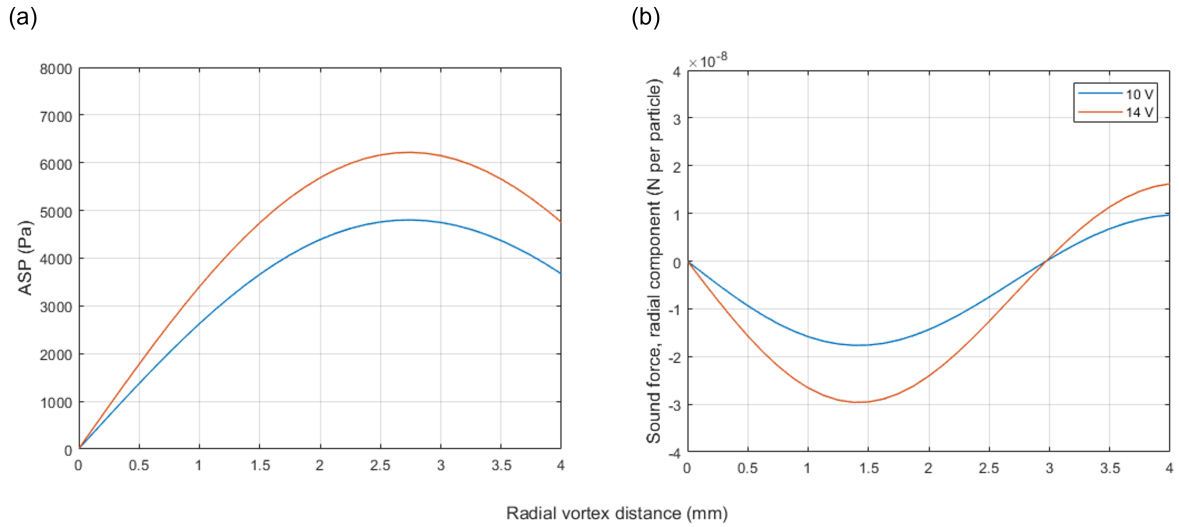


Figure 6.11: (a) ASP for 10 and 14 V. (b) Radial SRF for 10 and 14 V.

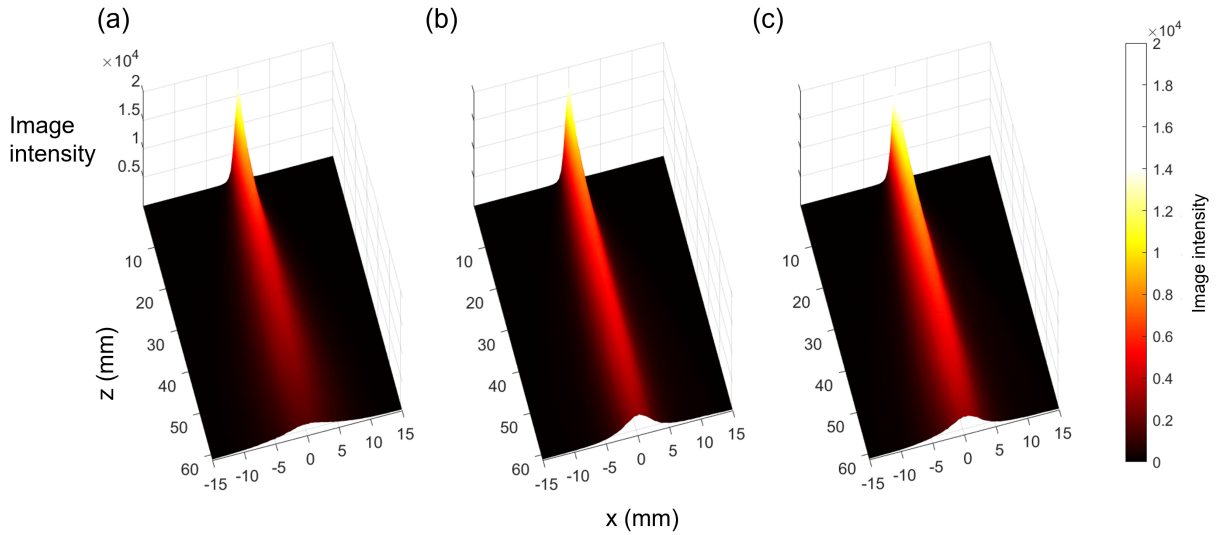


Figure 6.12: Surface plots of added frames from the high-speed camera of the first repeat for Ti6Al4V at (a) 0, (b) 10, and (c) 14 V.

The resulting PCD from the GBR fitted to the powder stream with no applied array voltage is shown in Fig. 6.13. There is a good qualitative match between 2D PCD distributions shown in Fig. 6.13(a) and (b). In Fig. 6.13(c), towards the nozzle area there is a divergence in the center-line PCD, which is also seen at other voltages. This might be

due to the depth-of-field being close to the powder stream diameter close to the nozzle; this means the values being measured from the video are not an accurate representation of the PCD. The e^{-1} powder half-width shown in Fig. 6.13(d) does have a close match, and diverges slightly as expected, due to gravitational acceleration of the particles, causing a measured smaller width downstream. Note that the GBR does not account for the gravitational acceleration of the powder.

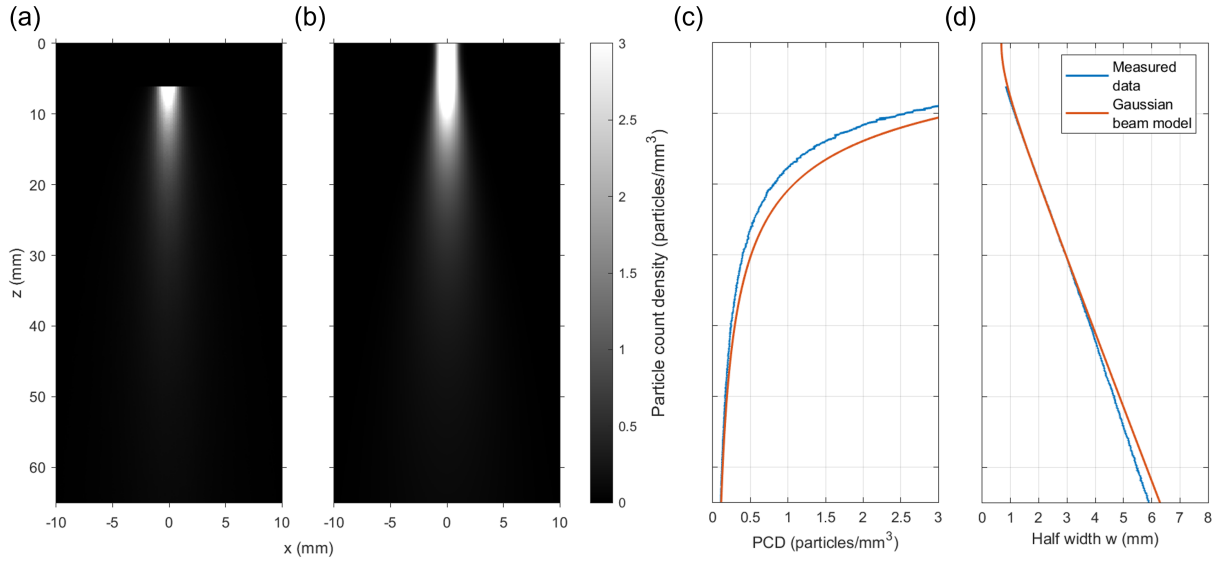


Figure 6.13: (a) Measured 2D PCD. (b) Simulated 2D PCD using the GBR model. (c) Center-line measured and simulated PCD. (d) Measured and simulated IRW half-widths. Figures (a) to (d) are for no applied SRF.

When the SRF is applied to the powder stream, one can observe a clear reduction of the downstream half-widths as seen in Figs. 6.14 and 6.15. At an applied array voltage of 10 V, the GBR model underestimates the degree of focusing, this is clearly seen in Fig. 6.14(d), and is also seen by the slightly higher measured center-line PCD downstream in Fig. 6.14(c).

At an applied array voltage of 14 V, the opposite happens; the GBR model overestimates the degree of focusing, as seen in Fig. 6.15(d). Also producing a much higher simulated center-line PCD downstream as seen in Fig. 6.15(c). As explained before, this might be due to air drafts that defocus the powder stream; another indication of this is the apparent change in slope of the half-width close to 30 mm downstream of the nozzle, seen in Fig. 6.15(d).

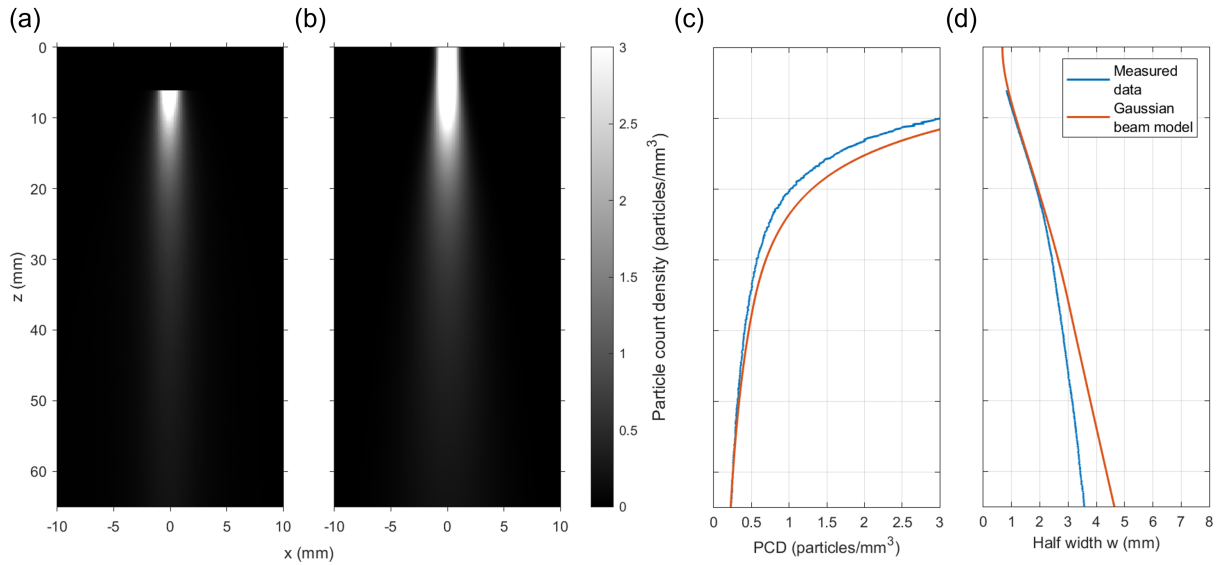


Figure 6.14: (a) Measured 2D PCD. (b) Simulated 2D PCD using the GBR model. (c) Center-line measured and simulated PCD. (d) Measured and simulated IRW half-widths. Figures (a) to (d) are for an applied SRF with an array voltage of 10 V.

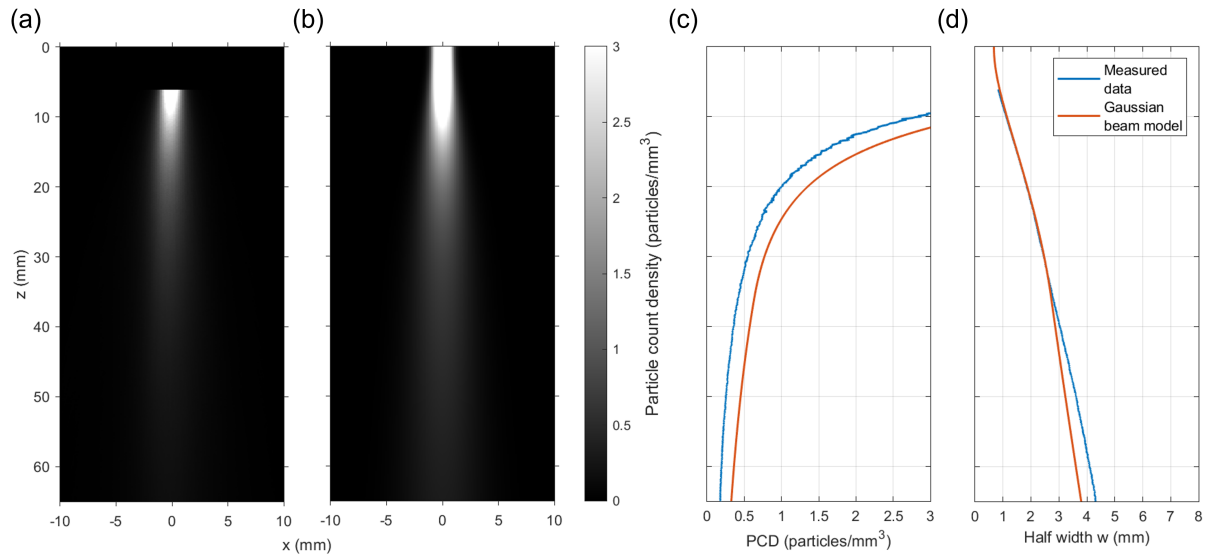


Figure 6.15: (a) Measured 2D PCD. (b) Simulated 2D PCD using the GBR model. (c) Center-line measured and simulated PCD. (d) Measured and simulated IRW half-widths. Figures (a) to (d) are for an applied SRF with an array voltage of 14 V.

6.5.3 Downstream particle stream characteristics

The powder stream widths downstream of the SRF and at the build plate are shown in Fig. 6.16. Following the 2D PCD results, the simulated widths are larger than the measured widths at 10 V and smaller at 14 V.

The discrepancy increases as expected the further downstream the width measurements are taken. At the build plate the maximum percent difference of 28% between measured and simulated values is at 10 V. Note that the measured widths at the build plate should be related to the fraction of material reaching the melt pool.

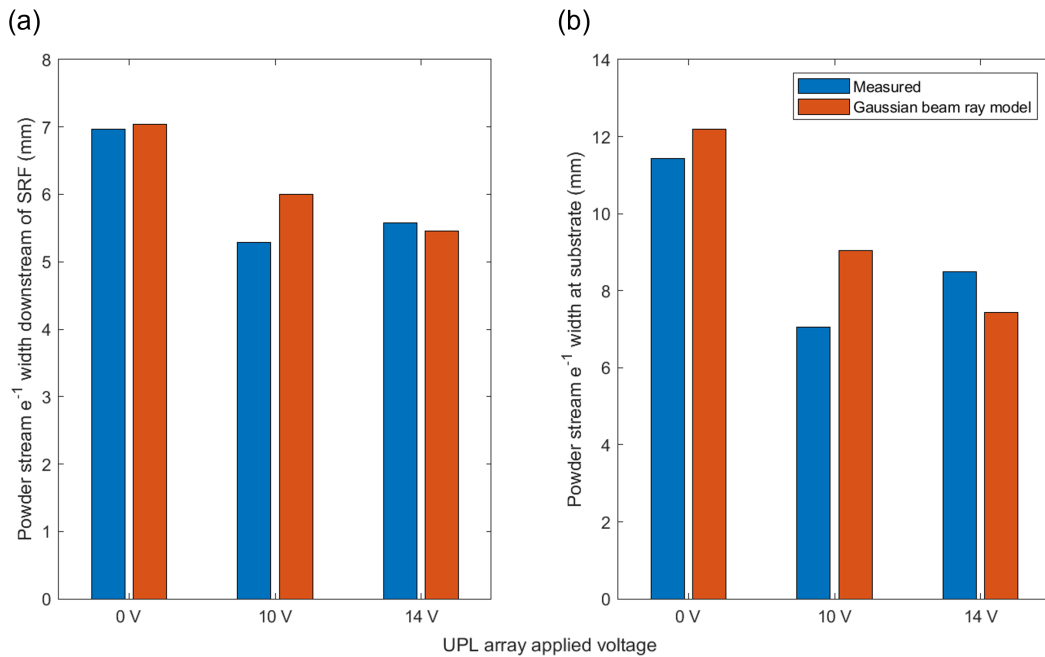


Figure 6.16: (a) e^{-1} widths downstream of the applied sound field. (b) e^{-1} widths at build plate location.

The powder stream profiles taken from the 2D PCD data and simulations are shown in Fig. 6.17. Although the e^{-1} widths differ between measurement and simulation, the approximate shape and height of the profiles match closely, except between the measured and simulated profiles at 14 V; again this might be due air drafts that are affecting the focusing, and have the average effect of the TS images of widening the Gaussian profile.

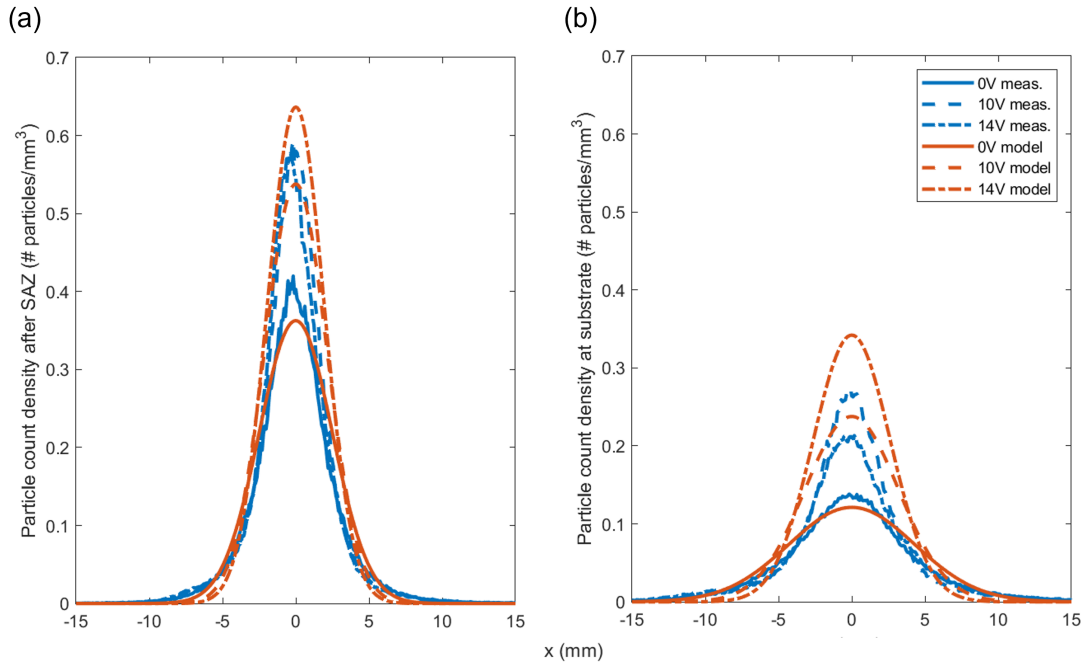


Figure 6.17: (a) PCD profiles downstream of the applied sound field. (b) PCD profiles at build plate location.

6.5.4 Track geometry

The measured cross-sectional area of the tracks and related catchment efficiencies are shown in Fig. 6.18. Note that the data reported in this section uses an extra repeat of two tracks at 800 W that were done after the DOE data was obtained. The two tracks that were redone are marked with an (r) in Table 6.1. These two tracks were redone because it is suspected that the original tracks were done in the wrong order. This is described further in Appendix O.

The proportionality constant for finding the catchment efficiency upper axis value was found to be $1.62 \times 10^5 \text{ m}^{-2}$, using a nozzle mass flowrate of 4.92 g/min (average of three repeats measured at the start of each plate, with a range of 4.8 to 5.0 g/min), a track deposition (laser) speed of 3 mm/s and a density for Ti6Al4V of 4430 kg/m³. One can see higher deposition rates taking place for all laser powers at 10 V compared to 0 V, and a slightly lower value at 14 V. This behavior matches the measured widths shown in Fig. 6.16, clearly indicating more material is being deposited in the track when the width, being controlled by the ultrasound array, is smaller.

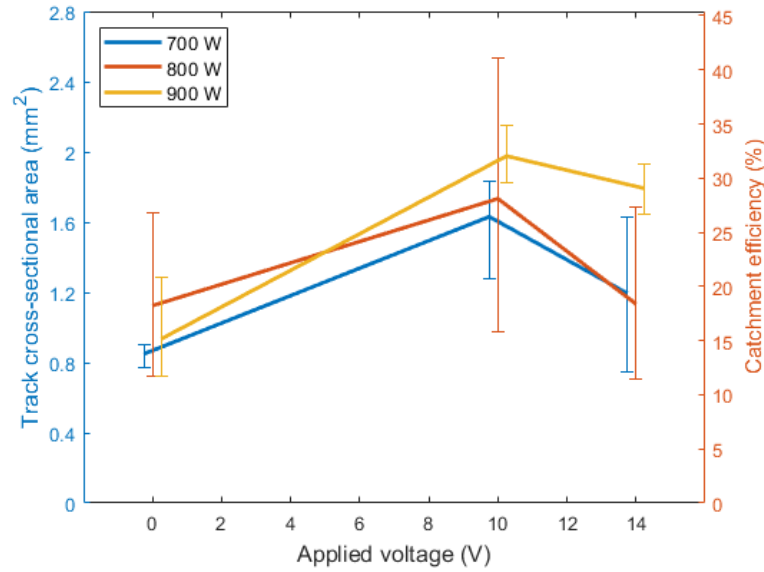


Figure 6.18: Track cross-sectional areas and catchment efficiencies at 15 mm.

The measured maximum height of the tracks are shown in Fig. 6.19 and the measured widths of the tracks are shown in Fig. 6.20. The maximum height data shows the same trend as the cross-sectional area plot in Fig. 6.18 which is expected since there is no substantial change in the track widths. This is expected as the track width is strongly dependent on the laser spot size which is not varied in this chapter.

The three repeats for the runs at 900 W, using 0 and 10 V UPL array applied voltage are shown in Fig. 6.21. One can clearly see that in all repeats the tracks are taller and have a higher cross-sectional area when the ultrasound array is active.

In order to see the effect of the UPL on a single track, two other tracks were printed at a laser power of 700 W. One control track was printed with no applied sound in order to check the change in profile as a function of track location. Its profile is shown in Figs. 6.22. Then another track was printed beside it where the sound was applied using 10 V half way along the track length, and its profile is shown in Fig. 6.23. Although the control track does increase in cross-sectional area (the area increases by 56%), the increase is not as pronounced as when the sound field is activated half way along the track, which produces an increase in cross-sectional area of 229%. The increase of cross-sectional area as the track is made when no sound is applied may be explained by the low baseline catchment efficiency of this particular setup; the low catchment means that there is a powder build-up towards the front of the track as the powder is being deposited.

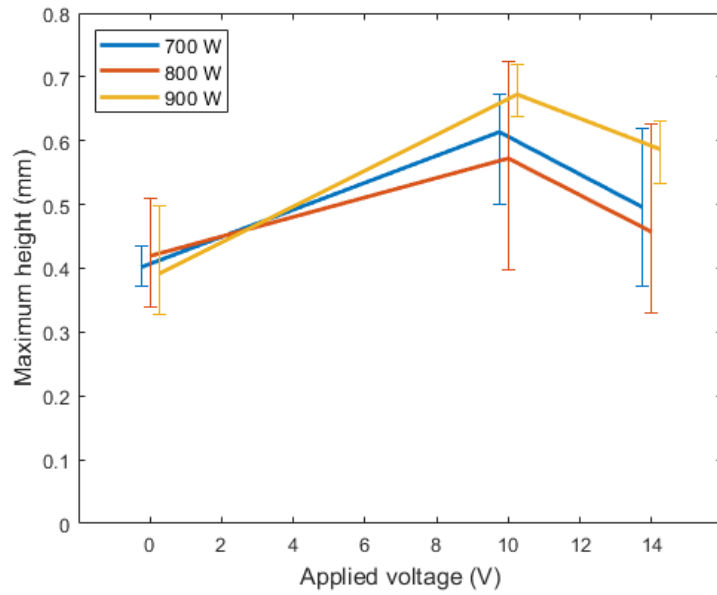


Figure 6.19: Track maximum heights at 15 mm.

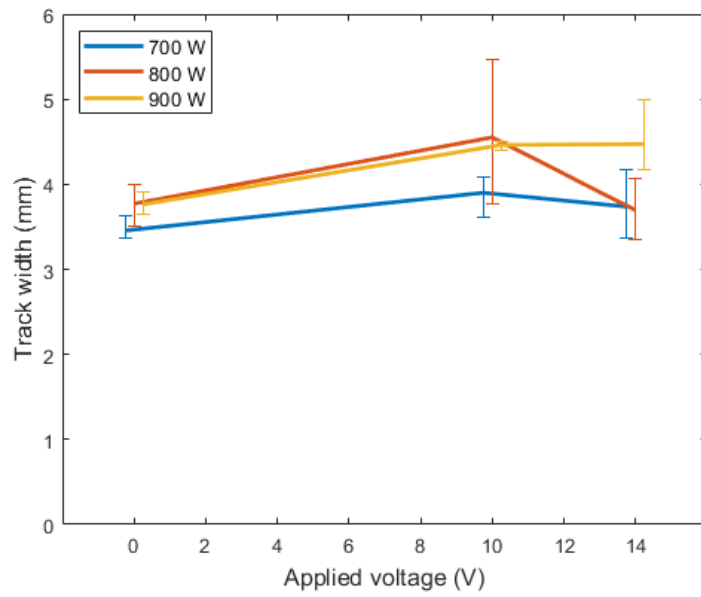


Figure 6.20: Track widths at 15 mm.

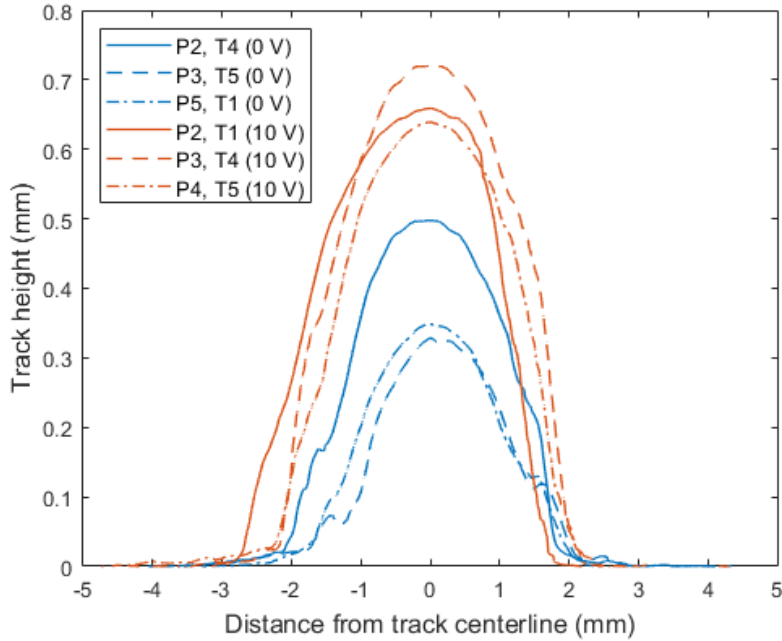


Figure 6.21: Track profiles at 15 mm for the three repeats at 0 and 10 V, at 900 W.

The profile along the track shown in Fig. 6.23 is shown in Fig. 6.24. As can be seen in the average track height, Fig. 6.24(b), taken normal to the red line in Fig. 6.24(a) and between the dotted lines, the height increases to about twice its original value, from halfway along the track to 8 mm after the track center.

6.5.5 Track dilution zone measurements

The track dilution measurements are shown in Fig. 6.25. For laser powers of 700 and 800 W, the dilution fraction and penetration depth decrease when more material is being deposited; this is expected since more of the fixed laser power goes towards melting more material. For a laser power of 900 W this relationship is not observed; one possible explanation for this behavior is that the standard deviation of these measurements at 900 W is much higher, hence no clear relationship, because the stability threshold for the tracks (the power threshold of vaporization) is exceeded [258]. The calculation steps in [258] to determine this threshold was carried out for the laser speed and spot size used in this chapter, using the averaged material properties at ambient and melting temperature, yielding a threshold power of 999 W. This approximate threshold power is close to the 900 W power being used.

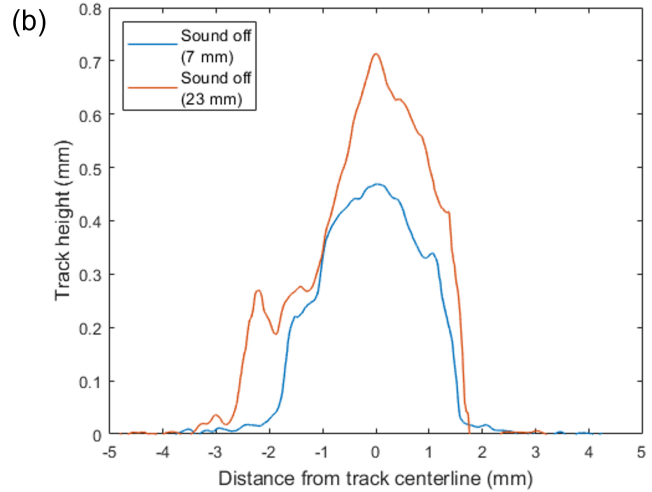
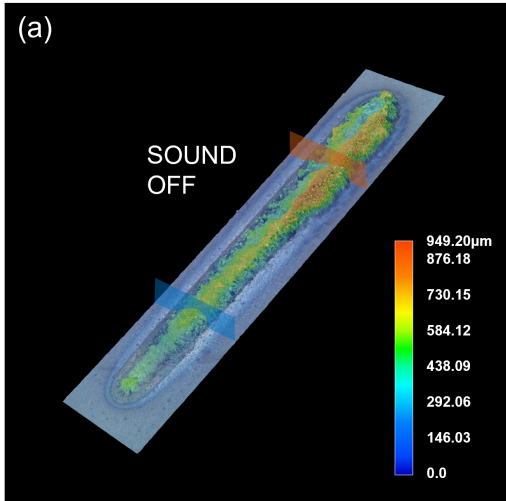


Figure 6.22: (a) 3D track profile for single track with no applied sound. (b) Track cross-sections at 7 and 23 mm from start of track.

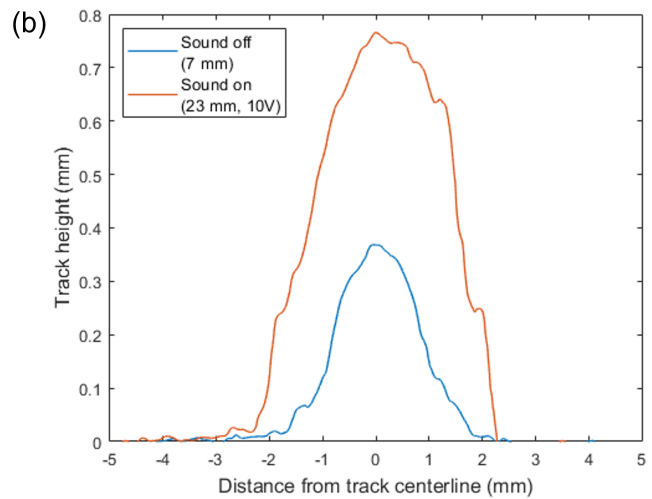
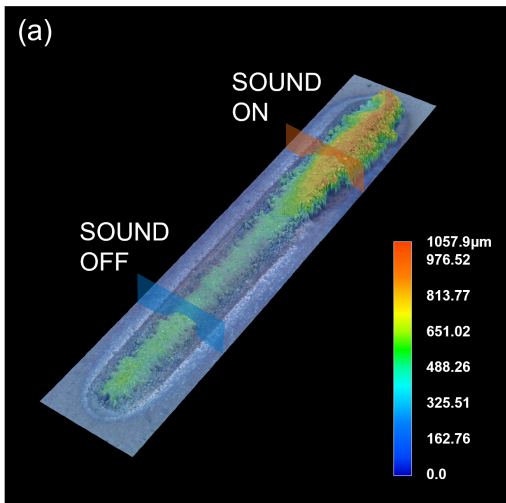


Figure 6.23: (a) 3D track profile for single track with applied sound at 10 V after half way along the track. (b) Track cross-sections at 7 and 23 mm from start of track.

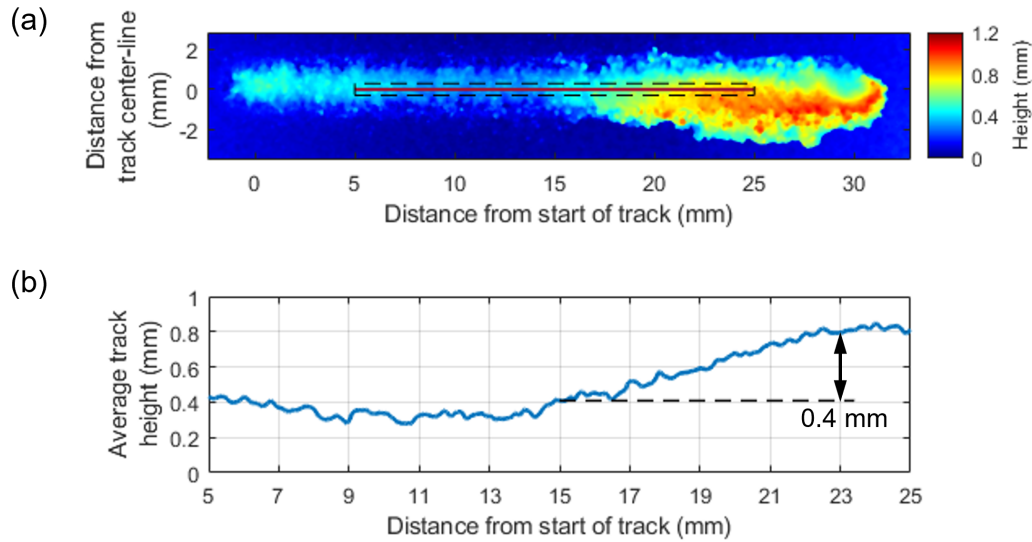


Figure 6.24: (a) Height map of single track with sound being applied halfway along the track. (b) Average height as a function of distance from start of track.

The HAZ width and depth do not vary substantially in all the runs with different applied sound fields, since the size of the HAZ zone depends on the total laser power being dissipated after it is used to melt the powder and build plate, which does not depend on the applied sound field.

6.6 Summary

Based on the results of this chapter the following conclusions were made:

- It was demonstrated that UPL technology can be used in a side feed LDED-PF setup to increase track height by 72%, and cross-sectional area and catchment by 111%, for an original height, area and catchment efficiency of 0.4 mm, 0.93 mm^2 and 15.15% respectively, when using a laser power of 900 W and an array applied voltage of 10 V
- Although the track height and cross-sectional area of the tracks increased, the width of the tracks did not substantially increase; this is possibly due to the laser spot size being constant for the experiments in this chapter

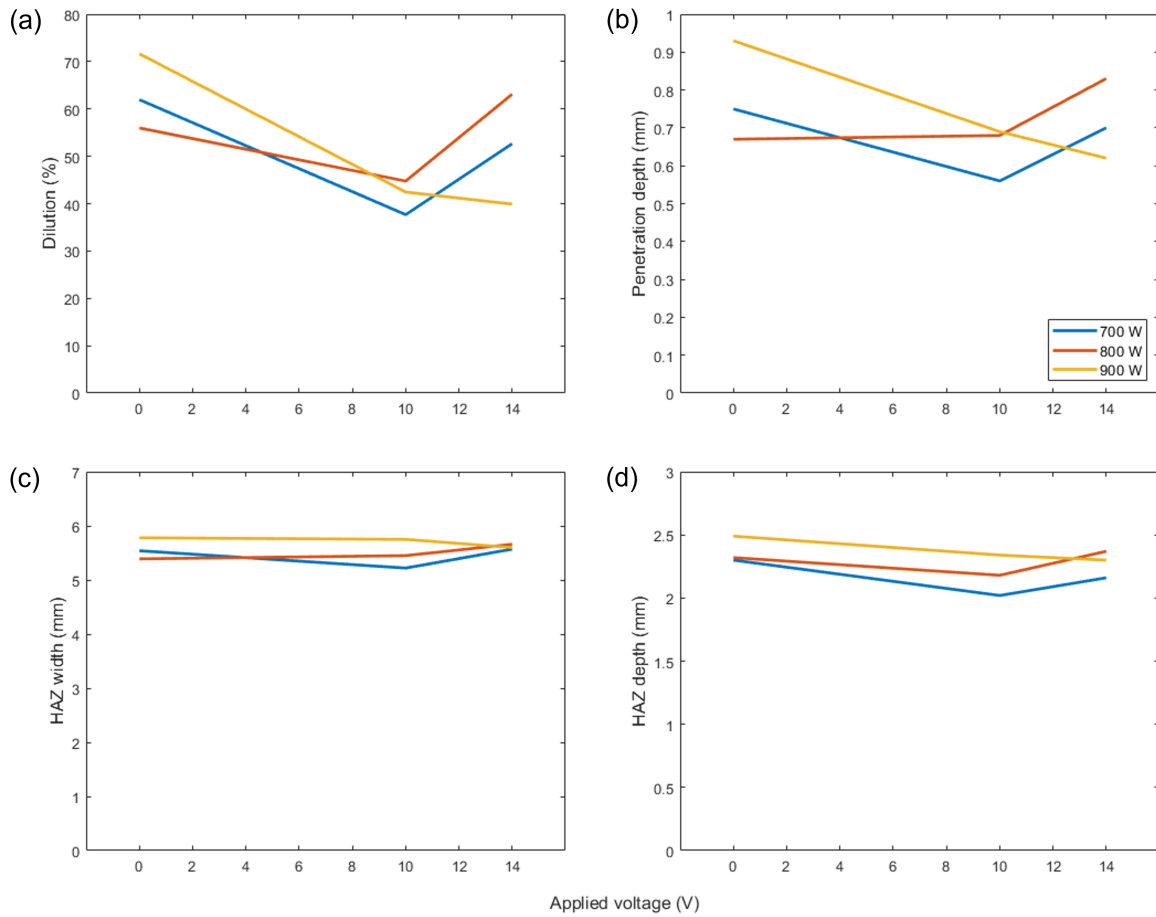


Figure 6.25: For etched samples: (a) dilution fraction, (b) penetration depth, (c) HAZ width, (d) HAZ depth.

Chapter 7

Conclusions and Future Work

7.1 Overall conclusions

In this thesis, ultrasonic-based techniques were developed for two requirements: 1) development of an in-situ non-destructive testing (NDT) system for metal AM processes, in particular using laser ultrasonics (LU), a non-contact NDT modality, and 2) development a setup for finer control of the in-situ placement of the feedstock used in metal AM processes, providing the ability to adaptively change the powder stream cross-sectional shape and size in DED-PF using sound radiation forces, to increase part quality and material utilization.

Regarding the LU setup applied to parts made by LPBF and the tests and reconstructions reported in Chapter 3, the following conclusions can be drawn:

- Defects with a size range from about 200 to 300 μm for bottom hole defects can be recognized from the background noise of the reconstructions, the minimum depth for accurately reconstructing defects at the right depth was about 0.8 mm for bottom hole and trapped powder defects
- The reconstructed defect shapes are tilted ellipses; this might be due to not taking into account the source, defect and/or receiver directivity in the PSM algorithm
- The trapped powder defects produced a satisfactory reconstruction even having less sound impedance mismatch between the metal and the trapped powder, compared to side and blind bottom hole defects. However, further LPBF parameter optimization is required for a required size and shape of artificial defect to be printed successfully

Regarding the implementation of ultrasonic particle lensing (UPL) technology used in DED-PF and reported in Chapters 4 and 6, the following conclusions can be drawn:

- The largest decrease in width, downstream of the applied sound field, was 30 and 31% for Ti6Al4V and SS 316L particles respectively, for a particle speed of 0.6 m/s. This was done using a DED-PF nozzle analog
- Using a more powerful ultrasound phased array, Ti6Al4V particles were successfully focused while tracks were being printed in a LDED-PF machine, at a higher particle speed of 3.6 m/s, which produced a maximum increase in track cross-sectional area of 111%. The focusing effect is maximum at 10 V and decreases slightly at 14 V. This corresponds to the observed widths at the location of the build plate when measuring the particle concentration distribution using a high-speed camera

In addition, regarding the Gaussian beam model reported in Chapter 5, the following conclusions can be drawn:

- The model is able to predict the normally distributed normal velocity components, and close to zero spatial dependence of powder particles close to the nozzle exit in a DED-PF nozzle analog
- Both the slope of the angle of the particle trajectories with respect to the z -axis as a function x and the r^2 values of this function, measured from the trajectories and derived from the model approach similar values when z is large, when the effect of gravitational acceleration is less pronounced
- It was also found that the effect of a focusing force field can be modeled as a gradient index (GRIN) lens in this formalism, and that one can compute the particle concentration distribution orders of magnitude faster than the Monte-Carlo type simulation described in Chapter 4, that takes into account every particle trajectory

7.2 Future work

Regarding LU applied to LPBF and the tests and reconstructions reported in Chapter 3, some future work that can be pursued toward the eventual aim of in-situ LU part inspection is the following:

- Investigating how the variance in the amplitude of A-scans is affected by factors such as generation laser power, surface laser absorptivity and in-situ roughness
- Investigating how to quantify the uncertainty of the reconstructed defect signals, based on modeling background noise due to grain scattering for example, and estimating the probability that a defect signal is present using a Bayesian framework [260]. These methods could be extended [261] to produce a probability of detection (POD) plot [262], and compare it to one found experimentally. PODs show the likelihood of detection as a function of a characteristic parameter of the flaw, such as its size. These plots are used when performing UT of aerospace components for example, where defect detection is of critical importance. PODs can also be generated in some cases by analytic modeling of the relevant sound propagation physics [263, 264], or using numerical simulations [265]. In [265], the application was the UT of AM components. Parameters such as defect size, which have a significant impact on inspection results, were specified with reasonable uncertainties and distributions based on an uncertainty propagation method.
- Using an algorithm for the single offset integral that is adaptive and has a quantifiable error. Another option is to bypass this issue by using Eq. 3.11 recording many k_h values as part of a frequency based TFM technique, however the measurement time will substantially increase
- Testing an extended PSM or SAR algorithm taking into account directivity functions and comparing it with the algorithm reported in Chapter 3
- Using a laser with a smaller pulse width (≈ 1 ns), and a detector with a corresponding larger frequency bandwidth, in order to increase the LU system's resolution. However, there is a trade-off between laser cost and pulse energy for a given pulse width
- Sample fabrication for very small artificial defects will be more challenging; making smaller and more accurate blind holes for example (without them closing in due to melting) might be possible with optimized LPBF process parameters tailored for the defect sample being printed or using diamond micro-drilling as a post-processing

step. Another option to investigate is using different LPBF process parameters to induce actual defects in a very small volume of the sample $< (0.5 \text{ mm})^3$, in order to have some control over the number and separation of the expected defects

- Trying the Fourier slice theorem based filter for more complicated geometries, i.e. tilted back-walls that produce tilted lines in the B-scan. This would correspond to applying LU when building a part that has a large down-facing slope for example. Further work will be required to quickly compute the reflection signals expected on the B-scan due to nearby surfaces in the component being printed (i.e. from the STL file). The filter could also be improved by explicitly using the 2D FT of the SLW signal instead of notch filters using one particular frequency
- Implementing the above algorithms and setup in a commercial or open source LPBF machine such as a PANDA 11 LPBF machine from OpenAdditive LLC

Regarding the implementation of UPL technology in DED-PF (Chapters 4 and 6), the following subjects could be investigated:

- Further tests will be necessary to have an accurate estimate of the variance of track and dilution zone geometric features, such as track cross sectional area, catchment efficiency and track height, shown in Figs. 6.18 and 6.19, as a function of array applied voltage
- A track geometry simulation like the one described in [40] could be used to help quantify the uncertainty in the measurements shown in Figs. 6.22 and 6.23, where the sound is applied half-way along the track. The simulation may explain the slight increase in track cross-sectional area along the track even when sound is not applied
- Further studies can be conducted to explicitly find the minimum offset distance between the nozzle and the build plate that does not affect the track or microstructure; this would also increase the baseline catchment efficiency. Increasing the transducer frequency would allow the size of the UPL effective “lens” to be smaller so the gap between the nozzle exit and build plate can be smaller as well, also increasing catchment efficiency. The current phase control setup does not allow for finer control of the force profile; the effective lens height and width ratio do not change with transducer frequency. Finer control of the force field profile may be done by adjusting both transducer phase and amplitude


- Better modeling of the effect of the SRF on the powder stream might be achieved by taking into account the change in the force field along the z-axis by using a group of GRIN lens elements in series instead of a single GRIN element
- The lower amount of focusing at 14 V might also be due to sound wave distortion effects due to the high ASP pressures that approach a significant fraction of atmospheric pressure causing non-linear propagation. These effects can be taken into account by using the angular spectrum approach for example, to find the required transducer signals to get a required sound field around the sound focal point, taking into account sound non-linearity
- The gas cyclone was designed and used to have finer control of the particle speed; the DMD-IC106 gas flow rates needed to get the speeds used in Chapters 6 are on the low end of the DMD-IC106 specifications, resulting in variable particle speeds. The use of a gas cyclone may not be required when using the DMD-IC106 machine if the setup is further optimized to work at higher particle speeds, or if a more powerful UPL array is used
- Tests can be carried out to measure the effect of using an Argon-Helium mix, as described in Appendix N, on the UPL-LDED-PF process. Currently available transducers could be tested for their response such as resonant frequency and sound intensity as a function of distance under an Argon atmosphere in order to produce more accurate sound propagation models and UPL-LDED-PF process without using a gas mix. Novel transducers could also be designed and fabricated to work under an Argon or other atmospheres
- Other more accurate fixturing and alignment methods could be used to increase the alignment between the nozzle center-line, the sound field focal point and the laser spot on the build plate
- The size of the array can be substantially reduced by running a smaller number of transducers at a higher voltage to produce a higher sound intensity per transducer, but may require active cooling. This can be done by integrating internal channels in the array that use the water loop used for cooling the LDED-PF machine's laser optics. One can also procure transducers that do not have a casing to reduce their form factor and attach them directly to the array; this will also improve heat transfer
- In order to print tracks of different sizes including adjusting their width, other features of the UPL-LDED-PF setup may need to be adjustable, for example using in-situ control of the laser spot width


- UPL technology may be used to change the cross-sectional area of the powder stream and deflect the powder stream by a small angle. This could be modeled using the Gaussian beam representation of the powder stream and the tensor ABCD law

The Gaussian beam model reported in Chapter 5 could be investigated further, or its range of applicability extended, in the following ways:

- Modeling the powder stream as a Gaussian beam, besides allowing the simulation of focusing from a radially symmetric force field, could also be used to model powder stream spot shape changes due to a non-symmetric force field, using the tensor ABCD law [244], and powder stream small angle deflection with a force field, using a decentered (with respect to a GRIN lens corresponding to an off-center vortex sound force field for example) Gaussian beam formalism [266]
- It may also be possible to use a coordinate transformation along the z axis in order to take into account gravitational acceleration
- Although the modeling of the powder flow inside and at the nozzle exit of a DED-PF nozzle was not investigated, the proposed particle concentration and velocity distributions for the particles downstream of the nozzle exit in Chapter 5 may be used to investigate the accuracy of those types of models. Also note the concentration distribution experimentally will approach a rectangular function at the nozzle exit; this may be modeled using a flattened Gaussian beam, which is known to approach a Gaussian beam profile as the propagation distance increases [267]. This has not been considered before since the nozzle exit diameter is usually much shorter than the nozzle/build plate distance in DED-PF. One simple case to study is a tube nozzle, with available experimental data for different tube aspect ratios, gas flows and particle properties [33, 231], and that could be simulated modeling the powder as a discrete phase, and using Lagrangian particle tracking with reflections, considering the coefficient of restitution, as a boundary condition [210]
- More accurate powder stream PCD measurements may be made using a laser sheet setup, more advanced particle segmentation methods (for particle number and size) compared to thresholding, and an estimate of the number of high-speed camera frames needed to get a required variance at each location of the measured PCD
- The powder stream model could be used for more accurate DED-PF melt pool simulations that include a powder stream [268] and modeling a laser beam with the Gaussian beam representation could be used in simulations of laser interaction with metal powder in the laser powder bed fusion process [269, 38]

Letters of Copyright Permission

Home Help Live Chat Sign in Create Account



On the application of sound radiation force for focusing of powder stream in directed energy deposition
Author: A. Martinez-Marchese, M. Ansari, M. Wang, A. Marzo, E. Toyserkani
Publication: Ultrasonics
Publisher: Elsevier
Date: January 2023
© 2022 Published by Elsevier B.V.

Journal Author Rights

Please note that, as the author of this Elsevier article, you retain the right to include it in a thesis or dissertation, provided it is not published commercially. Permission is not required, but please ensure that you reference the journal as the original source. For more information on this and on your other retained rights, please visit: <https://www.elsevier.com/about/our-business/policies/copyright#Author-rights>

[BACK](#) [CLOSE WINDOW](#)

© 2022 Copyright - All Rights Reserved | [Copyright Clearance Center, Inc.](#) | [Privacy statement](#) | [Data Security and Privacy](#)
| [For California Residents](#) | [Terms and Conditions](#) Comments? We would like to hear from you. E-mail us at customer-care@copyright.com

Permission for article adapted for Chapter 4



Directed energy deposition powder stream modeling using a Gaussian beam ray representation

Author: A. Martinez-Marchese, M. Klumpp, E. Toyserkani

Publication: Powder Technology

Publisher: Elsevier

Date: November 2022

© 2022 Elsevier B.V. All rights reserved.

Journal Author Rights

Please note that, as the author of this Elsevier article, you retain the right to include it in a thesis or dissertation, provided it is not published commercially. Permission is not required, but please ensure that you reference the journal as the original source. For more information on this and on your other retained rights, please visit: <https://www.elsevier.com/about/our-business/policies/copyright#Author-rights>

BACK

CLOSE WINDOW

Permission for article adapted for Chapter 5

SPRINGER NATURE LICENSE TERMS AND CONDITIONS

Dec 05, 2022

This Agreement between Mr. Alejandro P Martinez ("You") and Springer Nature ("Springer Nature") consists of your license details and the terms and conditions provided by Springer Nature and Copyright Clearance Center.

License Number	5442741052161
License date	Dec 05, 2022
Licensed Content Publisher	Springer Nature
Licensed Content Publication	Journal of Materials Engineering and Performance
Licensed Content Title	Metal Additive Manufacturing: A Review
Licensed Content Author	William E. Frazier
Licensed Content Date	Apr 8, 2014
Type of Use	Thesis/Dissertation
Requestor type	academic/university or research institute
Format	print and electronic
Portion	figures/tables/illustrations
Number of figures/tables /illustrations	1
Will you be translating?	no
Circulation/distribution	10000 - 19999
Author of this Springer Nature content	no
Title	Monitoring and Control of Metal Additive Manufacturing Processes Using Ultrasound
Institution name	University of Waterloo
Expected presentation date	Jan 2024
Portions	Figure 8
Requestor Location	Mr. Alejandro P Martinez 292-350 Columbia St. West Waterloo, ON N2L 6P7 Canada Attn: Mr. Alejandro Martinez
Total	0.00 CAD

Permission for Fig. 2.1

AIP PUBLISHING LICENSE TERMS AND CONDITIONS

Dec 05, 2022

This Agreement between Mr. Alejandro P Martinez ("You") and AIP Publishing ("AIP Publishing") consists of your license details and the terms and conditions provided by AIP Publishing and Copyright Clearance Center.

License Number	5442610063583
License date	Dec 05, 2022
Licensed Content Publisher	AIP Publishing
Licensed Content Publication	Applied Physics Reviews
Licensed Content Title	Laser powder bed fusion additive manufacturing of metals; physics, computational, and materials challenges
Licensed Content Author	W. E. King, A. T. Anderson, R. M. Ferencz, et al
Licensed Content Date	Dec 1, 2015
Licensed Content Volume	2
Licensed Content Issue	4
Type of Use	Thesis/Dissertation
Requestor type	Author (original article)
Format	Print and electronic
Portion	Figure/Table
Number of figures/tables	1
Will you be translating?	No
Title	Monitoring and Control of Metal Additive Manufacturing Processes Using Ultrasound
Institution name	University of Waterloo
Expected presentation date	Jan 2024
Portions	Figure 1
Requestor Location	Mr. Alejandro P Martinez 292-350 Columbia St. West Waterloo, ON N2L 6P7 Canada Attn: Mr. Alejandro Martinez
Total	0.00 CAD

Permission for Fig. 2.2

ELSEVIER LICENSE TERMS AND CONDITIONS

Dec 05, 2022

This Agreement between Mr. Alejandro P Martinez ("You") and Elsevier ("Elsevier") consists of your license details and the terms and conditions provided by Elsevier and Copyright Clearance Center.

License Number	5442751090038
License date	Dec 05, 2022
Licensed Content Publisher	Elsevier
Licensed Content Publication	Acta Materialia
Licensed Content Title	Additive manufacturing of metals
Licensed Content Author	Dirk Herzog, Vanessa Seyda, Eric Wycisk, Claus Emmelmann
Licensed Content Date	Sep 15, 2016
Licensed Content Volume	117
Licensed Content Issue	n/a
Licensed Content Pages	22
Start Page	371
End Page	392
Type of Use	reuse in a thesis/dissertation
Portion	figures/tables/illustrations
Number of figures/tables/illustrations	1
Format	both print and electronic
Are you the author of this Elsevier article?	No
Will you be translating?	No
Title	Monitoring and Control of Metal Additive Manufacturing Processes Using Ultrasound
Institution name	University of Waterloo
Expected presentation date	Jan 2024
Portions	Figure 4
Requestor Location	Mr. Alejandro P Martinez 292-350 Columbia St. West Waterloo, ON N2L 6P7 Canada Attn: Mr. Alejandro Martinez
Publisher Tax ID	GB 494 6272 12
Total	0.00 CAD

Permission for Fig. 2.3

ELSEVIER LICENSE TERMS AND CONDITIONS

Dec 05, 2022

This Agreement between Mr. Alejandro P Martinez ("You") and Elsevier ("Elsevier") consists of your license details and the terms and conditions provided by Elsevier and Copyright Clearance Center.

License Number	5442760561831
License date	Dec 05, 2022
Licensed Content Publisher	Elsevier
Licensed Content Publication	Additive Manufacturing
Licensed Content Title	An overview of Direct Laser Deposition for additive manufacturing; Part II: Mechanical behavior, process parameter optimization and control
Licensed Content Author	Nima Shamsaei,Aref Yadollahi,Linkan Bian,Scott M. Thompson
Licensed Content Date	Oct 1, 2015
Licensed Content Volume	8
Licensed Content Issue	n/a
Licensed Content Pages	24
Start Page	12
End Page	35
Type of Use	reuse in a thesis/dissertation
Portion	figures/tables/illustrations
Number of figures/tables /illustrations	1
Format	both print and electronic
Are you the author of this Elsevier article?	No
Will you be translating?	No
Title	Monitoring and Control of Metal Additive Manufacturing Processes Using Ultrasound
Institution name	University of Waterloo
Expected presentation date	Jan 2024
Portions	Figure 1
Requestor Location	Mr. Alejandro P Martinez 292-350 Columbia St. West Waterloo, ON N2L 6P7 Canada Attn: Mr. Alejandro Martinez
Publisher Tax ID	GB 494 6272 12
Total	0.00 CAD

Permission for Fig. 2.6

ELSEVIER LICENSE TERMS AND CONDITIONS

Dec 05, 2022

This Agreement between Mr. Alejandro P Martinez ("You") and Elsevier ("Elsevier") consists of your license details and the terms and conditions provided by Elsevier and Copyright Clearance Center.

License Number	5442760909173
License date	Dec 05, 2022
Licensed Content Publisher	Elsevier
Licensed Content Publication	International Journal of Heat and Mass Transfer
Licensed Content Title	Modeling of coaxial powder flow for the laser direct deposition process
Licensed Content Author	S.Y. Wen, Y.C. Shin, J.Y. Murthy, P.E. Sojka
Licensed Content Date	Dec 1, 2009
Licensed Content Volume	52
Licensed Content Issue	25-26
Licensed Content Pages	11
Start Page	5867
End Page	5877
Type of Use	reuse in a thesis/dissertation
Portion	figures/tables/illustrations
Number of figures/tables /illustrations	1
Format	both print and electronic
Are you the author of this Elsevier article?	No
Will you be translating?	No
Title	Monitoring and Control of Metal Additive Manufacturing Processes Using Ultrasound
Institution name	University of Waterloo
Expected presentation date	Jan 2024
Portions	Figure 7
Requestor Location	Mr. Alejandro P Martinez 292-350 Columbia St. West Waterloo, ON N2L 6P7 Canada Attn: Mr. Alejandro Martinez
Publisher Tax ID	GB 494 6272 12
Total	0.00 CAD

Permission for Fig. 2.7

ELSEVIER LICENSE TERMS AND CONDITIONS

Dec 05, 2022

This Agreement between Mr. Alejandro P Martinez ("You") and Elsevier ("Elsevier") consists of your license details and the terms and conditions provided by Elsevier and Copyright Clearance Center.

License Number	5442770036439
License date	Dec 05, 2022
Licensed Content Publisher	Elsevier
Licensed Content Publication	Journal of Materials Processing Technology
Licensed Content Title	Numerical investigation of gas-disperse jet flows created by coaxial nozzles during the laser direct material deposition
Licensed Content Author	O.B. Kovalev,I.O. Kovaleva,I. Yu. Smurov
Licensed Content Date	Nov 1, 2017
Licensed Content Volume	249
Licensed Content Issue	n/a
Licensed Content Pages	10
Start Page	118
End Page	127
Type of Use	reuse in a thesis/dissertation
Portion	figures/tables/illustrations
Number of figures/tables /illustrations	2
Format	both print and electronic
Are you the author of this Elsevier article?	No
Will you be translating?	No
Title	Monitoring and Control of Metal Additive Manufacturing Processes Using Ultrasound
Institution name	University of Waterloo
Expected presentation date	Jan 2024
Portions	Figures 2 and 7
Requestor Location	Mr. Alejandro P Martinez 292-350 Columbia St. West Waterloo, ON N2L 6P7 Canada Attn: Mr. Alejandro Martinez
Publisher Tax ID	GB 494 6272 12
Total	0.00 CAD

Permission for Fig. 2.8

SPRINGER NATURE

Holographic acoustic elements for manipulation of levitated objects

Author: Asier Marzo et al
Publication: Nature Communications
Publisher: Springer Nature
Date: Oct 27, 2015

Copyright © 2015, The Author(s)

Creative Commons

This is an open access article distributed under the terms of the [Creative Commons CC BY](#) license, which permits unrestricted use, distribution, and reproduction in any medium, provided the original work is properly cited.

You are not required to obtain permission to reuse this article.

To request permission for a type of use not listed, please contact [Springer Nature](#)

Permission for Figs. 2.11 and 2.12

References

- [1] Jess M Waller, Regor L Saulsberry, Bradford H Parker, Kenneth L Hodges, Eric R Burke, and Karen M Taminger. Summary of NDE of additive manufacturing efforts in NASA. In *AIP Conference Proceedings*, volume 1650, pages 51–62. American Institute of Physics, 2015.
- [2] SBIR-17-1-Z3.01-8823 | Abstract - In-Line Inspection of Additive Manufactured Parts Using Laser Ultrasonics. <https://sbir.nasa.gov/SBIR/abstracts/17/sbir/phase1/SBIR-17-1-Z3.01-8823.html>. Last visited on 06/12/2022.
- [3] Christopher B Scruby and Leslie E Drain. *Laser ultrasonics techniques and applications*. CRC press, 1990.
- [4] F Honarvar and A Varvani-Farahani. A review of ultrasonic testing applications in additive manufacturing: Defect evaluation, material characterization, and process control. *Ultrasonics*, 108:106227, 2020.
- [5] Yuyang Ma, Zhenlin Hu, Yun Tang, Shixiang Ma, Yanwu Chu, Xin Li, Wei Luo, Lianbo Guo, Xiaoyan Zeng, and Yongfeng Lu. Laser opto-ultrasonic dual detection for simultaneous compositional, structural, and stress analyses for wire + arc additive manufacturing. *Additive Manufacturing*, 31:100956, 2020.
- [6] Relativity Space Inc. <https://www.relativityspace.com/>. Last visited on 06/12/2022.
- [7] Launcher Inc. <https://launcherspace.com/>. Last visited on 06/12/2022.
- [8] Richard Russell, Douglas Wells, Jess Waller, Behrang Poorganji, Eric Ott, Tsuyoshi Nakagawa, Hector Sandoval, Nima Shamsaei, and Mohsen Seifi. Qualification and certification of metal additive manufactured hardware for aerospace applications. In *Additive Manufacturing for the Aerospace Industry*, pages 33–66. Elsevier, 2019.

- [9] Manufacturing Solutions | Formalloy. <https://www.formalloy.com/manufacturing-solutions>. Last visited on 06/12/2022.
- [10] Paul R Gradl, Christopher S Protz, and Tal Wammen. Additive manufacturing and hot-fire testing of liquid rocket channel wall nozzles using blown powder directed energy deposition Inconel 625 and JBK-75 alloys. In *AIAA Propulsion and Energy 2019 Forum*, page 4362, 2019.
- [11] Aerospace | Insstek. http://www.insstek.com/content/aerospace_view. Last visited on 06/12/2022.
- [12] ASTM, ISO. ASTM52900-15 Standard Terminology for Additive Manufacturing—General Principles—Terminology. *ASTM International, West Conshohocken, PA*, 3(4):5, 2015.
- [13] I Campbell, Olaf Diegel, J Kowen, and T Wohlers. *Wohlers report 2018: 3D printing and additive manufacturing state of the industry: annual worldwide progress report*. Wohlers Associates, 2018.
- [14] 3D HUBS. Additive manufacturing technologies: An overview. <https://www.hubs.com/knowledge-base/types-of-3d-printing/>. Last visited on 06/12/2022.
- [15] Scott M Thompson, Linkan Bian, Nima Shamsaei, and Aref Yadollahi. An overview of Direct Laser Deposition for additive manufacturing; Part I: Transport phenomena, modeling and diagnostics. *Additive Manufacturing*, 8:36–62, 2015.
- [16] William E Frazier. Metal additive manufacturing: a review. *Journal of Materials Engineering and Performance*, 23(6):1917–1928, 2014.
- [17] Dirk Herzog, Vanessa Seyda, Eric Wycisk, and Claus Emmelmann. Additive manufacturing of metals. *Acta Materialia*, 117:371–392, 2016.
- [18] Chor Yen Yap, Chee Kai Chua, Zhi Li Dong, Zhong Hong Liu, Dan Qing Zhang, Loong Ee Loh, and Swee Leong Sing. Review of selective laser melting: Materials and applications. *Applied physics reviews*, 2(4):041101, 2015.
- [19] Wayne E King, Andrew T Anderson, Robert M Ferencz, Neil E Hodge, Chandrika Kamath, Saad A Khairallah, and Alexander M Rubenchik. Laser powder bed fusion additive manufacturing of metals; physics, computational, and materials challenges. *Applied Physics Reviews*, 2(4):041304, 2015.

- [20] Silvia Vock, Burghardt Klöden, Alexander Kirchner, Thomas Weißgärber, and Bernd Kieback. Powders for powder bed fusion: a review. *Progress in Additive Manufacturing*, pages 1–15, 2019.
- [21] Tarasankar DebRoy, HL Wei, JS Zuback, T Mukherjee, JW Elmer, JO Milewski, Allison Michelle Beese, A Wilson-Heid, A De, and W Zhang. Additive manufacturing of metallic components—process, structure and properties. *Progress in Materials Science*, 92:112–224, 2018.
- [22] Hahn Choo, Kin-Ling Sham, John Bohling, Austin Ngo, Xianghui Xiao, Yang Ren, Philip J Depond, Manyalibo J Matthews, and Elena Garlea. Effect of laser power on defect, texture, and microstructure of a laser powder bed fusion processed 316L stainless steel. *Materials & Design*, 164:107534, 2019.
- [23] Y Morris Wang, Thomas Voisin, Joseph T McKeown, Jianchao Ye, Nicholas P Calta, Zan Li, Zhi Zeng, Yin Zhang, Wen Chen, Tien Tran Roehling, et al. Additively manufactured hierarchical stainless steels with high strength and ductility. *Nature materials*, 17(1):63–71, 2018.
- [24] Shuo Yin, Pasquale Cavaliere, Barry Aldwell, Richard Jenkins, Hanlin Liao, Wenya Li, and Rocco Lupoi. Cold spray additive manufacturing and repair: Fundamentals and applications. *Additive manufacturing*, 21:628–650, 2018.
- [25] Nima Shamsaei, Aref Yadollahi, Linkan Bian, and Scott M Thompson. An overview of Direct Laser Deposition for additive manufacturing; Part II: Mechanical behavior, process parameter optimization and control. *Additive Manufacturing*, 8:12–35, 2015.
- [26] OB Kovalev, IO Kovaleva, and I Yu Smurov. Numerical investigation of gas-disperse jet flows created by coaxial nozzles during the laser direct material deposition. *Journal of Materials Processing Technology*, 249:118–127, 2017.
- [27] Bi Zhang, Yongtao Li, and Qian Bai. Defect formation mechanisms in selective laser melting: a review. *Chinese Journal of Mechanical Engineering*, 30(3):515–527, 2017.
- [28] R. Vilar. 10.07 - laser powder deposition. In Saleem Hashmi, Gilmar Ferreira Batalha, Chester J. [Van Tyne], and Bekir Yilbas, editors, *Comprehensive Materials Processing*, pages 163 – 216. Elsevier, Oxford, 2014.

- [29] Chu Lun Alex Leung, Sebastian Marussi, Robert C Atwood, Michael Towrie, Philip J Withers, and Peter D Lee. In situ X-ray imaging of defect and molten pool dynamics in laser additive manufacturing. *Nature communications*, 9(1):1–9, 2018.
- [30] Saad A Khairallah, Andrew T Anderson, Alexander Rubenchik, and Wayne E King. Laser powder-bed fusion additive manufacturing: Physics of complex melt flow and formation mechanisms of pores, spatter, and denudation zones. *Acta Materialia*, 108:36–45, 2016.
- [31] H-W Mindt, O Desmaison, M Megahed, A Peralta, and J Neumann. Modeling of powder bed manufacturing defects. *Journal of Materials Engineering and Performance*, 27(1):32–43, 2018.
- [32] M Picasso, CF Marsden, JD Wagniere, A Frenk, and M Rappaz. A simple but realistic model for laser cladding. *Metallurgical and materials transactions B*, 25(2):281–291, 1994.
- [33] Ehsan Toyserkani, Amir Khajepour, and Stephen Corbin. *Laser cladding*. CRC press, 2004.
- [34] Yuze Huang, Mir Behrad Khamesee, and Ehsan Toyserkani. A comprehensive analytical model for laser powder-fed additive manufacturing. *Additive Manufacturing*, 12:90–99, 2016.
- [35] Yuze Huang, Mir Behrad Khamesee, and Ehsan Toyserkani. A new physics-based model for laser directed energy deposition (powder-fed additive manufacturing): From single-track to multi-track and multi-layer. *Optics & Laser Technology*, 109:584–599, 2019.
- [36] Srdja Zekovic, Rajeev Dwivedi, and Radovan Kovacevic. Numerical simulation and experimental investigation of gas–powder flow from radially symmetrical nozzles in laser-based direct metal deposition. *International Journal of Machine Tools and Manufacture*, 47(1):112–123, 2007.
- [37] SY Wen, YC Shin, JY Murthy, and PE Sojka. Modeling of coaxial powder flow for the laser direct deposition process. *International Journal of Heat and Mass Transfer*, 52(25-26):5867–5877, 2009.

- [38] Wim Devesse, Dieter De Baere, and Patrick Guillaume. Modeling of laser beam and powder flow interaction in laser cladding using ray-tracing. *Journal of Laser Applications*, 27(S2):S29208, 2015.
- [39] OB Kovalev, DV Bedenko, and AV Zaitsev. Development and application of laser cladding modeling technique: From coaxial powder feeding to surface deposition and bead formation. *Applied Mathematical Modelling*, 57:339–359, 2018.
- [40] DV Bedenko and OB Kovalev. Modelling of heat and mass transfer in the laser cladding during direct metal deposition. *Thermophysics and Aeromechanics*, 20(2):251–261, 2013.
- [41] W Ou, T Mukherjee, GL Knapp, Y Wei, and T DebRoy. Fusion zone geometries, cooling rates and solidification parameters during wire arc additive manufacturing. *International Journal of Heat and Mass Transfer*, 127:1084–1094, 2018.
- [42] Charles Hellier. *Handbook of nondestructive evaluation*. McGraw-Hill Education, 2001.
- [43] Leonardo De Chiffre, Simone Carmignato, J-P Kruth, Robert Schmitt, and Albert Weckenmann. Industrial applications of computed tomography. *CIRP annals*, 63(2):655–677, 2014.
- [44] Frank Natterer. *The mathematics of computerized tomography*. SIAM, 2001.
- [45] Ruzlaini Ghoni, Mahmood Dollah, Aizat Sulaiman, and Fadhil Mamat Ibrahim. Defect characterization based on eddy current technique: Technical review. *Advances in Mechanical Engineering*, 6:182496, 2014.
- [46] Clemente Ibarra-Castanedo, Francois Galmiche, Akbar Darabi, Mariacristina Pilla, Matthieu Klein, Adel Ziadi, Steve Vallerand, Jean-François Pelletier, and Xavier P Maldague. Thermographic nondestructive evaluation: overview of recent progress. In *Thermosense XXV*, volume 5073, pages 450–459. International Society for Optics and Photonics, 2003.
- [47] Timothy G Leighton. What is ultrasound? *Progress in biophysics and molecular biology*, 93(1-3):3–83, 2007.
- [48] Joseph W Goodman. *Introduction to Fourier optics*. Roberts and Company Publishers, 2005.

- [49] Josef Krautkrämer and Herbert Krautkrämer. *Ultrasonic testing of materials*. Springer Science & Business Media, 2013.
- [50] How to Analyse C-scan Mapping? <https://sonatest.com/resources/educational-notes/how-analyse-c-scan-mapping>. Last visited on 06/12/2022.
- [51] Community College Ultrasonic Testing. <https://www.nde-ed.org/NDETechniques/Ultrasonics/index.xhtml>. Last visited on 06/12/2022.
- [52] Lawrence E Kinsler, Austin R Frey, Alan B Coppens, and James V Sanders. Fundamentals of acoustics. *Fundamentals of Acoustics, 4th Edition, by Lawrence E. Kinsler, Austin R. Frey, Alan B. Coppens, James V. Sanders, pp. 560. ISBN 0-471-84789-5. Wiley-VCH, December 1999.*, page 560, 1999.
- [53] Tao Wan, Takashi Naoe, Takashi Wakui, Masatoshi Futakawa, Hironari Obayashi, and Toshinobu Sasa. Effects of grain size on ultrasonic attenuation in type 316L stainless steel. *Materials*, 10(7):753, 2017.
- [54] Anton Van Pamel. *Ultrasonic inspection of highly scattering materials*. PhD thesis, Imperial College London, 2015.
- [55] Haim Azhari. *Basics of biomedical ultrasound for engineers*. John Wiley & Sons, 2010.
- [56] Leo Leroy Beranek and Tim Mellow. *Acoustics: sound fields and transducers*. Academic Press, 2012.
- [57] Stephen A Mosey, Peter Charlton, and Ian Wells. A Modified Synthetic Aperture Focussing Technique Utilising the Spatial Impulse Response of the Ultrasound Transducer, 2013.
- [58] W Arnold, M Kroning, and F Walte. Imaging in Non-Destructive Testing. <https://www.ndt.net/article/imagingNDE2007/Arnold.pdf>. Last visited on 06/12/2022.
- [59] V Schmitz, P Höller, and KJ Langenberg. Reconstruction of defect geometries in ultrasonic NDT. *Review of Progress in Quantitative Nondestructive Evaluation*, 1986.
- [60] Karl-Jörg Langenberg, René Marklein, and Klaus Mayer. *Ultrasonic nondestructive testing of materials: theoretical foundations*. CRC Press, 2012.

- [61] Martin Spies, Hans Rieder, Alexander Dillhöfer, Volker Schmitz, and Wolfgang Müller. Synthetic aperture focusing and time-of-flight diffraction ultrasonic imaging—past and present. *Journal of Nondestructive Evaluation*, 31(4):310–323, 2012.
- [62] T Stepinski. SAFT performance in ultrasonic inspection of coarse grained metals. In *Proc. of the 6th Int. Conf. on NDE in Relation to Structural Integrity for Nuclear Pressurised Components, Budapest*, pages 8–10, 2007.
- [63] Tomas Olofsson. Phase shift migration for imaging layered objects and objects immersed in water. *IEEE transactions on ultrasonics, ferroelectrics, and frequency control*, 57(11):2522–2530, 2010.
- [64] H Dale Collins and R Parks Gribble. Acoustic holographic scanning techniques for imaging flaws in thick metal sections. In *Imaging Techniques for Testing and Inspection*, volume 29, pages 67–82. International Society for Optics and Photonics, 1972.
- [65] BP Hildebrand, TJ Davis, AJ Boland, and RL Silta. A portable digital ultrasonic holography system for imaging flaws in heavy section materials. *IEEE transactions on sonics and ultrasonics*, 31(4):287–294, 1984.
- [66] Richard Y Chiao, Robert S Gilmore, and Thomas G Kincaid. Ultrasonic synthetic-aperture holographic imaging. In *Review of Progress in Quantitative Nondestructive Evaluation*, pages 813–820. Springer, 1992.
- [67] KJ Langenberg, M Berger, Th Kreutter, K Mayer, and V Schmitz. Synthetic aperture focusing technique signal processing. *NDT international*, 19(3):177–189, 1986.
- [68] K Mayer, R Marklein, KJ Langenberg, and T Kreutter. An Ultrasonic Imaging System for Three-Dimensional High-Resolution Defect Imaging. In *Review of Progress in Quantitative Nondestructive Evaluation*, pages 967–974. Springer, 1990.
- [69] Deepa Dhamodharan. Investigation of Holographic Reconstruction Algorithms in Near-field Acoustical Holography. Master’s thesis, Hochschule Bremen, 2006.
- [70] Bruce W Drinkwater and Paul D Wilcox. Ultrasonic arrays for non-destructive evaluation: A review. *NDT & e International*, 39(7):525–541, 2006.
- [71] L.W. Schmerr. *Fundamentals of Ultrasonic Phased Arrays*. Springer International Publishing, 2014.

- [72] Colin Gilmore, Ian Jeffrey, and Joe LoVetri. Derivation and comparison of SAR and frequency-wavenumber migration within a common inverse scalar wave problem formulation. *IEEE transactions on geoscience and remote sensing*, 44(6):1454–1461, 2006.
- [73] Jenő Gazdag and Piero Sguazzero. Migration of seismic data. *Proceedings of the IEEE*, 72(10):1302–1315, 1984.
- [74] Gabor T Herman, Heang K Tuy, and Karl-Jörg Langenberg. *Basic Methods of Tomography and Inverse Problems*. Taylor & Francis, 1987.
- [75] Hans Rieder and Hans-Jürgen Salzburger. Alok-Imaging and -Reconstruction of Surface Defects on Heavy Plates with E.M.A.-Rayleigh Wave Transducers. In *Review of Progress in Quantitative Nondestructive Evaluation*, pages 1127–1135. Springer, 1989.
- [76] Florian Boßmann. *Model Based Defect Reconstruction in Ultrasonic Non-Destructive Testing*. PhD thesis, University of Göttingen, 2014.
- [77] KJ Langenberg, M Brandfaß, R Hannemann, T Kaczorowski, J Kostka, C Hofmann, R Marklein, K Mayer, and A Pitsch. Inverse Scattering with Acoustic, Electromagnetic, and Elastic Waves as Applied in Nondestructive Evaluation. In *Wavefield inversion*, pages 59–118. Springer, 1999.
- [78] KJ Langenberg and A Zimmer. Utilization of elastic wave mode conversion in electromagnetic diffraction tomographic imaging schemes. In *2009 International Conference on Electromagnetics in Advanced Applications*, pages 43–46. IEEE, 2009.
- [79] Joaquim Martins. Sensitivity Analysis, notes from AA222-Multidisciplinary Design Optimization course. <http://aero-comlab.stanford.edu/jmartins/aa222/aa222sa.pdf>. Last visited on 06/12/2022.
- [80] Robert Seidl and Ernst Rank. Iterative time reversal based flaw identification. *Computers & Mathematics with Applications*, 72(4):879–892, 2016.
- [81] Jean-Pierre Monchalin. Laser-ultrasonics: from the laboratory to industry. In *AIP Conference proceedings*, volume 700, pages 3–31. American Institute of Physics, 2004.
- [82] Jean-Pierre Monchalin. Laser-ultrasonics: principles and industrial applications. In *Ultrasonic and Advanced Methods for Nondestructive Testing and Material Characterization*, pages 79–115. World Scientific, 2007.

- [83] Steve D Sharples, Matt Clark, and Mike G Somekh. All-optical adaptive scanning acoustic microscope. *Ultrasonics*, 41(4):295–299, 2003.
- [84] CB Scruby, RJ Dewhurst, DA Hutchins, and SB Palmer. Quantitative studies of thermally generated elastic waves in laser-irradiated metals. *Journal of Applied Physics*, 51(12):6210–6216, 1980.
- [85] RJ Dewhurst, DA Hutchins, SB Palmer, and CB Scruby. Quantitative measurements of laser-generated acoustic waveforms. *Journal of Applied Physics*, 53(6):4064–4071, 1982.
- [86] KL Telschow and RJ Conant. Optical and thermal parameter effects on laser-generated ultrasound. *The Journal of the Acoustical Society of America*, 88(3):1494–1502, 1990.
- [87] JD Aussel, A Le Brun, and JC Baboux. Generating acoustic waves by laser: theoretical and experimental study of the emission source. *Ultrasonics*, 26(5):245–255, 1988.
- [88] W Arnold, B Betz, and B Hoffmann. Efficient generation of surface acoustic waves by thermoelasticity. *Applied physics letters*, 47(7):672–674, 1985.
- [89] F Alan McDonald. Practical quantitative theory of photoacoustic pulse generation. *Applied physics letters*, 54(16):1504–1506, 1989.
- [90] X Wang and X Xu. Thermoelastic wave induced by pulsed laser heating. *Applied Physics A*, 73(1):107–114, 2001.
- [91] Marie-Hélène Noroy, Daniel Royer, and Mathias Fink. The laser-generated ultrasonic phased array: Analysis and experiments. *The Journal of the Acoustical Society of America*, 94(4):1934–1943, 1993.
- [92] Marc Dubois, Franck Enguehard, Lionel Bertrand, Marc Choquet, and Jean-Pierre Monchalin. Modeling of laser thermoelastic generation of ultrasound in an orthotropic medium. *Applied physics letters*, 64(5):554–556, 1994.
- [93] S Dixon, T Harrison, Y Fan, and PA Petcher. Thermoelastic laser generated ultrasound using a ring source. *Journal of Physics D: Applied Physics*, 45(17):175103, 2012.
- [94] P Cielo, F Nadeau, and M Lamontagne. Laser generation of convergent acoustic waves for materials inspection. *Ultrasonics*, 23(2):55–62, 1985.

- [95] Xiao Wang, Michael G Littman, John B McManus, Mohsen Tadi, Young Sik Kim, Attila Askar, and Herschel Rabitz. Focused bulk ultrasonic waves generated by ring-shaped laser illumination and application to flaw detection. *Journal of applied physics*, 80(8):4274–4281, 1996.
- [96] István A Veres, Thomas Berer, and Peter Burgholzer. Numerical modeling of thermoelastic generation of ultrasound by laser irradiation in the coupled thermoelasticity. *Ultrasonics*, 53(1):141–149, 2013.
- [97] A Cavuto, F Sopranzetti, M Martarelli, and GM Revel. Laser-ultrasonics wave generation and propagation FE model in metallic materials. *J Clin Exp Dent*, 7:628–633, 2015.
- [98] Seyed Mehdi Mirsadeghi. Development of Non-contact Laser Ultrasonic System for Nondestructive Evaluation. Master’s thesis, University of Calgary, 2018.
- [99] RD Huber, DJ Chinn, OO Balogun, and TW Murray. High Frequency Laser-Based Ultrasound. In *AIP Conference Proceedings*, volume 820, pages 218–224. American Institute of Physics, 2006.
- [100] J-P Monchalin. Optical detection of ultrasound. *IEEE Transactions on Ultrasonics Ferroelectrics and Frequency Control*, 33:485–499, 1986.
- [101] Alain Blouin, D Levesque, C Neron, Denis Drolet, and J-P Monchalin. Improved resolution and signal-to-noise ratio in laser-ultrasonics by SAFT processing. *Optics Express*, 2(13):531–539, 1998.
- [102] Peter W Lorraine, Ralph A Hewes, and Denis Drolet. High resolution laser ultrasound detection of metal defects. In *Review of Progress in Quantitative Nondestructive Evaluation*, pages 555–562. Springer, 1997.
- [103] D Lévesque, A Blouin, C Néron, and J-P Monchalin. Performance of laser-ultrasonic F-SAFT imaging. *Ultrasonics*, 40(10):1057–1063, 2002.
- [104] Peter W Lorraine. Laser ultrasound imaging of Lamb waves in thin plates. In *Nondestructive Characterization of Materials VIII*, pages 67–72. Springer, 1998.
- [105] Theodosia Stratoudaki, Matt Clark, and Paul D Wilcox. Laser induced ultrasonic phased array using full matrix capture data acquisition and total focusing method. *Optics express*, 24(19):21921–21938, 2016.

- [106] Christian Padioleau, Paul Bouchard, René Héon, Jean-Pierre Monchalain, Francis H Chang, Tomy E Drake, and Kenneth I McRae. Laser ultrasonic inspection of graphite epoxy laminates. In *Review of Progress in Quantitative Nondestructive Evaluation*, pages 1345–1352. Springer, 1993.
- [107] FH Chang, TE Drake, MA Osterkamp, RS Prowant, JP Monchalain, R Heon, P Bouchard, C Padioleau, DA Froom, W Frazier, et al. Laser ultrasonic inspection of honeycomb aircraft structures. In *Review of Progress in Quantitative Nondestructive Evaluation*, pages 611–616. Springer, 1993.
- [108] C Néron, C Padioleau, A Blouin, and J-P Monchalain. Robotic laser-ultrasonic inspection of composites. In *AIP Conference Proceedings*, volume 1511, pages 353–359. American Institute of Physics, 2013.
- [109] Daniel Lévesque, Laurent Dubourg, and Alain Blouin. Laser ultrasonics for defect detection and residual stress measurement of friction stir welds. *Nondestructive Testing and Evaluation*, 26(3-4):319–333, 2011.
- [110] C Mandache, D Levesque, L Dubourg, and P Gougeon. Non-destructive detection of lack of penetration defects in friction stir welds. *Science and Technology of Welding and Joining*, 17(4):295–303, 2012.
- [111] D Lévesque, Y Asaumi, M Lord, C Bescond, H Hatanaka, M Tagami, and J-P Monchalain. Inspection of thick welded joints using laser-ultrasonic SAFT. *Ultrasonics*, 69:236–242, 2016.
- [112] Marc Dubois, Matthias Militzer, André Moreau, and Jean F Bussière. A new technique for the quantitative real-time monitoring of austenite grain growth in steel. *Scripta materialia*, 42(9), 2000.
- [113] Marc Dubois, André Moreau, and Jean F Bussière. Ultrasonic velocity measurements during phase transformations in steels using laser ultrasonics. *Journal of applied physics*, 89(11):6487–6495, 2001.
- [114] Tecnatom. tecnaLus: laser technology for the aeronautical sector. <https://www.tecnatom.es/en/blog/tecnalus-laser-technology-for-the-aeronautical-sector/>. Last visited on 06/12/2022.
- [115] Composites World. Nondestructive inspection: Better, faster and cheaper. <https://www.compositesworld.com/articles/nondestructive-inspection-better-faster-and-cheaper>. Last visited on 06/12/2022.

- [116] Mark A Osterkamp and David L Kaiser. Application of laser ultrasonics for the non-destructive inspection of complex composite aerospace structures. In *1st international symposium on laser ultrasonics: science, technology and applications*, July 2008.
- [117] Intelligent Optical Systems: Defect Monitoring & Inspection. <https://intopsys.com/defect-monitoring-inspection/>. Last visited on 06/12/2022.
- [118] Guangkai Sun, Zhenggan Zhou, Guanghai Li, and Wenbin Zhou. Development of an optical fiber-guided robotic laser ultrasonic system for aeronautical composite structure testing. *Optik*, 127(12):5135–5140, 2016.
- [119] Guangkai Sun, Liming Zhao, Mingli Dong, Xiaoping Lou, and Lianqing Zhu. Non-contact characterization of debonding in lead-alloy steel bonding structure with laser ultrasound. *Optik*, 164:734–744, 2018.
- [120] Geo Davis, Romesh Nagarajah, Suresh Palanisamy, Rizwan Abdul Rahman Rashid, Prabhu Rajagopal, and Krishnan Balasubramaniam. Laser ultrasonic inspection of additive manufactured components. *The International Journal of Advanced Manufacturing Technology*, 102(5-8):2571–2579, 2019.
- [121] Gleeble Products: LUMet[®] - Laser Ultrasonic Sensor for In-Situ Metallurgical Microstructure Studies. <https://www.gleeble.com/products/>. Last visited on 06/12/2022.
- [122] Bree M Sharratt. Non-destructive techniques and technologies for qualification of additive manufactured parts and processes: A literature review, 2015.
- [123] Marco Grasso and Bianca Maria Colosimo. Process defects and in situ monitoring methods in metal powder bed fusion: a review. *Measurement Science and Technology*, 28(4):044005, 2017.
- [124] Julien Lecompgnon, Samim Ahmadi, Philipp Hirsch, Christian Rupprecht, and Mathias Ziegler. Thermographic detection of internal defects using 2D photothermal super resolution reconstruction with sequential laser heating. *Journal of Applied Physics*, 131(18):185107, 2022.
- [125] Ronan McCann, Muhannad A Obeidi, Cian Hughes, Éanna McCarthy, Darragh S Egan, Rajani K Vijayaraghavan, Ajey M Joshi, Victor Acinas Garzon, Denis P Dowling, Patrick J McNally, et al. In-situ sensing, process monitoring and machine

- control in Laser Powder Bed Fusion: A review. *Additive Manufacturing*, 45:102058, 2021.
- [126] Sofia Catalucci, Adam Thompson, Samanta Piano, David T Branson, and Richard Leach. Optical metrology for digital manufacturing: a review. *The International Journal of Advanced Manufacturing Technology*, pages 1–20, 2022.
- [127] Adam Thompson, Ian Maskery, and Richard K Leach. X-ray computed tomography for additive manufacturing: a review. *Measurement Science and Technology*, 27(7):072001, 2016.
- [128] Anton Du Plessis, Stephan G le Roux, Johan Els, Gerrie Booysen, and Deborah C Blaine. Application of microCT to the non-destructive testing of an additive manufactured titanium component. *Case Studies in Nondestructive Testing and Evaluation*, 4:1–7, 2015.
- [129] Yongfeng Song, Joseph A Turner, Zuoxiang Peng, Chao Chen, and Xiongbing Li. Enhanced ultrasonic flaw detection using an ultrahigh gain and time-dependent threshold. *IEEE transactions on ultrasonics, ferroelectrics, and frequency control*, 65(7):1214–1225, 2018.
- [130] Ana Lopez, Ricardo Bacelar, Inês Pires, Telmo G Santos, José Pedro Sousa, and Luísa Quintino. Non-destructive testing application of radiography and ultrasound for wire and arc additive manufacturing. *Additive Manufacturing*, 21:298–306, 2018.
- [131] Hans Rieder, Martin Spies, Joachim Bamberg, and Benjamin Henkel. On- and offline ultrasonic characterization of components built by SLM additive manufacturing. In *AIP Conference Proceedings*, volume 1706, page 130002. AIP Publishing LLC, 2016.
- [132] Marvin Klein and James Sears. Laser ultrasonic inspection of laser clad 316LSS and Ti-6-4. In *International Congress on Applications of Lasers & Electro-Optics*, volume 2004, page 1006. Laser Institute of America, 2004.
- [133] D Lévesque, C Bescond, M Lord, X Cao, P Wanjara, and J-P Monchalain. Inspection of additive manufactured parts using laser ultrasonics. In *AIP Conference Proceedings*, volume 1706, page 130003. AIP Publishing LLC, 2016.
- [134] Sarah Everton, Phill Dickens, Chris Tuck, and Ben Dutton. Evaluation of laser ultrasonic testing for inspection of metal additive manufacturing. In *Laser 3D*

- Manufacturing II*, volume 9353, page 935316. International Society for Optics and Photonics, 2015.
- [135] Sarah Everton, Phill Dickens, Chris Tuck, and Ben Dutton. Using laser ultrasound to detect subsurface defects in metal laser powder bed fusion components. *Jom*, 70(3):378–383, 2018.
- [136] Anthony J Manzo, Shant Kenderian, and Henry Helvajian. Application of laser ultrasonic non-destructive evaluation technique to additive manufacturing. In *Laser 3D Manufacturing III*, volume 9738, page 973810. International Society for Optics and Photonics, 2016.
- [137] Célia Millon, Arnaud Vanhoye, Anne-Françoise Obaton, and Jean-Daniel Penot. Development of laser ultrasonics inspection for online monitoring of additive manufacturing. *Welding in the World*, 62(3):653–661, 2018.
- [138] Donatella Cerniglia, Michele Scafidi, Antonio Pantano, and R Lopatka. Laser ultrasonic technique for laser powder deposition inspection. *laser*, 6(150):13, 2013.
- [139] Donatella Cerniglia and Nicola Montinaro. Defect detection in additively manufactured components: Laser ultrasound and laser thermography comparison. *Procedia Structural Integrity*, 8:154–162, 2018.
- [140] Bruce W Drinkwater. Dynamic-field devices for the ultrasonic manipulation of microparticles. *Lab on a Chip*, 16(13):2360–2375, 2016.
- [141] Lev Petrovich Gor’kov. On the forces acting on a small particle in an acoustical field in an ideal fluid. In *Sov. Phys. Dokl.*, volume 6, pages 773–775, 1962.
- [142] Henrik Bruus. Acoustofluidics 7: The acoustic radiation force on small particles. *Lab on a Chip*, 12(6):1014–1021, 2012.
- [143] ZY Hong, JF Yin, W Zhai, N Yan, WL Wang, J Zhang, and Bruce W Drinkwater. Dynamics of levitated objects in acoustic vortex fields. *Scientific reports*, 7(1):7093, 2017.
- [144] Ralph S Budwig, Michael J Anderson, Gabriel Putnam, and Chris Manning. Ultrasonic particle size fractionation in a moving air stream. *Ultrasonics*, 50(1):26–31, 2010.

- [145] Ahmet Cicek, Nurettin Korozlu, Olgun Adem Kaya, and Bulent Ulug. Acoustophoretic separation of airborne millimeter-size particles by a Fresnel lens. *Scientific reports*, 7:43374, 2017.
- [146] Ramin J Imani and Etienne Robert. Estimation of acoustic forces on submicron aerosol particles in a standing wave field. *Aerosol Science and Technology*, 52(1):57–68, 2018.
- [147] Asier Marzo, Sue Ann Seah, Bruce W Drinkwater, Deepak Ranjan Sahoo, Benjamin Long, and Sriram Subramanian. Holographic acoustic elements for manipulation of levitated objects. *Nature communications*, 6:8661, 2015.
- [148] Asier Marzo, Mihai Caleap, and Bruce W Drinkwater. Acoustic virtual vortices with tunable orbital angular momentum for trapping of Mie particles. *Physical review letters*, 120(4):044301, 2018.
- [149] Marco AB Andrade, Thales SA Camargo, and Asier Marzo. Automatic contactless injection, transportation, merging, and ejection of droplets with a multifocal point acoustic levitator. *Review of Scientific Instruments*, 89(12):125105, 2018.
- [150] M Prisdrey, J Greenhall, F Guevara Vasquez, and B Raeymaekers. Ultrasound directed self-assembly of three-dimensional user-specified patterns of particles in a fluid medium. *Journal of Applied Physics*, 121(1):014302, 2017.
- [151] Asier Marzo and Bruce W Drinkwater. Holographic acoustic tweezers. *Proceedings of the National Academy of Sciences*, 116(1):84–89, 2019.
- [152] CJ Todaro, MA Easton, D Qiu, D Zhang, MJ Bermingham, EW Lui, M Brandt, DH StJohn, and M Qian. Grain structure control during metal 3D printing by high-intensity ultrasound. *Nature Communications*, 11(1):1–9, 2020.
- [153] Shuhao Wang, Jinsheng Ning, Lida Zhu, Zhichao Yang, Wentao Yan, Yichao Dun, Pengsheng Xue, Peihua Xu, Susmita Bose, and Amit Bandyopadhyay. Role of porosity defects in metal 3D printing: Formation mechanisms, impacts on properties and mitigation strategies. *Materials Today*, 2022.
- [154] Richard J Smith, Matthias Hirsch, Rikesh Patel, Wenqi Li, Adam T Clare, and Steve D Sharples. Spatially resolved acoustic spectroscopy for selective laser melting. *Journal of Materials Processing Technology*, 236:93–102, 2016.

- [155] Takahiro Hayashi, Naoki Mori, and Tomotake Ueno. Non-contact imaging of sub-surface defects using a scanning laser source. *Ultrasonics*, 119:106560, 2022.
- [156] Gerard T Schuster. *Basics of Seismic Imaging*. Cambridge University Press, 2010.
- [157] Kai-Ning Ying, Chen-Yin Ni, Lu-Nan Dai, Ling Yuan, Wei-Wei Kan, and Zhong-Hua Shen. Multi-mode laser-ultrasound imaging using Time-domain Synthetic Aperture Focusing Technique (T-SAFT). *Photoacoustics*, page 100370, 2022.
- [158] Ewen Carcreff and Dominique Braconnier. Comparison of conventional technique and migration approach for total focusing. *Physics Procedia*, 70:566–569, 2015.
- [159] Peter Lukacs, Geo Davis, Theodosia Stratoudaki, Stewart Williams, Charles N MacLeod, and Anthony Gachagan. Remote ultrasonic imaging of a wire arc additive manufactured Ti-6Al-4V component using laser induced phased array. In *2021 IEEE International Instrumentation and Measurement Technology Conference (I2MTC)*, pages 1–6. IEEE, 2021.
- [160] Lu-Nan Dai, Chen-Yin Ni, Kai-Ning Ying, Ling Yuan, Wei-Wei Kan, and Zhong-Hua Shen. Defect imaging based on laser ultrasonic frequency domain synthetic aperture focusing technology with separated generation–detection and 2-D equivalent velocity mapping. *Optics & Laser Technology*, 156:108485, 2022.
- [161] Alexander M Popovici. Reducing artifacts in prestack phase-shift migration of common-offset gathers. In *SEG Technical Program Expanded Abstracts 1994*, pages 684–687. Society of Exploration Geophysicists, 1994.
- [162] Kathryn Jinae Harke, Nicholas Calta, Joseph Tringe, and David Stobbe. Laser-based ultrasound interrogation of surface and sub-surface features in advanced manufacturing materials. *Scientific Reports*, 12(1):1–11, 2022.
- [163] Marvin B Klein, G David Bacher, Anders Grunnet-Jepsen, Daniel Wright, and William E Moerner. Homodyne detection of ultrasonic surface displacements using two-wave mixing in photorefractive polymers. *Optics communications*, 162(1-3):79–84, 1999.
- [164] R.C. Gonzalez, R.E. Woods, and S.L. Eddins. *Digital Image Processing Using MATLAB*. McGraw Hill Education, 2010.
- [165] Cheyne Gaw Ho, Rupert CD Young, Chris D Bradfield, and Chris R Chatwin. A fast Hough transform for the parametrisation of straight lines using Fourier methods. *Real-Time Imaging*, 6(2):113–127, 2000.

- [166] PA Petcher and S Dixon. A modified Hough transform for removal of direct and reflected surface waves from B-scans. *NDT & E International*, 44(2):139–144, 2011.
- [167] Ruye Wang. *Introduction to orthogonal transforms: with applications in data processing and analysis*. Cambridge University Press, 2012.
- [168] O Yilmaz and JF Claerbout. Prestack partial migration. *Geophysics*, 45(12):1753–1779, 1980.
- [169] Mohammed Albulayli and D Rakhmatov. Phase-shift depth migration for plane-wave ultrasound imaging. In *2018 40th Annual International Conference of the IEEE Engineering in Medicine and Biology Society (EMBC)*, pages 911–916. IEEE, 2018.
- [170] X. Li and G. F. Margrave. Prestack $v(z)$ f-k migration from common-offset sections. *CREWES Research Report*, 11:46.1–46.14, 1999.
- [171] J Douglas Faires and Richard L Burden. *Numerical Methods*. Brooks/Cole, 4th edition, 2012.
- [172] Daan Huybrechs and Stefan Vandewalle. On the evaluation of highly oscillatory integrals by analytic continuation. *SIAM Journal on Numerical Analysis*, 44(3):1026–1048, 2006.
- [173] Martin Hansen Skjelvareid. *Synthetic aperture ultrasound imaging with application to interior pipe inspection*. PhD thesis, Universitetet i Tromsø, 2012.
- [174] Tomer Sol. *Characterization of Additively Manufactured AlSi10Mg Using Time of Flight and Attenuation Measurements*. PhD thesis, Ben-Gurion University of the Negev, 2018.
- [175] JCF Millett, NK Bourne, GT Gray Iii, and IP Jones. The response of TiAl based alloys to one-dimensional shock loading. *Acta materialia*, 50(19):4801–4811, 2002.
- [176] Florian Kuisat, Fernando Lasagni, and Andrés Fabián Lasagni. Smoothing additive manufactured parts using ns-pulsed laser radiation. *Progress in Additive Manufacturing*, 6(2):297–306, 2021.
- [177] Zongcai Feng and Lianjie Huang. Formulating source radiation pattern in the wave equation. In *SEG Technical Program Expanded Abstracts 2020*, pages 2724–2728. Society of Exploration Geophysicists, 2020.

- [178] Tadeusz Stepinski. An implementation of synthetic aperture focusing technique in frequency domain. *iee transactions on ultrasonics, ferroelectrics, and frequency control*, 54(7):1399–1408, 2007.
- [179] M. Ansari, E. Jabari, and E. Toyserkani. Opportunities and challenges in additive manufacturing of functionally graded metallic materials via powder-fed laser directed energy deposition: A review. *Journal of Materials Processing Technology*, 294:117117, 2021.
- [180] Himani Siva Prasad, Frank Brueckner, and Alexander FH Kaplan. Powder catchment in laser metal deposition. *Journal of Laser Applications*, 31(2):022308, 2019.
- [181] Daniel Eisenbarth, Paulo Matheus Borges Esteves, Florian Wirth, and Konrad Wegener. Spatial powder flow measurement and efficiency prediction for laser direct metal deposition. *Surface and Coatings Technology*, 362:397–408, 2019.
- [182] Himani Siva Prasad, Frank Brueckner, and Alexander FH Kaplan. Powder incorporation and spatter formation in high deposition rate blown powder directed energy deposition. *Additive Manufacturing*, 35:101413, 2020.
- [183] Peter H Smith, James W Murray, Alex Jackson-Crisp, Joel Segal, and Adam T Clare. Magnetic manipulation in directed energy deposition using a programmable solenoid. *Journal of Materials Processing Technology*, 299:117342, 2022.
- [184] Marco AB Andrade, Nicolás Pérez, and Julio C Adamowski. Review of progress in acoustic levitation. *Brazilian Journal of Physics*, 48(2):190–213, 2018.
- [185] Hoseop Choi, Seunghyon Kang, Wooik Jung, Yoon-ho Jung, Sei Jin Park, Dae Seong Kim, and Mansoo Choi. Controlled electrostatic focusing of charged aerosol nanoparticles via an electrified mask. *Journal of Aerosol Science*, 88:90–97, 2015.
- [186] Yong-Le Pan, Aimable Kalume, Chuji Wang, and Joshua L Santarpia. Opto-aerodynamic focusing of aerosol particles. *Aerosol Science and Technology*, 52(1):13–18, 2018.
- [187] Y Huang, MB Khamesee, and E Toyserkani. Electrodynamic Concentration of Non-ferrous Metallic Particles in the Moving Gas-powder Stream: Mathematical Modeling and Analysis. *International Journal of Magnetism and Electromagnetism*, 5(1), 2019.

- [188] JS Sachdev, CPT Groth, and JJ Gottlieb. Numerical solution scheme for inert, disperse, and dilute gas-particle flows. *International journal of multiphase flow*, 33(3):282–299, 2007.
- [189] Mauro Murer, Valentina Furlan, Giovanni Formica, Simone Morganti, Barbara Previtali, and Ferdinando Auricchio. Numerical simulation of particle flow in laser metal deposition technology comparing Eulerian-Eulerian and Lagrangian-Eulerian approaches. *Journal of Manufacturing Processes*, 68:186–197, 2021.
- [190] François Forgues and James G McDonald. Higher-order moment models for laminar multiphase flows with accurate particle-stream crossing. *International Journal of Multiphase Flow*, 114:28–38, 2019.
- [191] Xibing Gong, Ted Anderson, and Kevin Chou. Review on powder-based electron beam additive manufacturing technology. In *International Symposium on Flexible Automation*, volume 45110, pages 507–515. American Society of Mechanical Engineers, 2012.
- [192] Alejandro Martinez and Ehsan Toyserkani. System and method of directed energy deposition using a sound field. PCT Patent, PCT/CA2021/050358.
- [193] Shiho Takemura, Ryo Koike, Yasuhiro Kakinuma, Yohei Sato, and Yohei Oda. Design of powder nozzle for high resource efficiency in directed energy deposition based on computational fluid dynamics simulation. *International Journal of Advanced Manufacturing Technology*, 105(10), 2019.
- [194] X Gao, XX Yao, FY Niu, and Z Zhang. The influence of nozzle geometry on powder flow behaviors in directed energy deposition additive manufacturing. *Advanced Powder Technology*, 33(3):103487, 2022.
- [195] Mohammad Taghi Nasiri and Mohammad R Movahhedy. A new design of continuous coaxial nozzle for direct metal deposition process to overcome the gravity effect. *Progress in Additive Manufacturing*, 7(2):173–186, 2022.
- [196] Lawrence E. Kinsler, Austin R. Frey, Alan Berchard Coppens, and James V. Sanders. *Fundamentals of Acoustics*. J. Wiley, 2000.
- [197] G. Ahmadi. Hydrodynamic forces - ME437/537 course notes at Clemson University. https://webpace.clarkson.edu/projects/fluidflow/public_html/courses/me537/1_2Drag.pdf. Last visited on 06/12/2022.

- [198] Jehnming Lin. Concentration mode of the powder stream in coaxial laser cladding. *Optics & Laser Technology*, 31(3):251–257, 1999.
- [199] Gangxian Zhu, Dichen Li, Anfeng Zhang, Gang Pi, and Yiping Tang. The influence of laser and powder defocusing characteristics on the surface quality in laser direct metal deposition. *Optics & Laser Technology*, 44(2):349–356, 2012.
- [200] HF Meier, AA Vegini, and M Mori. Four-phase Eulerian-Eulerian model for prediction of multiphase flow in cyclones. *The Journal of Computational Multiphase Flows*, 3(2):93–105, 2011.
- [201] Martin Alnæs, Jan Blechta, Johan Hake, August Johansson, Benjamin Kehlet, Anders Logg, Chris Richardson, Johannes Ring, Marie E Rognes, and Garth N Wells. The FEniCS project version 1.5. *Archive of Numerical Software*, 3(100), 2015.
- [202] Malvin H Kalos and Paula A Whitlock. *Monte Carlo Methods*. John Wiley & Sons, 2009.
- [203] UpnaLab. Ultrasonic Array. <https://www.instructables.com/id/Ultrasonic-Array/>. Last visited on 06/12/2022.
- [204] Asier Marzo, Tom Corkett, and Bruce W Drinkwater. Ultraino: An open phased-array system for narrowband airborne ultrasound transmission. *IEEE transactions on ultrasonics, ferroelectrics, and frequency control*, 65(1):102–111, 2018.
- [205] Andrew J Pinkerton and Lin Li. Modelling powder concentration distribution from a coaxial deposition nozzle for laser-based rapid tooling. *J. Manuf. Sci. Eng.*, 126(1):33–41, 2004.
- [206] S Chatterjee and B Price. *Regression Analysis by Example*. John Wiley & Sons, 1977.
- [207] MG Olsen and RJ Adrian. Out-of-focus effects on particle image visibility and correlation in microscopic particle image velocimetry. *Experiments in fluids*, 29(1):S166–S174, 2000.
- [208] Markus Raffel, Christian E Willert, Fulvio Scarano, Christian J Kähler, Steve T Wereley, and Jürgen Kompenhans. *Particle Image Velocimetry: A Practical Guide*. Springer, 2018.
- [209] A Kloosterman, C Poelma, and J Westerweel. Flow rate estimation in large depth-of-field micro-PIV. *Experiments in fluids*, 50(6):1587–1599, 2011.

- [210] Yanhua Bian, Xiuli He, Gang Yu, Shaoxia Li, Chongxin Tian, Zhiyong Li, Yanmei Zhang, and Junming Liu. Powder-flow behavior and process mechanism in laser directed energy deposition based on determined restitution coefficient from inverse modeling. *Powder Technology*, 402:117355, 2022.
- [211] James C Haley, Baolong Zheng, Umberto Scipioni Bertoli, Alexander D Dupuy, Julie M Schoenung, and Enrique J Lavernia. Working distance passive stability in laser directed energy deposition additive manufacturing. *Materials & Design*, 161:86–94, 2019.
- [212] Nikolaj A Fuks. *The Mechanics of Aerosols*. Dover Publications, 1989.
- [213] Hao Pang, Maximilian Klumpp, and Tobias Haecker. Modeling optical emission from a highly multi-mode step-index fiber via ray tracing and the limitations. *Appl. Opt.*, 60(35):10885–10892, Dec 2021.
- [214] PP Crooker, WB Colson, and J Blau. Representation of a Gaussian beam by rays. *American journal of physics*, 74(8):722–727, 2006.
- [215] PK Milsom. A ray-optic, Monte Carlo, description of a Gaussian beam waist–applied to reverse saturable absorption. *Applied Physics B*, 70(4):593–599, 2000.
- [216] Paul D Colbourne. Representation of Gaussian beams using rays. *International Journal of Mathematics, Game Theory, and Algebra*, 28(1):79–112, 2019.
- [217] Martin J Bastiaans. The Wigner distribution function applied to optical signals and systems. *Optics communications*, 25(1):26–30, 1978.
- [218] Orazio Svelto. *Principles of lasers*, volume 4. Springer, 1998.
- [219] A.E. Siegman. *Lasers*. University Science Books, 1986.
- [220] Daniel B. Allan, Thomas Caswell, Nathan C. Keim, Casper M. van der Wel, and Ruben W. Verweij. soft-matter/trackpy: Trackpy v0.5.0, apr 2021.
- [221] John C Crocker and David G Grier. Methods of digital video microscopy for colloidal studies. *Journal of colloid and interface science*, 179(1):298–310, 1996.
- [222] Dr S.T.C. Siklos. Projectile with linear drag - Dynamics and Relativity course notes at Cambridge U. <https://www.damtp.cam.ac.uk/user/tong/relativity/stephen.pdf>. Last visited on 06/12/2022.

- [223] Thomas F Coleman and Yuying Li. An interior trust region approach for nonlinear minimization subject to bounds. *SIAM Journal on optimization*, 6(2):418–445, 1996.
- [224] H.A. Haus and K.F. Šipilov. *Waves and Fields in Optoelectronics*. Prentice-Hall series in solid state physical electronics. Prentice-Hall, 1984.
- [225] Martin Van Buren and Nabeel A Riza. Foundations for low-loss fiber gradient-index lens pair coupling with the self-imaging mechanism. *Applied Optics*, 42(3):550–565, 2003.
- [226] Woonggyu Jung, Wladimir A Benalcazar, Adeel Ahmad, Utkarsh Sharma, Hao-hua Tu, and Stephen A Boppart. Numerical analysis of gradient index lens-based optical coherence tomography imaging probes. *Journal of biomedical optics*, 15(6):066027, 2010.
- [227] Daniel Mittleman. ENGN 2911T: Ultrafast Optics course slides. https://www.brown.edu/research/labs/mittleman/sites/brown.edu.research.labs.mittleman/files/uploads/lecture21_2.pdf. Last visited on 06/12/2022.
- [228] David Kessler and Roland V Shack. $y\bar{y}$ diagram, a powerful optical design method for laser systems. *Applied optics*, 31(15):2692–2707, 1992.
- [229] John Rogers, Michael E Harrigan, and Robert P Loce. The $Y-\bar{Y}$ diagram for radial gradient systems. *Applied optics*, 27(3):452–458, 1988.
- [230] Michael E Harrigan, Robert P Loce, and John Rogers. Use of the $Y-\bar{Y}$ diagram in GRIN rod design. *Applied optics*, 27(3):459–464, 1988.
- [231] R Vilar. Laser cladding. *Journal of laser applications*, 11(2):64–79, 1999.
- [232] Michael E Harrigan. Some first-order properties of radial gradient lenses compared to homogeneous lenses. *Applied optics*, 23(16):2702–2705, 1984.
- [233] Qian Wang, Jianyi Li, Abdalla R Nassar, Edward W Reutzler, and Wesley F Mitchell. Model-based feedforward control of part height in directed energy deposition. *Materials*, 14(2):337, 2021.
- [234] CL Druzgalski, A Ashby, G Guss, WE King, Tien T Roehling, and Manyalibo J Matthews. Process optimization of complex geometries using feed forward control for laser powder bed fusion additive manufacturing. *Additive Manufacturing*, 34:101169, 2020.

- [235] Zuo Li, Shang Sui, Xu Ma, Hua Tan, Chongliang Zhong, Guijun Bi, Adam T Clare, Andres Gasser, and Jing Chen. High deposition rate powder-and wire-based laser directed energy deposition of metallic materials: A review. *International Journal of Machine Tools and Manufacture*, page 103942, 2022.
- [236] Hua Tan, Chu Zhang, Wei Fan, Fengying Zhang, Xin Lin, Jing Chen, and Weidong Huang. Dynamic evolution of powder stream convergence with powder feeding durations in direct energy deposition. *International Journal of Machine Tools and Manufacture*, 157:103606, 2020.
- [237] Marc Röthlisberger, Marcel Schuck, Laurenz Kulmer, and Johann W Kolar. Contactless picking of objects using an acoustic gripper. *Actuators*, 10(4), 2021.
- [238] Xiaozheng Zeng and Robert J McGough. Optimal simulations of ultrasonic fields produced by large thermal therapy arrays using the angular spectrum approach. *The Journal of the Acoustical Society of America*, 125(5):2967–2977, 2009.
- [239] Dong-Lai Liu and Robert C Waag. Propagation and backpropagation for ultrasonic wavefront design. *IEEE transactions on ultrasonics, ferroelectrics, and frequency control*, 44(1):1–13, 1997.
- [240] Urvi Vyas and Douglas A Christensen. Extension of the angular spectrum method to calculate pressure from a spherically curved acoustic source. *The Journal of the Acoustical Society of America*, 130(5):2687–2693, 2011.
- [241] Ping Wu and Tadeusz Stepinski. Extension of the angular spectrum approach to curved radiators. *The Journal of the Acoustical Society of America*, 105(5):2618–2627, 1999.
- [242] Yigang Du and Jorgen Arendt Jensen. Feasibility of non-linear simulation for Field II using an angular spectrum approach. In *2008 IEEE Ultrasonics Symposium*, pages 1314–1317. IEEE, 2008.
- [243] Yigang Du, Henrik Jensen, and Jørgen Arendt Jensen. Comparison of simulated and measured nonlinear ultrasound fields. In *Medical Imaging 2011: Ultrasonic Imaging, Tomography, and Therapy*, volume 7968, pages 197–206. SPIE, 2011.
- [244] Q Lin, S Wang, J Alda, and E Bernabeu. Transformation of non-symmetric Gaussian beam into symmetric one by means of tensor ABCD law. *Optik*, 85(2):67–72, 1990.

- [245] Fuda Ning and Weilong Cong. Microstructures and mechanical properties of Fe-Cr stainless steel parts fabricated by ultrasonic vibration-assisted laser engineered net shaping process. *Materials Letters*, 179:61–64, 2016.
- [246] Weilong Cong and Fuda Ning. A fundamental investigation on ultrasonic vibration-assisted laser engineered net shaping of stainless steel. *International Journal of Machine Tools and Manufacture*, 121:61–69, 2017.
- [247] Changping Zhou, Fengchun Jiang, De Xu, Chunhuan Guo, Chengzhi Zhao, Zhenqiang Wang, and Jiandong Wang. A calculation model to predict the impact stress field and depth of plastic deformation zone of additive manufactured parts in the process of ultrasonic impact treatment. *Journal of Materials Processing Technology*, 280:116599, 2020.
- [248] Tatsuki Fushimi, Kenta Yamamoto, and Yoichi Ochiai. Acoustic hologram optimization using automatic differentiation. *Scientific reports*, 11(1):1–10, 2021.
- [249] Ambrish Singh, Sajjan Kapil, and Manas Das. A comprehensive review of the methods and mechanisms for powder feedstock handling in directed energy deposition. *Additive Manufacturing*, page 101388, 2020.
- [250] Markus Bambach, Irina Sizova, Fabian Kies, and Christian Haase. Directed energy deposition of Inconel 718 powder, cold and hot wire using a six-beam direct diode laser set-up. *Additive Manufacturing*, 47:102269, 2021.
- [251] Andreas Griewank and Andrea Walther. *Evaluating derivatives: principles and techniques of algorithmic differentiation*, volume 105. Siam, 2008.
- [252] Ole Stauning. FADBAD++: Flexible Automatic differentiation using templates and operator overloading in C++. <http://www.fadbad.com>. Last visited on 06/12/2022.
- [253] Ole Stauning. *Automatic validation of numerical solutions*. PhD thesis, IMM-DTU, 1997.
- [254] Per-Olof Persson. *Mesh generation for implicit geometries*. PhD thesis, Massachusetts Institute of Technology, 2005.
- [255] MT de Berg, Marc Van Kreveld, Mark Overmars, and Otfried Schwarzkopf. *Computational Geometry: Algorithms and Applications*. Springer Science & Business Media, 2000.

- [256] Alexander Schiftner, Mathias Höbinger, Johannes Wallner, and Helmut Pottmann. Packing circles and spheres on surfaces. In *ACM SIGGRAPH Asia 2009 papers*, pages 1–8. Association for Computing Machinery, 2009.
- [257] Anders Clausen and Erik Andreassen. On filter boundary conditions in topology optimization. *Structural and Multidisciplinary Optimization*, 56(5):1147–1155, 2017.
- [258] M Ansari, A Martinez-Marchese, Y Huang, and E Toyserkani. A mathematical model of laser directed energy deposition for process mapping and geometry prediction of Ti-5553 single-tracks. *Materialia*, 12:100710, 2020.
- [259] Sumair Sunny, Haoliang Yu, Ritin Mathews, Arif Malik, and Wei Li. Improved grain structure prediction in metal additive manufacturing using a dynamic kinetic Monte Carlo framework. *Additive Manufacturing*, 37:101649, 2021.
- [260] Long Bai, Alexander Velichko, and Bruce W Drinkwater. Grain scattering noise modeling and its use in the detection and characterization of defects using ultrasonic arrays. *IEEE Transactions on Ultrasonics, Ferroelectrics, and Frequency Control*, 66(11):1798–1813, 2019.
- [261] Ming Li, William Q Meeker, and R Bruce Thompson. Physical model-assisted probability of detection of flaws in titanium forgings using ultrasonic nondestructive evaluation. *Technometrics*, 56(1):78–91, 2014.
- [262] Jochen H Kurz, Anne Jüngert, Sandra Dugan, Gerd Dobmann, and Christian Boller. Reliability considerations of NDT by probability of detection (POD) determination using ultrasound phased array. *Engineering failure analysis*, 35:609–617, 2013.
- [263] JA Ogilvy. Model for predicting ultrasonic pulse-echo probability of detection. *NDT & E International*, 26(1):19–29, 1993.
- [264] Lester W Schmerr. *Fundamentals of ultrasonic nondestructive evaluation*, volume 122. Springer, 2016.
- [265] Xiangyu Lei, Håkan Wirdelius, and Anders Rosell. Simulation-Based Investigation of a Probability of Detection (POD) Model Using Phased Array Ultrasonic Testing (PAUT) Technique. *Journal of Nondestructive Evaluation*, 41(2):1–13, 2022.

- [266] Yangjian Cai and Qiang Lin. Decentered elliptical Gaussian beam. *Applied optics*, 41(21):4336–4340, 2002.
- [267] V Bagini, R Borghi, F Gori, AM Pacileo, M Santarsiero, Dario Ambrosini, and G Schirripa Spagnolo. Propagation of axially symmetric flattened gaussian beams. *JOSA A*, 13(7):1385–1394, 1996.
- [268] Mohamad Bayat, Venkata K Nadimpalli, Francesco G Biondani, Sina Jafarzadeh, Jesper Thorborg, Niels S Tiedje, Giuliano Bissacco, David B Pedersen, and Jesper H Hattel. On the role of the powder stream on the heat and fluid flow conditions during Directed Energy Deposition of maraging steel - Multiphysics modeling and experimental validation. *Additive Manufacturing*, 43:102021, 2021.
- [269] OB Kovalev, IO Kovaleva, and VV Belyaev. Ray tracing method for simulation of laser beam interaction with random packings of powders. In *AIP Conference Proceedings*, volume 1939, page 020028. AIP Publishing LLC, 2018.
- [270] Gary F Margrave and Michael P Lamoureaux. *Numerical methods of exploration seismology: With algorithms in MATLAB®*. Cambridge University Press, 2019.
- [271] Jon F Claerbout. *Imaging the earth's interior*, volume 1. Blackwell scientific publications Oxford, 1985.
- [272] Ray F Egerton et al. *Physical principles of electron microscopy*. Springer, 2005.
- [273] R.W. Leonard, A. Barone, R. Truell, C. Elbaum, and B.E. Noltingk. *Akustik II / Acoustics II*. Handbuch der Physik Encyclopedia of Physics. Springer Berlin Heidelberg, 2012.
- [274] Murata Electronics. Product specification for reference only. <https://www.murata.com/en-us/products/productdata/8797589340190/MASPOPSE.pdf>. Last visited on 06/12/2022.
- [275] Doug Lipinski (<https://scicomp.stackexchange.com/users/7733/doug-lipinski>). Applying the Runge-Kutta method to second order ODEs. Computational Science Stack Exchange. <https://scicomp.stackexchange.com/q/19022> (version: 2015-03-01).
- [276] Kai Hiltunen, Ari Jäsberg, Sirpa Kallio, Hannu Karema, Markku Kataja, Antti Koponen, Mikko Manninen, and Veikko Taivassalo. Multiphase flow dynamics: theory and numerics.

- [277] Alan Jeffrey. *Applied Partial Differential Equations: An Introduction*. Academic Press, 2003.
- [278] Claes Johnson. *Numerical Solution of Partial Differential Equations by the Finite Element Method*. Courier Corporation, 2009.
- [279] Francesco Ballio and Alberto Guadagnini. Convergence assessment of numerical Monte Carlo simulations in groundwater hydrology. *Water resources research*, 40(4), 2004.
- [280] Milton Abramowitz and Irene A Stegun. *Handbook of Mathematical Functions with Formulas, Graphs, and Mathematical Tables*. Dover publications, 1970.
- [281] Alex C Hoffmann and Louis E Stein. *Gas Cyclones and Swirl Tubes: Principles, Design, and Operation*. Springer Berlin Heidelberg, 2002.
- [282] Dzmitry Misiulia, Anders Gustav Andersson, and T Staffan Lundström. Effects of the inlet angle on the collection efficiency of a cyclone with helical-roof inlet. *Powder Technology*, 305:48–55, 2017.
- [283] RI Crane, LN Barbaris, and P Behrouzi. Particulate behaviour in cyclone separators with secondary gas extraction. *Journal of Aerosol Science*, 23:765–768, 1992.
- [284] S Habib Alavi, Cody Cowell, and Sandip P Harimkar. Experimental and finite element analysis of ultrasonic vibration-assisted continuous-wave laser surface drilling. *Materials and Manufacturing Processes*, 32(2):216–225, 2017.
- [285] T.G. Wang. High Temperature Acoustic Levitation. In *1983 Ultrasonics Symposium*, pages 1124–1128, 1983.
- [286] Emily W Leung and Taylor G Wang. Force on a heated sphere in a horizontal plane acoustic standing wave field. *The Journal of the Acoustical Society of America*, 77(5):1686–1691, 1985.
- [287] Alexandre Ermoline, Mirko Schoenitz, VK Hoffmann, and EL Dreizin. Experimental technique for studying high-temperature phases in reactive molten metal based systems. *Review of scientific instruments*, 75(12):5177–5185, 2004.
- [288] Louis Vessot King. On the acoustic radiation pressure on spheres. *Proceedings of the Royal Society of London. Series A-Mathematical and Physical Sciences*, 147(861):212–240, 1934.

- [289] Chun P Lee and Taylor G Wang. The acoustic radiation force on a heated (or cooled) rigid sphere - Theory. *The Journal of the Acoustical Society of America*, 75(1):88–96, 1984.
- [290] Chun P Lee and Taylor G Wang. Acoustic radiation force on a heated sphere including effects of heat transfer and acoustic streaming. *The Journal of the Acoustical Society of America*, 83(4):1324–1331, 1988.
- [291] Katsuya Yosioka and Yukihiro Kawasima. Acoustic radiation pressure on a compressible sphere. *Acta Acustica united with Acustica*, 5(3):167–173, 1955.
- [292] Kian-Meng Lim and Shahrokh Sepehri Rahnema. Calculation of acoustic radiation force and moment in microfluidic devices. In *International Journal of Modern Physics: Conference Series*, volume 34, page 1460380. World Scientific, 2014.
- [293] Ireneusz Grulkowski, Dawid Jankowski, and Piotr Kwiek. Acousto-optic interaction with the use of cylindrical ultrasonic waves in the laser cavity. *Applied optics*, 48(7):C81–C85, 2009.
- [294] Ireneusz Grulkowski, Dawid Jankowski, and Piotr Kwiek. Acousto-optic interaction of a Gaussian laser beam with an ultrasonic wave of cylindrical symmetry. *Applied optics*, 46(23):5870–5876, 2007.
- [295] Filip W Windels and O Leroy. The acousto-optical interaction of narrow laser beams under Raman-Nath conditions. *Journal of Optics A: Pure and Applied Optics*, 3(4):S12, 2001.
- [296] AP Loeber and EA Hiedemann. Investigation of stationary ultrasonic waves by light refraction. *The Journal of the Acoustical Society of America*, 28(1):27–35, 1956.
- [297] HG Aas and RK Erf. Application of Ultrasonic Standing Waves to the Generation of Optical-Beam Scanning. *The Journal of the Acoustical Society of America*, 36(10):1906–1913, 1964.
- [298] J Kolb and AP Loeber. The study of a sound field by means of optical refraction effects. *The Journal of the Acoustical Society of America*, 26(2):249–251, 1954.
- [299] Christopher T Wanstall, Ajay K Agrawal, and Joshua A Bittle. Implications of real-gas behavior on refractive index calculations for optical diagnostics of fuel-air mixing at high pressures. *Combustion and Flame*, 214:47–56, 2020.

- [300] Wolfgang Merzkirch. *Flow visualization*. Elsevier, 2012.
- [301] Camille Pauzon, Pierre Forêt, Eduard Hryha, Tanja Arunprasad, and Lars Nyborg. Argon-helium mixtures as Laser-Powder Bed Fusion atmospheres: Towards increased build rate of Ti-6Al-4V. *Journal of Materials Processing Technology*, 279:116555, 2020.
- [302] Mariusz Suchenek and Tomasz Borowski. Measuring sound speed in gas mixtures using a photoacoustic generator. *International Journal of Thermophysics*, 39(1):11, 2018.
- [303] Torbjörn Löfqvist, Jerker Delsing, and Kęstutis Sokas. Speed of sound measurements in gas-mixtures at varying composition using an ultrasonic gas flow meter with silicon based transducers. In *International Conference on Flow Measurement: 12/05/2003-14/05/2003*, 2003.
- [304] G Hallewell, G Crawford, D McShurley, G Oxoby, and R Reif. A sonar-based technique for the ratiometric determination of binary gas mixtures. *Nuclear Instruments and Methods in Physics Research Section A: Accelerators, Spectrometers, Detectors and Associated Equipment*, 264(2-3):219–234, 1988.
- [305] Charles D Hodgman, William Reed Veazey, and Robert C Weast. *Handbook of chemistry and physics: a ready-reference book of chemical and physical data*. Chemical Rubber Publishing Company, 1913.
- [306] Yunus A Cengel and Michael A Boles. *Thermodynamics: An Engineering Approach 6th Editon (SI Units)*. The McGraw-Hill Companies, Inc., New York, 2007.

APPENDICES

Appendix A

Derivations related to the Gor'kov potential

The radiation force due to sound is given by:

$$F = -\nabla U \quad (\text{A.1})$$

where U is the Gor'kov potential. This potential is given by [142, 143]:

$$U = V_p \left[f_1 \frac{1}{2} \kappa_m \langle p^2 \rangle - f_2 \frac{3}{4} \rho_m \langle v^2 \rangle \right] \quad (\text{A.2})$$

with:

$$f_1 = 1 - \frac{\kappa_p}{\kappa_m} \quad (\text{A.3})$$

and:

$$f_2 = \frac{2(\rho_p/\rho_m - 1)}{2\rho_p/\rho_m + 1} \quad (\text{A.4})$$

where V_p is the spherical particle volume and ρ is the density. The subscripts m and p correspond to the medium and particle respectively. $\kappa_a = 1/(\rho_a c_a^2)$ is the compressibility of the particle or the medium, where c_a is the speed of sound in the medium or particle. The angled brackets denote a one wavelength average of the instantaneous pressure and wave particle velocity squared (p^2 and v^2).

Forces due to sound on particles in a channel

The result given in [142], for particles flowing in a microfluidic channel with two parallel 180° out of phase transducers at opposing walls can be calculated by first finding the pressure and velocity fields.

The velocity field can be derived from the pressure field from the fact that the acoustic quantities v and p can be expressed via an acoustic velocity potential ϕ [142, 196]:

$$v = \nabla\phi \quad (\text{A.5})$$

$$p = j\rho_m\omega\phi \quad (\text{A.6})$$

Rearranging and substituting Eq. A.6 into Eq. A.5 yields:

$$v = -\frac{j}{\rho_m\omega}\nabla p \quad (\text{A.7})$$

The following complex pressure field:

$$p = jp_a \cos(kz)e^{-j\omega t} \quad (\text{A.8})$$

gives the following real pressure and, using Eq. A.7, the real velocity field [142]:

$$p = p_a \cos(kz) \sin(\omega t) \quad (\text{A.9})$$

$$v = -\frac{p_a}{\rho_m c_m} \sin(kz) \cos(\omega t) \quad (\text{A.10})$$

The final form of Eq. A.10 was obtained using $c_m = \omega/k$.

To find the time period averages found in Eq. A.2 one can use their definition in integral form:

$$\langle X \rangle = \frac{1}{\tau} \int_0^\tau X(t) dt \quad (\text{A.11})$$

in this case with $\tau = 2\pi/\omega$.

One could also use the one wavelength average of two imaginary harmonically varying fields (real-part rule) given by [142]:

$$\langle ab \rangle = \frac{1}{2} \Re(ab^*) \quad (\text{A.12})$$

where b^* stands for the complex conjugate of b .

Using Eq. A.11 on Eqs. A.9 and A.10 yields the following averaged values:

$$\langle p^2 \rangle = \frac{p_a^2}{2} \cos^2(kz) \quad (\text{A.13})$$

$$\langle v^2 \rangle = \frac{p_a^2 \kappa_m}{2 \rho_m} \sin^2(kz) \quad (\text{A.14})$$

This was done by calculating the two identities below:

$$\langle \sin^2(\omega t) \rangle = \int_0^{2\pi/\omega} \sin^2(\omega t) dt = \left[\frac{t}{2} - \frac{\sin(2\omega t)}{4\omega} \right]_0^{2\pi/\omega} = \frac{1}{2} \quad (\text{A.15})$$

$$\langle \cos^2(\omega t) \rangle = \int_0^{2\pi/\omega} \cos^2(\omega t) dt = \left[\frac{t}{2} + \frac{\sin(2\omega t)}{4\omega} \right]_0^{2\pi/\omega} = \frac{1}{2} \quad (\text{A.16})$$

Substituting Eqs. A.13 and A.14 into Eq. A.2 yields:

$$U = \frac{3}{4} V_p p_a^2 \kappa_m \left[f_1 \frac{1}{3} \cos^2(kz) - f_2 \frac{1}{2} \sin^2(kz) \right] \quad (\text{A.17})$$

Substituting Eq. A.17 into Eq. A.1, and using $V_p = 4\pi r_p^3/3$ where r_p is the particle's radius, gives the sound radiation force field obtained in [142]:

$$F = -\frac{\partial U}{\partial z} = 4\pi \Phi k r_p^3 E_{ac} \sin(2kz) \quad (\text{A.18})$$

with:

$$E_{ac} = \frac{p_a^2}{4\rho_m c_m^2} \quad (\text{A.19})$$

and:

$$\Phi = \frac{1}{3} f_1 + \frac{1}{2} f_2 \quad (\text{A.20})$$

Gor'kov potential in terms of pressure field derivatives

The Gor'kov potential can also be expressed in terms of the instantaneous pressure and its spatial derivatives by [147]:

$$U = K_1|p|^2 - K_2(|p_x|^2 + |p_y|^2 + |p_z|^2) \quad (\text{A.21})$$

with:

$$K_1 = V_p f_1 \frac{1}{4} \kappa_m = \frac{1}{4} V_p \left(\frac{1}{c_m^2 \rho_m} - \frac{1}{c_p^2 \rho_p} \right) \quad (\text{A.22})$$

and:

$$K_2 = V_p f_2 \frac{3}{4} \rho_m = \frac{3}{4} V_p \left[\frac{\rho_p - \rho_m}{\omega^2 \rho_m (\rho_m + 2\rho_p)} \right] \quad (\text{A.23})$$

Where p is the sound pressure field that can be sum of individual transducer fields, $|p|^2 = p \cdot p$ and the dot product operator in this case is defined in [147] as $a \cdot b = \Re(a)\Re(b) + \Im(a)\Im(b)$.

The first term of Eq. A.2 equals the one in Eq. A.21, since by inspection Eq. A.12 is equal to $(a \cdot b)/2$. Also in [142] $\langle a^2 \rangle$ is defined as $\langle aa \rangle$. For the second term in Eq. A.21, Eq. A.7 can be used to find $\langle v^2 \rangle$ using Eq. A.12:

$$\begin{aligned} \langle v^2 \rangle &= \frac{1}{2} \Re(vv^*) \\ &= \frac{1}{2\rho_m^2 \omega^2} \Re[(-j\nabla p)(-j\nabla p)^*] \\ &= \frac{1}{2\rho_m^2 \omega^2} \Re[(c_x \hat{i} + c_y \hat{j} + c_z \hat{k})(c_x^* \hat{i} + c_y^* \hat{j} + c_z^* \hat{k})] \\ &= \frac{1}{2\rho_m^2 \omega^2} \Re[(c_x c_x^* + c_y c_y^* + c_z c_z^*)] \\ &= \frac{1}{2\rho_m^2 \omega^2} (|p_x|^2 + |p_y|^2 + |p_z|^2) \end{aligned} \quad (\text{A.24})$$

Where $p = p_a + jp_b$, $c_h = -jp_h = p_{bh} - jp_{ah}$, a variable with subscript $h = x$ or y stands for partial derivative with respect to h , and the subscripts a and b stand for real and imaginary components. Substituting this equation into the second term of Eq. A.2 yields the second term in Eq. A.21.

Appendix B

Separable frequency based filter for B-scan

Following the matrix form of the discrete Fourier transform (DFT) [167], the 1D DFT in the time domain of $m \times n$ B-scan p along its n columns and the application of a filter J_f , also along columns, is given by:

$$P_f = W_m p \circ J_f^T \quad (\text{B.1})$$

where W_a is an $a \times a$ DFT matrix and \circ stands for matrix element-wise multiplication. The filtered signal is obtained by doing the inverse 1D DFT in the frequency domain of P_f :

$$p_f = \frac{1}{m} W_m^* P_f \quad (\text{B.2})$$

where W_a^* is an $a \times a$ matrix (that is also the conjugate transpose of W_a) that yields the inverse DFT.

One then would like to apply a filter in the spatial domain. Following the same for the application of the 1D DFT along columns, the DFT in the spatial domain along the rows m of p_f and the application of a filter J_k is given by:

$$P_{fk} = W_n p_f^T \circ J_k^T \quad (\text{B.3})$$

In order to obtain the original orientation of p , the inverse 1D DFT is done followed by a transpose:

$$p_{fk} = \left(\frac{1}{n}W_n^*P_{fk}\right)^T \quad (\text{B.4})$$

Afterwards one can apply the 2D DFT to the filtered B-scan, in order for PSM to be applied, using the following:

$$P_{tx} = W_m p_{fk} W_n \quad (\text{B.5})$$

One can show that Eq. B.5, without loss of generality, not considering zero padding and cropping between transforms, is equal to element-wise multiplying the 2D DFT of the original unfiltered B-scan data p by a 2D filter H_{LP} .

Substituting Eqs. B.1 to B.4 into Eq. B.5 yields:

$$P_{tx} = W_m \left(\frac{1}{n}W_n^*P_{fk}\right)^T W_n \quad (\text{B.6})$$

$$= W_m P_{fk}^T \left(\frac{1}{n}W_n^*W_n\right) \quad (\text{B.7})$$

$$= W_m P_{fk}^T \quad (\text{B.8})$$

$$= W_m (W_n p_f^T \circ J_k^T)^T \quad (\text{B.9})$$

$$= W_m (W_n p_f^T)^T \circ J_k \quad (\text{B.10})$$

$$= W_m p_f W_n \circ J_k \quad (\text{B.11})$$

$$= \left(W_m \frac{1}{m} W_m^*\right) P_f W_n \circ J_k \quad (\text{B.12})$$

$$= W_m p \circ J_f^T W_n \circ J_k \quad (\text{B.13})$$

$$= W_m p W_n \circ H_{LP} \quad (\text{B.14})$$

where $H_{LP} = J_f^T J_k$ is the required 2D frequency domain filter.

Appendix C

Derivation of the double square root equation

The scalar wave equation is given by [168, 73]:

$$\left(\frac{\partial^2}{\partial a^2} + \frac{\partial^2}{\partial z_a^2} - \frac{1}{v^2} \frac{\partial^2}{\partial t^2}\right)p(a, z_a, t) = 0 \quad (\text{C.1})$$

where a is the horizontal axis where either the sound receivers $a = r$ or sources $a = s$ are placed, and z_a is the depth downwards from the surface when the sound is being applied or measured. This is assuming the principle of reciprocity, meaning the receiver and source can be interchanged.

One solution to Eq. C.1 are 2D plane waves of the following form [173]:

$$p_{pw} = Ae^{j(k_a a + k_{z_a} z_a + \omega t)} \quad (\text{C.2})$$

where $j = \sqrt{-1}$, k_a and k_{z_a} are spatial frequency components and ω is the angular frequency. A diagram showing the coordinate axes that will be used and three example plane waves are shown in Fig. C.1

Plugging Eq. C.2 into Eq. C.1, one can check that the wave equation is satisfied if the following condition is met:

$$\left(\frac{\omega}{v}\right)^2 = k_a^2 + k_{z_a}^2 \quad (\text{C.3})$$

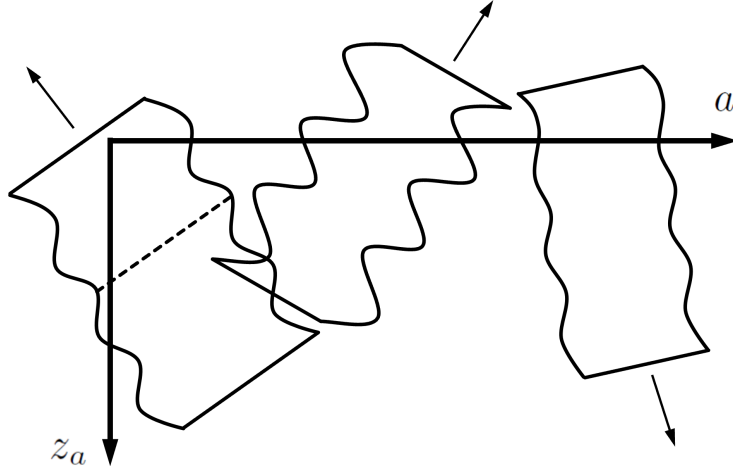


Figure C.1: Three plane waves of different amplitudes moving on the az_a plane in the direction indicated by the arrows. The a axis corresponds to the sample's surface where the sound waves are recorded. The dotted line indicates an isoline of constant phase γ .

The above equation is referred to as the dispersion relation [173]. Fourier transforming both sides of Eq. C.1 with respect to horizontal position a and time t using [168]:

$$P(k_a, z_a, \omega) = \iint p(a, z_a, t) e^{-j(k_a a + \omega t)} da dt \quad (\text{C.4})$$

and using the double differentiation property of the FT yields the following equation:

$$\frac{\partial^2 P}{\partial z_a^2} + \left[\left(\frac{\omega}{v} \right)^2 - k_a^2 \right] P = \frac{\partial^2 P}{\partial z_a^2} + k_{z_a}^2 P = 0 \quad (\text{C.5})$$

One can find a solution to Eq. C.5 by noting that a solution of the wave equation can be decomposed is an infinite sum of plane waves of the type given in Eq. C.2 that can be written as [173, 270]:

$$p(a, z_a, t) = \iint A(k_a, \omega) e^{j(k_a a + k_z z + \omega t)} dk_a d\omega \quad (\text{C.6})$$

Eq. C.6 is the inverse Fourier transform pair of Eq. C.4 where P is the following:

$$P(k_a, z_a, \omega) = A(k_a, \omega) e^{j k_z z} = P(k_a, 0, \omega) e^{j k_z z} \quad (\text{C.7})$$

Also note that Eq. C.7 is a solution to the following [73, 168]:

$$\frac{\partial P}{\partial z_a} = jk_{z_a} P \quad (\text{C.8})$$

The form of Eq. C.3 indicates there are two solutions for k_{z_a} with opposite signs, this corresponds to two versions of Eq. C.7. Since the waves are recorded in the horizontal axis a , and reflectors (the defects) will be present in the positive z axis, we are looking for solutions with upcoming waves [173]; i.e. waves moving with decreasing z_a towards the sample's surface at $z_a = 0$. The form of the dispersion equation that should be used in Eq. C.7 that gives these upcoming waves can be determined as follows. The intersections of the lines of constant phase γ perpendicular to the wave's motion with the z_a axis (see Fig. C.1) are given by:

$$z_{int} = \frac{\gamma - \omega t}{k_{z_a}} \quad (\text{C.9})$$

this was found by setting the complex phase in Eq. C.2 equal to γ and $a = 0$. By inspection, one can see that for increasing times the k_{z_a} value should have the same sign to the frequency ω in order to have a decreasing z_a . Therefore the expression for k_{z_a} that will be used from now on is:

$$k_{z_a} = \text{sign}(\omega) \sqrt{\left(\frac{\omega}{v}\right)^2 - k_a^2} \quad (\text{C.10})$$

This is the negative of the result in [173] and earlier articles, where the FT along frequency ω is done with a complex exponential of opposite sign to the widely used definition of the FT (Eq. C.4). When this definition of the FT is used, corresponding results to the ones in Chapter 3 are obtained [169]. Since the reflectors will be at a given depth z common to both sources and receivers ($z = z_s = z_r$), one can use the following expression [73, 271]:

$$\frac{\partial P}{\partial z} = \frac{\partial P}{\partial z_s} + \frac{\partial P}{\partial z_r} \quad (\text{C.11})$$

Let $x = (r + s)/2$ be a midpoint coordinate, and $h = (r - s)/2$ the half-offset. Using this coordinate change one can find that $k_s = (k_x - k_h)/2$ and $k_r = (k_x + k_h)/2$ [271].

Using Eqs. C.7, C.8 and C.11, and the spatial frequencies k_s and k_r in terms of k_x and k_h yields the following solution given by Eq. 3.8, and with k_z in this equation given by Eq. 3.9, which is the double square root (DSR) equation.

Appendix D

Newton's method design for computing the stationary point for SPA

The full phase function for Eq. 3.16 is given by:

$$\phi(k_h) = \text{sign}(\omega)\beta(k_h) - k_h h_0 \quad (\text{D.1})$$

with:

$$\beta(k_h) = z \left[\sqrt{\left(\frac{\omega}{v}\right)^2 - \left(\frac{k_x + k_h}{2}\right)^2} + \sqrt{\left(\frac{\omega}{v}\right)^2 - \left(\frac{k_x - k_h}{2}\right)^2} \right] \quad (\text{D.2})$$

and with the integration limits for Eq. 3.16 being $(-\alpha, \alpha)$, with α given by:

$$\alpha = \frac{2}{c} |f| - |k_x| \quad (\text{D.3})$$

For finding an SP we would like to find a value of $k_h = t$ such that $\phi'(t) = 0$. An example phase function ϕ is shown in Fig. D.1.

Initially Newton's method (NM) was implemented with an initial condition ($k_{h,new}$ in Algorithm 3) of zero. This would produce some iterations of the SP that would sometimes "overshoot" and produce a value outside the needed integration limits and had to be replaced by a value inside the interval. This was done using a weighted Bisection method [171], by setting the latest SP estimate inside the limits by a fraction of $1 - e_{tol}$ between the previous estimate of SP and the limit closest to the latest SP estimate, where $e_{tol} = 0.11$.

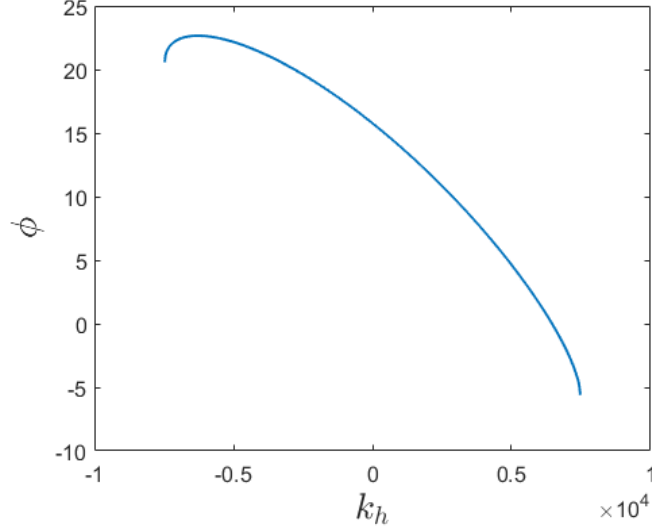


Figure D.1: An example phase function (a), with a frequency ω of 3.5×10^7 Hz, a spatial frequency k_x of -4.8×10^3 m $^{-1}$, and a depth z of 1.6 mm.

The value for e_{tol} was chosen since it gives the shortest computing time of 82 seconds out of 10 tested values as shown in Fig. D.2, however the minimum computation time is only 13% smaller than the maximum computation time of 95 seconds for the range of values tested.

For a better initial guess, one could try to approximate Eq. D.2 using a simpler function β_s and find an analytic solution for t such that $\phi'(t) \approx \beta'_s(t) - h_0 = 0$. Using a Taylor expansion about $k_h = 0$ with three terms (a quadratic function) and simplifying the final expression does not give a very good approximation at the integration limits since the function at the limits approach asymptotes. Note that using more terms will start being more costly than a NM iteration, since an initial guess using the Taylor expansion about $k_h = 0$ with three terms can be interpreted as a single iteration of NM. The number of NM iterations most evaluations of S take to compute the SP with an initial guess of zero is 5.

A better approximation was found by equating β_s to an ellipse, with the ellipse's vertices and co-vertices corresponding to the intersection of β with the k_h and ϕ axes. This is because Eq. D.2 can be interpreted as a sum of two shifted ellipses. Also this approximation has a close fit at the integration limits which have to be approximated accurately at low z values since the slope close to the integration limits increases; for example, the plot of ϕ shown in Fig. D.1 approaches a line with the same limit to limit slope, and a sharp dip at

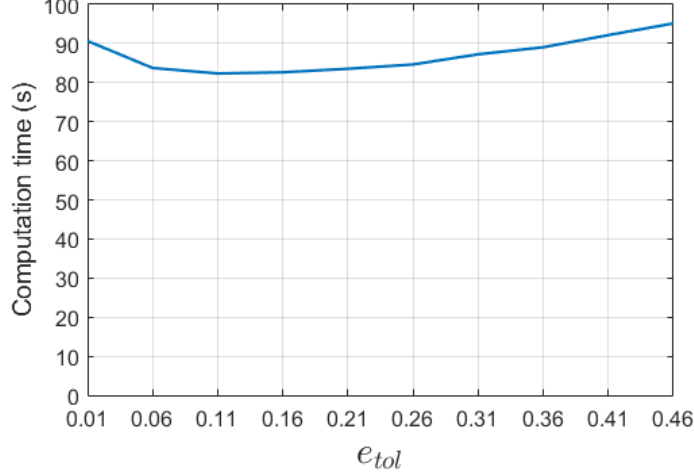


Figure D.2: The computation time for S with the PSM parameters used for the AlSi10Mg sample B-scans as a function e_{tol} .

the left limit.

The equation for ellipse β_s is:

$$\frac{k_h^2}{a^2} + \frac{\phi^2}{b^2} = 1 \quad (\text{D.4})$$

where $2a$ is the width along the k_h axis and $2b$ is the height along the ϕ axis. To match the functions at the k_h axis, $a = \alpha$. For matching functions on the ϕ axis, one should find the maximum of β (ϕ_{max}) by substituting $k_h = 0$ into Eq. D.2 and the value of β at the integration limits ($\phi_{k_h=\alpha}$), by substituting $k_h = \alpha$ into Eq. D.2. This gives the following value for b :

$$b = \phi_{max} - \phi_{k_h=\alpha} = z \left[2\sqrt{\left(\frac{\omega}{v}\right)^2 - \frac{k_x^2}{4}} - \sqrt{|k_x|\alpha} \right] \quad (\text{D.5})$$

The function β plotted with its three term Taylor expansion at $k_h = 0$ and the ellipse approximation plus $\phi_{k_h=\alpha}$ are shown in Fig. D.3.

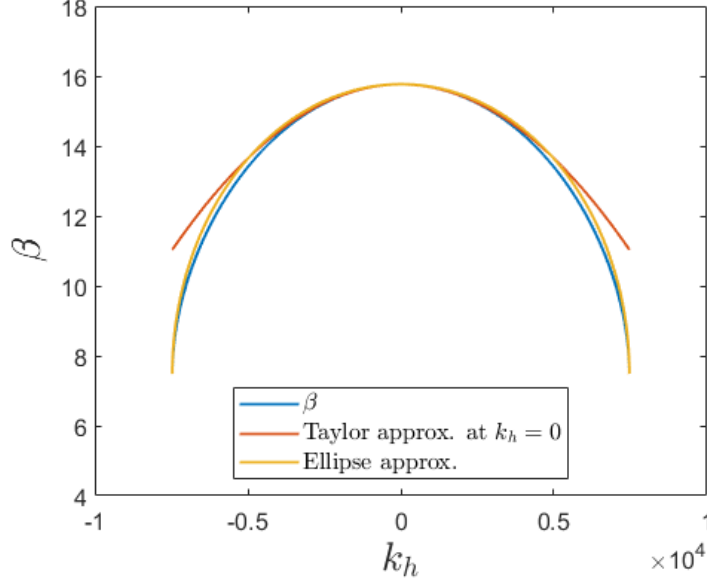


Figure D.3: Two different approximations for β .

Using Eq. D.4, using implicit differentiation and setting $\phi' = h_0$, one can find an initial guess for $k_h = t$ using β_s :

$$t = -\text{sign}(\omega) \min \left[\left(\frac{1}{a^2} + \frac{b^2}{a^4 h_0^2} \right)^{-1/2}, (1 - t_{tol})\alpha \right] \quad (\text{D.6})$$

where the value $-\text{sign}(\omega)$ is used to switch the sign of the guess based on which side of the ϕ axis the optimum location of ϕ will be [161], the \min operation is to catch any initial guesses outside the integration limits and $t_{tol} = 1 \times 10^{-4}$. Different values for t_{tol} were tried but it was found that the minimum computation time decreased with smaller values until approaching a constant computation time of 64 seconds. Using this initial guess, the number of NM iterations most evaluations of the entries in S take to compute the SP is 3. This reduces the computation time for all entries in S to 64 seconds, a 33% reduction from the original time, without optimizing for e_{tol} , of 95 seconds. A histogram of the number of iterations each NM variant takes for every SP calculation for the initial guess of zero and the guess given by Eq. D.6 are shown in Fig. D.4. One can see from the histogram that there is a large amount of iterations when using an initial guess of zero, therefore a better estimation for the initial guess would substantially reduce computation time as described above.

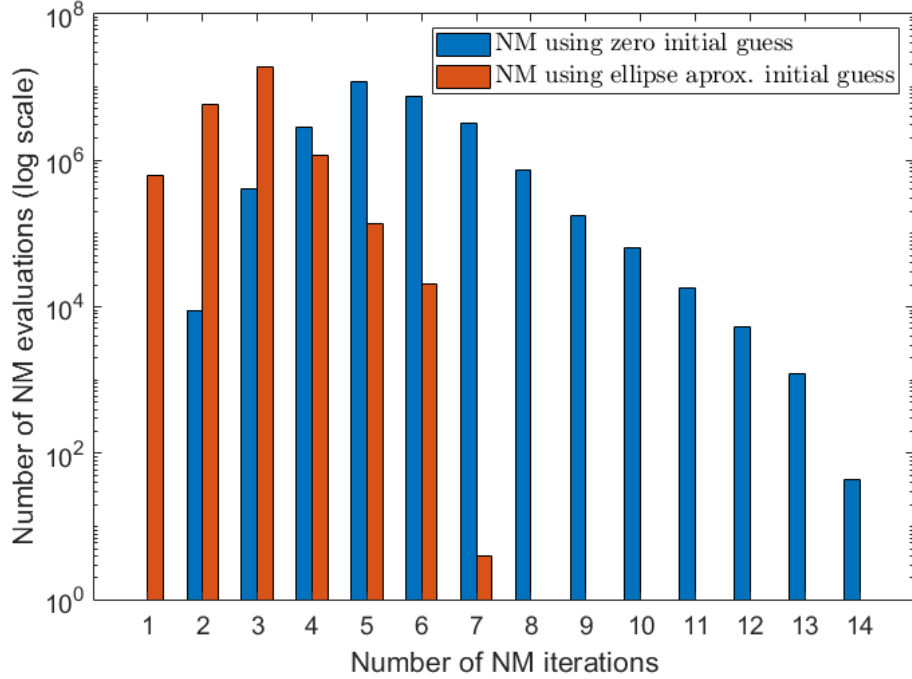


Figure D.4: Histogram for the number of NM iterations for each SP calculated.

The calculation of the SP using Eq. D.6 is shown in Algorithm 3. The convergence fractional tolerance used was $k_{tol} = 1 \times 10^{-4}$. Note that in MATLAB `1/0` has an output `Inf` that can be used for inequality computations to enter a while loop. The computation times for running 512 frequencies, 512 x intervals and 117 depths, with zero padding, giving a total of about 26 million applications of NM (a fraction of the total points do not satisfy line 7 in Algorithm 3) were measured on the computer setup described in Chapter 3.

Appendix E

Particle lensing model

A derivation of the analytic model for the concentration of particles with a uniform downward speed is shown below. A series of approximations can be made to arrive at an analytic expression for the angle change the particles experience after experiencing the acoustic force. Some of the variables that will be used are show in Fig. 4 of the main article.

Since the Gor'kov potential is proportional to the particle volume [142], the acoustic force is proportional to the square of the magnitude of the maximum averaged pressure near the sound focus point, and assuming the same shape and type of focusing sound field, the maximum acoustic force on the particles can be expressed as follows:

$$F_a = K_1 P_f^2 r_p^3 \quad (\text{E.1})$$

where K_1 is a focuser geometry, focus field type and acoustic properties of medium and particle dependent constant, P_f is the magnitude of the maximum averaged pressure nearest to the sound focus point and r_p is the particle radius. The P_f^2 dependence was tested by running `acousticHologram` on a particular UPL design, with a given P_a transducer value and then running the simulation again with twice this value. The resulting maximum force was indeed 4 times the original calculated force. The maximum averaged pressure near the sound focus point can be modeled as follows:

$$P_f = K_2 V_{pp} n d^{-1} \quad (\text{E.2})$$

where V_{pp} is the square wave voltage given to the driver board, n is the number of transducers in the phased array, and d is the distance between the phased array area and the

focus point. The voltage dependence is based on the fact that the sound pressure is proportional to the voltage [142]. Also note that the number of transducers is proportional to the phased array area, which is proportional to d^2 :

$$n = K_3 d^2 \rho_t \quad (\text{E.3})$$

where ρ_t is the transducer array planar density; how many transducers can fit into 1 m². Combining the above three equations yields:

$$F_a = K_a V_{pp}^2 d^2 \rho_t^2 r_p^3 \quad (\text{E.4})$$

One way the K_a constant may be found is by using the maximum force calculated by `acousticHologram`, and multiplying it by a chosen value to accurately approximate the sinusoidal force field in the z direction with a bounded constant force.

Using the Lagrangian simulation, it was observed that the aerodynamic drag for the particles of the density and size being considered is small relative to the acoustic radiation force. By taking into account the above information and approximating the sinusoidal force with a linear function close to the sound focus point and doing a force balance one can derive the following equation:

$$m_p \ddot{x} = -\frac{F_a}{l_{offset}} x \quad (\text{E.5})$$

where l_{offset} is the distance along the x direction from the sound focus point up to the distance where half the maximum x component of the acoustic force is measured. This distance should be slightly smaller than one quarter of the force field wavelength. Since the divergence angles from DED-PF are usually small, the equations can also be approximated using small θ value approximations. Solving Eq. E.5 for x with the initial conditions $x = r_i$ and $\dot{x} = u_z \tan(\theta_i)$ at $t = 0$ yields:

$$r_f = r_i \cos(\sqrt{a}t_i) + \frac{u_z \tan(\theta_i)}{\sqrt{a}} \sin(\sqrt{a}t_i) \approx r_i \left(1 - \frac{l_i}{2l_{offset}} \beta \right) + l_i \theta_i \quad (\text{E.6})$$

where r_i is the distance along the x direction between the sound focus point the particle farthest away from the sound focus point (the initial stream radius) and $a = F_a / (m_p l_{offset})$, and u_z is the particle downward speed in the z direction. This speed is the particle speed in the DED-PF process. Note that in order to have a linear approximation to the force field, F_a can be calculated as half of the peak force, and l_{offset} as the distance away

from the particle stream axis to half of the peak force. The variables $\alpha = r_i/l_{offset}$ and $\beta = F_a l_i/(m_p u_z^2)$ are dimensionless constants appearing in the derived solutions.

The particle speed after the acoustic force is applied is:

$$\dot{r}_f = -r_i \sqrt{a} \sin(\sqrt{a} t_i) + u_z \tan(\theta_i) \cos(\sqrt{a} t_i) \approx u_z \left[\theta_i \left(1 - \frac{l_i}{2l_{offset}} \beta \right) - \alpha \beta \right] \quad (\text{E.7})$$

where t_i is the particle interaction time with the acoustic force, and l_i stands for force interaction length in the z direction.

The particle deflection angle is therefore:

$$\theta_f = \arctan \left(\frac{\dot{r}_f}{u_z} \right) \approx \theta_i \left(1 - \frac{l_i}{2l_{offset}} \beta \right) - \alpha \beta \quad (\text{E.8})$$

This equation can be used to check the effect of different parameters on the particle deflection angle.

The distance traveled in the x direction after the force is applied along the interaction length is given by:

$$z = r_f + \frac{\dot{r}_f}{u_z} (l_T - l_i) \quad (\text{E.9})$$

where l_T is the distance between the particles right before the sound is applied and the work piece.

In order to get a high degree of particle focusing, it is recommended to have at least $l_i/l_T = 1$, with l_i being large enough to cover the high pressure sound region in the z direction. This also should minimize interactions of the sound field with the DED-PF nozzle tip and the work piece, in this case $r_T = r_f$. If a larger l_T value is used, such that $l_i/l_T \ll 1$, then the particle focusing happens in a similar way to an actual lens, and Eq. E.9 simplifies to:

$$r_f \approx r_f + \frac{\dot{r}_f}{u_z} l_T \approx r_i + l_T \left[\theta_i \left(1 - \frac{l_i}{2l_{offset}} \beta \right) - \alpha \beta \right] \quad (\text{E.10})$$

With the transducers being considered, the l_i value achievable is about 3 cm, meaning that l_T would need to be much higher than 3 cm. From a practical standpoint this is not feasible without further investigation due to the motion of the particle stream from a DED-PF machine when the nozzle is accelerating as well as the effect of gravity. Also

the laser beam geometry and power would need to be modified. With smaller transducers operating at a higher frequency a smaller l_i value could be achievable, which for a fixed l_T value and r_f might allow for a smaller deflection angle and correspondingly less power consumption from the transducer array.

Another question that can be answered with this model is if this type of force field can approximate a particle “lens”. One desirable property of an optical or electron lens as well as for acoustic particle focusing is that particles at x values from 0 to l_{offset} should intercept the z axis at some fixed focal distance l_f [272], which in the case of the above solutions is at some l_T that makes $r_f = 0$. Also, as it is shown in Appendix G, the divergence angle is proportional to r_i , i.e. $\theta_i = k_d r_i$, as well as being small.

Therefore this focal distance, assuming the focal length is longer than l_i , and using Eq. E.9, is given by:

$$l_f = l_i - \frac{r_f}{\dot{r}_f} u_z \approx l_i + \frac{u_z}{\sqrt{a}} \left[\frac{\sqrt{a} \cos(\gamma) + s_{sp} k_d \sin(\gamma)}{\sqrt{a} \sin(\gamma) - u_z k_d \cos(\gamma)} \right] \approx l_i + \frac{2u_z^2(1 + k_d l_i) - a l_i^2}{2a l_i + k_d (a l_i^2 - 2u_z)} \quad (\text{E.11})$$

where the first approximation is derived using the small angle approximation for $\tan()$, the second approximation uses the small angle approximations of $\sin()$ and $\cos()$, and $\gamma = \sqrt{a} l_i / u_z$.

Appendix F

Modeling and algorithms used in software library

Ultrasound transducers

In order to move particles with enough sound radiation force, a large spatially concentrated instantaneous pressure is needed. This pressure is a function of the dB level a transducer can produce at a fixed distance. The MA40S4S transducer from Murata electronics used in [147] and the main article can produce 120 dB at 40 kHz and a distance of 30 cm along their center axes (more information found in supplementary material of [147]).

The instantaneous sound field from the sound transducers was modeled with a circular plane piston source [196, 273]. The model piston source model was calibrated to match the transducer normal axis sound volume in dB and the directivity function for the transducer specifications at 40 kHz [274] and to match the ASP field results given in [147] (to account for the electronics producing a square wave). The model also can take into account the applied voltage, by noting that in the transducer specifications the 120 dB value at 30 cm was obtained using a voltage of 10 V root mean squared (rms) [274], the voltage used in [147] was 16 V peak-to-peak (pp) in a square wave, which after going through a MOSFET driver board becomes a sinusoidal wave (more information found in supplementary material of [147]). And that U_0 and P_a are proportional to the voltage applied to the transducer [142].

How the gradients related to the Gor'kov potential are derived

The derivatives used to get the gradients shown in [147] can be calculated using derivatives of the sound field via its corresponding Gor'kov potential, this was done using automatic differentiation [251, 79], and implemented in the FADBAD++ C++ header library [252].

The Gor'kov potential can be expressed in terms of the instantaneous pressure and its spatial derivatives as shown in [147]:

$$U = K_1|p|^2 - K_2(|p_x|^2 + |p_y|^2 + |p_z|^2) \quad (\text{F.1})$$

with K_1 and K_2 given by Eqs. 2.12 and 2.13 respectively.

$$K_1 = \frac{1}{4}V_p \left(\frac{1}{c_m^2 \rho_m} - \frac{1}{c_p^2 \rho_p} \right) \quad (\text{F.2})$$

$$K_2 = \frac{3}{4}V_p \left[\frac{\rho_p - \rho_m}{\omega^2 \rho_m (\rho_m + 2\rho_p)} \right] \quad (\text{F.3})$$

In Eq. F.1, p is the sound pressure field that is the sum of the individual transducer pressure fields, $|p|^2 = p \cdot p$ and the dot product operator in this case is defined in [147] as $a \cdot b = \Re(a)\Re(b) + \Im(a)\Im(b)$.

The force at a point can be derived by using the fact that $\vec{F} = -\nabla U$ and $(a \cdot b)_c = (a \cdot b_c) + (a_c \cdot b)$ where the subscript stands for partial derivative with respect to the subscript. The force components with $a = i, j, k$ are the following:

$$\vec{F} \cdot a = -2 \left[K_1(p \cdot p_a) - K_2 \sum_n (p_n \cdot p_{na}) \right] \quad (\text{F.4})$$

This expression can be used to compute particle trajectories (particle tracking) with the only approximation error coming from the integration of the particle motion, since Eq. F.4 uses the transducer model derivatives which are exact up to machine precision.

Particle tracking

Using Eq. F.4 one can calculate the applied force on a particle at a given point. This force and the medium drag force on the particle are all the applied forces on the particle. The sum of these forces can then be used to perform particle tracking.

The drag force on a particle can be expressed as:

$$F_D = -\frac{1}{2}C_D\rho_m A_p |\vec{v}| \vec{v} \quad (\text{F.5})$$

where C_D is the drag coefficient, A_p is the particle cross sectional area and \vec{v} is the velocity of the particle with respect to the surrounding gas flow [197]. The drag coefficient depends on the particle Reynolds number given by [197]:

$$Re_p = \frac{2\rho_m |\vec{v}| r_p}{\mu_m} \quad (\text{F.6})$$

The models of the drag coefficient given in [197] for $Re_p < 1$ and for Re_p from 1 to 1000 were implemented.

With these functions for the applied forces at a given spatial location, one can compute particle paths from an initial to a final position at a required time interval. This can be done using a 4th order Runge-Kutta (RK4) scheme [171] with a given fixed time step. The C++ code was written following the same form as shown in [275].

Appendix G

Eulerian powder stream model with novel initial condition

The equations used in [34] and explained in more detail in [198] for the density distribution of particles coming out of a DED-PF nozzle are based on a particle number concentration model given by [212]:

$$c = \frac{\Phi}{4\pi D z} e^{-u_z(x^2+y^2)/(4Dz)} \quad (\text{G.1})$$

where Φ is the number of particles per second from a point source, D is the diffusion constant, z is the axis of motion of the particles, x and y are the transverse axes and u_z is the average downward speed of the particles parallel to z . The units of c are number of particles per unit volume. Note that all the derivations discussed can also be done in time by using $z = u_z t$. Eq. G.1 is a solution to [212] (pg 212):

$$\frac{\partial c}{\partial z} - \frac{D}{u_z} \left(\frac{\partial^2 c}{\partial x^2} + \frac{\partial^2 c}{\partial y^2} \right) = 0 \quad (\text{G.2})$$

which after substituting $x^2 + y^2$ with r^2 is the same solution as the one for axisymmetric diffusion with a point source in cylindrical coordinates given by:

$$\frac{\partial c}{\partial z} - \frac{D}{u_z} \left(\frac{\partial^2 c}{\partial r^2} + \frac{1}{r} \frac{\partial c}{\partial r} \right) = 0 \quad (\text{G.3})$$

As described in the literature [34, 198, 199], the observed particle cloud spreads like a flattening Gaussian, with the sides of the Gaussian with a value of e^{-1} of the function's

peak spreading along diverging lines with an angle between them of 2θ and an initial distance between the sides of $2r_0$ which is the nozzle diameter. The half-angle θ can be measured from video data and used to find an effective D value for the model. This is done by equating the peak of Eq. G.1 times e^{-1} with the same equation at $r = R(z)$ (resulting in $e^{-1} = e^{-u_z R^2/(4Dz)}$) and solving for D , given by:

$$D = \frac{u_z R(z)^2}{4z} \quad (\text{G.4})$$

where $R(z) = r_0 + \tan(\theta)z$. The Φ value can be obtained from the other DED-PF relevant parameters as follows:

$$\Phi = \frac{\dot{m}}{m_p} \quad (\text{G.5})$$

where \dot{m} is the particle mass flow rate from the DED-PF nozzle and m_p is the particle mass. After substituting Eqs. G.4 and G.5 into Eq. G.1 and using r yields:

$$c = \frac{\dot{m}}{u_z m_p \pi R(z)^2} e^{-r^2/R(z)^2} \quad (\text{G.6})$$

If one does the same derivation using the e^{-2} radius one obtains the same equation as the one used in [34]. The experimental results were compared against a Eulerian continuous concentration distribution particle model given by the following equations:

$$\frac{\partial c}{\partial t} + \frac{1}{r} \frac{\partial(rcv)}{\partial r} - D \left(\frac{\partial^2 c}{\partial r^2} + \frac{1}{r} \frac{\partial c}{\partial r} \right) = 0 \quad (\text{G.7})$$

$$\frac{\partial(cv)}{\partial t} + \frac{1}{r} \frac{\partial(rcvv)}{\partial r} = \frac{c}{m_p} (F_d + F_{us}) \quad (\text{G.8})$$

Eqs. G.7 and G.8 are the same equations given in [188] and [200], written in cylindrical coordinates for one phase, assuming an axisymmetric solution, and an added diffusion term. Since the particle phase is considered to be dilute, as observed in the high-speed camera data, the above equations were not coupled to air except via the drag force term.

The drag body force term is given by [276, 200, 197]:

$$F_d = -\frac{1}{2} A_p \rho_f C_{Dv} (Re_p) v \quad (\text{G.9})$$

where A_p is the particle cross sectional area and ρ_f is the air density.

The function C_{Dv} is the drag coefficient times $|v|$, given by:

$$C_{Dv} = \frac{24}{k_{Re}}(1 + 0.15Re_p^{0.687}); \quad (\text{G.10})$$

where $k_{Re} = \rho_f d_p / \mu_f$ is the constant relating the particle Reynolds number and its relative speed with the air flow $Re_p = k_{Re}|v|$. Eq. G.10 produces accurate results when Re is between 1 and 1000 and closely approximates the drag for $Re < 1$ [197]. The value μ_f is the air viscosity. The drag coefficient equation is calculated this way to prevent a division by zero when v is zero.

The body ultrasound force term was designed to approximate a rapidly decaying sinusoidal field, that decays rapidly to a value close to zero at $r = 30\text{mm}$. This behavior was modeled by a sine wave times an exponential, given by:

$$f(r) = -\sin[2\pi(c_1 r + c_2 r^2)] \exp[-c_3(r - c_4)] \quad (\text{G.11})$$

where the term c_1 corresponds to the inverse of some average wavelength, c_2 is a correction for changing wavelength over x , while still having zero force at $x = 0$, c_3 is an exponential decay term c_3 and c_4 accounts for an offset of the decay envelope.

The force also changes as the particles move downwards. This was modeled using:

$$g(t) = \frac{1}{2} \left(\cos \left[\frac{2\pi}{t_{final}} \left(t - \frac{t_{final}}{2} \right) \right] + 1 \right) \quad (\text{G.12})$$

where the simulation time t_{final} (0.034 s) is given by the distance in the z direction the force is applied (20 mm) divided by the particle speed at the sound focus point (0.59 m/s). The final expression for the ultrasound body force is given by:

$$F_{us} = F_{max} f(r) g(t) \quad (\text{G.13})$$

where F_{max} is the computed maximum magnitude of the force from the x -axis.

In order to use Eqs. G.7 and G.8, one should have an expression for the diffusion term D . This can be found by plugging Eq. G.6 into Eq. G.3 and solving for D .

The diffusion term needed is given by:

$$D = \frac{1}{2} u_z R \tan(\theta) \quad (\text{G.14})$$

This diffusion term when used to solve Eqs. G.7 and G.8 with no body forces produces the concentration model given by Eq. G.6. However, as explained in Section 4.3.3, the use of a diffusion term will not produce an accurate model for coupling the powder stream with a force field.

One way to address this is the following; to use Eqs. G.7 and G.8 with no diffusion term with the same initial concentration and an initial particle speed distribution. This initial speed distribution needs to reproduce Eq. G.6 when no body forces are applied. This speed distribution can be found by equating the second advection term and the third diffusion term in Eq. G.7 and, using the initial known concentration c , solving for v :

$$\begin{aligned}
\frac{1}{r} \frac{\partial(rcv)}{\partial r} &= -D \left(\frac{\partial^2 c}{\partial r^2} + \frac{1}{r} \frac{\partial c}{\partial r} \right) \\
\frac{\partial(rcv)}{\partial r} &= -D \left(r \frac{\partial^2 c}{\partial r^2} + \frac{\partial c}{\partial r} \right) \\
rcv &= -Dr \frac{\partial c}{\partial r} \\
v(r, 0) &= -\frac{D}{c(r, 0)} \frac{\partial c(r, 0)}{\partial r}
\end{aligned} \tag{G.15}$$

After substituting Eqs. G.14 and G.6 at $z = 0$ in Eq. G.15, the required initial speed distribution is given by:

$$v(r, 0) = u_z \tan(\theta) \frac{r}{r_0} \tag{G.16}$$

This equation also satisfies Eq. G.8 when the body forces are zero. Substituting Eq. G.7 without the diffusion term into Eq. G.8 yields:

$$\frac{\partial v}{\partial t} + v \frac{\partial v}{\partial r} = 0 \tag{G.17}$$

This is the inviscid or dissipationless Burgers equation which for the initial condition given by Eq. G.16 by the method of characteristics has a solution given by [277]:

$$v(r, t) = \frac{r}{t + \frac{r_0}{u_z \tan(\theta)}} \tag{G.18}$$

The above solution and the concentration distribution given by Eq. G.6 can be shown by substitution to satisfy Eq. G.7 for all $t \geq 0$ when no body forces are applied.

The final 1D PDE system can be written as:

$$\frac{\partial c}{\partial t}r + cv + \frac{\partial(cv)}{\partial r}r = 0 \quad (\text{G.19})$$

$$\frac{\partial v}{\partial t} + v\frac{\partial v}{\partial r} = \frac{1}{m_p}(F_d + F_{us}) \quad (\text{G.20})$$

Eqs. G.19 and G.20 are the same as Eqs. G.7 and G.17 but without the diffusion term, with the applied forces, with extra terms by expanding them using the product rule, and multiplying all terms by r (if needed) to prevent issues with division by r when it has values close to zero. The only boundary condition needed to guarantee a unique solution to the problem is one for v at $r = 0$ mm. This is given by:

$$v(0, t) = 0 \quad (\text{G.21})$$

The concentration does not need boundary conditions to be enforced because the mass conservation equation (Eq. G.19) fixes the total area under the curve of c as it changes over time.

Eqs. G.19 and G.20 can be discretized in time using backward Euler [278]. The time discretized equations are given by:

$$(c_n - c_{n-1})\frac{r}{\Delta t} + c_nv_n + \frac{\partial(c_nv_n)}{\partial r}r = 0 \quad (\text{G.22})$$

$$(v_n - v_{n-1})\frac{1}{\Delta t} + v_n\frac{\partial v_n}{\partial r} = \frac{1}{m_p}[F_d(u_n) + F_{us}] \quad (\text{G.23})$$

where n denotes the current time step and $n - 1$ the previous time step. The above system can be solved using the FEniCS library [201]. The simulations were run with a radius of 20 mm and second order Lagrange finite elements [278].

In order to arrive at a grid or mesh and time step independent solution for this time dependent problem, one can check the percent change of a desired variable such as the peak concentration of the PCD found at the center and refining the mesh and time step based on the the Courant-Friedrichs-Levy (CFL) condition, and check if the percent change is below a required threshold. The value used for the threshold was 4%. Doubling the number of elements, and halving the time step keeping the ratio between the time step and the element size constant, the particle concentration values for SS 316L as an example shown in Table G.1 with and without sound radiation force being applied were obtained. The SS

316L at 16 V case took the longest to converge with a 5.06% at 40 elements and reaching 0.07% in the next subdivision, due to a high initial condition speed (Eq. G.16), due to a high spread angle, and applied sound force. The percent change for the Ti6Al4V at 0 V case was already below 4% in the first simulation using 5 elements, due to no force being applied and the measured spread angle being lower for SS 316L. Based on all the convergence analyses, all Eulerian simulations reported in Section 4.5.8 were run using 80 elements and a time step of 2.0 μ s.

Table G.1: Convergence analysis of Eulerian simulations for SS 316L at 0 and 10 V

Number of elements	Time step size (μ s)	Computation time (avg, mins)	0 V		10 V	
			Particle concentration (mm^{-3})	% change	Particle concentration (mm^{-3})	% change
5	32.0	0:9	0.462	NA	0.756	NA
10	16.0	0:21	0.526	12.18	0.991	23.75
20	8.0	0:58	0.546	3.67	1.010	1.87
40	4.0	2:54	0.545	0.16	0.998	1.20
80	2.0	8:38	0.543	0.41	0.993	0.59

The code run in FEniCS is as follows:

```
1 #Sound force field functions
2 class ForceField(UserExpression):
3     def eval(self, value, x):
4         def sin_exp_term(a):
5             return sin(2.0*pi/(4.0*F_offset)*a)*exp(-F_k*(a-F_offset))
6         value[0] = -F_max*sin_exp_term(x[0])
7 F_applied = ForceField(degree=deg)
8 cos_term = Expression("0.5*(cos(2.0*pi/t_final*(t-0.5)) + 1.0)",
9                       degree=deg, pi=pi, t_final=t_final, t=0.0)
10
11 #Aerodynamic drag functions
12 ReLn = Constant(ln(0.687))
13 def C_DtimesU(Re_p):
14     return 24.0/k_Re*(1.0 + 0.15*exp(Re_p*ReLn))
15 def F_drag(u,c):
16     Re_p = k_Re*abs(u)
17     return -0.5*A_p*rho_f*C_DtimesU(Re_p)*u
18
19 #FEA variational form
20 r = Expression('x[0]', degree=deg)
21 F = (c - c_1)*r*k_t*v_c*dx + (c*u)*v_c*dx + (c*u).dx(0)*r*v_c*dx + \
22     (u-u_1)*k_t*v_u*dx + u*u.dx(0)*v_u*dx - \
23     k_mp*(F_drag(u,c) + F_applied*cos_term)*v_u*dx
```

The solution loop is the following:

```
1 t = 0.0
2 while t <= t_final:
3     # Update force field based on time
4     t += dt
5     cos_term.t = t
6
7     # Solve variational problem for time step
8     J = derivative(F, w)
9     solve(F == 0, w, bcs, J=J)
10
11     # Update previous solution
12     w_n.assign(w)
```

Appendix H

Lagrangian powder stream model

The initial particle speed distribution given by Eq. G.16 can also be used as an initial condition in the 3D Lagrangian particle tracking model available in the `acousticHologram` C++ library. The library can be used to calculate the sound pressure and sound force field and the resulting particle paths. The library is described in more detail in Appendix G. The initial particle concentration at the hopper nozzle position can be approximated by a group of particles, chosen such that their probability function approaches the particle concentration function. This can be done using a uniformly distributed random number using Monte Carlo (MC) sampling [202]. In order to produce a probability distribution that matches the required distribution, using a function of a uniform random variable, when samples are drawn the cumulative probability distributions should match. The probability distribution for the powder, is given by Eq. G.6, normalized such that its probability density function has a total probability of one:

$$p(r) = \frac{1}{\pi R(z)^2} e^{-r^2/R(z)^2} \quad (\text{H.1})$$

In order to find the function that will produce this probability distribution using a uniform random number X , one has to equate their cumulative probability distributions

and solve for a sample radial position of Eq. H.1:

$$\begin{aligned}
F_G(r) &= F_u(X) \\
\int_0^r p(r)2\pi r dr &= X \\
1 - e^{-r^2/R(z)^2} &= X \\
r &= R(z)\sqrt{-\ln(1-X)} \\
r &= R(z)\sqrt{-\ln(X)}
\end{aligned} \tag{H.2}$$

Note that if X produces a uniform distribution $1 - X$ will also produce a uniform distribution.

One can relate the number of samples N to the number of particles that have moved through the nozzle for some time t . This time is given by:

$$t = \frac{m_p}{\dot{m}} N \tag{H.3}$$

In order to get the final concentration as a position from the stream axis $c(r)$, the number of samples is counted on a circular strip and its then divided by the area of the strip and by the distance given by $u_z t$ that gives the number of particles per unit volume:

$$c_i = \frac{N_i}{A_i u_z t} \tag{H.4}$$

where A_i is given by Eq. H.5 if i is greater than zero or equal to $\pi\Delta r^2/4$ if i is zero.

$$A_i = \pi\Delta r^2[(i + 1/2)^2 - (i - 1/2)^2] \tag{H.5}$$

Following a similar approach to convergence studies for deterministic simulations, procedure #1 described in Appendix G was used; first the RK4 time steps where refined to get an acceptable error, followed by refining the MC simulation, using an increasing number of simulated particle paths.

For the RK4 convergence study, the scalar value being considered is the distance between the end points of the particle trajectories, simulated at subsequent time step values. One should note that doing a percent change in scalar values would bias the calculated scalars if the end points are closer to the axis origin of the simulation.

The initial particle positions are at the start of the sound interaction length, perpendicular to the particle stream axis, from 0.2 to 4.8 mm, at 0.2 mm intervals (24 particles). The direction of the particles follows Eq. G.16, like in the full simulations. Since the applied force is close to axisymmetric, the errors that will be measured for these particle paths will be similar to any other paths around the particle stream axis.

The resulting end point distances as a function of distance from the particle stream axis, given as an example for SS 316L at 0 and 10 V are shown in Fig. H.1. As expected, the end point distances for 0 V without any applied sound force are lower, but not zero (with the Taylor terms being zero for straight line motion [171]), since the outward spreading particles are subject to the much lower sideways aerodynamic drag force.

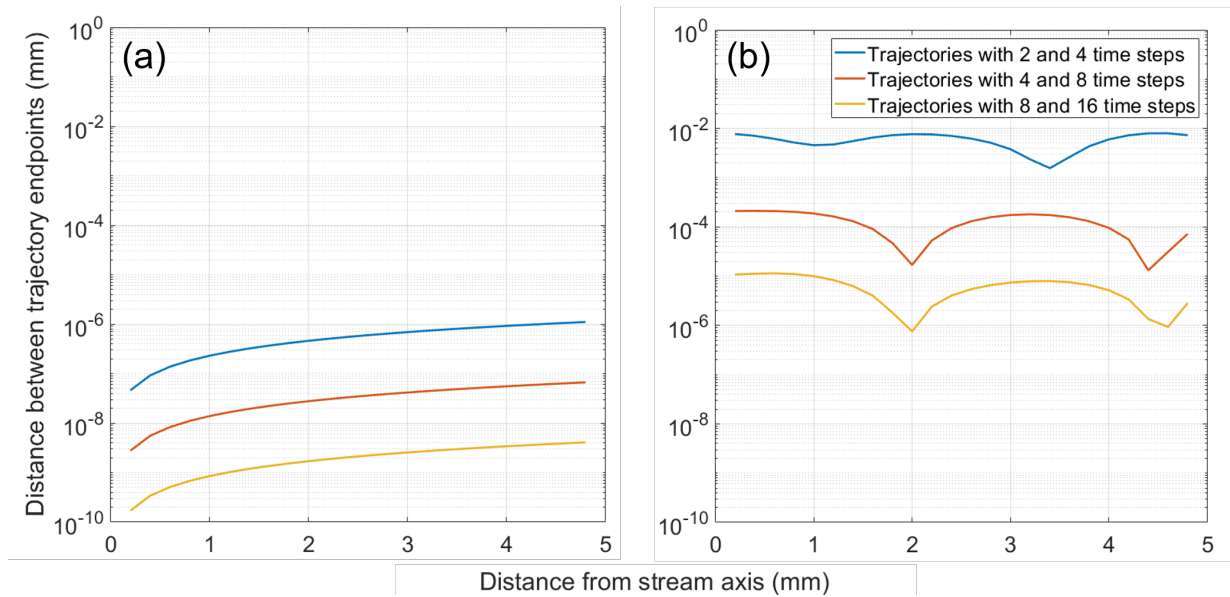


Figure H.1: Trajectory endpoint distance change for SS 316L at (a) 0 and (b) 10 V Lagrangian simulation runs.

Since the concentration values are calculated from determining which end points are within the corresponding radial samples, one can estimate the error due to the RK4 simulation by the ratio between the sampling possible variation area change to sampling area at $r = 0$, given by $4t/\Delta r$. Where t is the maximum end point distance change between to subsequent subdivisions of the time steps. For an chosen acceptable error of 2%, t should be lower than 0.0025 mm. Since the maximum end point distance t of 0.0080 mm (the blue line for the 10 V run in Fig. H.1), in the case of SS 316L at 10 V, the RK4 path simulations will be carried out using 4 time steps for the MC convergence study.

For the MC convergence study, the scalar that will be used is the root mean squared (RMS) error for the center-line concentration. In this MC simulation, the particle paths are sampling a probability distribution [279, 202]. When sampling an unknown probability distribution, one can have an approximation of the actual mean from the sample mean, given by:

$$\mu_a \approx \mu_s = \frac{1}{n} \sum_{i=1}^n f_i = \langle f \rangle \quad (\text{H.6})$$

where a stands for actual, s for sample, and n is the number of samples. The actual probability distribution has a variance, that can be approximated using the sample variance given by:

$$\sigma_a^2 \approx \sigma_s^2 = \frac{1}{n-1} \sum_{i=1}^n (f_i - \mu_s)^2 = \frac{n}{n-1} (\langle f^2 \rangle - \langle f \rangle^2) \quad (\text{H.7})$$

One should note that since one is sampling the distribution, the mean also has a variance. The square root of this variance is the sample mean RMS value, that approaches zero as the number of samples go to infinity:

$$RMS_{\mu_s} = \frac{\sigma_s}{\sqrt{n}} = \sqrt{\frac{1}{n-1} (\langle f^2 \rangle - \langle f \rangle^2)} \quad (\text{H.8})$$

As can be seen from Eq. H.8, the sample mean RMS value is proportional to $n^{-1/2}$.

The concentration sample means and variances as a function of number of particle paths for both 0 and 10 V SS 316L Lagrangian simulation runs, using a 0.5 mm sampling strip width, are shown in Fig. H.2.

Using the values from Fig. H.2, the sample mean RMS values as a function of the number of particle paths is shown in Fig. H.3. As can be seen from Fig. H.3, the RMS values for 0 and 10 V go below an acceptable 4% before using 12×10^4 and 6.6×10^4 paths respectively.

Using the values from Fig. H.2, the sample mean RMS values as a function of the number of particle paths is shown in Fig. H.3. As can be seen from Fig. H.3, the RMS values for 0 and 10 V go below an acceptable 4% before using 12×10^4 and 6.6×10^4 paths respectively.

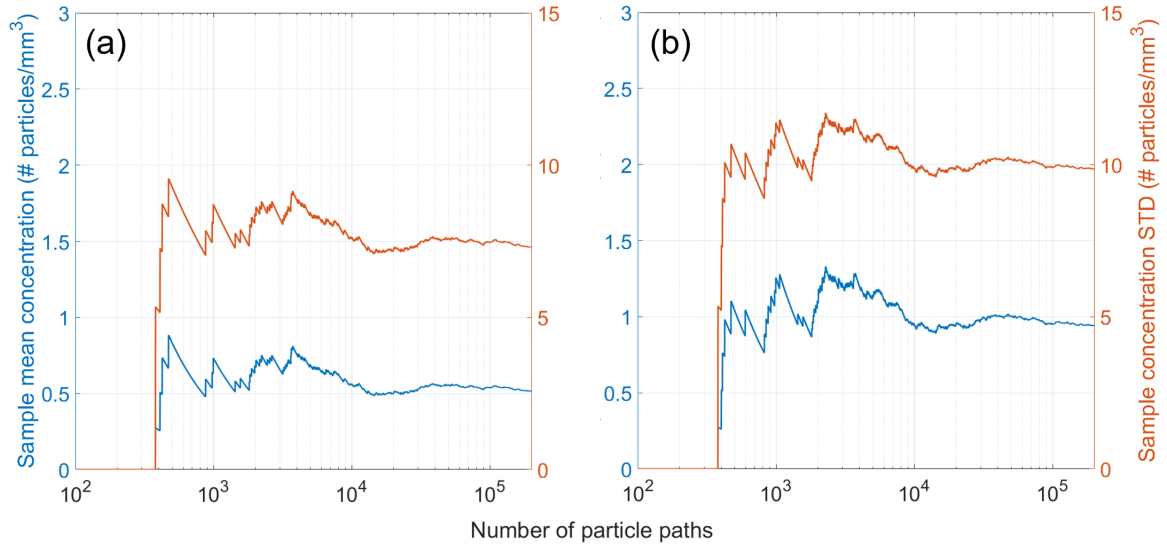


Figure H.2: Sample means and variances as a function of number of particle paths for SS 316L at (a) 0 and (b) 10 V Lagrangian simulation runs.

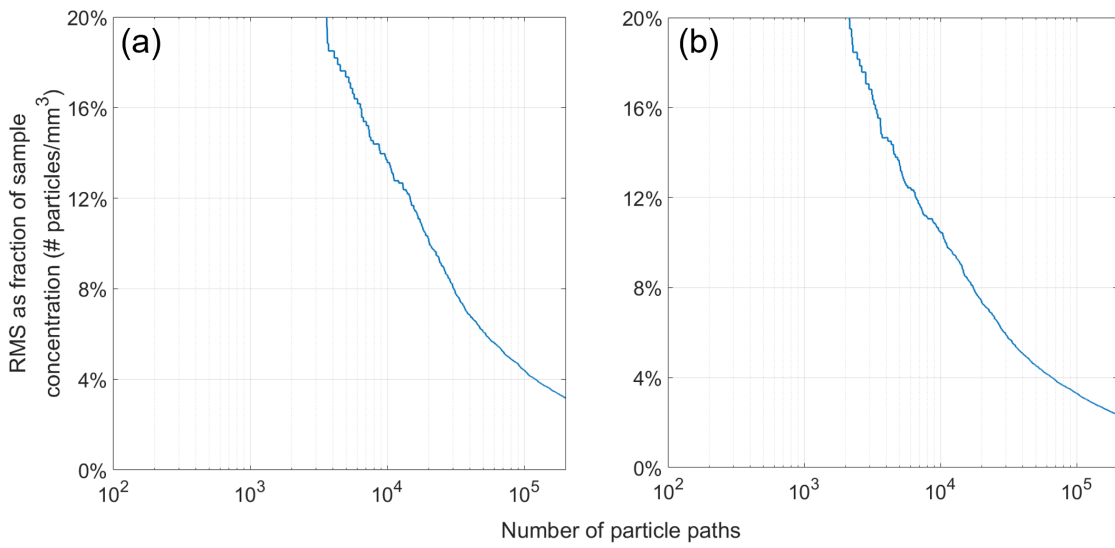


Figure H.3: Sample mean RMS values as a function of number of particle paths for SS 316L at (a) 0 and (b) 10 V Lagrangian simulation runs.

Based on the convergence analysis, the Lagrangian simulation results in Section 4.5.8 for all runs were run using using a 0.5 mm sampling strip width for the concentration values, and the RK4 time steps and number of particle paths shown in Table H.1.

Table H.1: Required RK4 time steps and number of particle paths for Lagrangian simulations for all particle materials and array voltages to reach convergence

Particle material	Applied voltage	Number of time steps for RK4 particle tracking	Number of points for MC computation ($\times 10^4$)	Computation time (mins)
Ti6Al4V	0	2	4.8	22:36
Ti6Al4V	8	4	2.4	22:48
SS 316L	0	2	12	56:29
SS 316L	10	4	6.6	62:09
SS 316L	16	4	2.2	20:44

Appendix I

Parameters for expected value of coefficient of determination in GBR

Here we want to calculate $\mathbb{E}(SS_{res})/\mathbb{E}(SS_T)$ from Eqs. 5.35-5.36 to then find the expected value of r^2 (Eq. 5.28). Note that:

$$\frac{\mathbb{E}(EE_{res})}{\mathbb{E}(EE_T)} = \frac{N}{N-1} \frac{\mathbb{E}(y_n^2) - \mathbb{E}[\mathbb{E}_{\theta_x}^2(y_n)]}{\mathbb{E}(y_n^2) - \mathbb{E}^2(y_n)} \xrightarrow{N \rightarrow \infty} \frac{\mathbb{E}(Y^2) - \mathbb{E}[\mathbb{E}_{\theta_x}^2(Y)]}{\mathbb{E}(Y^2) - \mathbb{E}^2(Y)}$$

For this we used:

$$\begin{aligned} \mathbb{E}([Y - \mathbb{E}_{\theta_x}(Y)]^2) &= \mathbb{E}(Y^2) - 2 \cdot \mathbb{E}[Y \cdot \mathbb{E}_{\theta_x}(Y)] + \mathbb{E}[\mathbb{E}_{\theta_x}^2(Y)] \\ &= \mathbb{E}_x[\mathbb{E}_{\theta_x}(Y^2)] - \mathbb{E}_x[\mathbb{E}_{\theta_x}^2(Y)] \end{aligned} \quad (\text{I.1})$$

$$\begin{aligned} \mathbb{E}([Y - \mathbb{E}(Y)]^2) &= \mathbb{E}(Y^2) - 2 \cdot \mathbb{E}[Y \cdot \mathbb{E}(Y)] + \mathbb{E}[\mathbb{E}^2(Y)] \\ &= \mathbb{E}_x[\mathbb{E}_{\theta_x}(Y^2)] - \mathbb{E}_x^2[\mathbb{E}_{\theta_x}(Y)] \end{aligned} \quad (\text{I.2})$$

Therefore $\mathbb{E}_{\theta_x}(Y)$ and $\mathbb{E}_{\theta_x}(Y^2)$ need to be calculated first:

$$\begin{aligned}
\mathbb{E}_{\theta_x}(Y) &\stackrel{\text{Eq. 5.32}}{=} \int_{-\frac{\pi}{2}}^{\frac{\pi}{2}} \theta_x \cdot f_{\theta_x}(\theta_x|x) d\theta_x \\
&\stackrel{\text{Eq. 5.29}}{=} \int_{\mathbb{R}} \frac{\arctan\left(\frac{k_x}{k}\right)}{\sqrt{2\pi}k_1(z)} \exp\left(-\frac{\left[k_x - k\frac{x}{R(z)}\right]^2}{2k_1^2(z)}\right) dk_x \\
&= \sum_{n=0}^{\infty} \frac{(-1)^n}{\sqrt{2\pi}k_1(z)(2n+1)k^{2n+1}} \int_{\mathbb{R}} k_x^{2n+1} \exp\left(-\frac{\left[k_x - k\frac{x}{R(z)}\right]^2}{2k_1^2(z)}\right) dk_x
\end{aligned}$$

where we used the substitution $\theta_x = \arctan\left(\frac{k_x}{k}\right)$ and the Taylor series for \arctan (which is absolutely convergent on \mathbb{R}).

The appearing integral can be calculated analytically with the gamma-function Γ :

$$\begin{aligned}
&\int_{\mathbb{R}} k_x^{2n+1} \exp\left(-\frac{\left[k_x - k\frac{x}{R(z)}\right]^2}{2k_1^2(z)}\right) dk_x \\
&= \int_{\mathbb{R}} \left[k_x + k\frac{x}{R(z)}\right]^{2n+1} \exp\left[-\frac{k_x^2}{2k_1^2(z)}\right] dk_x \\
&= \int_{\mathbb{R}} \sum_{m=0}^{2n+1} \binom{2n+1}{m} k_x^m \left[k\frac{x}{R(z)}\right]^{2n+1-m} \exp\left[-\frac{k_x^2}{2k_1^2(z)}\right] dk_x \\
&= \sum_{m=0}^{2n+1} \binom{2n+1}{m} \left[k\frac{x}{R(z)}\right]^{2n+1-m} k_1^m(z) \int_{\mathbb{R}} \left[\frac{k_x}{k_1(z)}\right]^m \exp\left(-\frac{\left[\frac{k_x}{k_1(z)}\right]^2}{2}\right) dk_x \\
&= \sum_{m=0}^{2n+1} \binom{2n+1}{m} \left[k\frac{x}{R(z)}\right]^{2n+1-m} k_1^{m+1}(z) \int_{\mathbb{R}} u^m \exp\left(-\frac{u^2}{2}\right) dk_x \\
&= \sum_{m=0}^{2n+1} \binom{2n+1}{m} \left[k\frac{x}{R(z)}\right]^{2n+1-m} k_1^{m+1}(z) 2^{\frac{m-1}{2}} [1 + (-1)^m] \Gamma\left(\frac{m+1}{2}\right) \\
&= \sum_{l=0}^{2n+1} \binom{2n+1}{2l} \left[k\frac{x}{R(z)}\right]^{2n+1-2l} k_1^{2l+1}(z) 2^{\frac{2l+1}{2}} \Gamma\left(\frac{2l+1}{2}\right)
\end{aligned}$$

Here we used the binomial expansion for $(a+b)^N$.

From this follows:

$$\mathbb{E}_{\theta_x}(Y) = \frac{1}{\sqrt{\pi}} \sum_{n=0}^{\infty} \frac{(-1)^n}{2n+1} \sum_{l=0}^n \binom{2n+1}{2l} \left[\frac{k}{k_1(z)} \right]^{2l} \left[\frac{x}{R(z)} \right]^{2(n-l)+1} 2^l \Gamma\left(\frac{2l+1}{2}\right) \quad (\text{I.3})$$

$$\Rightarrow \mathbb{E}_x^2[\mathbb{E}_{\theta_x}(Y)] = 0 \quad (\text{I.4})$$

because $x^{2(n-l)+1}$ is an odd function and f_x is an even function. From Eq. I.3 one can write:

$$\begin{aligned} \mathbb{E}_{\theta_x}(Y) &= \sum_{N=0}^{\infty} a_N x^{2N+1} \\ \Rightarrow \mathbb{E}_{\theta_x}^2(Y) &= \sum_{N=1}^{\infty} b_N x^{2N} \end{aligned}$$

Similarly to the calculation above one can interchange the integral with the power series and needs to calculate:

$$\begin{aligned} \mathbb{E}_x(x^{2N}) &= \int_{\mathbb{R}} x^{2N} \exp\left[-2\frac{x^2}{w^2(z)}\right] \sqrt{\frac{2}{\pi w^2(z)}} dx \\ &= \sqrt{\frac{2}{\pi w^2(z)}} \int_{\mathbb{R}} \left[\frac{2x}{w(z)}\right]^{2N} \left[\frac{w(z)}{2}\right]^{2N} \exp\left(-\frac{\left[\frac{2x}{w(z)}\right]^2}{2}\right) dx \\ &= \sqrt{\frac{2}{\pi w^2(z)}} \left[\frac{w(z)}{2}\right]^{2N} \int_{\mathbb{R}} u^{2N} \exp\left(-\frac{u^2}{2}\right) \frac{w(z)}{2} du \\ &= \sqrt{\frac{2}{\pi w^2(z)}} \left[\frac{w(z)}{2}\right]^{2N+1} 2^{\frac{2N-1}{2}} [1 + (-1)^{2N}] \Gamma\left(\frac{2N+1}{2}\right) \\ &= \frac{1}{\sqrt{\pi}} \left[\frac{w^2(z)}{2}\right]^N \Gamma\left(\frac{2N+1}{2}\right) \\ \Rightarrow \mathbb{E}_x[\mathbb{E}_{\theta_x}^2(Y)] &= \frac{1}{\sqrt{\pi}} \sum_{N=1}^{\infty} b_N \left[\frac{w^2(z)}{2}\right]^N \Gamma\left(\frac{2N+1}{2}\right) \end{aligned} \quad (\text{I.5})$$

Now only $\mathbb{E}(Y^2)$ is missing for Eqs. I.1 and I.2. For this define c_n by:

$$\arctan^2(x) = \sum_{n=2}^{\infty} c_n x^n \Rightarrow c_{2k} = \sum_{m=0}^{k-1} \frac{(-1)^{k-1}}{(2m+1)[2(k-m)-1]} \quad (\text{I.6})$$

Then one can calculate $\mathbb{E}_{\theta_x}(Y^2)$ similarly to $\mathbb{E}_{\theta_x}(Y)$:

$$\begin{aligned}
\mathbb{E}_{\theta_x}(Y^2) &= \int_{\mathbb{R}} \frac{\arctan^2\left(\frac{k_x}{k}\right)}{\sqrt{2\pi}k_1(z)} \exp\left(-\frac{\left[k_x - k\frac{x}{R(z)}\right]^2}{2k_1^2(z)}\right) dk_x \\
&= \sum_{n=2}^{\infty} \frac{c_n}{\sqrt{2\pi}k_1(z)k^n} \int_{\mathbb{R}} k_x^n \exp\left(-\frac{\left[k_x - k\frac{x}{R(z)}\right]^2}{2k_1^2(z)}\right) dk_x \\
&= \sum_{n=2}^{\infty} \frac{c_n}{\sqrt{2\pi}k_1(z)k^n} \sum_{m=0}^n \binom{n}{m} \left[k\frac{x}{R(z)}\right]^{n-m} k_1^{m+1}(z) \\
&\quad 2^{\frac{m-1}{2}} [1 + (-1)^m] \Gamma\left(\frac{m+1}{2}\right) \\
&= \sum_{n=2}^{\infty} \frac{c_n}{\sqrt{2\pi}} \sum_{m=0}^n \binom{n}{m} \left[\frac{k_1(z)}{k}\right]^m \left[\frac{x}{R(z)}\right]^{n-m} \\
&\quad 2^{\frac{m-1}{2}} [1 + (-1)^m] \Gamma\left(\frac{m+1}{2}\right)
\end{aligned}$$

The expected value:

$$\mathbb{E}_x\left(\left[\frac{x}{R(z)}\right]^{n-m}\right) = \frac{1}{\sqrt{\pi}} \left[\frac{w(z)}{2R(z)}\right]^{n-m} 2^{\frac{n-m-2}{2}} [1 - (-1)^{n-m}] \Gamma\left(\frac{n-m+1}{2}\right)$$

finishes the calculation:

$$\begin{aligned}
&= \mathbb{E} (Y^2) \\
&= \mathbb{E}_x [\mathbb{E}_{\theta_x} (Y^2)] \\
&= \frac{1}{\pi} \sum_{n=2}^{\infty} c_n \sum_{m=0}^n \binom{n}{m} \left[\frac{k_1(z)}{k} \right]^m 2^{\frac{m}{2}} \frac{1 + (-1)^m}{2} \Gamma \left(\frac{m+1}{2} \right) \left[\frac{w(z)}{2R(z)} \right]^{n-m} \\
&\quad 2^{\frac{n-m}{2}} \frac{1 + (-1)^{n-m}}{2} \Gamma \left(\frac{n-m+1}{2} \right) \\
&= \frac{1}{\pi} \sum_{n=2}^{\infty} c_n 2^{-\frac{n}{2}} \sum_{l=0}^{\lfloor \frac{n}{2} \rfloor} \binom{n}{2l} \left[\frac{k_1(z)}{k} \right]^{2l} \Gamma \left(\frac{2l+1}{2} \right) \left[\frac{w(z)}{R(z)} \right]^{n-2l} \\
&\quad \frac{1 + (-1)^{n-2l}}{2} \Gamma \left(\frac{n-2l+1}{2} \right) 2^{2l} \\
&= \frac{1}{\pi} \sum_{k=1}^{\infty} c_{2k} \left[\frac{w^2(z)}{2R^2(z)} \right]^k \sum_{l=0}^k \binom{2k}{2l} \left[\frac{k_1(z)}{k} \right]^{2l} \left[\frac{w(z)}{R(z)} \right]^{-2l} \Gamma \left(\frac{2l+1}{2} \right) \Gamma \left[\frac{2(k-l)+1}{2} \right] 2^{2l} \\
&= \frac{1}{\pi} \sum_{k=1}^{\infty} \left(\sum_{m=0}^{k-1} \frac{(-1)^{k-1}}{(2m+1)[2(k-m)-1]} \right) \left[\frac{w^2(z)}{2R^2(z)} \right]^k \sum_{l=0}^k \binom{2k}{2l} \left[\frac{2k_1(z)R(z)}{kw(z)} \right]^{2l} \\
&\quad \Gamma \left(\frac{2l+1}{2} \right) \Gamma \left[\frac{2(k-l)+1}{2} \right] \\
&= \frac{1}{\pi} \sum_{k=1}^{\infty} \left[-\frac{w^2(z)}{2R^2(z)} \right]^k \left(\sum_{m=0}^{k-1} \frac{-1}{(2m+1)[2(k-m)-1]} \right) \sum_{l=0}^k \binom{2k}{2l} \left[\frac{2k_1(z)R(z)}{kw(z)} \right]^{2l} \\
&\quad \Gamma \left(\frac{2l+1}{2} \right) \Gamma \left[\frac{2(k-l)+1}{2} \right]
\end{aligned}$$

where we used Eq. I.6 to calculate c_{2k} . With this formula and Eqs. I.1, I.2, I.4, I.5 one can calculate expected value in Eq. 5.28. The result in the paraxial approximation is given by Eq. 5.37.

Appendix J

Automatic differentiation in the acousticHologram library

Computing the sound field model and its derivatives involves computing the Bessel function of the first kind and order 1 divided by x , $J_1(x)/x$, which may include values of x equal or very close to zero. This corresponds to evaluating the sound field right in front of an ultrasound transducer. This will produce a division by zero error in C++ at zero, and very inaccurate values for values close to zero due to rounding error. One can evaluate the limit of $J_1(x)/(x)$ for x approaching 0, yielding 0.5, showing that the function is defined there. One can use an equivalent expression without division by x , using the following recurrence relation for $J_{n+1}(x)$ [280]:

$$J_{n+1}(x) = \frac{2n}{x} J_n(x) - J_{n-1}(x) \quad (\text{J.1})$$

Rearranging and evaluating for $n = 1$ yields:

$$\frac{J_1(x)}{x} = \frac{1}{2}[J_2(x) + J_0(x)] \quad (\text{J.2})$$

One can then use this expression instead to avoid a division by zero error. In order for the automatic differentiation library FADBAD++ to evaluate the derivatives more efficiently, x should be evaluated first and stored in a separate variable (using the FADBAD++ type) and then used in Eq. J.2. However the library needs to be extended to evaluate Bessel functions of the first kind.

In the FADBAD++ library, forward mode automatic differentiation is done by parsing a C++ function into a code-list; a set of constant, unary or binary operations. This is called arity or number of dependencies. The code-list can be also written as a directed acyclic graph (DAG) [253]. This is done using operator overloading. Note the operator overloading automatically takes care of expressions such as $a+b+c$ by sequential evaluations i.e $(a+b)+c$. As an example, one can find the derivative of the following expression:

$$y = x_1x_2 + x_1x_2\sin(x_2) + x_2x_3^2 \quad (\text{J.3})$$

Following the notation in [253], the expression can be written as:

$$\begin{aligned} \tau_1 &= x_1, \quad \tau_2 = x_2, \quad \tau_3 = x_3 \\ \tau_4 &= \tau_1\tau_2 \\ \tau_5 &= \sin(\tau_2) \\ \tau_6 &= \tau_4\tau_5 \\ \tau_7 &= \tau_2\tau_3 \\ \tau_8 &= \tau_3\tau_7 \\ \tau_9 &= \tau_4 + \tau_6 \\ \tau_{10} &= \tau_8 + \tau_9 \end{aligned}$$

Note the expression can be broken down into operations that are at most binary in arity. One can compute the derivatives of the expression (τ_{10}) with respect to $x_1 = \tau_1$ for example. This is done by evaluating the derivatives of the code-list in order. Using $\partial\tau_j/\partial\tau_k = \hat{\tau}_{j,k}$:

$$\begin{aligned} \hat{\tau}_{1,1} &= 1, \quad \hat{\tau}_{2,1} = 0, \quad \hat{\tau}_{3,1} = 0 \\ \hat{\tau}_{4,1} &= \hat{\tau}_{4,1} + \hat{\tau}_{4,2}\hat{\tau}_{2,1} = \tau_2 + \tau_1(0) = \tau_2 \\ \hat{\tau}_{5,1} &= \hat{\tau}_{5,2}\hat{\tau}_{2,1} = -\cos(\tau_2)(0) = 0 \\ \hat{\tau}_{6,1} &= \hat{\tau}_{6,4}\hat{\tau}_{4,1} + \hat{\tau}_{6,5}\hat{\tau}_{5,1} = \tau_5(\tau_2) + \tau_4(0) = \tau_5\tau_2 \\ \hat{\tau}_{7,1} &= \hat{\tau}_{7,2}\hat{\tau}_{2,1} + \hat{\tau}_{7,3}\hat{\tau}_{3,1} = \tau_3(0) + \tau_2(0) = 0 \\ \hat{\tau}_{8,1} &= \hat{\tau}_{8,3}\hat{\tau}_{3,1} + \hat{\tau}_{8,7}\hat{\tau}_{7,1} = \tau_7(0) + \tau_3(0) = 0 \\ \hat{\tau}_{9,1} &= \hat{\tau}_{4,1} + \hat{\tau}_{6,1} = \tau_2 + \tau_5\tau_2 \\ \hat{\tau}_{10,1} &= \hat{\tau}_{8,1} + \hat{\tau}_{9,1} = 0 + \tau_2 + \tau_5\tau_2 = \tau_2 + \tau_5\tau_2 = x_2 + x_2\sin(x_2) \end{aligned}$$

Note that when the x values are known, one can compute a single value for each derivative in the code-list, by using the τ and $\hat{\tau}$ values from earlier entries in the code list.

Forward mode AD is like symbolic differentiation except that the intermediate derivatives are being evaluated while the total derivative is obtained. This decreases the amount of needed memory since the representation of expressions for every trace is not being stored.

In FADBAD++, one can implement the forward differentiation C++ type for $J_n(x)$ as follows:

```

1  template <typename T, typename U>
2  INLINE2 FTypeName<T,0> jn(const U& a, const FTypeName<T,0>& b) {
3      FTypeName<T,0> c(Op<T>::myJn(a,b.val()));
4      if (!b.depend()) return c;
5      T tmp( (Op<T>::myJn(a-1, b.val()) - Op<T>::myJn(a+1, b.val()))*Op<T>::
6              myInv(Op<T>::myTwo()) );
7      c.setDepend(b);
8      for(unsigned int i=0;i<c.size();++i) c[i]=tmp*b[i];
9      return c;
10 }
11 template <typename T, typename U, unsigned int N>
12 INLINE2 FTypeName<T,N> jn(const U& a, const FTypeName<T,N>& b) {
13     FTypeName<T,N> c(Op<T>::myJn(a,b.val()));
14     if (!b.depend()) return c;
15     T tmp( (Op<T>::myJn(a-1, b.val()) - Op<T>::myJn(a+1, b.val()))*Op<T>::
16             myInv(Op<T>::myTwo()) );
17     c.setDepend(b);
18     for(unsigned int i=0;i<N;++i) c[i]=tmp*b[i];
19     return c;
20 }

```

The two instances of the function account for the use of a heap allocation for the code-list, or a stack structure which is faster [252]. The stack structure can be used by using `F<double,n>` where `n` is the number of independent variables that will be needed to find derivatives. In the case of the `acousticHologram` library, the number of independent variables is fixed and its simply the number of dimensions (3).

The variable `tmp` is the derivative of J_n with respect to the variable inside the function and its given by [280]:

$$\frac{\partial J_n(x)}{\partial x} = \frac{1}{2}[J_{n-1}(x) - J_{n+1}(x)] \quad (\text{J.4})$$

The line `c[i]=tmp*b[i]` computes the unary chain rule for every independent variable. Note that the only derivatives needed in the `acousticHologram` library are $J_n(x)$ with respect to x and not n , which would require writing a general function to go over the code-list and to check if one has derivatives with respect to x or n or both and then use the appropriate function. This is done in the case of the exponential function in FADBAD++.

Appendix K

Array mesh computation

The modified DistMesh computation steps [254] for computing the triangular mesh of an open convex surface are shown in Algorithm 6. The original algorithm for closed surfaces is implemented in the function `distmeshsurface()` in the DistMesh MATLAB library. The modifications are highlighted by the bolded descriptions.

The function starts by generating points on a sphere and their connectivity matrix (that records what 3 points belong a given triangular element in the mesh), projected from a uniform point grid around the sphere, then the elements and associated points are removed if any of the points in an element are below or above the required sphere zone. This is done using the custom function `meshZAxisCrop()`. The surface projection operation is done using the distance function of the sphere surface $d(p_i)$. This particular implementation works by taking into account that the openings of the sphere zone are circles normal to the z-axis, which is also the sphere zone's axis of symmetry. The initial sphere is centered at the origin.

Algorithm 6 Sphere zone open surface DistMesh computation steps

```
1: while max[sqrt(sumc[(p - p0)2])/h0 > dptol do  
    ▷ Array element-wise operations, sum is along column entries  
2:   p0 = p  
3:   if max[sqrt(sumc[(p - pold)2])/h0 > ttol then  
    ▷ Re-triangulation step, check first if Δp is large enough  
4:     pold = p  
5:     p ← (0, 0, -rs), (0, 0, rs)  
    ▷ Add points so elements formed at openings can be removed  
6:     t = convexHull(p)          ▷ Use MATLAB convex hull function to update t  
7:     (p, t) = meshZAxisCrop(p, t, hl, hu)    ▷ Remove elements formed at openings  
8:     b = bars(p, t)             ▷ Find unique mesh edges “bars”  
9:   end if  
10:  p = barSystemForwardEuler(p)    ▷ Single iteration of core DistMesh algorithm  
  
11:  for i = 1 to current # of nodes do  
12:    dp = d(pi)  
    ▷ Project points back to surface using d(pi) numerical gradient (normal to surface)  
13:    dx = {d[(pix + ε, piy, piz)] - dp}/ε  
14:    dy = {d[(pix, piy + ε, piz)] - dp}/ε  
15:    dz = {d[(pix, piy, piz + ε)] - dp}/ε  
16:    pix = pix - dpdx, piy = piy - dpdy, piz = piz - dpdz  
    ▷ Note that |∇d| = 1 for a distance function  
  
17:    if piz < hl then ▷ Project points outside (hl, hu) z-range back to boundaries  
18:      piz = hl, rp = √(pix2 + piy2), (pix, piy) = (pixrl/rp, piyrl/rp)  
19:    end if  
20:    if piz > hu then  
21:      piz = hu, rp = √(pix2 + piy2), (pix, piy) = (pixru/rp, piyru/rp)  
22:    end if  
23:  end for  
24: end while  
25: return p
```

In Algorithm 6, p is an N by 3 array with N mesh points with their x , y and z coordinates in each column, t is an M by 3 connectivity array with M elements, where the mesh point number of each element is in each column, and b is a P by 2 array with P edges, where the mesh point number of each edge is in each column. Other variables used are the re-triangulation tolerance $t_{tol}=0.1$, algorithm termination tolerance $dp_{tol}=1\times 10^{-8}$, the lower sphere zone height is h_l , the upper sphere zone height is h_u , and the sphere radius is r_s . Note that $0 < h_l < h_u < r_s$. The variables r_l and r_u are the radius of the circle given by the intersection of the sphere zone and a plane normal to the z -axis at $z = h_l$ and h_u respectively.

In the core DistMesh algorithm the corresponding spring (or bar) system given by the edges of the mesh is solved for equilibrium: the sum of the forces in each spring is minimized by solving the force balance system:

$$F(p) = 0 \tag{K.1}$$

using an explicit Euler method:

$$p_{n+1} = p_n + t_a F(p_n) \tag{K.2}$$

where $t_a=0.2$. In this process the spring structure spreads out covering the area to be meshed. In order for the nodes to spread far enough, the actual equilibrium edge length l_0 inputted in the algorithm's MATLAB function is multiplied by a scaling factor F_{scale} . A satisfactory value for this factor was found by trial and error to be 1.05. Each node motion iteration moves the nodes out of the surface being meshed. The distance function is used to determine where to project the points back to the surface (line 12 in Algorithm 6). A similar process was added to project the points back to the open boundaries. The net effect is that nodes move tangent to the surface and the boundaries after spreading out.

Appendix L

Fabrication and alignment of UPL array/frame assembly

Array fabrication

Two of the fabrication steps for the array are shown in Fig. L.1. The array was printed in one piece at the lowest angle possible in order to have the layers as parallel as possible to the array and to minimize support volume. The array right after printing is shown in Fig. L.1(a). Fig. L.1(b) shows a close-up of the array after support removal, showing the engraved transducer numbering.

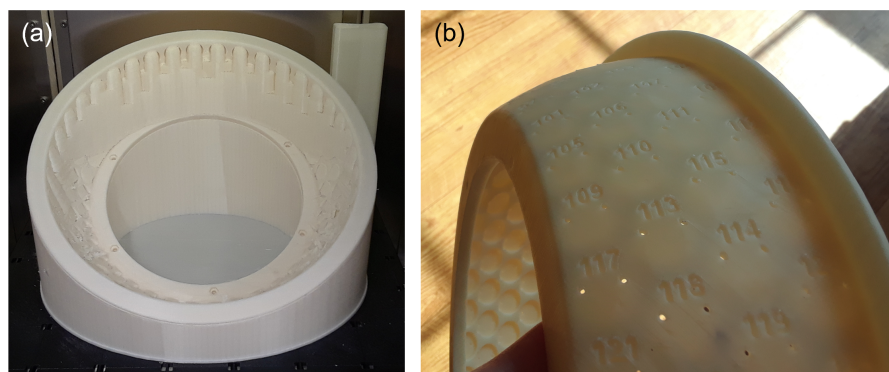


Figure L.1: (a) Array printed in a single piece. (b) Close-up of the printed array numbering.

Gas cyclone

In order to decouple the DM3D gas flow rate from the particle speed, a gas cyclone with a copper tube extension was designed. This was required to investigate the sound focusing effect at different particle speeds, while having the minimum flowrate required to carry the powder from the hopper all the way to the processing area. The cyclone is able to slow down the metal particles by separating them from the bulk gas flow. The copper tube extension at the dust exit allows for the slowed down particles to be accelerated to a wide range of speeds depending on the dust exit flow, which can be adjusted with an adjustable valve downstream of the cyclone outlet. The extension also protects the cyclone from the heat of the processing area.

In order to be able to print the cyclone in one piece and also to have less of a turning angle for the inlet section to reduce pressure losses, a Helical-roof cyclone design was chosen. Information on selecting inlet dimensions for a Helical-roof cyclone can be found in [281, 282]. It is known that a higher inlet angle decreases separation efficiency and decreases pressure drop [282]. A recommended particle separation efficiency/pressure drop compromise angle reported is 10-15°. Based on the other cyclone dimensions a 16° inlet angle was selected in the design, and the cyclone was titled by 25° for printing, such that maximum overhang angle when printing is 49°. The cyclone has other features such as a 45° chamfer to reinforce the top of the cyclone body and the start of the barb fitting, as well as prevent support generation in that area and ribs to prevent deformation while in use and to reinforce the tube section that also reinforces the copper tube.

The tube used for the nozzle was a 101 copper, 0.032" thick, 1/8" outside diam. tube from McMaster-Carr (SKU #: 8965K22), with a cut length of 100 mm. The tube was glued with epoxy close to the end of the tube section as well as by applying epoxy close to the start of the hole section by drilling a hole in that area in order to have a seal close to the cyclone vortex end.

The inlet fitting was a male 1/4" BSPP to 8 mm push-in adapter (FESTO, part type: QS-1/4-8). The fitting attaches to an 8 mm pneumatic plastic tube (FESTO, part type: PUN-H-8x1.25-BL), serving as an extension, that attaches to the DM3D powder feed tube with an 8 mm to 8 mm push-in adapter (FESTO, part type: QS-8). The female thread was printed with the cyclone and was rethreaded using a 1/4" BSPP thread tap (McMaster-Carr, SKU #: 3023N11). The inlet fitting thread was covered with silicon tape before threading it into the cyclone inlet.

The barb fitting is used to attach an anti-static silicone rubber tube (16 mm inner, 20 mm outer diam.) from McMaster-Carr (SKU #: 1909T51) to take the cyclone outlet

emissions away from the processing area. The tube is attached to a miniature chrome-plated brass ball valve (3/8" inner diam., McMaster-Carr, SKU #: 1909T51) using two aluminum male 1/2" NPT to 5/8" barb fittings (ICT Billet, part #: AN840-10-08A). The assembled cyclone and other construction and design stages are shown in Fig. L.2.

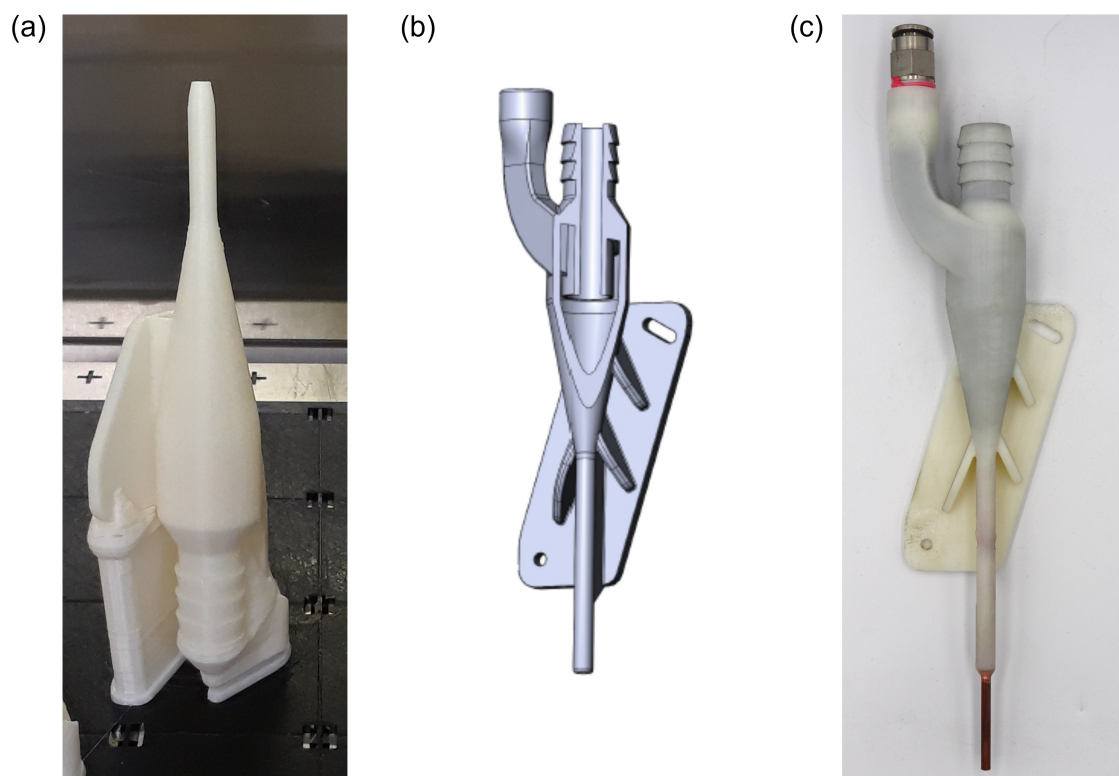


Figure L.2: (a) Previous prototype printed in one piece with no internal supports. (b) Gas cyclone CAD with section view showing inlet area and vortex finder. (c) Printed and assembled cyclone with fitting and copper tube extension.

Calculations may be carried out based on Barth particle separation model in [281] with the volume PSD for Ti6Al4V powder being used to estimate what fraction of the incoming mass, and at what particle size volume average, will be at cyclone outlet. This will give an overestimation of the outlet emissions since there is a small fraction of the flow at the cyclone hopper exit which increases the cyclone's separation efficiency. This cyclone setup is referred to as a cyclone with secondary gas extraction, since part of flow takes lingering particles close to cyclone vortex end [283]. In this case the secondary gas flow and separated powder is the powder/gas mix leaving the nozzle.

The long narrow copper tube was able to accelerate Ti6Al4V, 80 μm particles to a speed of 2.0 m/s or higher for the DM3D setup used in Chapter 6 (20 l/min at the cyclone inlet), by restricting the cyclone outlet flow, using the adjustable outlet valve.

Further measurements were conducted also measuring the outlet flowrate when adjusting the valve, with 12 l/min at the cyclone inlet. For a flow of 6 l/min at the outlet the speed was 2.9 m/s and increased to 16.7 m/s when the outlet has a flow of 0 l/min (closed ball valve).

Frame design

The approximate shape of the frame assembly components were designed using Altair Inspire software, using the topology optimization (TO) facility. The final CAD designs informed by the TO results and the TO results can be found in Fig. L.3. The settings used in the DM3D adapter TO were: stiffness maximization with 5% volume fraction and a minimum thickness of 1 cm. The settings for the UPL array adapter TO were the same except that a 10% volume fraction and a minimum thickness of 1.4 cm were used. The default material properties were used. The grey volumes are fixed geometry, and the Brown volume is the TO result. The boundary conditions (BCs) for the DM3D adapter TO were: fixed support of the top surface of the ring attaching to the DM3D machine, and 1 N downward force for the attachment bolt holes for the UPL array adapter. Note that the resulting optimized shape will be the same regardless of the absolute value of the load since a linear finite element model was used in Altair Inspire. The BCs for the UPL adapter were: fixed support for the attachment bolt holes and a uniform 1 N downward force for the lower surface of the ring attaching to the UPL array.

For the DM3D adapter one can observe in the TO result that the amount of material decreases towards the back of the component where the position setting tab is located. The front of the final CAD is quite different from the TO result due to increasing the height

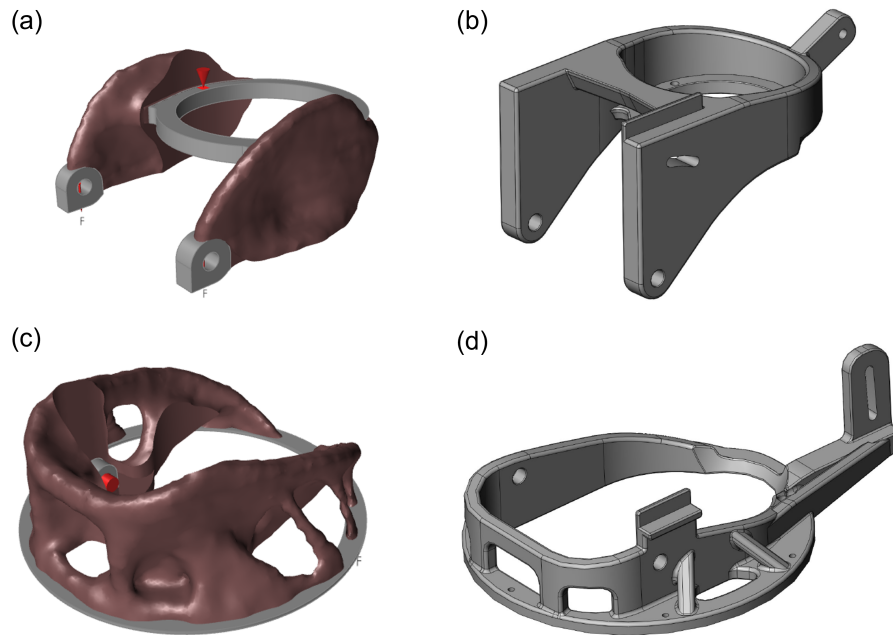


Figure L.3: (a) DM3D adapter TO result. (b) Final DM3D adapter CAD. (c) UPL array adapter TO result. (d) Final UPL array adapter design.

of the part as well as adding a flat area at the top to measure the angle of the part with respect to the UPL array. For the UPL array adapter TO result one can see the same trend of decreasing mass towards the back of the part as well as side struts being generated for the sides, both these features were incorporated in the final CAD. Note that the final CAD design geometry was later simplified so that the DM3D adapter attaches from the inside of the part.

Frame alignment procedure

The distance between the UPL assembly and the laser optics assembly (LOA) along the laser center-line can be adjusted by using laser cut PVC plastic rings of 1 and 2 mm thicknesses. The rings have an inner diameter of 82.55 mm, an outer diameter of 100.8 mm, with 5.1 mm diameter holes placed at a radius of 45.4 mm, and at an angle interval of 15°. A number of rings are placed in the UPL frame part that attaches to the LOA, shown in Fig. L.4(a), depending on the required offset.

The angle between the LOA and the laser center-line can be adjusted by placing the UPL assembly on the alignment frame, and loosening all the bolts shown in Fig. L.4 that are numbered. The alignment frame has three alignment areas that have a small lip used to line up the frame with the UPL array.

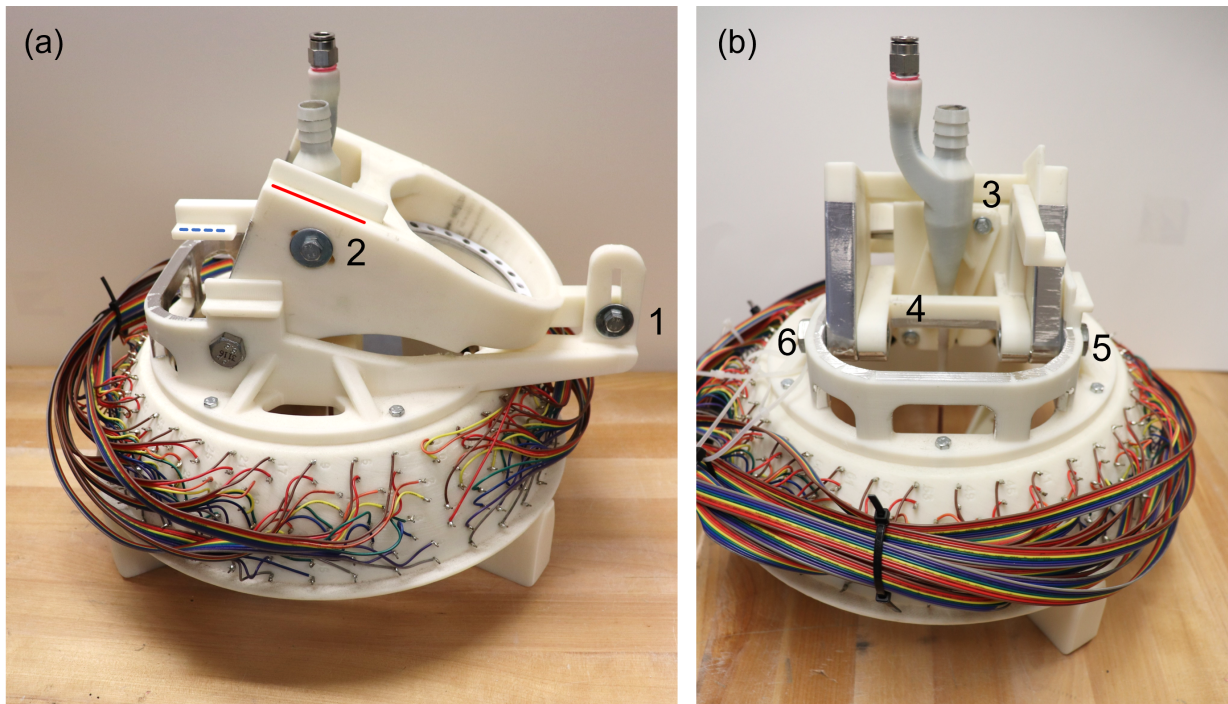


Figure L.4: (a) Side and (b) front view of the UPL assembly, placed on top of the alignment frame.

Then an “alignment tip” is placed on the nozzle tip and the tip is placed on the groove on the alignment frame to line up the nozzle with respect to the UPL array center-line. This is shown in the insert in Fig. L.5(a). Then using a level with an angle indicator placed in the solid red line in Fig. L.4 one can chose the required angle and then set the angle by tightening bolt number 1. Then one can adjust the rest of the bolts shown in Fig. L.4 in the order following their numbering in the figure, while checking the alignment tip is aligned with the alignment frame.

Note that when bolt number 3 is not tightened, the gas cyclone can rotate about bolt number 4 for adjusting the alignment. One can check that the gas cyclone is level by checking that the surface along the blue dotted line in Fig. L.4(a) is level.

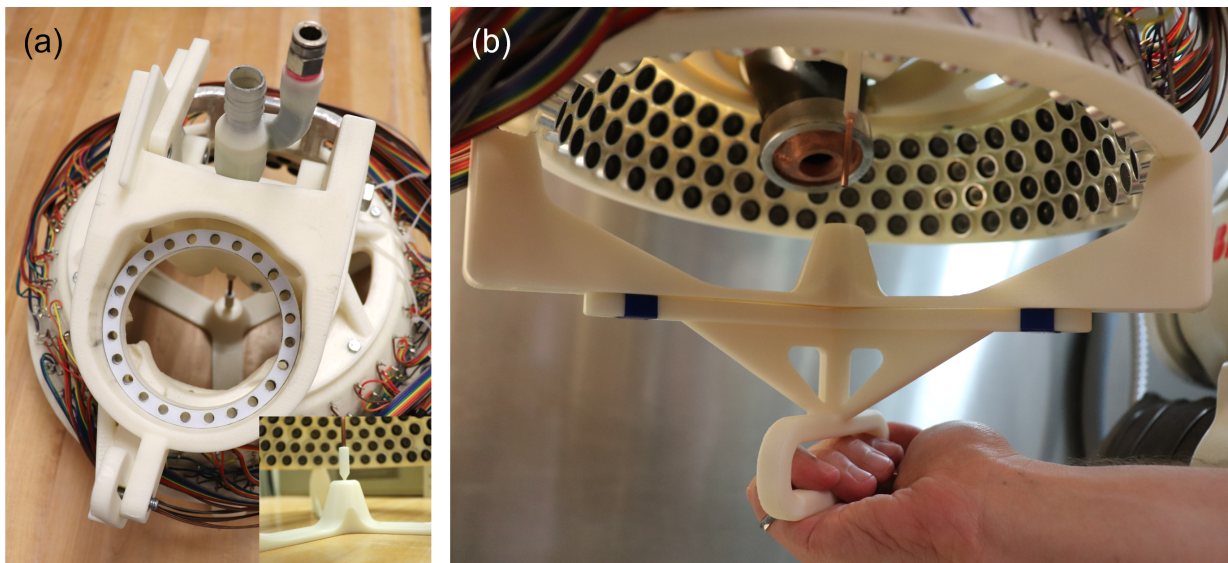


Figure L.5: (a) Aligned nozzle at set angle showing alignment tip on groove of alignment frame. (b) Alignment frame with attached handle to check the final alignment after installing on UPL assembly on LOA.

As seen in Fig. L.5(b), one can attach a handle to the alignment frame with three bolts to check the final alignment after installing on UPL assembly on LOA.

The alignment frame and its handle were printed on a Stratasys F370 with no infill (solid) and a layer height of 0.1778 mm. The build material was F123 ABS. The alignment tip was printed with no infill on a Stratasys J750 machine, with a resolution of 27 μm , using the hard Vero material.

Appendix M

Sound-particle-laser interactions

Sound field and melt pool interaction

The UPL-LDED-PF setup was tested down to a distance of about 30 mm between the nozzle tip and the build plate. A drilling effect in the melt pool (about 1 mm deep) was observed, corresponding to ultrasound vibration-assisted laser surface drilling setup [284]. The mechanism described in [284] for observed increased drilling depth is due to droplet ejection due to mechanical vibration; this was observed for a frequency of 20 kHz and vibration displacement of 27 μm .

Particle-sound interaction when particle is being heated by a laser

Although the UPL-LDED-PF setup described in Chapter 6 was designed to minimize particle-sound interaction while subject to laser irradiation, this might not be the case in other possible setups such as a coaxial laser setup.

The effect of a particle having a temperature higher or lower than the medium on the the force exerted by sound on the particle was measured in [285, 286, 287]. A theoretical model of this interaction is derived using King's derivation [288] for sound radiation forces, assuming no convection or gravity [289]. A more comprehensive model is derived by the authors in [289] to include convection and acoustic streaming [290].

A modern derivation of Gor'kov's theory for sound radiation forces can be found in [142]. Introductory notes comparing King's, Yosioka and Kawasima [291], and Gor'kov's derivations can be found in [292].

Sound field and laser interaction

Interaction between airborne ultrasound and a laser was shown to take place in [293], this was done to focus light using a cylindrical piezoelectric shell. This was modelled using a successive diffraction model, using the Fourier optics formalism [294]. This extends the work for an arbitrary Gaussian beam and a plane sound wave described in [295].

As stated in [295], for a beam diameter much smaller than the sound wavelength, the maximum deflection of a narrow laser beam in one sound time period due to sound waves in a fluid is given by [296]:

$$d_{max} = a\delta \left(\frac{dn}{dx}\right)_{max} = a\delta \frac{dn}{dP} \left(\frac{dP}{dx}\right)_{max} \quad (\text{M.1})$$

where a is the distance from the sound field to the line where d_{max} is measured, δ is the effective "width" of the sound field n is the optical index of refraction, x the axis perpendicular to δ and a , and P is the sound pressure. More details on the geometry the model is based on can be found in [297].

The dn/dP term can be found using the Lorentz–Lorenz equation in terms of specific volume and the equation for compressibility in terms of specific volume [296]. The $(dP/dx)_{max}$ term can be found by approximating the sound pressure as a plane wave given by $p = P_{max} \sin(2\pi x/\lambda)$ [298]. In this case p gives the largest pressure along x at some instant in one sound time period.

The final expression is given by [296]:

$$d_{max} = a\delta \frac{\kappa}{6n} (n^2 - 1)(n^2 + 2) \frac{2\pi}{\lambda} P_{max} \quad (\text{M.2})$$

where κ is the gas compressibility λ is the sound wavelength in the medium. Since n is very close to 1 for an ideal gas [299], one can simplify this expression further to get:

$$d_{max} \approx a\delta \kappa (n - 1) \frac{2\pi}{\lambda} P_{max} \quad (\text{M.3})$$

The index of diffraction can be found using the Gladstone-Dale relation given by [300]:

$$n = k\rho + 1 \tag{M.4}$$

where k is the Gladstone-Dale constant for a gas at a certain temperature and light wavelength (weakly dependent on both properties) and ρ is the gas density [300]. Using as an example the values of k for Ni and Ar (2.38×10^{-4} and 1.57×10^{-4} respectively [300]) and their densities given in Table N.2, together with the “worst case” parameters in Table M.1, gives a maximum deflection of 8 and 9 μm respectively. Using Eq. M.3 instead of M.2 gives an error of less than 0.1% for both gases.

Table M.1: Table showing parameters used for Eq. M.2 (all in SI units).

Parameter	Value
a	50.0×10^{-3}
δ	10.0×10^{-3}
κ	9.87×10^{-6}
P_{max}	8.0×10^3
f	40.0×10^3

The compressibility κ in Table M.1 is given by P_{atm}^{-1} for an ideal gas. This can be found using the ideal gas equation and the equation for compressibility in terms of volume. The wavelength is found using c/f , where c is the speed of sound in the medium and f is the sound transducer frequency. The speed of sound in an ideal gas can be found using Eq. N.4 and the values in Table N.2.

Although sound waves can be used to affect a laser beam when using water as a medium [298] and has been shown to be possible in air when using a different setup [293], the current setup is not expected to affect the laser beam when using Ni.

Appendix N

UPL feed gas considerations

Due to the oxygen and water content of air, a noble gas needs to be used. Two such gases that have similar properties are Nitrogen (Ni) and Argon (Ar).

Gas selection will depend on the following factors:

1. Sound speed should be as close as possible to prevent stretching/contraction of waves; the focusing process depends on waves reaching the focusing area with the required phase shift that was set at the ultrasound transducers
2. Sound speed should be as close as possible to prevent refraction of waves at medium shielding gas interface. This might be less of an issue when carrier gas jet is laminar
3. Similar acoustic impedance to allow most of the sound power to reach the focusing area inside the carrier gas jet

The wavelength is related to sound speed by:

$$\lambda = c/f \tag{N.1}$$

where c is the medium dependent sound speed and f is the ultrasound transducer frequency. Which means the fractional change in wavelength $(\lambda_2 - \lambda_1)/\lambda_1$ between two media is equal to the fractional change in sound speed $\beta = (c_2 - c_1)/c_1$. The change in angle from the incident angle of a wave through a change in medium is given by Snell's law as $\sin(\theta_i)/\sin(\theta_t) = c_1/c_2$ [196]. In terms of β this is given as:

$$\theta_\Delta = \frac{\theta_t - \theta_i}{\theta_i} = \frac{1}{\theta_i} \arcsin \left[\sin(\theta_i) \frac{c_2}{c_1} \right] - 1 \approx \beta \tag{N.2}$$

where the approximate expression is derived using small angle approximations. The fraction of sound power transmitted to a different medium as a fraction of incident power when the sound waves are normal to the interface is given by $\alpha_t = I_t/I_i = 4z_1z_2/(z_1 + z_2)^2$ [196] and in terms of fractional change in impedance $\gamma = (z_2 - z_1)/z_1$ its given by:

$$\alpha_t = 4 \frac{\gamma + 1}{(\gamma + 2)^2} \approx 1 - \frac{\gamma^2}{4} \quad (\text{N.3})$$

where the Taylor expansion approximation is valid for small values of γ . The acoustic properties of air, Ni and Ar, together with the fractional change with respect to air are given in Table N.1. As shown in Table N.1, there is a 1.6 and 7.1% change in wavelength when using Ni and Ar respectively and the transmitted power is 100 and 98.5% respectively. One can see from the table and Eq. N.3 that a mismatch in impedance corresponds to a smaller decrease in α_t compared to the sound speed related factors. One can see that Ni overall is much closer to air's relevant acoustic properties, particularly the fractional change in sound speed.

Table N.1: Table showing relevant gas acoustic properties in SI units, and fractional changes with respect to air and α_t values in percentages. θ_Δ was calculated at $\theta_i = 10^\circ$.

Gas	air	Ni	Ar
c	347	353	323
β	NA	1.6	-7.1
θ_Δ	NA	1.7	-7.2
z	409	402	524
γ	NA	-1.7	28
α_t	NA	100	98.5

What may be done to have an even better match for the sound speed or impedance of air, instead of using Ni, is a mix of two gases, if one of the gases has a lower sound speed or acoustic impedance and one a larger sound speed or acoustic impedance than air, one can deduce there will be mix ratio that produces a sound speed or acoustic impedance equal to air. This is the case for Ar and He. This blend has been used in LPBF to print Ti6Al4V [301] and its commercially available from Praxair as a welding gas mixture.

One can estimate the speed of sound for a blend of ideal gases using [302, 303]:

$$c_{mix} = \sqrt{\frac{\gamma_{mix} R_0 T}{M_{mix}}} \quad (\text{N.4})$$

where γ_{mix} is the specific heat ratio (c_p/c_v) of the mix, R_0 is the universal gas constant, T is the absolute temperature and M_{mix} is the molar mass of the mix. One could get more accurate results using the Van der Walls state equation [304]. The a and b Van der Walls state equation correction constants are low for He but Ar has a large a constant [305]. However in [304], a comparison was done between the ideal gas law and Van der Walls derived speed of sound for Ni with similar properties to Ar and the calculated values at 30 °C and 1 atm were equal to 4 significant figures. The specific heat ratio can be modeled as a weighted sum of each of the heat capacities [303]:

$$\gamma_{mix} = \frac{\sum x_i c_{pi}}{\sum x_i c_{vi}} \quad (\text{N.5})$$

where x_i is the mole fraction of each component, equal to volume fraction (using the ideal gas law), c_{pi} is the specific heat at constant volume for each component and c_{vi} is the specific heat at constant pressure for each component. The molar mass of the mix can be modeled by [302, 303]:

$$M_{mix} = \sum x_i M_i = \frac{R_0 T}{P} \sum x_i \rho_i \quad (\text{N.6})$$

where M_i is the molar mass of each component, P is absolute pressure and T is absolute temperature in Kelvins. Note the densities should be measured at the common pressure P and temperature T (for the values used in the ratio calculation, atmospheric pressure and 300 K) since the M_i values are element dependant constants. The second relationship is given by the ideal gas law for each component. Substituting Eqs. N.5 and N.6 into Eq. N.4 yields:

$$c_{mix} = \sqrt{P \frac{\gamma_{mix}}{\sum x_i \rho_i}} \quad (\text{N.7})$$

The density of the mix can be found using:

$$\rho_{mix} = \sum x_i \rho_i \quad (\text{N.8})$$

where ρ_i is the density of each component at the common temperature and pressure. Using Eqs. N.7 and N.8, the acoustic impedance of the mix is then given by:

$$z_{mix} = c_{mix} \rho_{mix} = \sqrt{P \gamma_{mix} \sum x_i \rho_i} \quad (\text{N.9})$$

One can get a smaller impedance difference by finding the volume fraction between Ar and He that gives the same sound speed; as can be seen in Fig. N.1, at a value of about 85% the β value for the mix is close to zero.

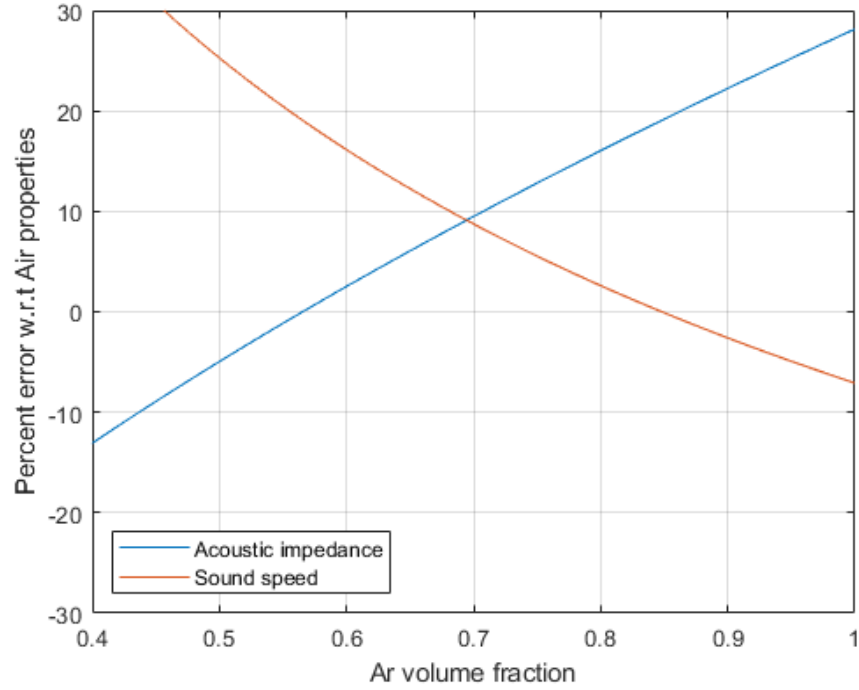


Figure N.1: Percent differences in sound speed and impedance w.r.t air as a function of volume fraction of Ar in Ar-He gas mix.

One can find the exact volume ratio of the mix that gives $\beta = 0$ by solving for one of the volume fractions such as for Ar in Eq. N.7. Using two components (Ar and He), the volume fractions can be written as $x_{Ar} = x$ and $x_{He} = 1 - x$. Eq. N.7 can be written as Eq. N.10.

$$\frac{c_{mix}^2}{P} [x c_{vAr} + (1 - x) c_{vHe}] [x \rho_{Ar} + (1 - x) \rho_{He}] = [x c_{pAr} + (1 - x) c_{pHe}] \quad (\text{N.10})$$

Eq. N.10 can be solved for x by solving for the root of the polynomial $ax^2 + bx + c$ in the range of 0 to 1, with a , b and c given by Eqs. N.11.

$$\begin{aligned}
A &= c_{air}^2/P \\
B &= c_{vAr} - c_{vHe} \\
C &= \rho_{Ar} - \rho_{He} \\
a &= ABC \\
b &= AB\rho_{He} + ACc_{vHe} - c_{pAr} + c_{pHe} \\
c &= Ac_{vHe}\rho_{He} - c_{pHe}
\end{aligned} \tag{N.11}$$

All the values used to determine x for matching the sound speed of air, using the c_p , c_v and R values found in [306], at 1 atm and 300 K are shown in Table N.2.

Table N.2: Table showing relevant gas properties in SI units. Density and sound speed where calculated using the ideal gas law.

Gas	Air	Ni	Ar	He
c_p	1005.0	1039.0	520.3	5192.6
c_v	718.0	743.0	312.2	3115.6
R	287.0	296.8	208.1	2076.9
ρ	1.177	1.138	1.623	0.163
c	347	353	323	1019
z	409	402	524	166

Note that under the ideal gas assumption (density being $P/(RT)$), the volume fraction x from Eqs. N.11 is independent of temperature, assuming the heat capacities are close to constant around 300 K which is the case for gases under the ideal gas law assumption. Using the values in Table N.2 and Eqs. N.11 to solve for x , the required volume ratio of gases to match the sound speed of air is 85% Argon and 15% Helium. This produces a gas mix with $\theta_\Delta = \beta = 0$, $\gamma = 19\%$ and $\alpha_t = 99\%$.

Appendix O

Repeat of adjacent tracks

In the first set of 27 tracks for the DOE, the cross-sectional area values at 800 W and 10 V did not show an appreciable change from the same values at 0 V. This is of course possible due to random variation in the current process setup or other unknown factors at that power. However, as described in Section 6.5.4, it is suspected that tracks 2 and 3 in plate 2 were done in the wrong order. This is because of the following reasons:

- Such a difference in cross-sectional area due to power is not expected since the change in power is not large and an effect was seen on both a lower and a higher powers
- The difference between the maximum and minimum values were large for both sets of data at 0 and 10 V and 800 W compared to all other sets of data
- When this was further investigated, it was observed that the two experimental values causing the above observation were two tracks beside each other

The cross-sectional area, height and width plots, as plotted in Section 6.5.4, with the original data and the suspected data in the opposite order are shown in Fig. O.1. As one can see from the figure, the data from the two tracks in the opposite order shows an effect at 800 W at 10 V, and also has a lower difference of maximum and minimum values (most noticeably at 0 V). In order to test this hypothesis, the UPL array and frame were re-installed in the DM3D machine and the two tracks were run again in the position on the plate. This is the final data reported in the Section 6.5.4 of the main article. The new data confirms there is an effect at 800 W, but the difference between the maximum and minimum values is larger; this is expected to happen since the UPL setup was reinstalled in the DM3D machine when the two tracks were made.

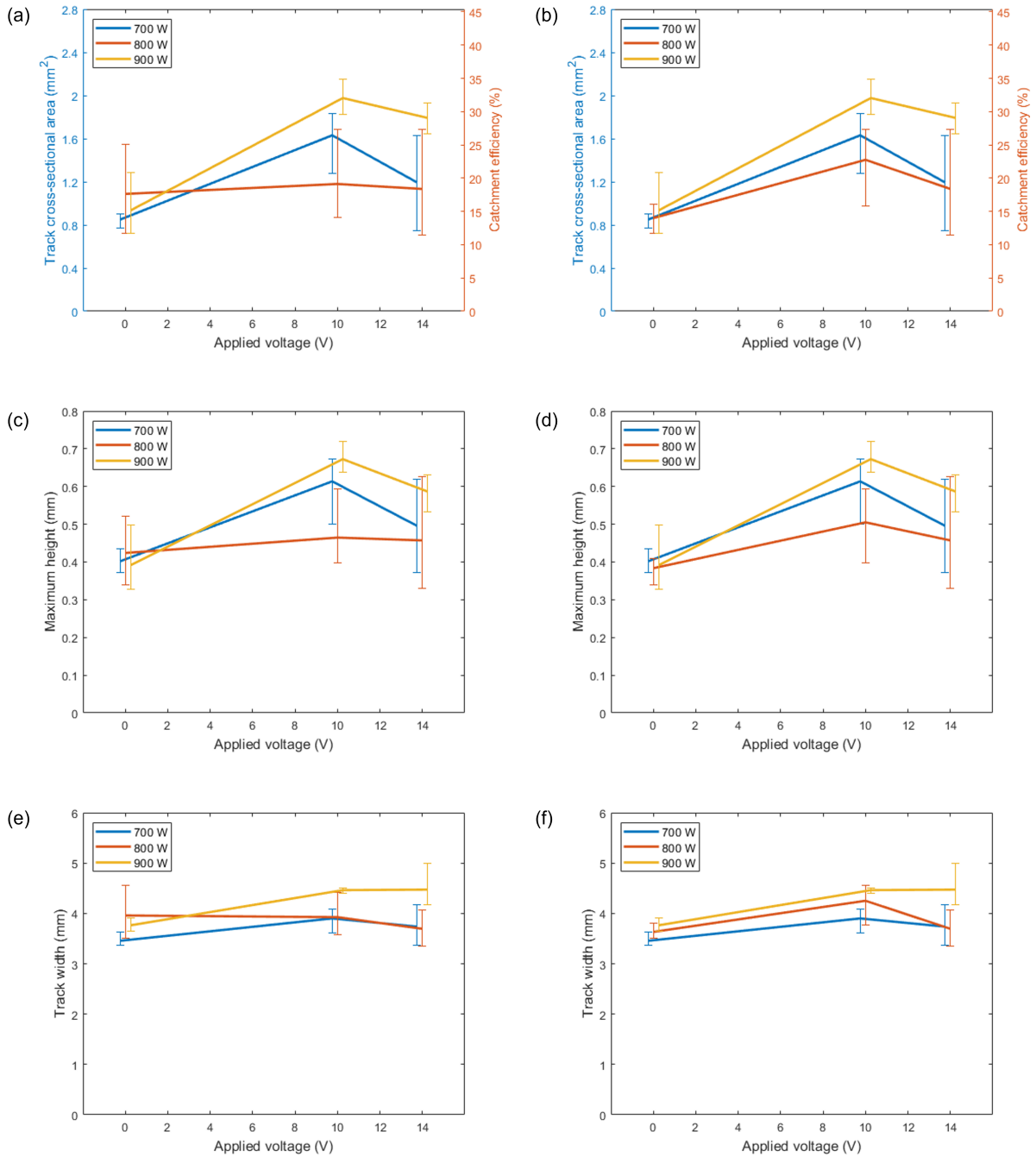


Figure O.1: Track (a) CS areas, (c) maximum heights, and (e) widths using original data. Track (b) CS areas, (d) maximum heights, and (f) widths using original data with tracks 2 and 3 in plate 2 in opposite order.